Spanwise forcing for turbulent skin friction reduction

An experimental investigation into active and passive flow control

M. W. (Max) Knoop

Delft University of Technology

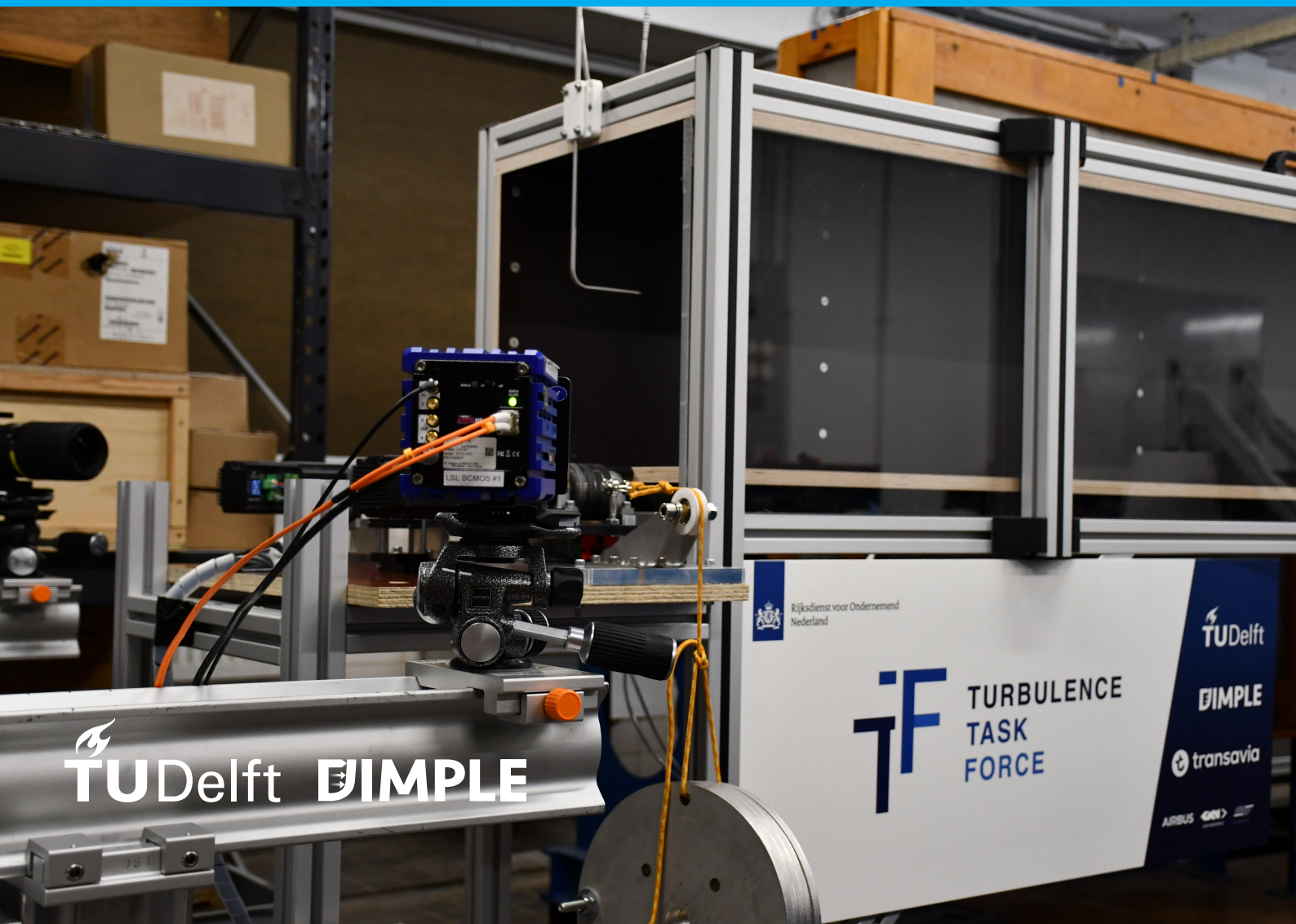

Spanwise forcing for turbulent skin friction reduction

An experimental investigation into active and passive flow control

by

M. W. (Max) Knoop

in partial fulfillment of the requirements for the degree of

Master of Science
in Aerospace Engineering

at the Delft University of Technology

To be defended on Thursday, April 13, 2023, at 13:30

Student number:	4551826	
Thesis committee:	Prof. dr. ir. L. L. M. (Leo) Veldhuis	Delft University of Technology
	Dr. ir. B. W. (Bas) van Oudheusden	Delft University of Technology
	Dr. ir. F. F. J. (Ferry) Schrijer	Delft University of Technology
	Dr. M. (Morgan) Li	Delft University of Technology
	Ir. F. H. (Friso) Hartog	Dimple Aerospace B.V.

TU Delft DIMPLE

Delft University of Technology

Faculty of Aerospace Engineering
Department of Flow Physics and Technology

The undersigned hereby certify that they have read and recommend to the Faculty of Aerospace Engineering for acceptance the thesis titled **Spanwise forcing for turbulent drag reduction** by **M. W. (Max) Knoop** in partial fulfilment of the requirements for the degree of **Master of Science** in **Aerospace Engineering**.

Dated: April 13, 2023

Chair of supervisory committee:

Dr. ir. B. W. (Bas) van Oudheusden

Supervisors:

Dr. ir. F. F. J. (Ferry) Schrijer

Ir. F. H. (Friso) Hartog

Readers:

Prof. dr. ir. L. L. M. (Leo) Veldhuis

Dr. M. (Morgan) Li

Preface

For the better part of a year, I have had the pleasure of working on the fascinating topic of turbulent drag reduction. During this year, which may be characterised as a turbulent time in the good sense of the word, I discovered that doing research is very close to my heart. This topic specifically allowed me to dive deep into turbulence and flow control mechanics. Aiming for this in-depth understanding was a real driver of my motivation. Even though a complete understanding of turbulence is paradoxically impossible, the road towards pursuing this goal has inspired me. This brings me to the end phase of the thesis. It is a weird feeling that all this hard work from the past year ends with a big stack of paper and a few hours of defence. I am, however, one of the lucky ones in that I have the opportunity to continue this exciting research for my doctorate degree. I am looking forward to what is to come!

First, I would like to express my gratitude to my close friends and family. These past months have not always been easy for me. I could not have finished this work without the support of the people closest to me. Thanks to my former rowing teammates and closest friend; Hidde, Jim, Tim, and Hajo, you have really supported me throughout my thesis. Always good banter or up for the occasional weeknight out, but also there for me on a more serious note. I want to thank my close friend Arjan, for all the cycling rides, dinners and good conversations we had. My family have been a great support for me. Credit goes to my dad and Tinneke for the numerous brainstorming sessions on my literature survey and thesis, the effective interview preparation, and for taking good care of me during my "writing retreats", thanks for all the support. I want to thank my mom for our numerous hikes this past year. Specifically, our holiday of hiking over 300 km throughout the Spanish Pyrenees was amazing. Lastly, I am thankful to everyone else who is dear to me and have supported me throughout this journey.

I want to thank everyone who has supervised and supported me throughout this project. Thank you Friso, for your support as my daily supervisor. It was great to share the enthusiasm we both have for this topic. Your work ethic always made me aim for the highest standards, which paid off; I am very glad about the results we achieved over the past months. I want to thank my supervisors from the TU Delft, Bas and Ferry, it has been wonderful working with you guys. I am happy that we can continue collaborating in the upcoming four years. Thanks to Olaf and Michiel, I am grateful for the amazing working environment and the opportunities Dimple has provided me with. I am looking forward to pursuing our quest for drag reduction together. This thesis would not have been possible without Wiebe en Lennart from BerkelaarMRT, thank you guys for designing and building our experimental apparatus. I want to thank Giulio and Giulia for teaching me the ins and outs of HWA and PIV and their endless support during my experimental campaigns. I want to thank all the students at Dimple, it was great to work with peers who share the same work ethic and compassion for this topic.

Finally, I would like to thank the author Robert M. Pirsig. He may not have contributed towards my work directly. Still, his books *Zen and the art of motorcycle maintenance* and the sequel Lila were inspiring for me. His work revolves around the central idea of Quality. In his so-called 'metaphysics of Quality', he promotes a Quality, or value-centred worldview compared to the subject-object reference system. I found this alternative perspective refreshing and invigorating, sparking my interest in philosophy. I would like to end with a quote from his first book:

> You are never dedicated to something you have complete confidence in. No one is fanatically shouting that the sun is going to rise tomorrow. They know it's going to rise tomorrow. When people are fanatically dedicated to political or religious faiths or any other kinds of dogmas or goals, it's always because these dogmas or goals are in doubt.

Max Knoop
Delft, March 2023

Abstract

Turbulent drag reduction (DR) is a crucial research area, as this can contribute to significant energy and emission reductions in various industrial and transportation applications. One such technique is the active flow control method of spanwise forcing. Spanwise forcing introduces a spatio-temporal spanwise wall oscillation as a boundary contrition. Consequently, a phase-varying spanwise velocity profile is generated, that poses useful interaction with the near-wall turbulence resulting in a drag-reduced flow state. DR values of over 40% have been found in both numerical and experimental realisations.

The objective of this thesis is twofold. Firstly, the idea is proposed that spanwise forcing can be realised passively by geometric surface modifications to create a spatially varying spanwise velocity profile. Secondly, supporting the first objective is the idea of investigating active flow control, in this case spatial spanwise forcing, which can aid in the development of passive techniques. The underlying philosophy is gaining understanding of the key factors and mechanisms that contribute to DR by studying active techniques. Subsequently, these leanings can be applied to advance the development of passive techniques. This research rationale is combined with a new pathway for turbulent DR. By actuating the outer-scaled low-frequency turbulent structures in the logarithmic layer, instead of the conventional approach targeted at high-frequency inner-scaled structures. Unlike the decreasing trend observed in inner-scaled actuation (ISA), outer-scaled actuation (OSA) exhibits a positive correlation between DR and Re_τ, making it particularly useful for practical applications that operate under high Reynolds number conditions, such as long-distance pipelines or aviation.

The first part of the thesis investigates the DR and OSA potential of passive techniques. Three techniques are considered: dimples, sinusoidal undulations and oblique wavy walls. Eight test plates are realised for direct force measurements and a detailed investigation into the scale-specific streamwise turbulence kinetic energy using hot-wire anemometry (HWA). From the direct force measurements, the DR trends with Re_τ are inconclusive due to uncertainties originating from a correction term and the results falling within the 95% confidence interval. A slight reduction of outer-scaled energy is observed for the sinusoidal undulations, hinting at effective OSA. Furthermore, one of the oblique wavy walls shows a broadband energy reduction in the wall-normal region $10 \leq y^+ \leq 100$.

The second part of the thesis is focused on active flow control, specifically, the method of spatial spanwise forcing. A research gap was identified for spatial forcing, with no experimental realisations to date and only a number of numerical studies. Furthermore spatial forcing is of interest since it shows the closest analogy to a passive counterpart. An experimental setup is proposed, titled the steady spanwise excitation setup (SSES). The experimental setup realises spatial forcing using a series of spanwise running belts that run in alternating spanwise directions so as to generate a spatial square wave forcing. The thesis presents a proof of concept of the aerodynamic working using a prototype setup with four belts. Stereo particle image velocimetry (PIV) measurements show that a significant flow control effect can be realised with this type of forcing, with a maximum DR value over 39%. Accordingly, the turbulent stresses are significantly reduced. The spanwise velocity profiles are in qualitative agreement with the model based on the laminar solution, with an almost exact match at $y^+ \leq 10$.

It is considered worthwhile to conduct additional research into the initial findings that suggest passive OSA. In order to investigate the related hypotheses more thoroughly, both balance and HWA experiments should be carried out at higher Re_τ values, to have a more significant influence of the outer-scaled structures. Secondly, with an effective proof of concept for spatial forcing, developing a full-scale experimental setup is deemed valuable. Recommendations are the extension of the streamwise extent of the actuation surface and the use of wider belts. Furthermore, extending the setup to allow for OSA is proposed.

Contents

List of Figures

List of Tables

Nomenclature

Acronyms and Abbreviations

CFR	Constant flow rate
CPG	Constant pressure gradient
CPI	Constant power input
DNS	Direct numerical simulation
DR	Drag reduction
DUT	Delft University of Technology
GSL	Generalised Stokes layer
HWA	Hot Wire Anemometry
ISA	Inner-scaled actuation
LDV	Laser Doppler Velocimetry
LES	Large eddy simulation
NPS	Net power saving
NR	Not reported
OSA	Outer-scaled actuation
OW	Oscillating wall
OWW	Oblique wavy wall
PIV	Particle Image Velocimetry
QSV	Quasi-streamwise vortex
SSES	Steady spanwise excitation setup
SSL	Spatial Stokes layer
SU	Sinusoidal undulation
SW	Standing/steady wave
TKE	Turbulence kinetic energy
TSL	Temporal Stokes layer
TW	Travelling wave
VLSM	Very large-scale motion

Greek Symbols

α	Oblique wave angle
δ	Boundary layer thickness
δ^*	Displacement thickness
δ_s	Penetration depth generalised- and spatial Stokes layer
δ_t	Penetration depth temporal Stokes layer
δ_v	Viscous length scale
δ_{99}	99% boundary layer thickness
η	Outer scaled wall-normal distance
κ	Von Kármán constant
λ	wavelength
μ	Dynamic viscosity
ν	Kinematic viscosity
ω	Frequency
Φ	Power spectral density
Π	Wake parameter
ρ	Density
τ	Shear stress
τ_w	Wall shear stress
θ	Momentum thickness
ξ	Non-dimensional pressure gradient

Non-Greek Symbols

ΔB	Shift in the additive constant of the logarithmic law
$\mathcal{T}$	Equivalent period
$\mathcal{U}$	Convection velocity
$\mathcal{W}$	Wake function
$\overline{I_x}$	Spatial development term of the FIK identity
$\tilde{u_i}$	Phase wise velocity fluctuations
A	Spanwise velocity amplitude
Ai	Airy function
B	Additive constant of the logarithmic law
c	Wavespeed

C_d	Drag coefficient
C_f	Skin friction coefficient
D	Dimple/sinusoidal undulation diameter
D	Spanwise displacement amplitude
d	Dimple/sinusoidal undulation depth
f	Frequency
f_c	Cut-off frequency
F_f	friction drag
H	Shape factor
H	Wall-normal displacement amplitude
h	Half height channel flow
k_x	Streamwise wavenumber
l	Characteristic length scale
l	Hot-wire sensor length
L_x	Streamwise dimple spacing
L_z	Spanwise dimple spacing
P	Turbulence kinetic energy production
P_{in}	Power input
r	Dimple/sinusoidal undulation rounding radius
Re	Reynolds number
Re_τ	Frictional Reynolds number
S	Surface area
T	Period of oscillation
t	time
U	Characteristic velocity scale
u', v', w'	Streamwise, wall-normal and spanwise velocity fluctuations
u, v, w	Streamwise, wall-normal and spanwise velocity components
U_∞	Freestream velocity
u_τ	Skin friction velocity
W	Sinusoidal undulation spanwise displacement amplitude
x, y, z	Streamwise, wall-normal and spanwise coordinates

Superscripts

$*$	Expressed in viscous units, scaled with actual u_τ
$+$	Expressed in viscous units, scaled with reference $u_{\tau 0}$
$-$	Mean
$\tilde{}$	Phase fluctuation component

Subscripts

dev	Development length
exp	Experiment
ls	Large-scale component
mod	Model
ss	Small-scale component
w	Evaluated at the wall
bump	Bump profile
composite	Composite profile
inner	Inner profile
outer	Outer profile

1

Introduction

The aviation industry contributes 2.4% to the total global CO2 emissions (Graver et al., 2019), and accounts for about 5% of global warming if non CO2 related effects are also considered (Nelson, 2018). Taking into account the growth of the sector, it is projected that CO2 emissions could increase by up to 25% by 2050 (Graver et al., 2019). To combat the growing environmental impact of the aviation industry, IATA and the aviation industry stakeholders set out the goal of neutral carbon growth from 2020 onward and carbon emission reduction of 50% in 2050 relative to the 2005 baseline (IATA, 2019). Their actions to reach these goals are set out in the roadmap in Figure 1.1. A substantial reduction in emissions is made through sustainable aviation fuels. Technological advancements make up another large portion of the plan's emission reductions. One of these technological advancements is flow control for turbulent drag reduction (DR). This is an area of high impact on emissions, with turbulent drag contributing to over 50% in the drag breakdown (Figure 1.2).

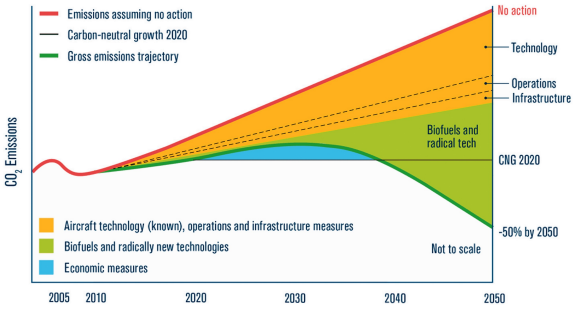

Figure 1.1: Roadmap for CO2 reduction goals for the aviation industry by IATA (2019).

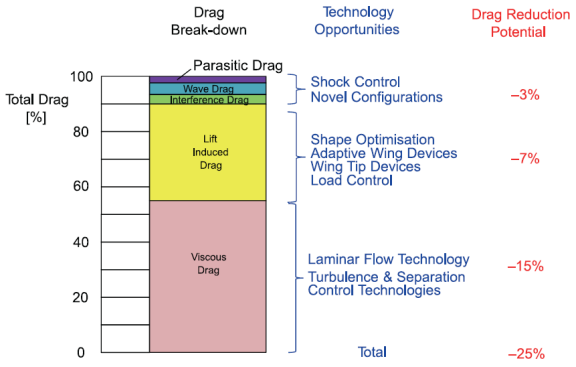

Figure 1.2: The drag breakdown, corresponding technological opportunities and drag reduction potential (Abbas et al., 2017).

Flow control can take two forms; either active, which uses a system architecture of sensors and actuators to apply actuation based on the sensed flow state, or passive, by employing geometric surface modifications or other surface treatments to create the desired control effect (Gad-el-Hak, 2000). Examples of active techniques are opposition control (Choi et al., 1994) and spanwise forcing (Quadrio et al., 2009). Their advantage is a high DR potential at the cost of complex practical implementations and the requirement of input power. On the other hand, passive techniques like riblets (Walsh, 1983) are easier to apply by (retro)fitting existing aircraft, at the cost of a lower DR potential. Riblets are the only passive technique in air that has proven itself for a reliable and substantial DR (Luchini and Quadrio, 2022). However, they still suffer some downsides in practical applications due to their microscopic size and sensitivity to the boundary layer state.

This brings the author to the motivation behind this thesis. The MSc. thesis is part of a larger research project that envisions *the development of passive flow control techniques for turbulent drag reduction that can reliably be applied in practical applications.* As such, it aims to contribute to impact and reduce the fuel burn in aviation, towards a more sustainable future.

1.1. Central concepts in the thesis

This research is built upon the trinity of three essential concepts, which are: (i) the outer-scaled actuation (OSA) pathway for turbulent drag reduction, (ii) spatial spanwise forcing as an active flow control technique, and (iii) passive recreation spanwise forcing. The three pillars are shortly introduced in the following subsections. The relation of these three concepts to the current work is depicted in Figure 1.3. The conceptual outline is further elaborated in the subsequent section that discusses the research philosophy.

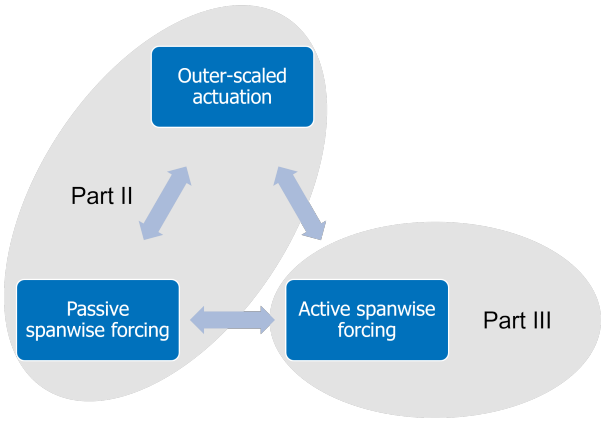

Figure 1.3: Conceptual outline of thesis based on the three important pillars; outer-scaled actuation, active spanwise forcing, and passive spanwise forcing.

1.1.1. Outer-scaled actuation

The first pillar is the outer-scaled actuation (OSA) pathway for turbulent DR, which involves aiming flow control at outer-scaled coherent turbulent structures in the logarithmic layer. These structures become increasingly dominant with Re_τ, in contrast to conventional inner-scaled actuation (ISA) that interacts with Re_τ invariant small-scale structures in the near-wall region. The advantage of OSA is that the DR margin increases with Re_τ, compared to a declining trend for the conventional ISA pathway. This makes OSA of particular interest for practical applications at high Re_τ like the aviation industry or the maritime sector.

1.1.2. Active spanwise forcing

The second pillar is the predetermined active flow control method of spanwise forcing, which uses spatio-temporal in-plane wall oscillations. The wall oscillations result in a phase-varying spanwise velocity profile, or Stokes layer, to pose a useful interaction with near-wall turbulence and reduce skin friction. Spanwise forcing has shown great potential as an active technique, with DR values over 40% and substantial net power savings (Ricco et al., 2021). In particular spatial spanwise forcing is of interest since this is the closest analogy to a passive counterpart. Regarding the OSA pathway, the first applications of OSA spanwise forcing have been successfully made by Marusic et al. (2021) and Chandran et al. (2022).

1.1.3. Passive spanwise forcing

The third pillar of this thesis work focuses on passively recreating spatial spanwise forcing through geometric surface deformations. The idea is that such a technique introduces a spatially varying spanwise velocity profile similar to the Stokes layer found under spatio-temporal wall oscillations. While several passive techniques exist, like dimples (van Nesselrooij et al., 2016) or oblique wavy walls (Chernyshenko, 2013), that are hypothesised to recreate spatial forcing, the added pressure drag resulting from surface modifications often nullifies any skin friction savings (Ghebali et al., 2017; van Campenhout et al., 2022). The idea of applying the OSA pathway to passive techniques for spanwise forcing is proposed to overcome this challenge. The hypothesised increasing DR margin with Re_τ, may result in a net DR at flight Reynolds numbers by offsetting the pressure drag penalty.

1.2. Research philosophy

This research proposes a new design philosophy to develop passive flow control techniques for industrial applications. First, the potential of OSA is promising. Specifically, the positive correlation between Re_τ and DR. Secondly, a central idea in the thesis is integrating active flow control with the development of passive flow control techniques. Active flow control allows for more significant flow modulation effects and better control over actuation parameters, which can help uncover flow modulation effects and working mechanisms. By investigating active techniques, research can identify the critical drivers behind the desired flow control response. With this knowledge, passive flow control techniques can be developed to realise such forcing. Predetermined active flow control techniques are of particular interest. The reason is that passive forcing cannot have a reactive component by definition. This research philosophy is outlined in a five-step methodology that is presented below:

1. Select an outer-scaled actuation predetermined active flow control technique that shows the potential to be translated into passive forcing.
2. Preliminary assessment of the potential to target outer-scaled flow structures for a number of passive techniques.
3. Develop the selected active flow control technique that employs outer-scaled actuation.
4. Study the working mechanism and flow modulation effects of the active technique, and note which specific forcing, modulation effects and working mechanisms are responsible for the drag reduction.
5. Use the findings from (4), to further develop a flow control technique that can recreate the desired forcing passively.

In light of this methodology, the thesis work is scoped. This study is focused on completing steps (1) and (2), and makes the first developments in step (3). The scope in relation to the three pillars is presented in Figure 1.3. Firstly, step (1) was addressed in a literature survey preceding this work (Knoop, 2023). Spanwise forcing was found to show most potential, specifically spatial forcing, since this shows the closest analogy to a passive counterpart. Step (2) is addressed in Part II of this work, which presents a preliminary investigation into passive spanwise forcing in combination with the application of OSA. The aim is not to develop these techniques for optimum performance but to investigate if outer-scaled spanwise forcing is possible with passive techniques. Part III presents the first developments regarding step (3). For this, a prototype experimental setup was developed as a proof of concept for spatial forcing. The concept uses a series of continuous belts running in alternating spanwise directions so as to generate a spatial square wave forcing. The prototype setup only allows for ISA due to a limited streamwise extent of the actuation surface. However, the concept can be extended to OSA if a full-scale setup is developed.

1.3. Research objectives

The research objective for this thesis is twofold. Firstly, the aim is to investigate passive OSA. Secondly, the development of an experimental setup for spatial spanwise forcing as a proof of concept. The main objective for the thesis is formulated as follows:

Experimentally investigate the potential of near-wall spatial spanwise forcing for turbulent drag reduction by (i) a preliminary assessment of passive techniques targeted at outer-scaled flow structures and (ii) the development and characterisation of an active experimental setup for this purpose.

The main objective is further specified through the following sub-objectives:

1. Assess the potential for outer-scaled actuation by means of passive flow control techniques.
2. Develop and realise an experimental setup that is able to create active spatial periodic forcing as a proof of concept.
3. Investigate the flow modulation effects and drag reduction potential of inner-scaled actuation using the active prototype setup for spatial periodic forcing.

1.4. Research questions

To achieve the research objectives, a set of specific research questions are formulated:

1. **To what extent can outer-scaled flow structure modulation effects through spatial periodic forcing be experimentally investigated within the available resources?**
   (a) How can spatial periodic forcing be realised using passive flow control methods? Would such methods be suitable for investigation in the present experimental conditions?
   (b) Is it possible to attain flow conditions with a substantial influence of outer-scaled flow structures? Can their distinct contribution to the total turbulent kinetic energy be observed?
   (c) How can spatial periodic forcing be realised using an experimental active flow control setup? To what extent are the wave parameters controllable? Can such a setup theoretically target the outer-scaled flow structures in the present experimental conditions?
2. **What is the drag reduction potential of outer-scaled actuation using passive spatial periodic forcing?**
   (a) What are the drag characteristics of the selected techniques in terms of total integral drag?
   (b) How does the drag performance relate to the frictional Reynolds number? Can increased effectiveness of drag performance be observed as a function of the frictional Reynolds number, similar to trends by Marusic et al. (2021)?
   (c) What is the effect of the selected techniques on the outer-scaled streamwise turbulence kinetic energy?
3. **What are the flow modulation effects associated with active spatial periodic forcing?**
   (a) Are there undesired effects on the turbulence and skin friction of the experimental setup due to the physical implementation of spatial periodic forcing?
   (b) What is the effect of the characteristic wave parameters A^+ and λ_x^+ on the mean streamwise velocity and stress profiles? Can a drag-reduced state be observed? How does the behaviour relate to the existing literature?
   (c) How are the small- and large-scale structures affected in terms of turbulence kinetic energy?
   (d) What are the downstream effects of the actuation? Over what spatial extent can a drag-reduced state be observed? How does this compare to the results of Ricco and Wu (2004)?
   (e) Can a spatial Stokes layer be observed? How do the spanwise velocity profiles compare to the laminar solution? What is the penetration depth of the Stokes layer?

1.5. Report overview

The theoretical background is presented in Part I. The OSA pathway and necessary boundary layer theory are discussed in Chapter 2. Subsequently, Chapter 3 gives a detailed overview of spanwise forcing.

The main body of the thesis is given in Part II and Part III, which aims to address the research questions. Part II serves as a preliminary investigation into the potential of passive OSA, hereby addressing research questions (1a), (1b) and (2). The methodology is presented in Chapter 4 followed by the experimental results in Chapter 5. This part is concluded in Chapter 6.

Part III focuses on the development of an active experimental setup to realise spatial spanwise forcing as a proof of concept, thereby addressing questions (1c) and (3). This part of the thesis is presented in paper format, which can be found in Chapter 7. Supplementary material to answer the remaining research questions is presented in Chapter 8. Concluding remarks for this part can be found in Chapter 9. A detailed methodology on the hot-wire anemometry (HWA) and particle image velocimetry (PIV) post-processing procedures is presented in Appendix C and Appendix B respectively.

The thesis is concluded inPart IV. The general conclusions can be found in Chapter 10, and recommendations and future outlook are presented in Chapter 11.

I

Theoretical background

2

Large-scale structures in turbulent boundary layers

This chapter discusses the influence of large-scale flow structures in the turbulent boundary layer, and lays out a approach for turbulent drag reduction by exploiting said structures. The necessary boundary layer theory for this literature report is presented in Section 2.1. Small-scale coherent structures are shortly discussed in Section 2.2. Following this, the theory on large-scale structures is discussed in Section 2.3. Section 2.4 introduces a new pathway dubbed outer-scaled actuation (OSA) for turbulent drag reduction, that exploits the large-scale flow structures.

2.1. Boundary layer theory

This section lays out the relevant boundary layer theory required for this literature survey. As may be clear from the title of this report, the focus of this report will be on turbulent boundary layers. All theory and equations are based on the book of White and Corfield (2006) unless stated otherwise. A right-handed Cartesian coordinate system is adopted as a frame of reference, the x, y, and z directions correspond to the streamwise, wall-normal and spanwise directions. The positive streamwise and wall-normal are aligned with the flow direction and away from the wall respectively. The corresponding velocity components are u, v, and w. The velocity components are represented as the summation of a mean and a fluctuating component indicated by an overbar and prime respectively (e.g. $u = \overline{u} + u'$).

2.1.1. Boundary layer properties

This section presents a number of relevant boundary layer properties for its analysis. They are: Reynolds number, boundary layer thickness, displacement thickness, momentum thickness and the shape factor.

Reynolds number

The Reynolds number is a useful parameter to describe the state of a boundary layer. It is a ratio of the inertial forces over the viscous forces of a fluid, defined as:

$$Re = \frac{\rho U l}{\mu} = \frac{U l}{\nu} \tag{2.1}$$

Here ρ, μ and ν are the fluid's density, dynamic viscosity, and kinematic viscosity respectively. U and l are the characteristic velocity and length scales. The velocity scale is usually set to the freestream velocity. The length scale is for example set as the cylinder diameter for flow past a cylinder. In boundary layer flows the development length (x) from the start of the boundary layer can be used.

Boundary layer thickness

In fully developed channel flows with height $2h$, the boundary layer thickness is defined as:

$$\delta = h \tag{2.2}$$

For external boundary layers, which will be the focus of this report, the thickness is usually approximated by δ_{99}, defined as the height at which 99% of the freestream velocity is reached:

$$\delta \approx \delta_{99} = y\big|_{u=0.99U_\infty} \tag{2.3}$$

Based on theoretical relations δ can be approximated for zero-pressure gradient boundary layers using the 1/7th power law:

$$\frac{\delta}{x} = \frac{0.17}{Re_x^{1/7}} \tag{2.4}$$

Where Re_x is the Reynolds number based on the freestream velocity and streamwise development length of the boundary layer.

Displacement thickness

The displacement thickness is related to the displacement of streamlines due to the boundary layer compared to an inviscid flow. It is defined as the integral of velocity deficit over the boundary layer height.

$$\delta^* = \int_0^\delta \left(1 - \frac{u}{U_\infty}\right) dy \tag{2.5}$$

The power law approximation is given by:

$$\frac{\delta^*}{x} = \frac{0.020}{Re_x^{1/7}} \tag{2.6}$$

Momentum thickness

The momentum thickness is a measure of momentum loss in the boundary layer and is related to the integral drag. It is defined as:

$$\theta = \int_0^\delta \frac{u}{U_\infty}\left(1 - \frac{u}{U_\infty}\right) dy \tag{2.7}$$

The power law approximation is given by:

$$\frac{\theta}{x} = \frac{0.017}{Re_x^{1/7}} \tag{2.8}$$

Shape factor

The shape factor is the ratio of displacement over momentum thickness. It is a non-dimensional measure for the velocity profile shape:

$$H = \frac{\delta^*}{\theta} \tag{2.9}$$

A low value of H represents a fuller profile and a high value to a more empty one. For the Blasius laminar boundary layer profile the shape factor is $H = 2.59$, and for turbulent boundary layers $H \approx 1.2 - 1.4$.

2.1.2. Skin friction

Shear stress develops due to the shearing motion of differential fluid velocities at different heights in the boundary layer. This shear stress is defined as:

$$\tau = -\rho\overline{u'v'} + \mu\frac{\partial u}{\partial y} \tag{2.10}$$

The shear stress has two terms, first the Reynolds shear stress ($\overline{u'v'}$) which is a turbulent contribution, and secondly the viscous contribution ($\frac{\partial u}{\partial y}$). A specific case of the shear stress is the wall shear stress given in Equation 2.11, due to the no-slip and no-penetration conditions the Reynolds stress is zero at the surface, which means the wall shear stress is only governed by the viscous term.

$$\tau_w = \mu\frac{\partial u}{\partial y}\bigg|_{y=0} \tag{2.11}$$

From the wall shear stress a skin friction coefficient can be defined as:

$$C_f = \frac{\tau_w}{\frac{1}{2}\rho U_\infty^2} \tag{2.12}$$

The power law approximation of C_f is given by:

$$\frac{C_f}{x} = \frac{0.027}{Re_x^{1/7}} \tag{2.13}$$

The total skin friction drag is the surface integral of the wall shear stress over the to-be studied surface as presented in Equation 2.14.

$$F_f = \int_S \tau_w dS \tag{2.14}$$

In this literature study, the focus is on methods and ways of reducing skin friction drag in the turbulent boundary layer. In general, the boundary layer profile of the turbulent boundary layer is *fuller* compared to its laminar counterpart, meaning it will have a steeper slope of the near wall velocity profile resulting in larger skin friction.

2.1.3. Non-dimensional scaling and boundary layer regions

In the turbulent boundary layer two distinct regions in the wall-normal direction can be identified, the inner and outer region respectively. The inner region is scaled with inner scales or so-called viscous scales. For this, the skin friction velocity u_τ and kinematic viscosity ν are used. The skin friction velocity is defined as:

$$u_\tau = \sqrt{\frac{\tau_w}{\rho}} \tag{2.15}$$

Based on this the viscous length scale is defined as:

$$\delta_v = \frac{\nu}{u_\tau} \tag{2.16}$$

When a variable is non-dimensionalized using inner scales, it is denoted by a superscript '+'. As an example the non-dimensional freestream velocity and wall-normal coordinate are:

$$u^+ = \frac{u}{u_\tau} \tag{2.17}$$

$$y^+ = \frac{y}{\delta_v} \tag{2.18}$$

Outer scaling is performed using δ and U_∞. As an example, the wall-normal coordinate can be scaled according to Equation 2.19.

$$\eta = \frac{y}{\delta} \tag{2.19}$$

An important form of the Reynolds number is the frictional Reynolds number (Equation 2.20). The skin friction velocity and boundary layer thickness are used as characteristic scales, resulting in the ratio of the outer over the inner length scale.

$$Re_\tau = \frac{u_\tau \delta}{\nu} = \frac{\delta}{\delta_v} \tag{2.20}$$

As above mentioned two regions are defined in the boundary layer. The inner region, where the viscous shear dominates, and the outer region, where the turbulent shear dominates. Both regions can be described by a scaling law in non-dimensional form. The inner law is described by Equation 2.21, it can be seen that the velocity profile is only a function of the wall coordinate in this region.

$$u^+ = f(y^+) \tag{2.21}$$

The outer law, also called the defect law, is a function of the outer scaled wall-normal coordinate and non-dimensional quantity ξ related to the pressure gradient. The argument is made that the wall influences this region only through a velocity deficit or retardation of the flow ($U_\infty - \bar{u}$).

$$\frac{U_\infty - \bar{u}}{u_\tau} = g(\eta, \xi) \quad \text{with} \quad \xi = \frac{\delta}{\tau_w}\frac{dp_e}{dx} \tag{2.22}$$

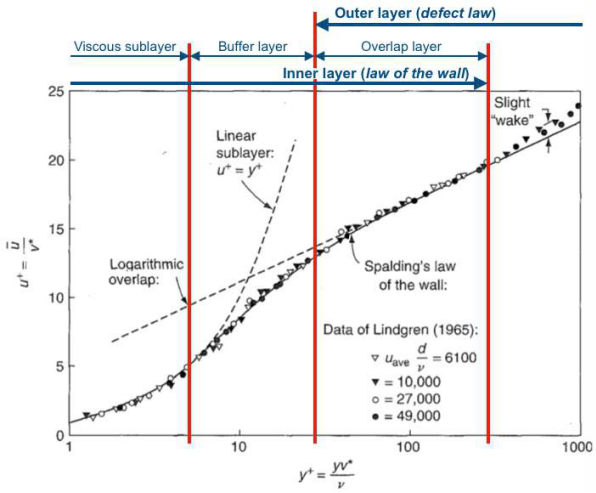

Figure 2.1: Boundary layer regions in the logarithmic velocity profile, figure adapted from White and Corfield (2006).

In Figure 2.1 the distinctive boundary layer regions can be seen. The inner- and outer region overlap in the overlap region, where both the viscous and turbulent shear are important. A new law can be obtained by equating both scaling laws, which results in a logarithmic relation for the overlap region, also known as the log layer, which shows up as a linear region as a result of the logarithmic wall-normal axis. In viscous scales, this log law is given by Equation 2.23. Where κ and B are near-universal constants for the canonical boundary layer, the values proposed by Coles and Hirst (1969) are $k \approx 0.41$ and $B \approx 5.0$. The frictional Reynolds number is a measure of scale separation between the inner and outer layer, as such the size of the log layer increases with increasing Re_τ. The size of the logarithmic region bound by inner and outer scales respectively, the conventional estimate is: $30\delta_v \leq y \leq 0.15\delta$ and in inner scales: $30 \leq y^+ \leq 0.15Re_\tau$ (Smits et al., 2011).

$$u^+ = \frac{1}{\kappa}\ln(y^+) + B \tag{2.23}$$

The inner layer is further divided into three separate regions. Firstly, the viscous sublayer, which only exists very close to the wall when $y^+ \leq 5$, where the viscous forces dominate. Therefore the velocity profile is linear: $u^+ = y^+$. Secondly, the earlier mentioned overlap layer is found at the outer edge of the inner region. Lastly, the buffer layer is the region between the viscous sublayer and the log layer. This region shows neither linear nor logarithmic behaviour. The buffer layer exists between $5 \leq y^+ \leq 30$. In summary, the three regions are defined as follows:

$0 \leq y^+ \leq 5$	Viscous sublayer	$u^+ = y^+$
$5 \leq y^+ \leq 30$	Buffer layer	
$30 \leq y^+ \leq 0.15Re_\tau$	Overlap layer	$u^+ = \frac{1}{\kappa}\ln(y^+) + B$

2.1.4. Taylor's hypothesis and convection velocity

In flow measurement techniques hot wire anemometry (HWA) allows for the collection of high-frequency temporal data but it only consists of a single point measurement. Spatial flow measurements can be obtained using particle image velocimetry (PIV), but here the high temporal frequency is lacking unless high frequency PIV is employed. To overcome the discrepancy of spatial resolution in HWA measurements, Taylor's frozen turbulence hypothesis was introduced (Taylor, 1938). Taylor's hypothesis allows for the transformation of temporal to spatial data under the assumption that turbulence is frozen. The frozen turbulence assumption states convective time scale is much larger than the advective one. This leads to the transformation using the convection velocity $\mathcal{U}$:

$$\lambda_x = \frac{\mathcal{U}}{f} \tag{2.24}$$

Furthermore, for a direct transformation between temporal and spatial coordinates, Taylor's hypothesis is applied as:

$$x = \mathcal{U}t \tag{2.25}$$

The convection velocity can be assumed as the local mean velocity in a large portion of the boundary layer. In the region of high shear, i.e. close to the wall, the convection velocity however differs from the mean. The convection velocity can be found by cross-correlating two velocity signals at a known streamwise distance (Δx), this will result in a correlation peak located at Δt (Kim and Hussain, 1992). Physically this is the time it takes for the coherent structures to convect a distance Δx downstream. From this, the convection velocity is defined as:

$$\mathcal{U} = \frac{\Delta x}{\Delta t} \tag{2.26}$$

In Figure 2.2 an example of these cross-correlations can be seen. Using this approach Kim and Hussain (1992) found a fixed convection velocity of $\mathcal{U}_w^+ = 10$ in the near-wall region for $y^+ \leq 10$. Their findings are presented in Figure 2.3, where the streamwise convection velocity can be seen to be constant and larger than the mean in the near-wall region. Similar findings were made by Krogstad et al. (1998) and Del Álamo and Jiménez (2009).

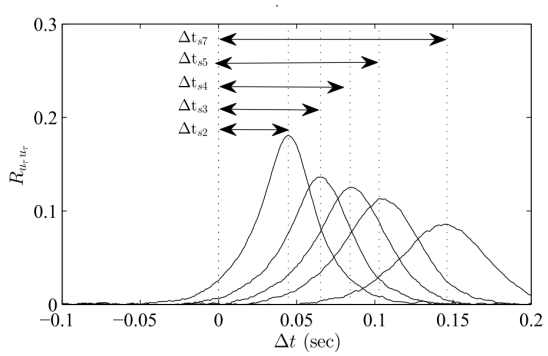

Figure 2.2: Cross-correlation of skin friction obtained using hot wire films, from left to right the curves indicated an increasing streamwise separation between the sensors (Talluru, 2014).

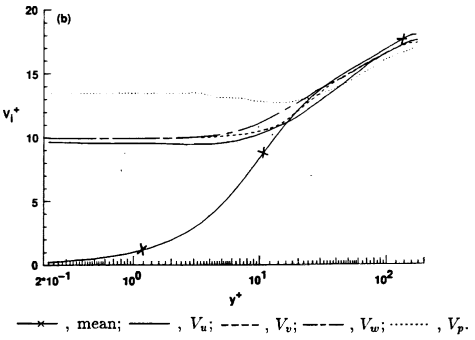

Figure 2.3: The results for the convection velocity found by Kim and Hussain (1992), streamwise convection velocity indicated by V_x.

2.2. The near-wall cycle

A large portion of turbulence kinetic energy (TKE) production originates from the near-wall region, which in turn contributes to the turbulent skin friction. The TKE production can be defined by (Panton, 2001):

$$P = -\overline{u'v'}\frac{dU}{dy} \tag{2.27}$$

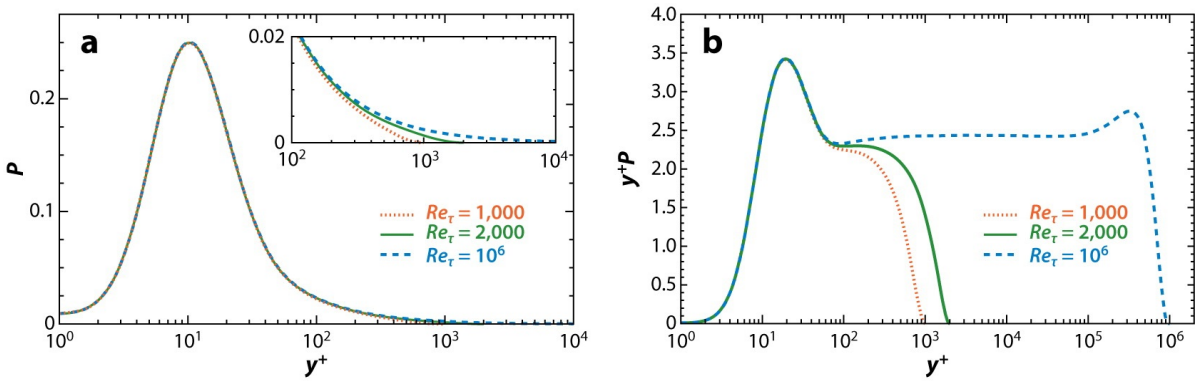

Figure 2.4: Turbulence kinetic energy production for a range of Reynolds numbers: (a) semi-logarithmic representation and (b) premultiplied representation (where equal areas represent equal contributions to the total production). Data from Marusic et al. (2010b), figure adapted by Smits et al. (2011).

In Figure 2.4 production profile over the boundary layer height can be seen. It shows a large peak at $y^+ = 12$ which is a result of an auto-generating cycle between near-wall coherent structures creating turbulent

fluctuations; the so-called near-wall cycle. Jiménez and Pinelli (1999), explain that the near-wall cycle is a result of the interaction between two types of coherent structures; the streamwise velocity streaks located close to the wall and the quasi-streamwise vortices (QSVs) in the buffer layer.

As to the cyclic nature between the two entities, the QSVs are believed to be responsible for the creation of the streaks. The QSVs create an upward motion of low momentum fluid at the wall and a downward motion of higher momentum towards the wall, resulting in an alternating pattern of high- and low-velocity streaks in the near-wall region. A schematic of this is presented in Figure 2.5. The generation of the QSVs is generally less understood but Jiménez and Pinelli (1999) hypothesise that streaks give rise to the QSVs presumably by inflectional instabilities in the velocity profile.

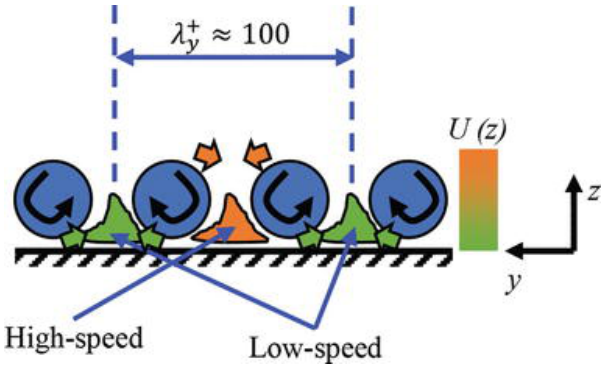

Figure 2.5: A schematic representation of the near-wall cycle between the streaks and quasi-streamwise vortices (Harun and Lotfy, 2018).

The low-speed streaks were first observed by Kline et al. (1967) using hydrogen bubble visualisation as shown in Figure 2.6. They are streamwise elongated regions of low momentum fluid. The streaks oscillate in the wall-normal direction in the region of $y^+ \leq 12$, and were found to become unstable and break up when lifted higher into the region $10 \leq y^+ \leq 30$. This breaking up, or bursting, is responsible for increased turbulence activity and fluctuations, increasing the TKE production. Their spanwise spacing is approximately $\lambda_z^+ = 100$, and the streamwise extent is around $\lambda_x^+ = 1{,}000$.

The QSVs are regions of concentrated vorticity aligned in the streamwise direction, with a streamwise extent of over $100\delta_v$ (Miyake et al., 1998). The structures were first identified by Clark and Markland (1971) who observed counter-rotating streamwise vortices in the region above the streaks at $7 \leq y^+ \leq 70$ with a slight inclination from the wall (3° to 7°), therefore naming them quasi-streamwise.

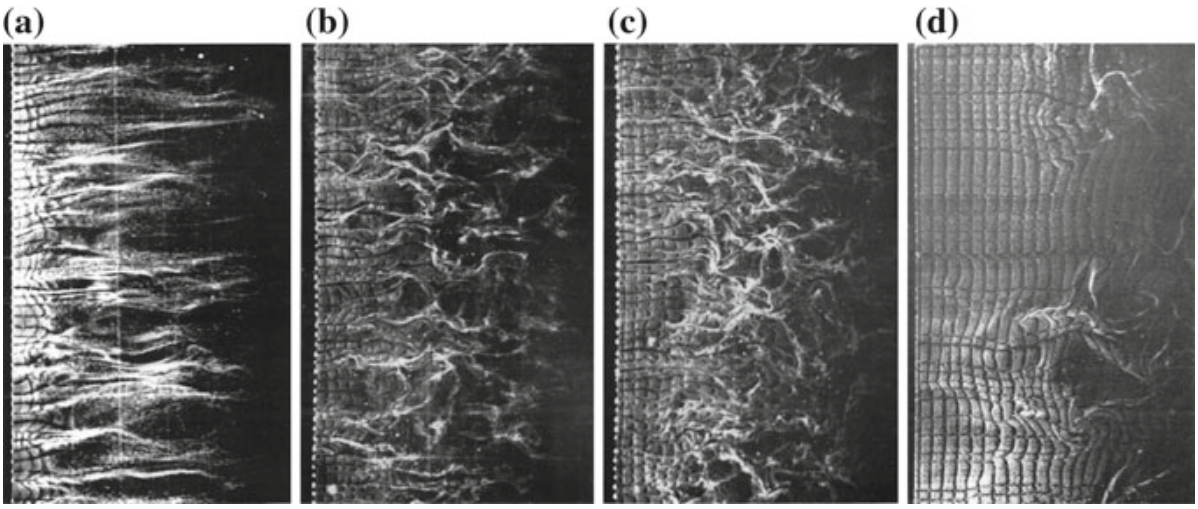

Figure 2.6: Hydrogen bubble flow visualisation of the low-speed streaks by Kline et al. (1967): (a) $y^+ = 2.7$, (b) $y^+ = 38$, (c) $y^+ = 101$ and (d) $y^+ = 407$.

As part of the near-wall cycle, so-called ejection and sweep events occur. These events are associated with the QSVs that provide the transfer of low and high momentum fluid between different regions in the boundary layer. Ejection events describe the ejection of low-momentum momentum fluid from the wall towards higher

regions. The low momentum corresponds to negative streamwise fluctuations $u' < 0$, and moving away from the wall corresponds to positive wall-normal velocity i.e. $v' > 0$. Sweep events originate as an opposing reaction to the ejections, where high-speed fluid moves towards the wall. Following the same analogy, these events correspond to positive streamwise fluctuations $u' > 0$ and a negative wall-normal component $v' < 0$. The sweep and ejection events can be characterised using a quadrant representation of the streamwise and wall-normal velocity fluctuations u' and v'. Such a quadrant is shown in Figure 2.7, the ejection and sweep events are then found in quadrants Q2 and Q4. Wallace et al. (1972) showed that the main contribution to the Reynolds shear stress stems from these Q2 and Q4 effects. Furthermore, these events are associated with negative $\overline{u'v'}$ and hence they contribute positively to TKE production according to Equation 2.27.

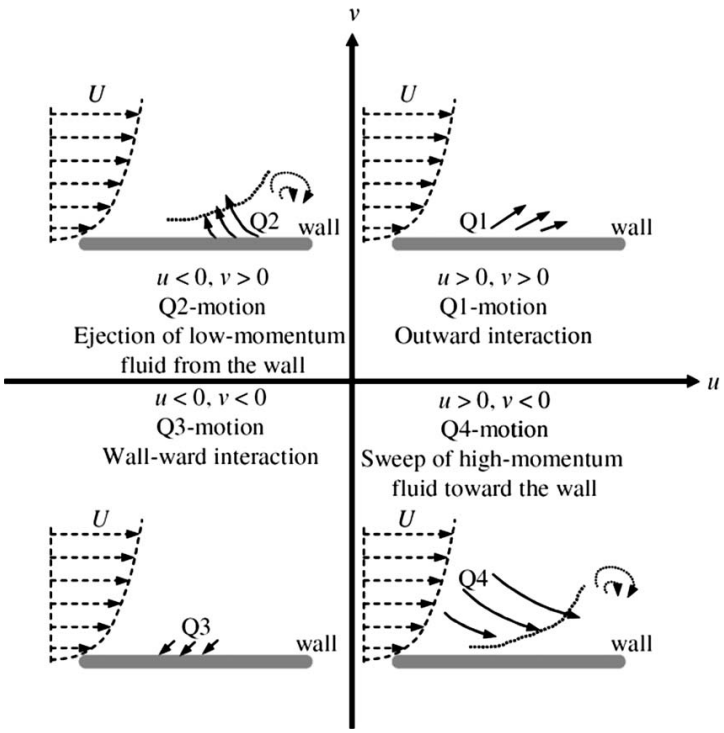

Figure 2.7: Quadrant view of u' and v' and the events for each quadrant (Cai et al., 2009).

2.3. Very large-scale motions

The coherent structures discussed so far are restricted to the near-wall region. A lot of useful insight is obtained from the analysis of coherent structures in these regions, however, the log layer presents its own structures that add to the dynamics of turbulence. The structures are large in scale compared to the near-wall motions and follow an outer scaling. They are often referred to as very large-scale motions (VLSMs) or superstructures (Smits et al., 2011). This section aims to first explore the characteristics of VLSMs, followed by an elaboration on the influence of VLSMs in the near-wall region.

The reason why most of the earlier research on coherent structures is limited to the near-wall region is that this coincides with the peak of TKE production at $y^+ = 12$, which can be observed in Figure 2.4 (a). However, if one considers the bulk contribution to the TKE production, the pre-multiplied production (Py^+) presented in Figure 2.4 (b) is more useful. Here equal areas represent equal contributions to the total production. At low Re_τ values that are often used in experiments, the bulk production indeed originates from the near-wall regions. However when Re_τ increases the log layer grows in size, as a result, TKE production from the logarithmic layer grows to be dominant. The crossover at which the contributions from the near-wall region and log layer are equal is at $Re_\tau = 4{,}200$ (Marusic et al., 2010b).

2.3.1. Characteristics of VLSMs

Structures in the log region were first identified by Blackwelder and Kovasznay (1972) the structures showed strong coherence in time and spatial coherence up to 10δ. These were later identified as long meandering structures of spanwise alternating positive and negative velocity fluctuations, and named very large-scale motions (Kim and Adrian, 1999; Balakumar and Adrian, 2007; Hutchins and Marusic, 2007a). In Figure 2.8 an example of the VLSMs observed by Hutchins and Marusic (2007a) can be seen. The structures follow an outer scaling: their streamwise extent is in the order of $\lambda_x \approx 15-20\delta$ with a spanwise spacing of $\lambda_z \approx 0.3-0.5\delta$. The most energetic structures can be found at the geometric mean location of the log layer at $y/\delta = 0.06$. (Hutchins and Marusic, 2007a).

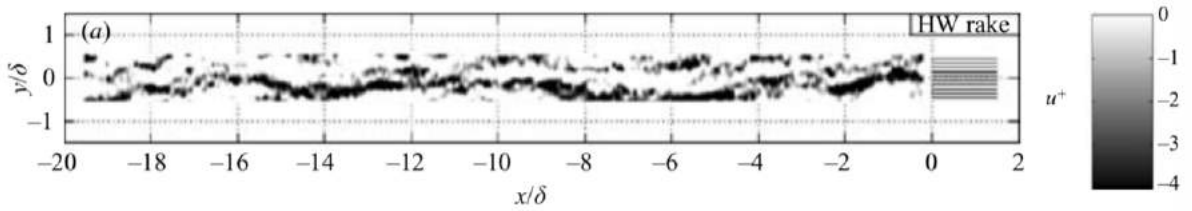

Figure 2.8: Example of VLSMs at $y/\delta = 0.15$ for $Re_\tau = 14{,}380$ obtained using a hot-wire rake. The x-axis is reconstructed using Taylor's hypothesis and a convection velocity based on the local mean (Hutchins and Marusic, 2007a).

The influence of the VLSMs and their scale dependence on frictional Reynolds number were visualised by Hutchins and Marusic (2007a) though the boundary layer spectrograms as presented in Figure 2.9. The spectrogram shows contours of the pre-multiplied spectral energy of the streamwise velocity fluctuations ($k_x\Phi_{u'u'}/u_\tau^2$) over the boundary layer height. The x-axis corresponds to the boundary layer height, the y-axis presents the spectral wavelength in inner and outer scales on the left and right sides respectively. For the low Re_τ case a clear energetic site can be seen, indicated by the white '+', located at $y^+ = 15$ and $\lambda_x^+ = 1{,}000$, corresponding to the near-wall cycle. As Re_τ increases to 7,300, the emergence of a second energetic site (black '+') can be observed as a result of the VLSMs, located at $y/\delta = 0.06$ with $\lambda_x = 6\delta$. The lower length scale compared to $15-20\delta$ is due to the decorrelation of the single-point measurement under the meandering motion (Hutchins and Marusic, 2007a).

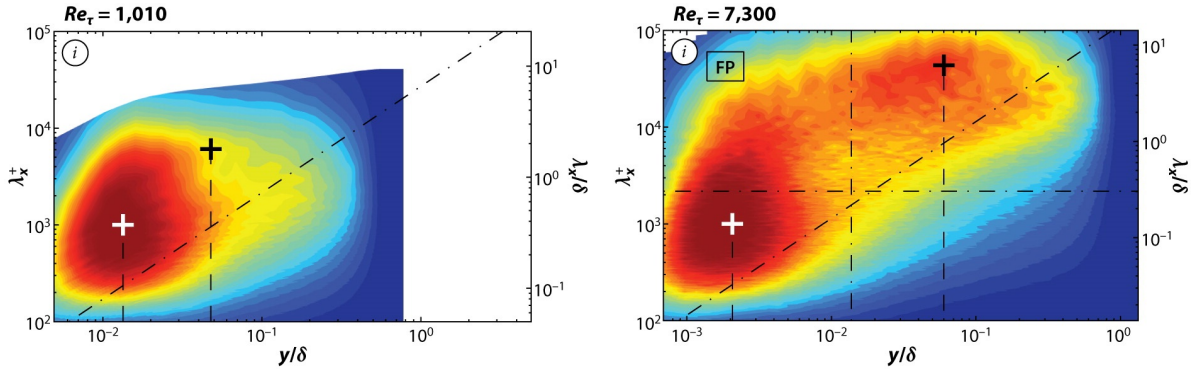

Figure 2.9: The spectrograms of the pre-multiplied spectral energy of the streamwise velocity fluctuations $k_x\Phi_{uu}/u_\tau^2$ for $Re_\tau = 1010$ and $Re_\tau = 7300$ from Hutchins and Marusic, 2007a. The inner a outer energetic sites are indicated with white and black '+' signs. Figure adapted by and obtained from (Smits et al., 2011).

A key observation by Hutchins and Marusic (2007a) is that the inner site of the near-wall cycle shows no Re_τ dependence and has a fixed magnitude while the outer site of the VLSMs shows growth with Reynolds number. This is further supported by Marusic et al. (2010b) who decomposed the streamwise turbulence intensity (which is the integral spectral energy) into a small- and large-scale component using a spectral cut-off filter at $\lambda_x = \delta$. In Figure 2.10 this decomposition can be seen, (a) presents the decomposition and the total turbulence fluctuations at $Re_\tau = 7{,}300$, (b) shows the small- and large-scale components for increasing Reynolds numbers of $Re_\tau = 3{,}900, 7{,}300, 19{,}000$. Here it can be seen that the small scales are invariant with Reynolds number and a clear growth of the large scale TKE is observed. It is unclear if this growing strength of the outer peak is bounded or tends to a limit with increasing Reynolds number, however, the increasing

contribution is still found for up to $Re_\tau = 19{,}000$.

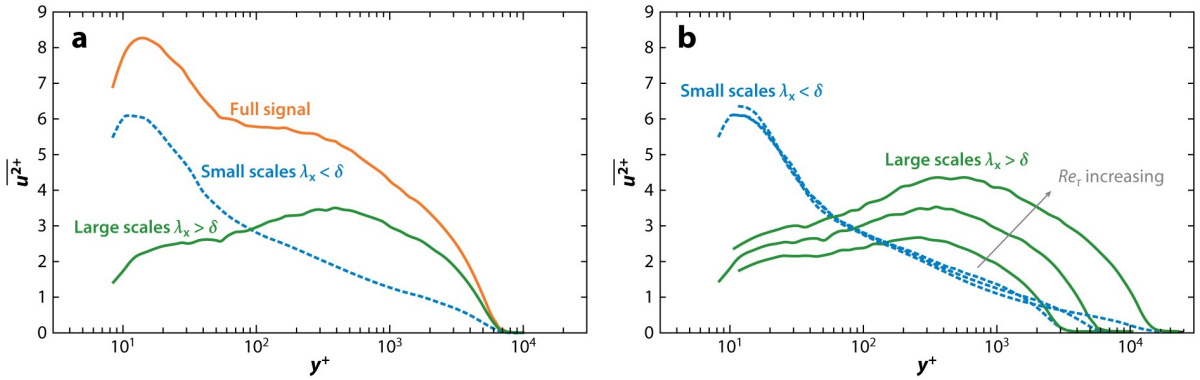

Figure 2.10: Scale decomposition of the streamwise turbulence intensity profile $\overline{u'^2}/u_\tau^2$. (a) for $Re_\tau = 7{,}300$, combined with the total signal and (b) for $Re_\tau = 3{,}900$, 7,300, 19,000. Data from Marusic et al. (2010b), figure adapted by Smits et al. (2011).

2.3.2. Effects on the near-wall turbulence

Apart from their presence in the log layer, VLSMs also influence the near-wall turbulence. Two effects were identified as footprinting and modulation.

Footprinting

Firstly, a so-called footprinting effect is observed, which means the VLSMs in the log layer have a footprint on the turbulence in the near-wall region. In the paper of Hutchins and Marusic (2007a) this footprinting was explained based on the channel flow simulations of Del Alamo et al. (2004). In Figure 2.11 the streamwise velocity fluctuations in the log-region and buffer region are presented in the top figures. Firstly the difference in scales between the buffer layer and log layer can be observed, in the log region small scale structures are absent. When closely observing Figure 2.11 (b) a weak superimposed footprint from the large-scale motions can be observed. This effect is brought out when filtering is applied, using a simple $h/2 \times h/2$ Gaussian. The large-scale structures in the log layer clearly emerge, however, more interestingly the filtered near-wall fields show very similar structures. This is the footprinting or superimposition of the VLSMs to the near-wall region. The large scale footprint was observed earlier by Abe et al. (2004) for a channel flow DNS and using LES by Tsubokura (2005). Similarly, Hutchins et al. (2005) has shown a measurable correlation between the log region and the near-wall regions, concluding low wavenumber energy leaching into the near-wall region.

The conclusion of Hutchins et al. (2005) is supported by the boundary layer energy spectrograms in Figure 2.9. The growth of the inner peak can be observed, under the influence of the emergence of the outer site. The energy of larger wavelengths (i.e. low wavenumbers) in the order of $\lambda_x^+ \gtrsim 10^4$ is increases with an increasing Reynolds number. This additional low wavenumber energy is essentially a superimposed footprint of the VLSMs on the near-wall turbulence. Hutchins and Marusic (2007b) show that for $Re_\tau = 7{,}300$ the magnitude of the near-wall energy is dictated for about a quarter by the VLSMs in the log region using the scale decomposition in Figure 2.10. As aforementioned this outer peak is believed to grow with Reynolds number, therefore the strength of low wavenumber energy in the near-wall region also increases. Due to the additional low wavenumber energy, the near-wall peak of turbulence intensity grows as observed in Figure 2.10. Hutchins and Marusic (2007a) proposed an empirical formulation of this peak by fitting a line to existing measurement data:

$$\overline{u'^{2+}}_{peak} = 1.036 + 0.965 \ln(Re_\tau) \tag{2.28}$$

Modulation of small-scale turbulence

Besides the footprinting effect, Hutchins and Marusic (2007b) observed that the magnitude of small-scale fluctuations in the near-wall regions are influenced by the large-scale log region motions. The raw velocity signal was decomposed into a small- and large-scale component at a cut-off wavelength of $\lambda_x = \delta$ as presented in Figure 2.12. The large-scale component in Figure 2.12 (b) shows regions of positive and negative fluctuations, which correspond to these VLSMs, a region of negative fluctuations is indicated between the

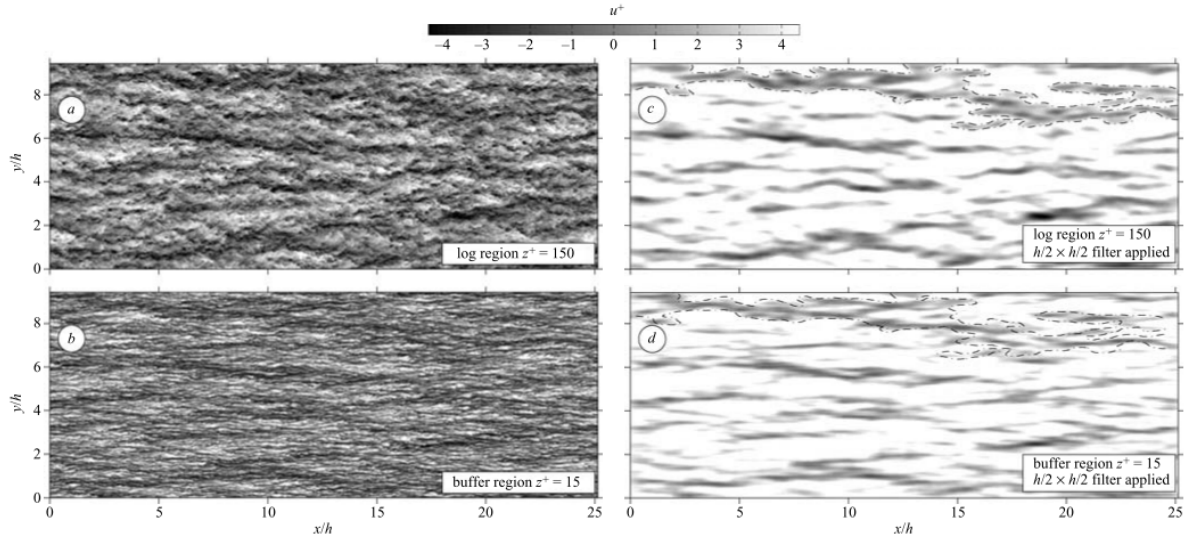

Figure 2.11: Instantaneous velocity fluctuations of the DNS channel flow at $Re_\tau = 934$ by Del Alamo et al. (2004), (c) and (d) show the filtered velocity fluctuations using a Gaussian $h/2 \times h/2$ filter (Hutchins and Marusic, 2007a).

dashed lines. In Figure 2.12 (c) the effect of this negative large-scale fluctuations region can be seen on the small scales. A reduction in the magnitude of the small-scale fluctuations is observed, which becomes more evident if the wavelengths $\lambda_x^+ \leq 1,000$ are considered. This effect on the near-wall fluctuations is similar to pure amplitude modulation. Hutchins and Marusic (2007b) have shown that this effect is significant, at $y^+ = 15$ the turbulence intensity under positive large-scale fluctuations is about 17% larger compared to the decelerated region. The modulation effect is believed to grow with increasing Reynolds number because of the growing energetic content of the large scales. The modulation effect has also been observed for the other fluctuating components and Reynolds stresses.

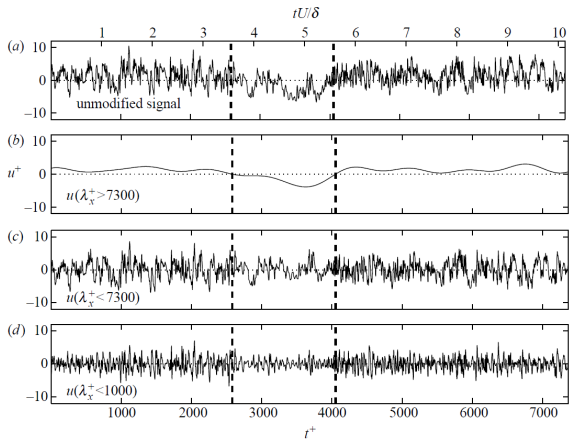

Figure 2.12: Fluctuating signal in the near-wall region at $y^+ = 15$, (a) raw signal, (b) large-scale fluctuations $\lambda_x \geq 7,300$, (c) small-scale fluctuations $\lambda_x \leq 7,300$, (d) small-scale fluctuations $\lambda_x \leq 1,000$ (Hutchins and Marusic, 2007b).

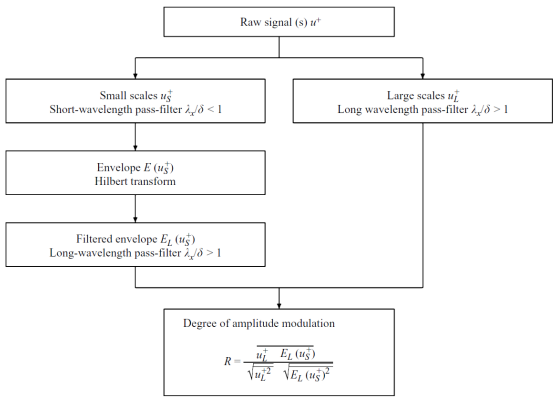

Figure 2.13: Decoupling procedure by Mathis et al. (2009) to obtain the modulation coefficient R.

Amplitude modulation can be understood using a simple example. Consider two simple sinusoidal signals, the carrier signal with frequency f_c is modulated by an envelope signal of lower frequency f_e. The spectral energy will show a peak at the original f_c plus two additional peaks at $f_c \pm f_e$. With regards to the example, the small-scale signal is considered the carrier which is modulated by the large-scale component. This means that even at low pass filtering the signal to obtain the small-scale components a large-scale influence is retained. Fourier analysis will tend to mask the modes of amplitude modulated signals, especially in the case of turbulence where both the carrier and envelope contain widely separated broadband energy

(Hutchins and Marusic, 2007b).

Mathis et al. (2009) further investigated the relationship between the large- and small-scale structures in the boundary layer. To overcome the masking in Fourier analysis, the authors demodulated the signal using the Hilbert transform. This essentially allows them to obtain the modulation envelope of the small-scale signal. The high-pass filtered envelope is then used to calculate the correlation coefficient R that is a measure for the degree of modulation. The procedure is outlined in Figure 2.13. The paper presents strong evidence confirming the initial observations about the modulation effect by Hutchins and Marusic (2007b). Furthermore, they confirm an increasing degree of modulation as the Reynolds number increases.

2.4. A new pathway to turbulent skin friction reduction

This section presents a new pathway to turbulent drag reduction by exploiting large-scale flow structures. The large-scale pathway or outer-scaled actuation (OSA) is promising for drag reduction at high Reynolds numbers. Conventional flow control techniques for turbulent drag reduction, focus on attenuating the inner-peak associated with small-scale turbulence and is therefore named inner-scale actuation (ISA). Examples are riblets (Walsh, 1983) and spanwise forcing (Quadrio et al., 2009). In comparison to the ISA pathway, OSA is targeted at the large-scale flow structures associated with the log layer.

In Section 2.3 it was shown that the small-scale TKE is invariant with Re_τ while the outer peak grows in strength as Re_τ increases. This is further elucidated in Figure 2.14 that shows the wall-shear stress spectra and the inner- and outer-scaled contributions to the shear stress as a function of Re_τ. In Figure 2.14 (b) it can be seen that the inner-scaled (indicated in green) contribution to the wall-shear stress stays fixed while the low wavenumber outer-scaled (red) contribution grows as the Reynolds number increases. This means the small-scale contribution to the total TKE shows a declining trend as Re_τ grows. As such, the drag reduction margin of ISA declines with Re_τ. By employing OSA, an increasing trend is expected between drag reduction and Re_τ. This makes the new pathway interesting for high Reynolds number applications.

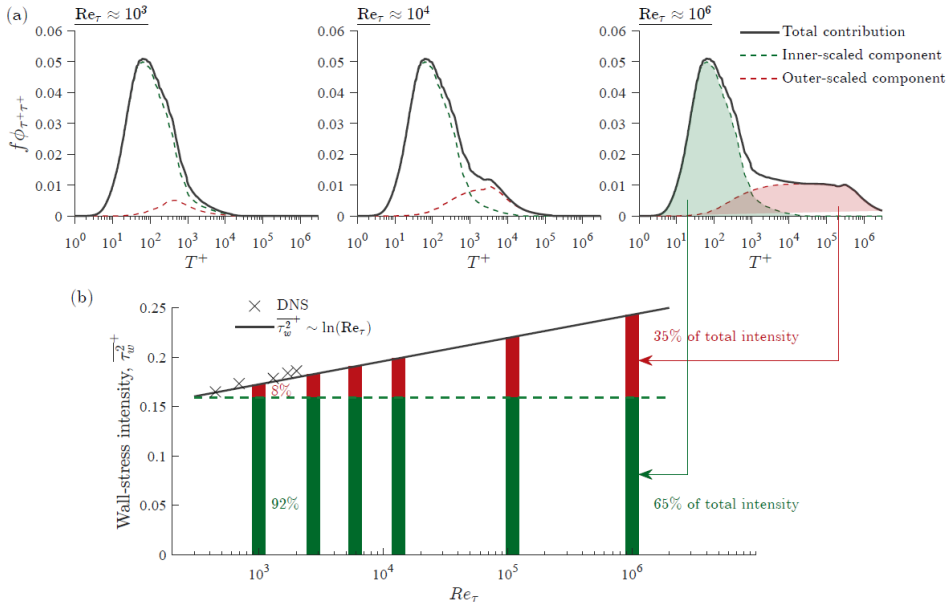

Figure 2.14: Contribution of inner- and outer-scaled turbulent structures to (a) the wall shear stress spectra for $Re_\tau \approx 10^3, 10^4, 10^6$ and (b) the wall shear stress. The predictive model of Marusic et al. (2010a) was used to compute the spectra. (Chandran et al., 2022)

An example of OSA flow control is the experiment by Abbassi et al. (2017). Opposition control using wall-normal jets was applied to the large-scale structures which were sensed at the wall through their footprint. Their control architecture was effective at attenuation the TKE of the outer peak, as well as reducing the footprinting and modulation in the near-wall region. This pathway has not seen much attention in passive and predetermined flow control. However, a recent paper by Marusic et al. (2021), exploited this pathway using spanwise forcing. In line with the hypothesis mentioned above, they showed that the drag reduction trends favourably with Re_τ, compared to a declining trend for ISA actuation.

3

Spanwise forcing through wall motion

This chapter provides details on the active flow control method of spanwise forcing though wall motion, that was selected to be the focus of this thesis. The relevant theoretical background is presented in Section 3.1. Following this is a historical overview of the existing body of literature in Section 3.2. The drag reduction and net power saving potential is discussed in Section 3.3. Section 3.4 elucidates the working mechanisms responsible for drag reduction. With regards to practical applications of this technique, non-sinusoidal forcing and the OSA pathway are discussed in Section 3.5 and Section 3.6, furthermore the practical considerations are presented in Section 3.7.

3.1. Theoretical background on spanwise wall motion

This section aims to provide the theoretical background required for the in-depth analysis of spanwise wall motion to follow.

3.1.1. Three forms of spanwise wall motion

This flow control method works on the concept of imposing a periodic wall movement in the spanwise direction. Three forms of spanwise wall motion exist: oscillating wall (OW) or temporal forcing, standing wave (SW) or spatial forcing, and streamwise travelling waves (TW). The latter is a combination of spatial and temporal forcing in the form of a spatial wave which propagates in the streamwise direction. The three actuation schemes are presented in Figure 3.1 below.

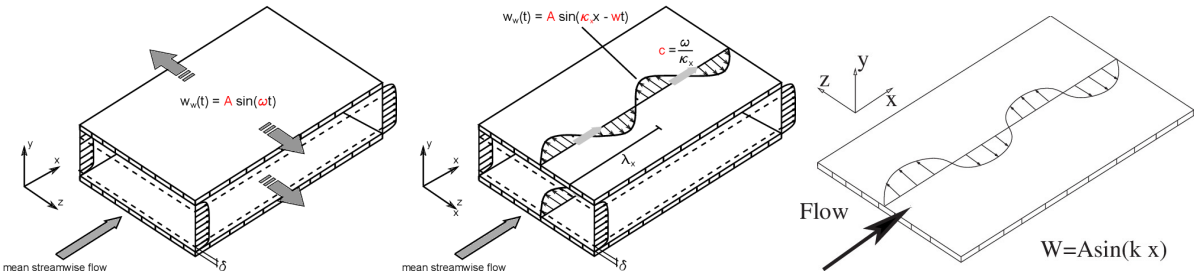

(a) Wall oscillations (Gatti, 2015). (b) Streamwise travelling waves (Gatti, 2015). (c) Standing waves (Yakeno et al., 2009).

Figure 3.1: Actuation schematics for the three types of spanwise wall motion

TW wall motion is the most general form of spanwise wall motion, since it contains both a temporal and a spatial mode in the form of a frequency (ω) and wavenumber (k_x). A is the spanwise velocity amplitude of the wall motion i.e. the maximum velocity the wall will move at. The wall motion is imposed through a sinusoidal function for the spanwise wall velocity (w_w):

$$w_w(x,t) = Asin(k_x x - \omega t) \tag{3.1}$$

The TW will propagate in the streamwise direction with a wavespeed c which is defined as:

$$c = \frac{\omega}{k_x} \tag{3.2}$$

The OW and SW forcing are obtained by setting k_x and λ_x to zero for either forcing respectively. In the OW case one usually considers the period (T) instead of the angular frequency, the two are related through $\omega = 2\pi/T$. This way the wall motion is imposed as:

$$w_w(t) = Asin\left(\frac{2\pi}{T}t\right) \tag{3.3}$$

For SW forcing the transformation $k_x = 2\pi/\lambda_x$ is applied, to obtain a wavelength instead of the wavenumber. The wall motion is imposed as:

$$w_w(x) = Asin\left(\frac{2\pi}{\lambda_x}x\right) \tag{3.4}$$

For scaling and comparison purposes the relevant parameters are non-dimensionalized in viscous units as:

$$A^+ = \frac{A}{u_\tau} \tag{3.5}$$

$$T^+ = \frac{Tu_\tau^2}{\nu} \tag{3.6}$$

$$\lambda_x^+ = \frac{\lambda_x u_\tau}{\nu} \tag{3.7}$$

Another relevant parameter that can be defined is the peak-to-peak spanwise displacement amplitude of the wall, which is defined in Equation 3.8. For the standing wave, the displacement is undefined, since the wall will not displace back and forth but rather has a fixed wall velocity at each location in space.

$$D = \frac{AT}{\pi} \tag{3.8}$$

Lastly, it is useful to define the equivalent time step ($\mathcal{T}$), which is the equivalent period that is seen by a moving observer. For TW and SW forcing, the equivalent period seen by the near-wall turbulence can be used to make a comparison to the temporal case. For this the convection velocity is used, which is approximately $\mathcal{U}_w^+ \approx 10$ in the near-wall region (Kim and Hussain, 1992; Krogstad et al., 1998; Del Álamo and Jiménez, 2009). One can also use this to estimate an equivalent wavelength for standing forcing by applying Equation 3.10.

$$\mathcal{T} = \frac{\lambda_x}{\mathcal{U}_w - c} \tag{3.9}$$

$$\lambda_{x,eq} = \mathcal{T}\mathcal{U}_w \tag{3.10}$$

3.1.2. Laminar Stokes layer

A spanwise velocity profile will develop resulting from spanwise forcing, due to viscous effects in the near-wall region. At the wall, the spanwise velocity is dictated by the imposed wall motion, which decays to zero when moving in the positive wall-normal direction. Under conventional actuation parameters (i.e. $T^+ \approx 100$) this profile is mostly confined to the viscous sublayer and lower part of the buffer layer, where the viscous forces dominate. Therefore it is valid to use the laminar boundary layer equations. Stokes (1851) introduced the solution for the oscillating wall, also referred to as the temporal Stokes later (TSL), which is defined as follows:

$$w(y,t) = A\exp\left(-y\sqrt{\frac{\pi}{\nu T}}\right)\cos\left(\frac{2\pi t}{T} - y\sqrt{\frac{\pi}{\nu T}}\right) \tag{3.11}$$

The solution for the TSL can be non-dimensionalized in viscous units according to:

$$w^+(y^+,t^+) = A^+\exp\left(-\frac{y^+}{\delta_t^+}\right)\cos\left(\frac{2\pi t^+}{T^+} - \frac{y^+}{\delta_t^+}\right) \tag{3.12}$$

Here δ_t^+ is the penetration depth of the Stokes layer, defined as the location where the spanwise velocity decays to $w^+ = e^{-1}A^+$:

$$\delta_t^+ = \sqrt{\frac{T^+}{\pi}} \tag{3.13}$$

It has been shown that the laminar Stokes layer indeed matches the phase averaged turbulent profiles (i.e. the actual turbulent Stokes layer) for actuation parameters close to the optimum of $T^+ \approx 100$ or below (Choi et al., 2002; Yao et al., 2019). If T^+ gets too large, the Stokes layer will penetrate deeper into the boundary layer and the assumption of the laminar solution becomes invalid.

In the case of streamwise travelling waves, the classical Stokes layer does not apply anymore because of the added spatial component. Quadrio and Ricco (2011) introduced the concept of the laminar generalised Stokes layer (GSL), which is an analytic relation for the laminar Stokes layer in both spatial and temporal space. They derived the GSL by applying the concept of travelling waves to a laminar Poiseuille flow and found the following relation with normalization constant C and Ai, which is the Airy function of the first kind:

$$w(x,y,t) = A\Re\left\{ Ce^{i(k_x x-\omega t)} Ai\left[e^{\pi i/6}\left(\frac{k_x \left.\frac{\partial u}{\partial y}\right|_{y=0}}{\nu} \right)^{1/3} \left(y - \frac{\omega}{k_x \left.\frac{\partial u}{\partial y}\right|_{y=0}} \right) \right] \right\} \tag{3.14}$$

$$C = \frac{1}{Ai\left[e^{\pi i/3}\left(\frac{k_x \left.\frac{\partial u}{\partial y}\right|_{y=0}}{\nu} \right)^{1/3} \left(\frac{\omega}{k_x \left.\frac{\partial u}{\partial y}\right|_{y=0}} \right) \right]} \tag{3.15}$$

With a penetration depth δ_s that now also depends on the slope of the streamwise velocity profile instead of only on the characteristic wave parameters:

$$\delta_s = \left(\frac{\nu}{k_x \left.\frac{\partial u}{\partial y}\right|_{y=0}} \right)^{1/3} \tag{3.16}$$

In non-dimensional form, the relation simplifies to:

$$w^+(x^+,y^+,t^+) = A^+\Re\left\{ C^+ e^{i(k_x^+ x^+ - \omega^+ t^+)} Ai\left[e^{\pi i/6}\left(\frac{y^+}{\delta_s^+} - \frac{\omega^+}{\delta_s^+ k_x^+} \right) \right] \right\} \tag{3.17}$$

$$C^+ = \frac{1}{Ai\left[e^{\pi i/3} \frac{\omega_x^+}{\delta_s^+ k_x^+} \right]} \tag{3.18}$$

Where the penetration depth is now defined based on the wavenumber or wavelength as:

$$\delta_s^+ = \left(\frac{1}{k_x^+} \right)^{1/3} = \left(\frac{\lambda_x^+}{2\pi} \right)^{1/3} \tag{3.19}$$

For the GSL Quadrio and Ricco (2011) compared the laminar GSL and the turbulent counterpart using the data of a large number of travelling wave simulations by Quadrio et al. (2009). When the equivalent period is below the threshold, $\mathcal{T}^+ \leq 120$, excellent agreement is found between the analytical and numerical solutions. If this threshold is exceeded the penetration depth increases, and the laminar and turbulent solutions decouple. The authors also showed that the solution of the GSL is undefined in the oscillating wall case since $k_x = 0$, Quadrio and Ricco (2011) demonstrated using an asymptotic analysis that in the limit of k_x going to zero, the GSL solution approaches the solution of the TSL. In case of SW forcing, there will be no wavespeed i.e. $\omega = 0$, the GSL reduces to the so-called spatial Stokes layer (SSL) where $C = 1/Ai(0)$:

$$w^+(x^+,y^+) = A^+\Re\left\{ Ce^{ik_x^+ x^+} Ai\left[e^{\pi i/6}\left(\frac{y^+}{\delta_s^+} \right) \right] \right\} \tag{3.20}$$

In Figure 3.2 a comparison between the TSL and SSL for $T^+ = 100$ and $\lambda_x^+ = 1{,}000$ respectively can be seen. Both profiles have a strong resemblance to each other. This is in line with the earlier explained equivalent period, which will be $\mathcal{T}^+ = 100$ for the SSL.

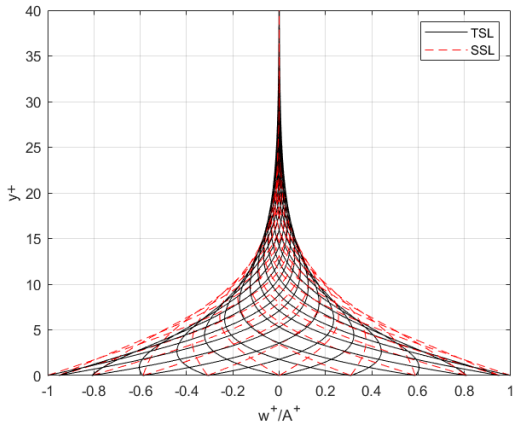

Figure 3.2: The temporal and spatial Stokes layer for one phase, with $T^+ = 100$ and $\lambda_x^+ = 1,000$.

3.1.3. Performance characteristics

The purpose of these spanwise transverse forcing schemes is to obtain a drag reduction with respect an unactuated case. To assess the performance, two metrics are used, drag reduction (DR) and net power saving (NPS).

The DR margin is defined as the change in skin friction drag or wall shear stress with respect to the unactuated case, it is multiplied by 100 to get a percentage of drag reduction. Here the quantities with a subscript zero indicate the unactuated case:

$$\mathrm{DR}(\%) = 100\left(1 - \frac{\tau_w}{\tau_{w,0}}\right) \tag{3.21}$$

It is important to also consider the power input for the actuation. This power input is defined as a percentage of the pumping power of the unactuated flow. The pumping power is equal to $P_x = \tau_w U_\infty$ for boundary layers and $P_x = 2\tau_w U_b$ for channel flows. Where U_b is the bulk velocity, the multiplication with two is due to the top and bottom walls. The input power for the spanwise motion is then defined by the slope of the spanwise velocity profile at the wall which dictates the friction that has to be overcome:

$$P_{in}(\%) = \frac{100\mu}{P_x(t_f - t_i)} \int_{t_i}^{t_f} \int_S w_w \left.\frac{\partial w}{\partial y}\right|_{y=0} dS dt \tag{3.22}$$

Here t_i and t_f are the initial and final time for the temporal average, S is the surface area over which the actuation is present. Note that this relation does not consider mechanical and electrical losses and only gives the theoretical power to drive the flow under transverse actuation. The net power saving is the metric indicating how much energy is saved in total, so taking into account the input power. In the case of constant flow rate conditions the net power savings is simply the difference between the drag reduction and the input power:

$$\mathrm{NPS}(\%) = \mathrm{DR} - P_{in} \tag{3.23}$$

3.1.4. Flow constraints and scaling

As a result of a DR, the wall shear stress and thereby u_τ decreases. Therefore a choice has to be made for the non-dimensional scaling of the boundary layer profiles. Scaling can be performed by either the canonical reference friction velocity $u_{\tau 0}$ or the actual one u_τ. Scaling with the reference $u_{\tau 0}$ will show absolute changes in the turbulence statistics while using u_τ allows for a useful comparison of the near-wall turbulence statistics. In case of the mean profile, scaling with $u_{\tau 0}$ shows a thickening of the viscous sublayer, while the profiles collapse in the log layer. The opposite will be seen for scaling with u_τ, with similarity in the viscous sublayer and an upward shift of the logarithmic region.

For numerical simulations of internal flows, a constraint has to be set that drives the flow in the streamwise direction. In general, two options are available to impose this flow: imposing a constant flow rate (CFR), or by imposing a constant pressure gradient (GPG). The use of the CFR constraint is the most common. Like in a boundary layer the shear stress will reduce as a result of DR in CFR flows. In CPG flows, however, the

wall shear stress will not change but the bulk velocity in the channel increases. When the velocity profiles are scaled with $u_{\tau 0}$ the differences between the actuated and uncontrolled flow of the two constraints can be seen in Figure 3.3. The CPG and CFR constraints result in the same profiles as scaling with u_τ and $u_{\tau 0}$ for the boundary layer flow. Due to the changing viscous scales in CFR conditions, Re_τ decreases, which can lead to relaminarization at low values of Re_τ. A third constraint is occasionally used in literature, the one of constant power input (CPI), which means the sum of the power to drive the flow and the actuation power is kept fixed. When a drag reduction is obtained, both an increase in flow rate and a decrease in wall shear stress arise.

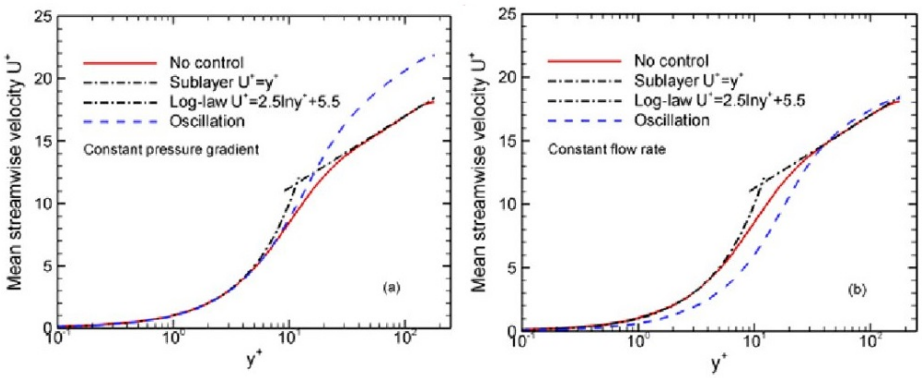

Figure 3.3: Comparison of the velocity profiles: (left) CPG and (right) CFR (Zhou and Ball, 2008).

3.1.5. Velocity decomposition under spanwise periodic motion

For statistical analysis of turbulent velocity signals one can apply Reynolds decomposition. This means the signal is decomposed into two parts, a mean indicated by an overbar like $\overline{u_i}$ and the stochastic velocity fluctuations around the means mean of the signal indicated by a prime like u_i'.

Due to oscillatory forcing an additional phase-wise component is introduced. For statistical analysis it is important to decompose the velocity signal into three parts; the mean components, a phase-wise fluctuation component and the stochastic velocity fluctuations. The additional decomposition into the phase-wise components means that the fluctuations are incoherent with the phase-wise velocity introduced by the forcing. The decomposition looks as follows where the phase-wise fluctuations are defined as $\widetilde{u_i}$:

$$u_i = \overline{u_i} + \widetilde{u_i} + u_i' \tag{3.24}$$

Yakeno et al. (2009) showed that for the TSL and SSL, the streamwise and wall-normal phase fluctuations are small compared to the spanwise component. Furthermore, the wall-normal phase fluctuations for temporal forcing are identically zero.

3.2. Historical overview

This section presents an overview of the body of academic literature on spanwise wall motion. A number of review papers have been consulted in the writing of this overview (Choi, 2000; Quadrio, 2011; Leschziner, 2020; Luchini and Quadrio, 2022). In particular the review of Ricco et al. (2021), has proven to be very useful, it presents a detailed and extensive overview of (almost) all the work in the field. All the literature is summarised in two tables, Table 3.1 provides an overview of the experimental work and Table 3.2 presents the numerical studies. The tables are adapted from Ricco et al. (2021) and are supplemented with the latest research. The three actuation schemes are indicated by their acronyms. Furthermore, the distinction is made between boundary layer flows, channel flows and pipe flow. In the numerical overview, the imposed flow constraint is shown, the table only contains direct numerical simulations (DNS) i.e. resolving all the turbulent scales. Where available the actuation parameters are presented and the maximum drag reduction is indicated.

The experimental research is mostly confined to boundary layer flows, the main reason for this is the easier realisation of spanwise forcing in a wind tunnel compared to a channel flow. Additionally, the majority of the research is focused on the OW, only three papers consider TW forcing and SW forcing has not been realised experimentally as of now. The field of numerical research is larger than the experimental work, one of the reasons is the relatively easy implementation of the spanwise velocity boundary condition. Most of

the numerical studies use the channel flow geometry, since this allows for periodic boundary conditions and smaller domains compared to external flows, reducing the computational costs. In both fields relatively low frictional Reynolds numbers are considered, with the maximum being $Re_\tau = 1,125$ and $Re_\tau = 2,108$ in the experimental and numerical field respectively. With the exception of the papers by Marusic et al. (2021) and Chandran et al. (2022), they experimentally attained a frictional Reynolds number up to $Re_\tau = 12,800$ for upstream travelling waves.

Study	Forcing	Re_τ	T^+	A^+	D^+	λ_x^+	Max DR (%)
Boundary layer flow							
Laadhari et al. (1994)	OW	450	60 – 303	1.7 – 8.4	160		36
Sanderson (1997)	OW						22
Trujillo et al. (1997), Trujillo (1999)	OW (water)	632 – 962	56 – 333	2.3 – 17.1	120 – 360		35
Choi et al. (1998), Choi and Clayton (2001), Choi (2002)	OW	549	69 – 480	2.6 – 18.2	400		45
Wu (2000)	OW (water)	633		max 56			32
Kiesow and Plesniak (2003)	Constant (water)	653					NR
Ricco and Wu (2004)	OW (water)	257 – 633	42 – 83	9 – 17	240		32
Gouder et al. (2013)	OW	1025	100	2 – 4	66 – 133		16
Kempaiah et al. (2020)	OW	570	94 – 700	0.6 – 3.3	100		15
Bird et al. (2018)	OW, TW	1125	100	12		$0, \pm 1366$	21.5
Marusic et al. (2021)	TW	6000	104	12		4488	25
		6000 – 9700	362, 348	7.8, 4.9		7853, 4488	16
		9700 – 12800	604 – 1100	5.0, 3.5		7853, 10472	13
Channel flow							
Gatti et al. (2015)	OW	150 – 440	33 – 279	1.4 – 4.6	2404 – 6992		2.4
Pipe flow							
Choi and Graham (1998)	OW (water)	633 – 962	$\approx 50 - 650$		340 – 500		24
Auteri et al. (2010)	TW (water)	175	$\omega^+ = -0.25 - 0.25$	13.8		511 – 1532	33

Table 3.1: Overview of experimental work on spanwise forcing. NR = not reported.

Study	Forcing	Constraint	Re_τ	A^+	T^+	λ_x^+	Max DR (%)
Channel flow							
Jung et al. (1992)	OW	CFR	200	12	100		40
Baron and Quadrio (1996)	OW	CFR	200	4, 9, 13, 17	100		40
Miyake et al. (1997)	OW	CPG (CPI?)	150	12	100		35
Choi et al. (2002)	OW	CFR	100	1 – 20	1 – 200		45.4
	OW	CFR	200	5 – 20	50 – 200		39.2
	OW	CFR	400	5 – 20	50 – 200		34.1
Quadrio and Ricco (2003)	OW	CFR	200	3 – 27	50 – 200		50
Quadrio and Ricco (2004)	OW	CFR	200	1.5 – 27	5 – 750		44.7
Xu and Huang (2005)	OW	CFR	173	15	90		36
Zhou and Ball (2006)	OW	CFR	180	3.9 – 15.6	25 – 200		42.5
		CPG	180	3.9 – 15.6	25 – 200		49.9
Ricco and Quadrio (2008)	OW	CFR	200	D^+ = 100, 200, 300	28 cases		36
			400	12	30, 125, 200		28.1
Ricco et al. (2012)	OW	CPG	200	12	0 – 500		33 ($T^+_{opt} = 70$)
Touber and Leschziner (2012)	OW	CFR	200	12	50 – 1000		38.5
			500	12	100, 200		32.4
			1000	12	100		29
Yakeno et al. (2014)	OW	CPG	150	3, 7, 12	16 – 500		42.8 ($T^+_{opt} = 75$)
Agostini et al. (2014)	OW	CFR	1000	12	100, 200		29
Hasegawa et al. (2014)	OW	CPI	200		γ varied		NR
Gatti et al. (2015)	OW	CFR	200	3.6	53		10
Ge and Jin (2017)	OW	CPG	180	12	100		31
Gatti et al. (2018a)	OW	CPI	200	4.5	125.5		17.2
Yao et al. (2019)	OW	CFR	200	12	16 – 628		35.3
			497	12	16 – 628		28
			1000	12	16 – 628		25.9
			1998	12	63 – 157		23.3
Yuan et al. (2019)	OW	CFR	200	3, 6, 12, 18	50, 100, 200		41.6
Yang and Hwang (2019)	OW	CFR	800	12	100		25
Quadrio et al. (2009)	TW	CFR	200	12 (2 – 30)	ω^+-k_x^+ plane		48 (60)
			100	12	NR	NR	RLM
			400	12	NR	NR	42
Gatti and Quadrio (2013)	TW	CFR	199, 951	12	5 lines in ω^+-k_x^+ plane		49, 42
	TW		2108	12	NR	NR	37
Hurst et al. (2014)	TW	CFR	200	12	35 – 628	393 – 3142	50
	TW		400	12	35 – 628	393 – 3142	44
	TW		800	12	35 – 628	393 – 3142	40
	OW		1600	12	63 – 105		22
	SW		1600	12		1000 – 1250	33
Gatti and Quadrio (2016)	TW	CFR	199	12 (2-20)	ω^+-k_x^+ plane		50
	TW	CFR	948	12 (2-20)	ω^+-k_x^+ plane		39
	TW	CFR,GPG	200	7			25
	TW	CFR,GPG	1000	7			17
Gatti et al. (2018b)	TW	GPG	200	7			36.4
	TW	CFR/GPG	1000	7			26.6, 27.7
Viotti et al. (2009)	SW	CFR	200	1-20		50 – 3000	52
Yakeno et al. (2009)	SW	CFR	150	1 – 10		200 – 2500	55
	OW	CFR	150	1 – 10	25 – 300		35
Pipe flow							
Quadrio and Sibilla (2000)	OW	CFR	172	3, 6, 8, 12, 14	50, 100, 150		40
Nikitin (2000)	OW	CFR	133	3, 6, 9	NR		8, 20, RLM
Choi et al. (2002)	OW	CFR	150	5, 10, 20	5 – 200		RLM
Duggleby et al. (2007)	OW	CPG	150	20	50		38
Coxe et al. (2019)	OW	CPG	170, 360	10	100		37, 36

Study	Forcing	Constraint	Re_τ	A^+	T^+	λ_x^+	Max DR (%)
Boundary layer flow							
Yudhistira and Skote (2011)	OW		271	17, 26	118		37, 40
Skote (2012)	OW		259	6, 12	132		19, 30
				11.3	67		29
Lardeau and Leschziner (2013)	OW		577	12	80, 100, 120, 200		25
Skote et al. (2015a)	OW		456	10.7	76.4		26
Skote et al. (2019)	OW		259	12	30, 176		20, 26
Skote (2022)	OW		259	12	100		32
Skote (2011)	SW		271	17		1300	46
Skote (2013)	SW		259	6, 12		1320	24, 51
Mishra and Skote (2015)	SW		234	2 – 20		85, 171, 341	36
Skote et al. (2015b)	TW		259	12	176	384	42

Table 3.2: Overview of numerical work on spanwise forcing. NR = not reported, RLM = relaminarization.

3.2.1. Early works: The introduction of oscillatory wall motion

The research on wall motion was arguably inspired by the earlier work of Bradshaw and Pontikos (1985), who performed measurements on an infinite swept wing, where the sweep was "induced" by suction slots angled at 35°. They found a drag-reduced state for the swept wing case compared to the two-dimensional boundary layer. Furthermore, they made a key observation, in that the rate of change of the spanwise velocity profile ($\partial^2 w/\partial y \partial \Phi$), and not the stokes strain ($\partial w/\partial y$) itself, was the cause for the drag reduced state. This would cause the near-wall structures to be tilted in the spanwise direction resulting in a drag reduction. If the slope of the spanwise velocity profile would be constant i.e. the rate of change would be zero, the near wall turbulence would readapt to a new two-dimensional state.

The field starts with the direct numerical simulation (DNS) of Jung et al. (1992). The oscillatory wall forcing was introduced in two ways, through a spanwise pressure gradient and by wall motion. No significant differences between the two forcing methods were found. A range of periods was tested at $Re_\tau = 200$, with the optimum period of $T^+ = 100$ giving rise to a drag reduction of 40%. Following, Laadhari et al. (1994) replicated the work of Jung et al. (1992) in a wind tunnel. A wall oscillation was created using a crank-shaft mechanism as presented in Figure 3.4. A maximum drag reduction of DR = 36% was found, their findings were confirmed by Trujillo et al. (1997) and Trujillo (1999). In a simulation by Baron and Quadrio (1996) the drag reduction was shown to monotonically increase with increasing A^+. This resulted in a maximum DR of 40% at $A^+ = 17$.

Using thee-dimensional hot-wire probes Laadhari et al. (1994) captured the turbulent statistics. Reductions in the Reynolds shear stress ($\overline{u'v'}$) were found up to 50%. In the drag-reduced states, a thickening of the viscous sublayer was observed. Similarly, Baron and Quadrio (1996) found an upward shift of the turbulent fluctuations in the wall-normal direction and Trujillo et al. (1997) observed the same upward shift of the log region, all indicative of a drag reduced flow. Furthermore, Baron and Quadrio (1996) found a reduction of the turbulence kinetic energy (TKE) production and dissipation terms in the near-wall region.

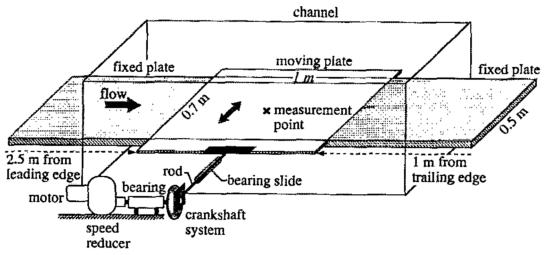

Figure 3.4: The experimental setup by Laadhari et al. (1994) where the oscillating wall is driven by a crank-shaft mechanism.

An interesting result was put forward by Sanderson (1997). Their work has not been published, but the results were shortly summarised in the review paper by Ricco et al. (2021). It is shown that a minimum spanwise displacement amplitude of $\Delta z^+ \approx 80$ is required for an effective drag reduction. The minimum displacement

is comparable to the spacing of the near-wall streaks at $z^+ \approx 100$, hinting at the idea that the spanwise motion possibly interacts with the near-wall cycle.

A substantial contribution to the academic body was made by Choi and his coworkers. The only experimental realisation of wall oscillation in a pipe flow was made by Choi and Graham (1998), a maximum DR of 25% was found. The drag reduction was found to a plateau value with increasing circumferential velocity amplitude, in line with the findings of Baron and Quadrio (1996) for A^+.

3.2.2. The first working mechanisms uncovered

The first flow visualisations were presented by Choi et al. (1998) and Choi and Clayton (2001) which showed the tilting of the near-wall streaks. It was hypothesised that the tilting of the near-wall streaks caused a negative spanwise vorticity, responsible for the upward shift of the log region and a reduced slope of the streamwise velocity profile at the wall. Choi et al. (2002) performed a large number of channel flow simulations for various actuation parameters and three Reynolds numbers, namely $Re_\tau = 100$, 200 and 400. Additionally a set of pipe flow simulations were performed at $Re_\tau = 150$. A key result is an empirical relation for the DR by correlating the actuation parameters, Reynolds number and the Stokes layer through a scaling parameter V^+:

$$V_c^+ = \frac{a_y^+ y_d^+}{A^+ Re_\tau^{0.2}} \tag{3.25}$$

Where a_5^+ is the spanwise velocity acceleration magnitude at $y^+ = 5$, and y_d^+ a penetration depth where the spanwise velocity decays to half of A^+, are obtained from the TSL. The DR and scaling parameter collapse for the empirical trend of DR $= 1000V_c^{+2} + 50V_C^+$. In Figure 3.5 it can be seen that the early numerical and experimental work agrees well with this empirical relation.

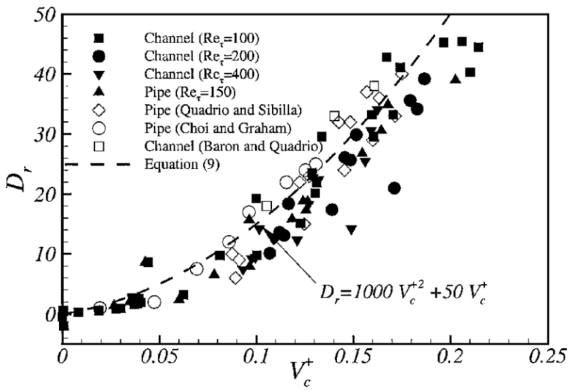

Figure 3.5: Drag reduction versus the proposed scaling parameter V_c^+, symbols indicate numerical and experimental data, dashed line presents the empirical fit by of Choi et al. (2002).

The study by Miyake et al. (1997) explored the transient effects of a starting up oscillations at $Re_\tau = 150$. A steady state DR = 35% was reached after five periods. Likewise, Quadrio and Ricco (2003) studied the initial response of the oscillating wall. Within the first period, the spanwise velocity profile closely matched the laminar TSL, and again a slower development of the DR was observed. On that same note, the spatial development of the drag reduction in streamwise direction was investigated by Ricco and Wu (2004). At the start of the actuation a large rise in drag reduction happens between $0 \leq x/\delta \leq 0.3$, but it takes around 3δ to establish the steady DR value. When the wall motion stops the readjustment to the unperturbed value of shear stress happens over a smaller spatial extent.

Further flow visualisations using hydrogen bubbles were performed by Ricco (2004). They found that the low-speed streaks were significantly affected, exhibiting cyclic tilting in the spanwise direction, with a reduction in length and an increase in the spanwise spacing between them. Moreover, the streaks are displaced relative to the quasi-streamwise vortices. It is hypothesised by the author that this relative displacement breaks up the interaction between the two entities reducing the strength of the near-wall cycle. This is in part supported by the observation of a significant reduction in ejection events.

The work of Quadrio and Ricco (2004) is notable in the field for its large parametric study on wall oscillations. In review of the earlier research, a parameter sweep of T^+ and A^+ was performed at $Re_\tau = 200$. A

total of 250 channel flow simulations were performed to create DR and NPS maps for the selected parameter space. The maps are presented later in Figure 3.9. The A^+ behaviour is in line with earlier observations and the optimum of $T^+ = 100$ was confirmed. A maximum DR of 45% was found at $A^+ = 27$. The NPS map shows a clear maximum at $A^+ = 5$ and $T^+ = 125$. They confirmed the empirical relation by Choi et al. (2002) to hold up to the optimum value of T^+, followed by a rapid decorrelation when the period was further increased.

3.2.3. The introduction of generalised spanwise forcing: streamwise travelling waves

The research on spanwise forcing so far was focused on simulations and experiments using wall oscillations. Quadrio et al. (2009) introduced the addition of a spatial mode, resulting in a spatio-temporal travelling wave. The authors performed simulations in the $k_x - \omega$ parameter space at $Re_\tau = 200$ and $A^+ = 12$. This gave rise to the widely known *'Quadrio map'* (Figure 3.11a), which presents the DR in the $k_x - \omega$ plane. In most of the plane, a modest reduction was found, with a small region of high DR having a maximum of 48%. Additionally, a region of drag increase was identified when the wavespeed is close to the near-wall convection velocity of the turbulent structures.

Their work inspired standing or spatial wave (SW) forcing that is obtained when setting the temporal mode to zero. SW forcing was first discussed in the two key papers of Viotti et al. (2009) and Yakeno et al. (2009). All the work on this forcing entails numerical studies, to date no experimental realisations of spatial forcing have been made. The effect of amplitude and wavelength was investigated by Viotti et al. (2009) in a set of channel flow simulations. The maximum DR of 52% was found for $A^+ = 20$ and $\lambda_x^+ = 1{,}250$. A comparison was made to the OW of Quadrio and Ricco (2004) using Equation 3.10. Both actuation schemes show the same trends for DR and NPS, with a higher DR of about 20-30% compared to the OW case. The laminar solution of the SSL and TSL were shown to match the turbulent profiles from DNS data.

Yakeno et al. (2009) added to this work by performing over 250 simulations to create parameter maps of A^+ and T^+ or λ_x^+ for temporal and spatial forcing respectively. The DR and NPS maps showed striking similarities between the two forcing schemes, where the SSL is again more effective and attains higher DR and NPS values, but qualitatively the maps show good agreement. A factor of approximately 10 is found between T^+ and λ_x^+, which is in agreement with equivalent period transformation ($\mathcal{T}$) using the near-wall convection velocity of $\mathcal{U}_w^+ = 10$.

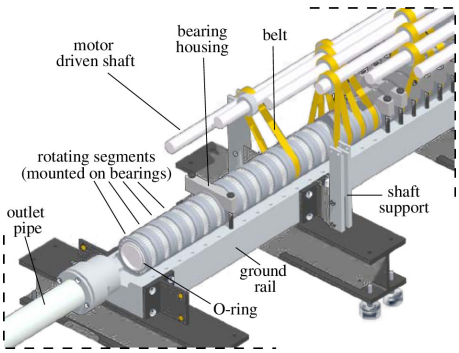

Figure 3.6: Experimental setup by Auteri et al. (2010) for TW forcing in a pipe flow.

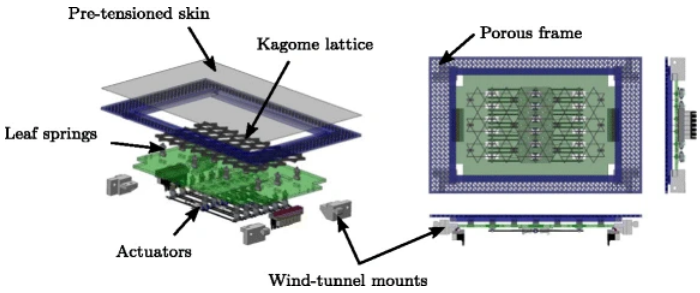

Figure 3.7: Experimental setup by Bird et al. (2018), TW forcing realised using a Kagome lattice.

Quadrio et al. (2009) also inspired the first experimental realisation of TW forcing by Auteri et al. (2010), due to the higher DR and NPS potential compared to the OW. Their experimental setup can be seen in Figure 3.6. A pipe flow was used where individual pipe segments could rotate in azimuthal direction. The sinusoidal waveform was discretized using 2, 3 or 6 segments respectively. Experiments were performed along two horizontal lines in the $\omega - k_x$ plane to make a comparison to the results of Quadrio et al. (2009). Qualitatively the DR trends were matched but at a lower absolute DR value. With a maximum DR of 33% compared to 48% for the numerical case.

Channel flow experiments using TW forcing were performed by Bird et al. (2018). The actuation was realised using a Kagome lattice as presented in Figure 3.7 which could be deformed in combination with a flexible skin. They showed that the trends matched literature by Quadrio and Ricco (2004) and Auteri et al. (2010), although a lower magnitude DR was obtained attributed to small out-of-plane displacements of the

surface.

The works on travelling waves also inspired Quadrio and Ricco (2011) to present the laminar solution of the Stokes layer for TW forcing. Their derivation of the GSL is widely used in all subsequent work on spanwise forcing, for example, to estimate the power input required for the spanwise motion.

3.2.4. Detailed investigation: working mechanisms and Reynolds number effects

Touber and Leschziner (2012) and Agostini et al. (2014) put the focus of their studies on further uncovering the working mechanism of the spanwise forcing by analysing the phase averaged turbulence statistics. Touber and Leschziner (2012) performed simulations for various periods from $T^+ = 50-1000$, at $A^+ = 12$ and $Re_\tau = 500$ An interesting observation put forward, in line with the earlier work of Bradshaw and Pontikos (1985), is that a weakening of the low-speed streaks was observed if the rate of change of the Stokes strain was high, and increase in strength when the change rate is slower. Agostini et al. (2014), confirmed the finding that the Stokes strain is an important driver of the DR. In addition, they identified the skewness, which is the wall-normal derivative of the angle of the velocity vector with respect to the freestream $\partial\Theta/\partial y$. Drag reduction occurred at intervals of high skewness. They observed hysteresis of all turbulence statistics, reflected in the drag reduction phase which is longer than the drag increasing phase. The phase-wise asymmetry of skewness was hypothesised to be responsible for the hysteresis.

Among others Gatti and Quadrio (2013), Hurst et al. (2014), and Gatti and Quadrio (2016), elucidated on the Reynolds number effects of spanwise forcing. Gatti and Quadrio (2013) investigated TW forcing, a decreasing trend in DR was found: 39% to 24% for $Re_\tau = 200-2,100$. In the $k_x-\omega$ plane they observed a shift towards higher wavenumbers and frequencies of the high DR region, in addition, the DI region became wider and decreased in magnitude. They argued that the DR margin can be correlated to the Reynolds number by a power law in the form of $DR \propto Re_\tau^{-a}$. Following, Hurst et al. (2014) investigated the Reynolds number effects of travelling waves at $A^+ = 12$ for $Re_\tau = 200$, 400 and 800. A modest decrease of the drag reduction margin was found to decrease from DR = 50% to DR = 40%. They observed that the power law scaling adopted by Gatti and Quadrio (2013), is highly dependant on the actuation parameters and is therefore not universal.

The study of Gatti and Quadrio (2016) further elaborated on the Reynolds number effects of TW forcing. Two Reynolds numbers were considered, namely $Re_\tau = 200$ and $Re_\tau = 1,000$. The $k_x-\omega$ parameter space of Quadrio et al. (2009) was extended with third variable, A^+, between $A^+ = 2-20$. A total of 4020 simulations were performed. For further analysis and comparison, they used the map at $A^+ = 12$. Their results are in agreements with the earlier work of Gatti and Quadrio (2013) and Hurst et al. (2014). In response to the conclusion that the power law scaling is not universal, a universal scaling was proposed using the ΔB. By relating the Reynolds number independent ΔB shift to the skin friction coefficient of the unactuated flow, the drag reduction for any Reynolds number can be found.

3.2.5. Breakthrough: the introduction of outer-scaled actuation

Recently an interesting contribution to the research on spanwise forcing was made by Marusic et al. (2021). As mentioned in Section 2.3, a large portion of flow control for drag reduction uses inner-scaled actuation (ISA), the same goes for the research on spanwise forcing. The authors conducted an experiment using TW forcing, OSA was performed by reducing the actuation frequency to target the outer-scaled structures. The wavelength was sized in the order of δ, and the period of oscillation was increased up to $T^+ = 1,100$. At low Re_τ, this is not effective since no significant outer-scaled contribution is found. However, Marusic et al. (2021) showed that a significant drag reduction of 13% could be obtained at $Re_\tau = 12,800$ for $T^+ = 600$. Adding to this is the positive NPS of up to 10 %, compared to no NPS for small-scale actuation. This has shown that the outer-scaled structures can indeed be targeted using spanwise motions, which is promising for further development, especially when it comes to industry applications at high Re_τ.

3.3. Drag reduction and net power saving potential

This section discusses the potential for drag reduction (DR) and net power savings (NPS) for the three actuation schemes discussed in this chapter. Firstly, in Subsection 3.3.1 the response of the DR and NPS are related to the actuation parameters for the three actuation schemes. Parametric studies to this response are mostly restricted to low Reynolds number channel flow simulations, therefore the effects at higher Reynolds numbers are discussed in Subsection 3.3.2. This is followed by an elaboration on the spatial development effects present in boundary layer flows in Subsection 3.3.3.

3.3.1. Relation to actuation parameters

First, the effect of spanwise velocity amplitude is discussed since all three forcing schemes have similar DR and NPS trends as a result of changing A^+. Following this is the elaboration of the characteristic wave parameters for each of the three forcing individually.

The spanwise velocity amplitude

Consider Figure 3.8, which shows the DR and NPS response with A^+ for a streamwise travelling wave by Quadrio et al. (2009). The DR shows a monotonically increasing response with increasing A^+, where it tends to a constant value or plateau in the limit, qualitatively the other two schemes show the same behaviour. For the NPS the response looks different, for low amplitudes the NPS is increasing up to a maximum at $A^+ = 6$, followed by a decline. This is a result of the balance between the increasing power input and DR as A^+ increases. For OW and SW forcing the maximum NPS is found at an amplitude of approximately $A^+ = 5$ and $A^+ = 7$ respectively for similar Reynolds numbers (Quadrio and Ricco, 2004; Yakeno et al., 2009).

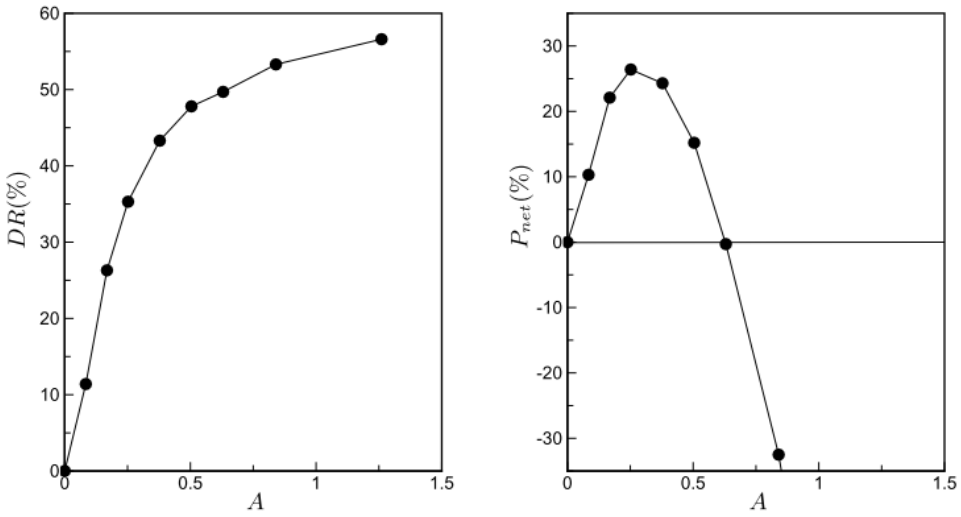

Figure 3.8: (left) DR and (right) NPS as functions of forcing amplitude A for a TW forcing, with actuation parameters $\omega = 0.16$, $k_x = 1.66$, and $Re_\tau = 200$. Note that the actuation parameters are not scaled to viscous units, in viscous units the amplitudes range from $A^+ = 0-30$ and $A^+ = 0-20$ for the DR and NPS respectively. (Quadrio et al., 2009)

Oscillating wall: T^+

The characteristic parameter that defines the OW forcing is the period T^+, and for practical applications also the peak-to-peak displacement D^+. In Figure 3.9 the DR and NPS maps in the parameter space T^+ and A^+ of Quadrio and Ricco (2004) are presented. Additionally, isolines of D^+ are shown in the DR map.

The response for T^+ period shows an optimum DR at the period $T^+ = 100$ independent of A^+. A maximum DR of 45% is found at $A^+ = 27$. The optimum is shifted to a slightly larger period and lower spanwise velocity amplitude on the NPS map, with NPS = 7% for $T^+ = 125-150$ and $A^+ = 4.5$ The isolines of D^+ show an increasing DR with decreasing period, however, the DR is not sensitive to the period around the optimum and is almost constant. The nearly constant DR happens because of the trade-off between period and amplitude, if T^+ is decreased A^+ increases having an opposite effect on the drag.

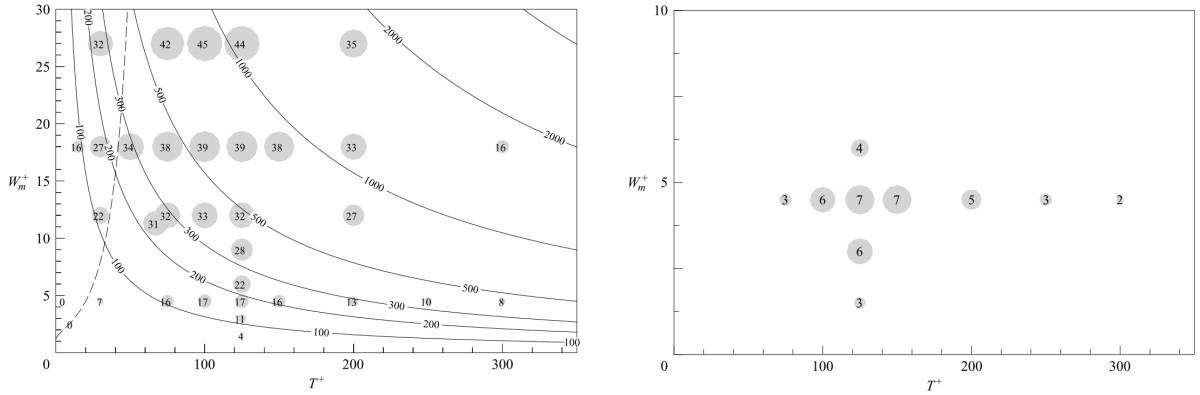

(a) DR map (b) NPS map

Figure 3.9: (a) DR and (b) NPS maps for OW forcing, between T^+ and A^+ (W_m^+). Solid lines indicate the iso-D^+ lines. Only positive NPS values are provided. DNS simulations at $Re_\tau = 200$. (Quadrio and Ricco, 2004)

Standing wave: λ_X^+

The characteristic parameter for standing wave forcing is the streamwise wavelength λ_x^+. In Figure 3.10, the DR and NPS response with streamwise wavelength are presented for a number of A^+ from Viotti et al. (2009). The optimum DR is found at $\lambda_x^+ = 1{,}250$, which is again independent on A^+, reaching a DR of 45% at the the largest $A^+ = 12$. A comparison is made with the OW through the transformation of Equation 3.10. A striking similarity of the DR trend can be seen, but the magnitude is higher for spatial forcing. Viotti et al. (2009) concluded that the DR potential of spatial forcing is 20-30% higher than the temporal case. The NPS response, shows a positive NPS for all the wavelengths at $A^+ = 6$, while below $\lambda_x^+ = 1{,}000$ negative NPS are found for $A^+ = 12$. The largest NPS of 22% is found at $\lambda_x^+ = 1{,}000$ and $A^+ = 6$.

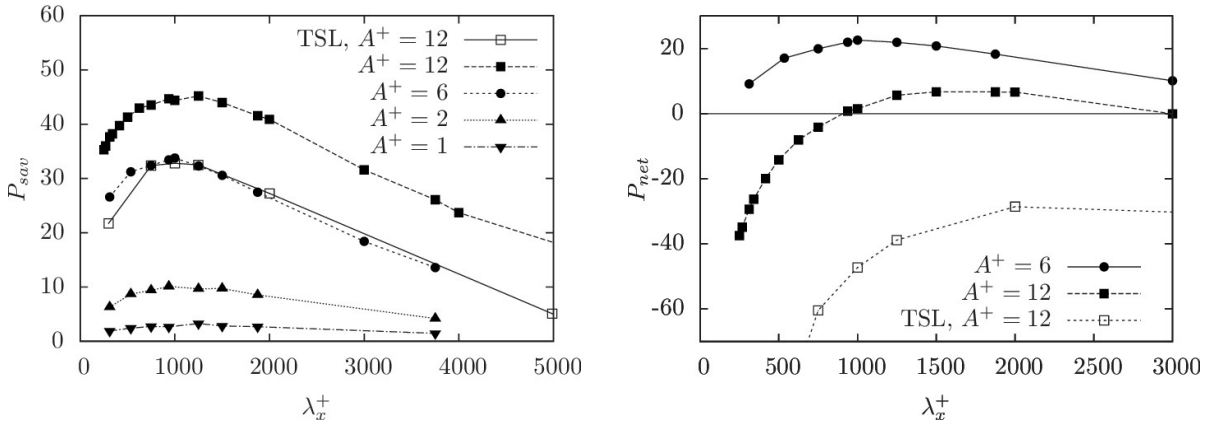

(a) DR (b) NPS

Figure 3.10: DR (P_{sav}) and NPS (P_{net}) response for SW forcing, as a function of λ_x^+. A comparison is made to the OW (TSL) from Quadrio and Ricco (2004) using the transformation $\lambda_x^+ = \mathcal{U}_c^+ T^+$. DNS simulations at $Re_\tau = 150$. (Viotti et al., 2009)

Travelling wave: k_x^+ & ω^+

Streamwise travelling waves are defined based on the characteristic parameters: k_x^+ and ω^+. Additionally the wavespeed c^+ (Equation 3.2) is a parameter of interest. In Figure 3.11, the DR and NPS maps at $A^+ = 12$ of Quadrio et al. (2009) are presented. The wave can propagate in either the down- and upstream direction associated with a positive and negative frequency respectively. The region left of the y-axis corresponds to backward travelling waves while the right side represents forward travelling waves. Note that these maps also present the oscillating wall case along the horizontal axis ($k_x = 0$) and the standing wave case along the vertical axis ($\omega = 0$).

For the backward travelling waves a modest value of DR is found on the complete quadrant, where the DR is more sensitive to the oscillation frequency compared to the wavenumber. The largest DR is obtained when

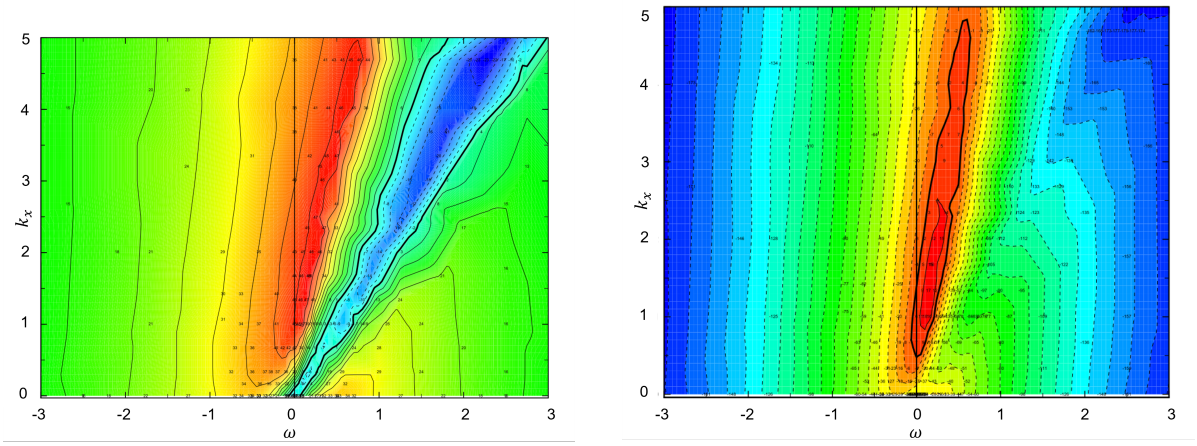

(a) DR map

(b) NPS map

Figure 3.11: DR and NPS maps for TW foricng, between the frequency (x-axis) and wavenumbers (y-axis) for $A^+ = 12$. Thin black lines indicate iso values, the thick black line indicated 0%. Warm colors (red) indicate high NPS, cool colors (blue) indicate negative DR. Note that the actuation parameters are not scaled to viscous units. DNS simulations at $Re_\tau = 200$. (Quadrio et al., 2009)

the frequency is zero i.e. the spatial standing wave. The NPS for the backwards travelling waves is almost completely negative except for a small portion at low to zero frequency.

The drag reduction response of the forward travelling waves is more complex. Firstly a narrow region of large DR is observed, with a maximum of DR = 48% larger than the 34% and 42% for the temporal and spatial forcing. The high DR region does also dictate the optima of these two respective forcing, where it crosses the horizontal and vertical axis. This way it can also be seen that SW forcing has a higher DR and NPS potential compared to the OW. Because of the narrow ridge of high DR, the DR is sensitive to the exact actuation parameters. The NPS of TW forcing is mostly negative except for a small crest region dictated by the high DR area, with a maximum of NPS = 18%.

The high DR region is accompanied by a high drag increase (DI) crest up to DI = 23%. Quadrio et al. (2009) explains that the region lays on a straight line that crosses the origin, associated with fixed wavespeed. At the crest of the DI region, the wavespeed is equivalent to the convection velocity of the near-wall turbulence. This means the near wall turbulence will not experience any unsteady transverse forcing since the convection velocity coincides with the wavespeed. The DI region is approximately bounded by $c^+ = \mathcal{U}_w^+ \pm 2$.

3.3.2. Reynolds number dependence

So far, spanwise forcing shows potential, both in terms of isolated DR as well as NPS. However, one major drawback of the parametric studies discussed is the restriction to moderate and low Reynolds numbers around $Re_\tau = 200$. In practical applications operation conditions are at much higher Re_τ. For example Reynolds numbers in the order of $Re_\tau = \mathcal{O}(6,000)$ for long-distance oil pipelines and up to $Re_\tau = \mathcal{O}(100,000)$ along the fuselage of commercial airliners (Marusic et al., 2021).

It was first observed by Choi and Graham (1998) that the DR margin showed a decrease with increasing Re_τ. Following this Choi (2002) suggested that DR scaled according to a simple power law, where the exponent a is dictated by the actuation parameters:

$$DR \propto Re_\tau^{-a} \tag{3.26}$$

The power law scaling was adopted by other studies like the experimental work of Ricco (2004) and the numerical work of Quadrio and Ricco (2004), Quadrio et al. (2009), and Touber and Leschziner (2012). Throughout the literature, widely varying exponents were found ranging from $a = 0.06 - 0.4$. In Figure 3.12 Hurst et al. (2014) showed that the exponent is not trivially defined and is sensitive to the actuation parameters.

The Re_τ-dependant effects on the DR map by Quadrio et al. (2009) were analysed by Gatti and Quadrio (2013) between $Re_\tau = 200$ and $Re_\tau = 2100$. The qualitative effects are presented in Figure 3.13. The high DR region has shifted upwards towards higher wavenumbers and frequency. The maximum DR was reduced from 37 - 29%. It was also found that the DI cone gets wider in the parameter space, but decreases in magnitude (i.e less drag increase). Gatti and Quadrio (2016) further explored the exponential scaling for two Reynolds

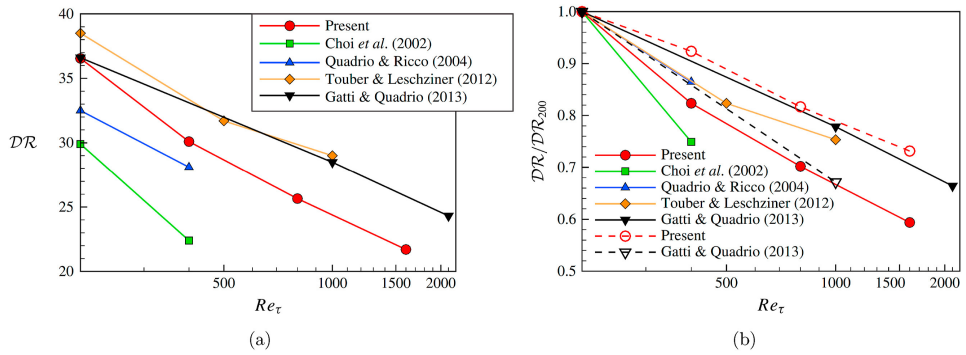

Figure 3.12: Comparison by Hurst et al. (2014) of the DR with Re_τ for five different studies shows that the power exponents a is not trivially defined and dependant on actuation parameters; (a) percentage drag reduction; (b) Relative drag reduction to the reference at $Re_\tau = 200$.

numbers $Re_\tau = 200$ and $Re_\tau = 1000$ performing simulations in the $\omega^+ - k_x^+$ plane of Quadrio et al. (2009). They mapped the exponent a on the same parameter space. In line with the findings of Hurst et al. (2014), they found that a is sensitive to actuation parameters and not useful as a universal scaling law.

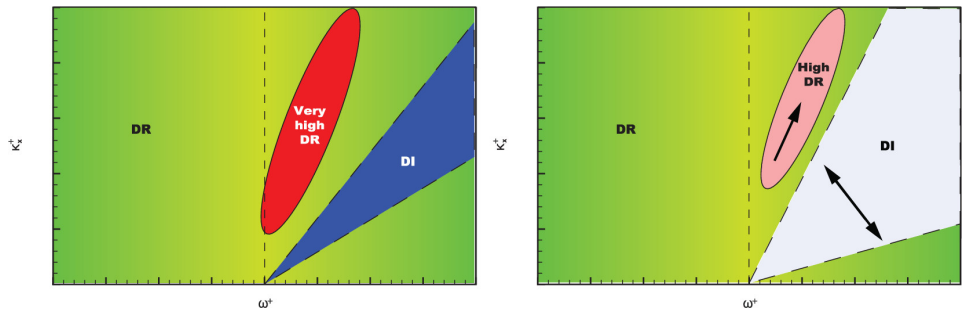

Figure 3.13: Qualitative Reynolds number effects on the DR in the $\omega^+ - k_x^+$ (Gatti and Quadrio, 2013).

Gatti and Quadrio (2016) proposed an alternative way of scaling for the Reynolds number effects. The idea is based on the upward shift of the logarithmic portion of the velocity profile when scaled using the actual friction velocity. This increases the constant B in Equation 2.23, the so-called ΔB shift. The predictive model assumes that ΔB is independent of the Reynolds number when scaled with the actual friction velocity i.e. ΔB^*. This idea was first proposed for flow over riblets by Luchini (1996). In Figure 3.14 the striking similarity between the DR map of Quadrio et al. (2009) and the ΔB^* shift can be observed. By a theoretical analysis using the log law between the actuated and unactuated case Gatti and Quadrio (2016) found Equation 3.27.

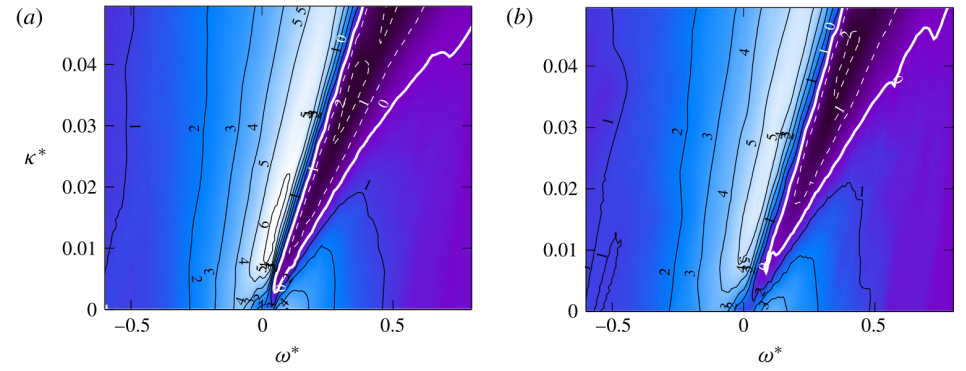

Figure 3.14: ΔB^* shift for (a) $Re_\tau = 200$ and (b) $Re_\tau = 1{,}000$ in the same parameter space as the DR map of Quadrio et al. (2009). Lines indicate iso-ΔB^* values, dashed lines are negative and the thick lines indicate the zero value. (Gatti and Quadrio, 2016)

$$\sqrt{\frac{2}{C_f}} - \sqrt{\frac{2}{C_{f,0}}} = \frac{1}{\kappa}\ln\left(\frac{Re_\tau}{Re_{\tau,0}}\right) + \Delta B \tag{3.27}$$

Equation 3.27 relates the drag reduction to the upward shift and the skin friction coefficient of the unactuated case, which is then simply a function of the Reynolds number. In Equation 3.28 the result for CFR conditions can be seen, under CPG conditions it simplifies further and the second term can be omitted. The DR can then be calculated based on the unactuated skin friction coefficient $C_{f,0}$ for any Reynolds number.

$$\Delta B^+ = \sqrt{\frac{2}{C_{f,0}}}\left(\frac{1}{\sqrt{1-\mathrm{DR}/100}} - 1\right) - \frac{1}{2\kappa}\ln(1-\mathrm{DR}/100) \tag{3.28}$$

3.3.3. Spatial development in boundary layers

Fully developed channel flow simulations are a useful tool to gain insight into the drag reduction response and working mechanisms of spanwise forcing. Their spatial homogeneity means the turbulence will experience a fixed forcing throughout the channel. In the case of a boundary layer flow, the turbulence develops with downstream distance, as the boundary layer grows. This means the inner and outer scales change as the boundary layer develops, with fixed dimensional actuation parameters, the non-dimensional parameters will change over the actuation distance. Moreover, in experiments, the spanwise forcing is usually applied to a section of the boundary layer, with no forcing upstream and downstream of this. This has implications for the drag reduction, which requires a certain spatial development to attain its maximum.

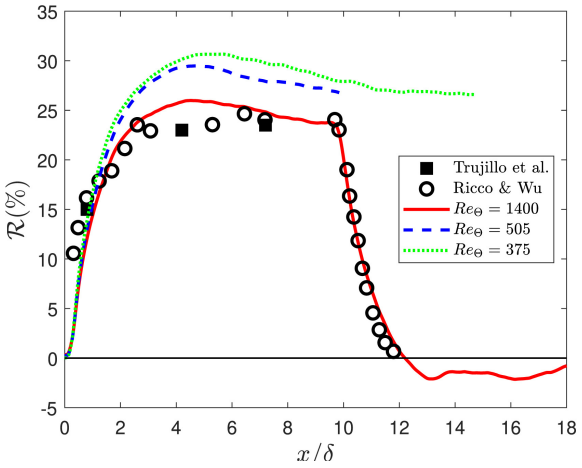

Figure 3.15: Spatial development of the drag reduction with downstream distance. $x/\delta = 0$ marks the start of the actuation. Actuation parameters are $T^+ = 67$ and $A^+ = 11.3$. Black squares, experiments of Trujillo et al. (1997); open circles, experiments of Ricco and Wu (2004); lines, DNS simulations by Skote et al. (2019).

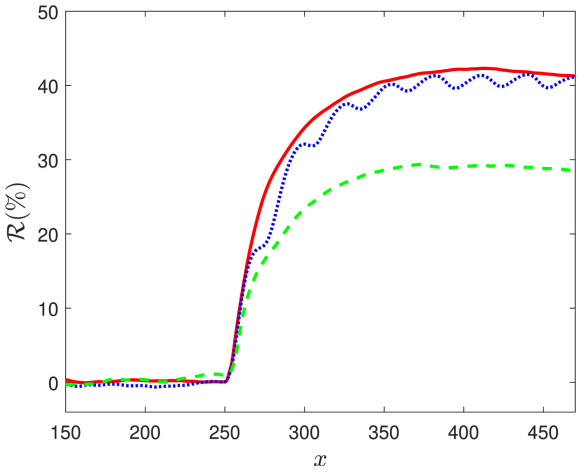

Figure 3.16: Spatial development for the three types of spanwise forcing. $x = w50$ marks the start of the actuation, with $Re_\theta = 505$. All actuation's are performed at $A^+ = 12$. Green dashed line, OW $T^+ = 132$; blue dotted line, SW $\lambda_x^+ = 1320$; red solid line, TW $T^+ = 176$ and $\lambda_x^+ = 348$. (Skote et al., 2015b)

Experimentally the spatial development of the drag reduction in the boundary layer was analysed by Ricco and Wu (2004). They performed oscillating wall experiments in a water flow facility, the actuated area covered a streamwise distance of $x = 660$ mm. Measurements were taken in the viscous sublayer using Laser Doppler velocimetry (LDV) measurements and hot-film anemometer (HFA). In Figure 3.15, the spatial development of the DR can be seen, the downstream distance is non-dimensionalized with the boundary layer thickness. No measurements were taken at $x/\delta \leq 0.3$ because of the small gap between the oscillating wall and the stationary test section. An initial fast response is observed within a distance of $x/\delta = 1$ to DR = 17%. This is followed by a more slow rise to the fully developed drag reduction of DR = 23 % at around $x/\delta = 3$. The drag increase downstream of the forcing shows a steep exponent-like decline and occurs over a smaller distance compared to the drag reduction, returning to the unperturbed drag state within 2δ.

On the numerical front, a large number of boundary layer DNS simulations were performed by the group of Skote. In the paper of Skote et al. (2019) matched the non-dimensional actuation parameters of Ricco and Wu (2004) for three Reynolds numbers, being $Re_\theta = 1400$, 505 and 375 respectively. In Figure 3.15 the comparisons between their results can be seen. The results of $Re_\theta = 1400$ which match the Reynolds number of

Ricco and Wu (2004) are in good agreement, especially in the region downstream of the oscillating wall. For all three Reynolds numbers, the maximum drag reduction is reached after $4-5\delta$. Skote et al. (2015b) also analysed the spatial development of the three different forcing schemes discussed in this chapter, which is presented in Figure 3.16. It can be seen that the three actuation schemes show a similar drag rise response, where the fully developed drag reduction is reached at the same distance.

The idea could also be put forward that the spatial drag reduction is a function of the number of spanwise oscillatory periods (i.e. the equivalent period $\mathcal{T}^+$) the near-wall turbulence has experienced, however, this is most likely not the case. In the results of Figure 3.16 the equivalent time-step between the temporal and spatial forcing ($\mathcal{T}^+ = 132$) compared to the travelling wave ($\mathcal{T}^+ = 50$) is about three times larger, but qualitatively the spatial transience is the same. This means the spatial DR onset is indeed a function of a spatial length scale, and seems to be independent of the characteristic actuation parameters.

3.4. Working mechanism

This section aims to provide insight into the working mechanisms behind the drag reduction of spanwise wall motion. This research into this topic is largely focused on wall oscillations, therefore this control scheme is discussed unless stated otherwise. The insight into the working mechanisms of the OW is still valuable, because of the close similarity of the TSL to the GSL. Hence, the working principles are expected to translate to any form of generalised spanwise wall motion.

3.4.1. Effects on the mean-flow and turbulence statistics

One of the much-observed effects of drag reduced flow is the thickening of the viscous sublayer or upward shift in the logarithmic profile when scaling with $u_{\tau 0}$ and u_τ respectively. This can be seen in the results of the experiments by Ricco (2004). In Figure 3.17a scaling with $u_{\tau 0}$ shows that under wall oscillations the points in the viscous sublayer shift right while the logarithmic region collapses for all cases. This scaling brings out the absolute differences with respect to the unactuated case. It highlights that the wall oscillations only alter the dynamics in the buffer layer while the outer layer remains unchanged. The opposite can be observed in Figure 3.17b when scaling with u_τ, similarity in the viscous sublayer is expected accompanied with the upward shift of the logarithmic region.

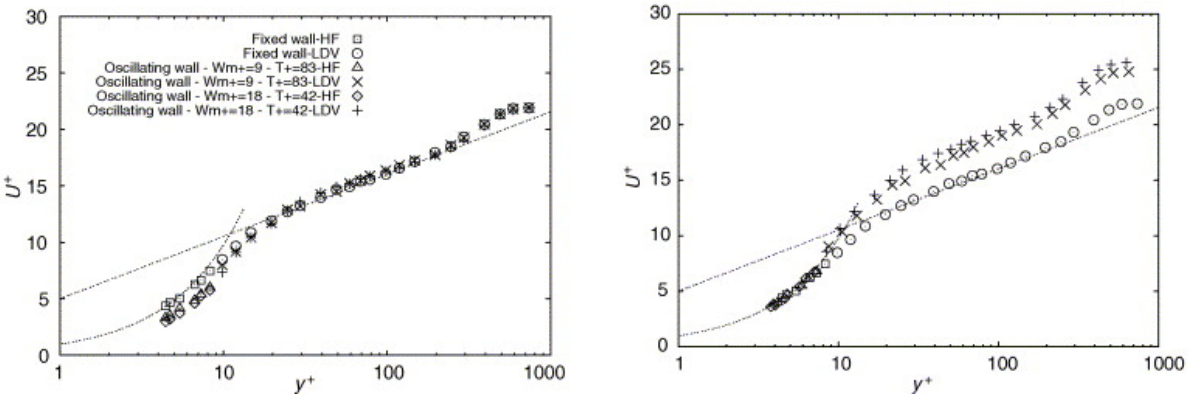

(a) Scaling with $u_{\tau 0}$.

(b) Scaling with u_τ.

Figure 3.17: Mean velocity profiles under wall oscillations scaled with $u_{\tau 0}$ and u_τ. Dotted lines indicate $u^+ = y^+$ and $u^+ = \frac{1}{\kappa}\ln(y^+) + B$. (Ricco, 2004)

Ricco (2004) also showed the effect of wall oscillations on the turbulent stresses. In Figure 3.18a the streamwise velocity fluctuations profile can be seen. A large reduction of streamwise TKE can be observed in the buffer layer where the peak at $y^+ \approx 15$ is strongly attenuated. In addition the peak shifts away from the wall due to the increase in viscous length scale. A reduction of Reynolds stress can also be observed in Figure 3.18b, where the attenuation extend into the logarithmic layer.

The transport equation for the streamwise stress was studied by Touber and Leschziner (2012). They found that under spanwise forcing, the production is strongly reduced in the buffer layer and dissipation is largely attenuated in the viscous sublayer. Touber and Leschziner (2012) also investigated the phase-averaged

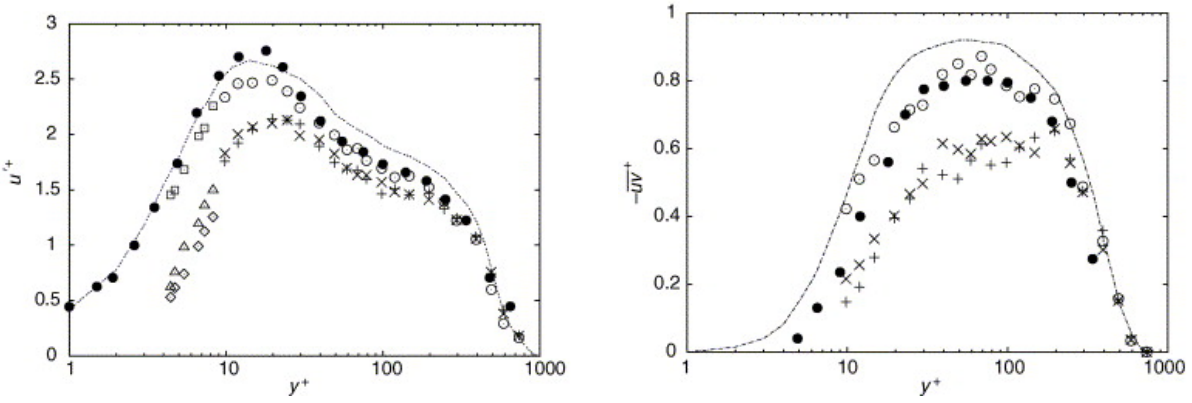

(a) Streamwise velocity fluctuations

(b) Reynolds stress

Figure 3.18: Turbulence statistics profiles under wall oscillations scaled with $u_{\tau 0}$. Legend is displayed in Figure 3.17a, black dots are experiments of De Graaff and Eaton (2000), dashed line is DNS of Spalart (1988) (Ricco, 2004).

enstrophy and individual vorticity components, the results are presented in Figure 3.19. The largest attenuation is observed for the spanwise vorticity ($\widetilde{\omega_z\omega_z}$). The wall-normal vorticity ($\widetilde{\omega_y\omega_y}$) is associated with the low-speed streaks and also shows a large reduction. Hence, this indicated a reduction of the strength of the near-wall energetic structures that linked to a skin friction reduction. The quasi-streamwise vortices associated with $\widetilde{\omega_x\omega_x}$ are not significantly affected by the wall motion.

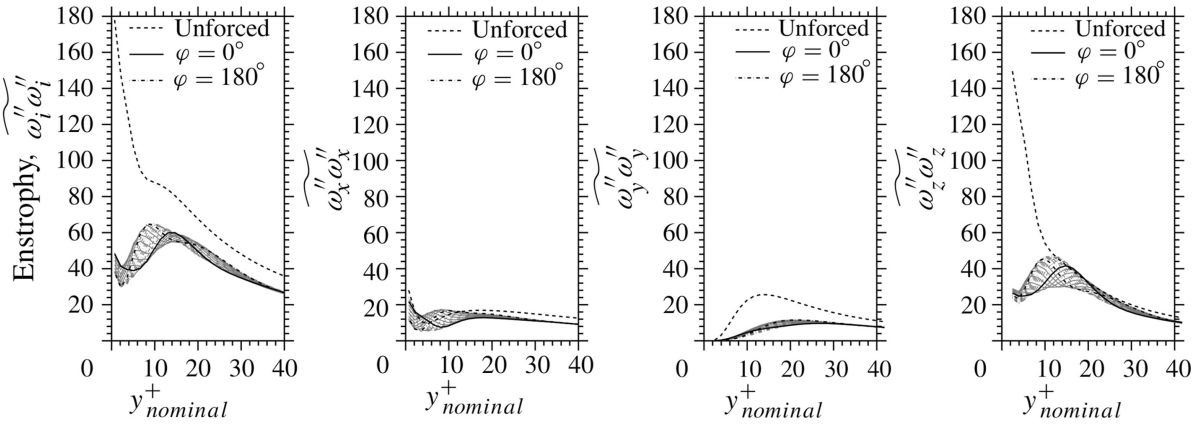

Figure 3.19: Phase averaged enstrophy profiles (over 50 periods of oscillation) and contribution of the individual components. Numerical simulations of wall oscillations at $Re_\tau = 500$ and $T^+ = 100$. (Touber and Leschziner, 2012)

3.4.2. Negative spanwise vorticity

Based on the flow visualisations performed by Choi and Clayton (2001) and Choi (2002) presented a conceptual model for the working mechanism, based on the flow visualisation of Choi et al. (1998). The authors observed that the spanwise motion would reduce the mean spanwise vorticity, by tilting the streamwise vorticity vector in the spanwise direction. This spanwise tilting of the streamwise vortices results in a negative spanwise vorticity during both the negative and positive parts of the oscillatory cycle. This is confirmed by the aforementioned findings of Touber and Leschziner (2012). In Figure 3.20 the spanwise tilting of the near-wall structures can be seen, with the associated induced negative spanwise vorticity due to the wall oscillations.

Using this observation they proposed a simple model, modelling the negative spanwise vorticity as a point source at $y^+ = 15$, where the reduction in $\widetilde{\omega_y\omega_y}$ is the largest. In Figure 3.21 their model can be seen. The modelled vorticity influences the streamwise velocity profile through its induction, reducing the slope of the velocity profile in the near-wall region and shifting up the logarithmic portion of the velocity profile above $y^+ = 15$, which is in line with the changes in mean flow behaviour resulting from spanwise forcing. Choi et al. (1998) noted that the vortex strength was not strong enough to introduce inflectional points in the velocity profile, so no increase in burst events is expected.

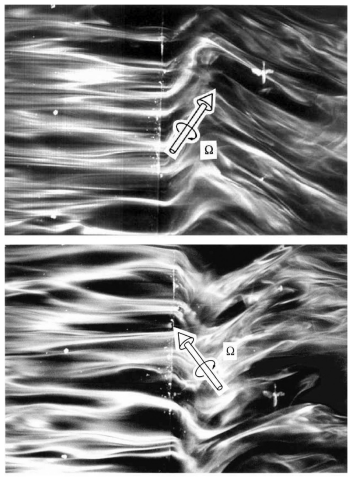

Figure 3.20: Cyclic tilting of the near wall structures and the associated tilting of the streamwise vorticity vector observed by Choi et al. (1998).

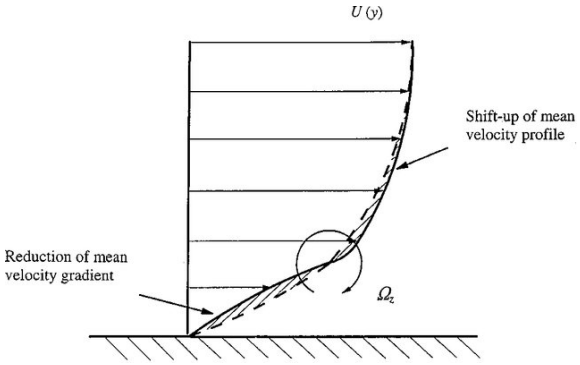

Figure 3.21: The proposed model by Choi et al. (1998) where the created negative spanwise vorticity is responsible for drag reduction.

3.4.3. Interaction of the Stokes layer with the near-wall cycle

Akhavan et al. (1993) used the DNS simulations of Jung et al. (1992) to analyse the flow structures in the turbulent boundary layer. A spanwise shift of the QSVs with respect to the near wall streaks was observed, as well as a reduction in streak strength. They suggested the working mechanism that the continuous displacement of the two structures, breaks up the turbulence-generating interaction of the near-wall cycle. The reduced near-wall cycle strength then directly translates to a reduction in TKE and wall shear stress. Baron and Quadrio (1996) elaborated on the findings by Akhavan et al. (1993). They argued that the penetration depth of the Stokes layer should be confined to the region of the streaks and affect the QSVs minimally, this would result in the biggest lateral displacement between the two entities. Using this reasoning they found an optimal period of $T^+ = 100$.

Choi (2002) further elaborated on this and argued that the near-wall cycle is effectively targeted if the spanwise wall displacement is larger than the correlation of spanwise velocity fluctuations which is 50 wall units (Choi, 2002), meaning the spatial correlation between the near wall streaks and streamwise vortices is effectively broken. The findings of Sanderson (1997) agree with this, who found a minimum spanwise wall displacement of $\Delta z^+ = 80$ is required for effective DR.

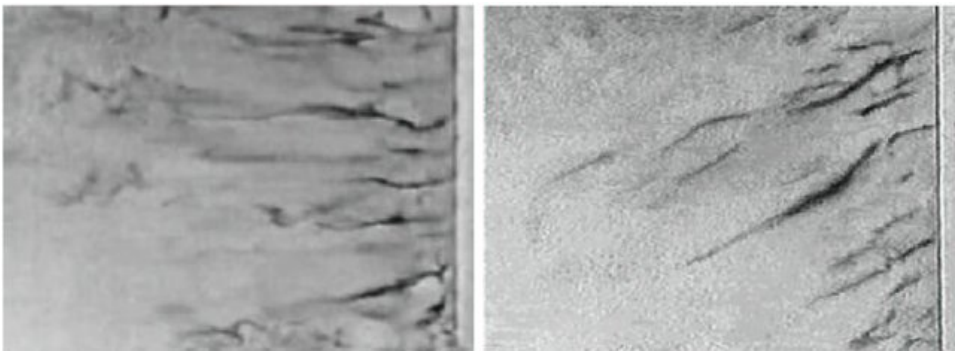

Figure 3.22: Flow visualisation presented by Ricco (2004), top view (x-z plane) of hydrogen bubble lines are released at $y^+ = 5$, the frame size is $x^+ = 1000$ by $z^+ = 750$. (left) unactuated flow, (right) actuated flow at $T^+ = 167$ and $A^+ = 9$ with phase $\Phi \approx T^+/2$.

This working mechanism was further elucidated by Ricco (2004) using hydrogen bubble visualisations in the near-wall region. In Figure 3.22 the lateral displacement of the streaks at $y^+ = 5$ can be seen from a top-down view. A theoretical calculation using the TSL was made to estimate a maximum lateral displacements $\Delta z^+ = 122$ of the streaks at $y^+ = 5$, which compared well to the measured value of $\Delta z^+ = 110$ for 50 visualised streaks. Furthermore, they showed a clear trend between the inclination angle of the streaks and the drag reduction, where the drag reduction increases as the inclination gets larger.

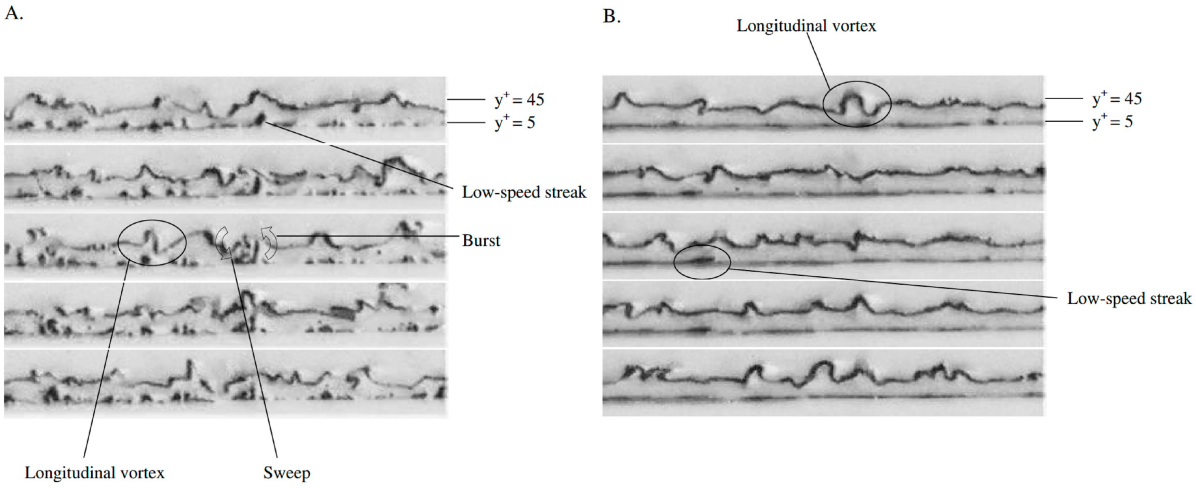

Figure 3.23: Flow visualisation presented by Ricco (2004) in a channel end-view (y-z plane), hydrogen bubble lines are released at $y^+ = 5$ and 25 respectively, the time separation between frames is $t^+ = 5.4$ (increasing timestep from top to bottom), the frame width is $z^+ = 900$. (A) unactuated flow, (B) actuated flow at $T^+ = 67$ and $A^+ = 17$.

Hydrogen bubble visualisation was also performed in the end-view of the channel, with bubbles released at $y^+ = 5$ and $y^+ = 25$ to visualise the streaks and QSVs. In the actuated case, a clear reduction of turbulence activity can be observed, with both the streaks and the quasi-streamwise vortices showing a less chaotic behaviour. As a result of this, a reduction of sweep and ejection events can be observed. This presents strong qualitative evidence for the theory of a broken interaction between the two entities and a reduction in overall strength of the near-wall cycle. In this context Yakeno et al. (2014) applied conditional averaging to analyse the effects of Q2 (ejection) and Q4 (sweep) events. The skin friction reduction stems from a large reduction in Q2 events, as the period increases above $T^+ \leq 125$, the drag reduction diminishes by an increase in Q4 events. They found the reduction in Q2 events to occur when the spanwise velocity at $y^+ = 10$ counteracts the rotating motion of the QSVs. The enhancement of Q4 events at large T^+ results from the spanwise tilting of the coherent structures which increases the vorticity and sweep events.

3.4.4. Phase averaged dynamics

Touber and Leschziner (2012) and Agostini et al. (2014, 2015) discussed the effects of the phase averaged dynamics throughout an oscillatory cycle. Firstly it is important to understand that there is a time-dependent response of DR for spanwise forcing. This temporally fluctuation DR response is highlighted in Figure 3.24 for

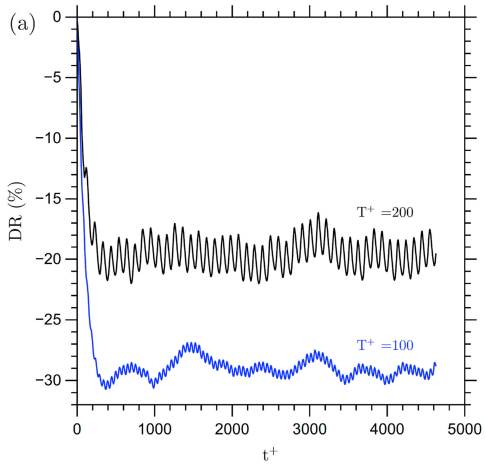

Figure 3.24: The time response of drag reduction for a period of $T^+ = 100$ and $T^+ = 200$ at $Re_\tau = 1000$, note that a positive DR is indicated as negative (Agostini et al., 2014).

$T^+ = 100$ and $T^+ = 200$. A clear transient response of the drag reduction can be seen, where the fluctuations

are larger for the non-optimal period of $T^+ = 200$. The differences can be explained by the deeper penetration of the Stoke layer at $T^+ = 200$, increasing the shear-induced turbulence production in the buffer layer. This explains the transient behaviour of the drag reduction but does not provide further evidence of the working mechanisms behind the drag reduction itself.

Touber and Leschziner (2012) focused on the low-speed streaks in their analysis. In line with the results of Ricco (2004) they found the streaks to be cyclically dragged under spanwise motion. Furthermore, they observed the streak strength to vary throughout the cycle. The varying strength was attributed to the rate of change of the Stokes strain ($\partial^2 w/\partial y \partial \Phi$) i.e. the varying of the gradient of the spanwise velocity profile with phase. A strong weakening of the streaks was observed when the stokes strain changed at a high temporal rate in the buffer layer. The streaks were found to increase in strength again when the Stokes strain varied slowly. From this, it was concluded that the temporal dependence of the varying stokes strain vector is a key mechanism in reducing the strength of the streaks, and therefore the drag reduction.

Agostini et al. (2014) elaborated on this idea, by performing a simulation at the non-optimal period of $T^+ = 200$ to bring out the phase varying drag reduction during the actuation cycle. Contour plots of the Stokes strain and various other phase averaged statistics over one oscillatory period were used in their analysis. Figure 3.25 shows three phase-averaged plots, firstly the changing of skin friction with phase, followed by the contours of stokes strain, and the rate of change of the stokes strain over the boundary layer. A dashed line is presented at the level of $y^+ = 13.5$ because several turbulence statistics show their maximum here. Looking at the rate of change of the Stokes strain (Figure 3.25 (c)) in the buffer layer (at the indicated height of $y^+ = 13.5$), the skin friction shows a decline at high absolute values of the Stokes strain rate, while it recovers back to a maximum if the rate of change is slow, confirming the findings of Touber and Leschziner (2012).

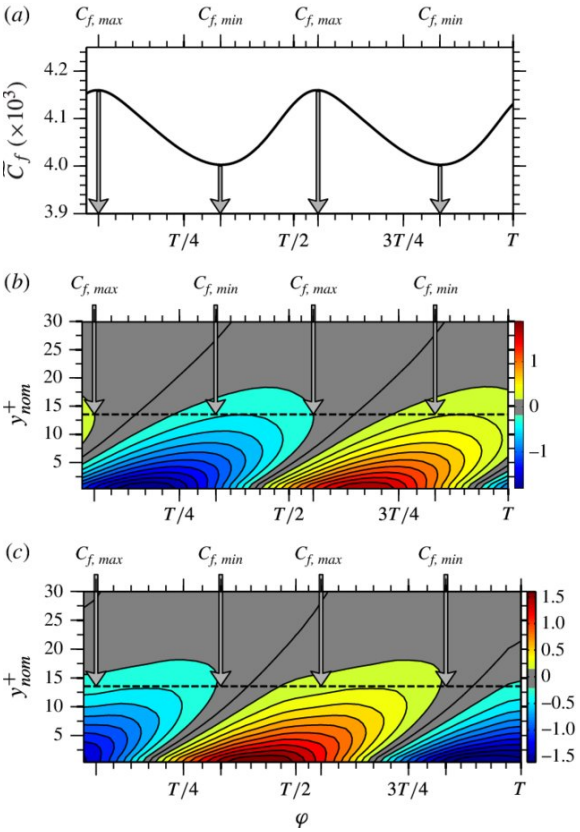

Figure 3.25: Phase averages skin friction and turbulence statistics over one oscillatory period of $T^+ = 200$ at $Re_\tau = 1{,}000$. (a) Skin friction coefficient; (b) Stoke strain, $\partial \bar{w}/\partial y$; (c) phase wise derivative of stokes strain (Agostini et al., 2014).

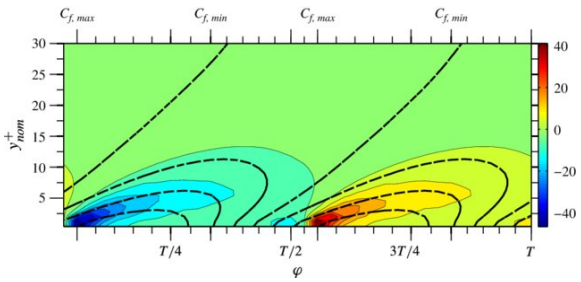

Figure 3.26: Phase averages skewness over one oscillatory period of $T^+ = 200$ at $Re_\tau = 1{,}000$ (Agostini et al., 2014).

Agostini et al. (2014) also pointed out the hysteresis effect or asymmetric cycle of the skin friction i.e. the phase of the declining skin friction is larger compared to the increase. This is reflected in the Stokes strain rate, where the high strain rate phase, responsible for the weakening of the streaks is larger than the low strain rate portion. They identified the flow skewness as a significant influence on the weakening of the

streaks. The skewness is defined as the wall-normal derivative of the angle of the velocity vector with respect to the streamwise direction, the phase contour plot can be seen in Figure 3.26. The skewness relates to the idea of the broken spatial interaction of the streaks and quasi-streamwise vortices, when a large skewness is present the flow angle between successive heights is large suggesting the spanwise displacement of the two entities. The highest values of skewness are located in the viscous sublayer, and they live near the skin friction maxima. This high skewness pertains over the phase region where the skin friction reduces and the streaks weaken.

3.4.5. Time-dependant interaction with the near-wall cycle

The above-mentioned phase wise interaction of the Stokes layer with the near-wall cycle explains the transient behaviour of the drag reduction. However looking at Figure 3.24 close to the optimal period of $T^+ = 100$ the time-dependant fluctuations have a much smaller amplitude compared to the non-optimal case. Touber and Leschziner (2012) explained that the streaks take a certain time to recover back to their unactuated strength. The recovery time was estimated by Blesbois et al. (2013) to be $t^+ = \mathcal{O}(50)$. Meaning that the streaks will have a longer time to restrengthen under larger periods when the skewness and strain rate are at lower levels. This results in larger fluctuations from the mean in the non-optimal period of $T^+ = 200$.

The idea of this time-dependent interaction with the turbulence was also put forward by Quadrio and Ricco (2004), who argued that the actuation period should be below a threshold value to effectively interact with the near-wall cycle. The threshold is that half the actuation period happens on a time scale lower than the typical lifetime of the turbulent structures. The half period is used since the direction of strain is not important and the large strain rate region occurs in both the positive and negative half of the cycle. This typical lifetime (T_l^+) value was estimated by Quadrio and Luchini (2003), who calculated the autocorrelation of a channel flow in space and time at $Re_\tau \approx 180$. The lifetime scale is then found by the integration of this autocorrelation along the path of maximum correlation, which was found to be $T_l^+ = 60$. This gives the condition of $T^+ \leq 120$. Quadrio and Ricco (2004) concluded that when T^+ gets too large and the threshold is exceeded, the near-wall cycle has sufficient time to readapt to the unperturbed state between successive cycles and the drag reduction decreases.

For the general case i.e. travelling waves, Quadrio et al. (2009) put forward the reasoning that the equivalent period seen from the turbulent fluctuations ($\mathcal{T}^+$) should be used as this mechanism is related to the time-dependent interaction with the turbulence. This was further elucidated by Quadrio and Ricco (2011). In Figure 3.27 they showed the clear correlation between the drag reduction and the Stokes layer thickness when the threshold is satisfied (black and grey symbols) while there is no correlation anymore when $\mathcal{T}^+ \geq 120$ (white symbols). Based on their observations Quadrio and Ricco (2011) concluded that for an effectively interaction of the GSL with the near-wall cycle two conditions should be satisfied: (1) the wave speed should differ significantly from the near-wall turbulence convection velocity (otherwise the TW lays on the DR crest from Figure 3.11a), and (2) the equivalent period seen by the turbulent fluctuations should be sufficiently small compared to the survival timescale of the near-wall turbulence.

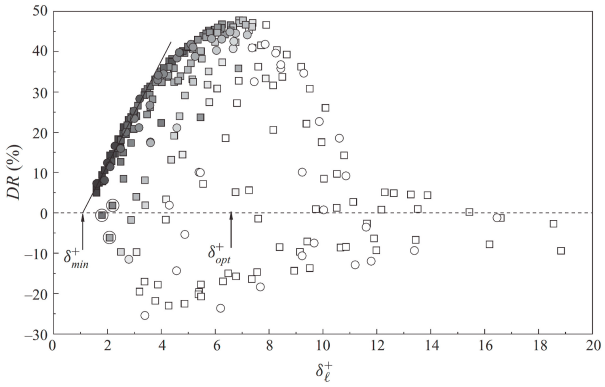

Figure 3.27: Plot of Laminar stokes layer thickness (δ_l^+) and drag reduction. Color scale indicates the equivalent time step, black indicates $\mathcal{T}^+ = 0$ and white indicates $\mathcal{T}^+ \geq 120$ (Quadrio and Ricco, 2011).

3.5. Non-sinusoidal forcing

This section discusses the effects of non-sinusoidal spanwise forcing. For practical applications, these types of waveforms may be preferred over conventional forcing for easier implementation of periodic excitations. In particular, two papers were found that focus on non-sinusoidal forcing. Cimarelli et al. (2013) simulated a number of non-sinusoidal waveforms for the OW and Mishra and Skote (2015) investigated a half square wave for SW forcing.

The alternative temporal waveforms by Cimarelli et al. (2013) can be seen Figure 3.28. Three periods and amplitudes were tested: $T^+ = 62.5$, 125 and $A^+ = 2.25$, 4.5, 9. The results of their simulations for waveforms (a), (b), (e), (f) and (j) are presented in Figure 3.29. The rows show power input (P_{in}), DR (R), and NPS (S) respectively. All waveforms have the same qualitative DR trend as the sinusoidal forcing (open symbols). Except for the square wave (b), all other waveforms have a lower DR compared to the sinusoidal forcing. An optimum NPS of 7.8% is found for the sinusoidal waveform at $A^+ = 4.5$ and $T^+ = 125$, in agreements with Quadrio and Ricco (2004) who found a NPS of 7.3%.

A predictive model was developed by Cimarelli et al. (2013) to estimate the NPS for an arbitrary waveform. They extended the formulation of the classic Stokes layer for a given waveform decomposed as a Fourier series. The DR was linked to the penetration depth of the adapted Stokes profile, the spanwise shear was used to estimate the power input. Using only the first Fourier harmonic, an optimised waveform was designed for low A^+ actuation resulting in $NPS = 6\%$ compared to $NPS = 5\%$ for the sinusoidal waveform.

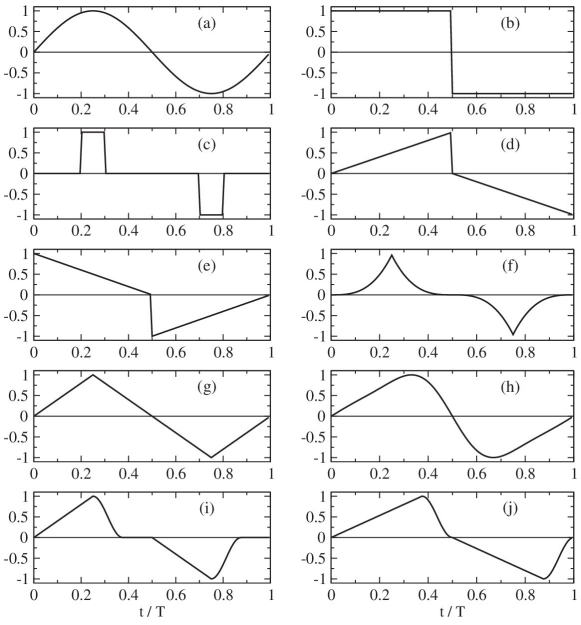

Figure 3.28: Non-sinusoidal waveforms of OW forcing from the DNS simulations of Cimarelli et al. (2013).

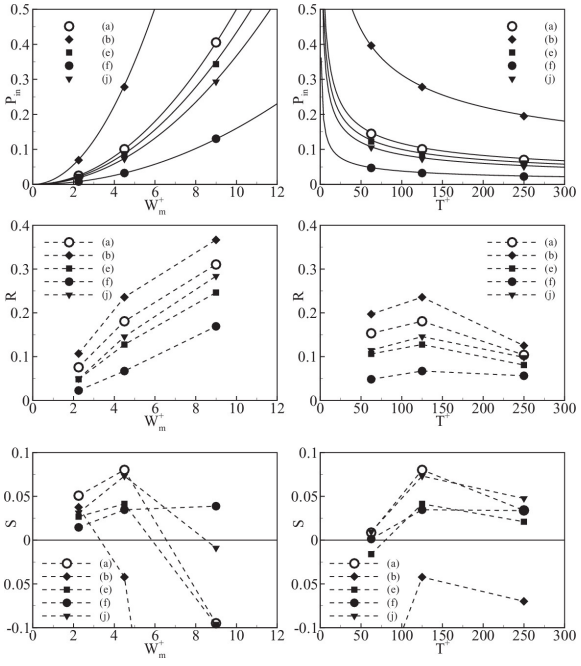

Figure 3.29: P_{in}, DR and NPS results for the non-sinusoidal forcing by Cimarelli et al. (2013).

Mishra and Skote (2015) explored the potential of a standing half square wave with the philosophy that this would result in reduced energy expenditure and thereby higher NPS. The half square wave was modelled using a smooth step function to prevent numerical instabilities associated with a sharp step function. A maximum NPS of 18% was obtained at $A^+ = 10$. A higher NPS is thus obtained to compared to the NPS of 6% for SW forcing at a similar amplitude of $A^+ = 12$ (Viotti et al., 2009). Furthermore, the optimum NPS is obtained at higher amplitudes compared to the SW optimum at $A^+ = 6$. These results confirm their hypothesis.

In conclusion, both papers show that non-sinusoidal forcing has the potential to create similar or even higher DR and NPS margins compared to conventional actuation. This means the non-sinusoidal function is a candidate for the practical implementation of spanwise forcing. Specifically, the square wave for SW forcing, this is further elaborated on in Section 3.7. In addition, the predictive model by Cimarelli et al. (2013) has the potential to be extended to the GSL for an arbitrary waveform described by a Fourier series.

3.6. Outer-scaled actuation pathway

To date, the entire body of literature on spanwise forcing focuses on inner-scaled actuation (ISA) by reducing the strength of the near-wall cycle, except for the recent work by Marusic et al., 2021. They explore the potential of OSA using TW spanwise forcing. The boundary layer facility at the University of Melbourne was used to get experimental conditions of up to $Re_\tau = 12{,}800$ for a sufficient outer-scaled influence. OSA was achieved by increasing the period of oscillation to $T^+ = 600 - 1{,}100$ compared to $T^+ \approx 140$ for ISA. The wavelength was fixed and sized in the order of δ. Their results are summarised in Figure 3.30.

For ISA, the results match the Reynolds number scaling of Gatti and Quadrio (2016), with a declining DR with Re_τ, decreasing from between 30-25% for $Re_\tau = 951 - 6{,}000$. For this actuation scheme, a negative NPS is obtained of approximately -25%. Due to the increasing influence of large-scale structures on the turbulence with Re_τ, the opposite trend could be observed for OSA. The prediction of Gatti and Quadrio (2016) breaks down and a DR is now positively correlated with Reynolds number increasing from 0% to 13% for $Re_\tau = 951 - 12{,}800$. Even though the DR margin is lower than for ISA, a positive NPS is obtained at higher Reynolds numbers. The reason for this is that input power scales with $\omega^{5/2}$ (Quadrio and Ricco, 2011), leading to a reduced input power at the higher values of T^+ needed for OSA.

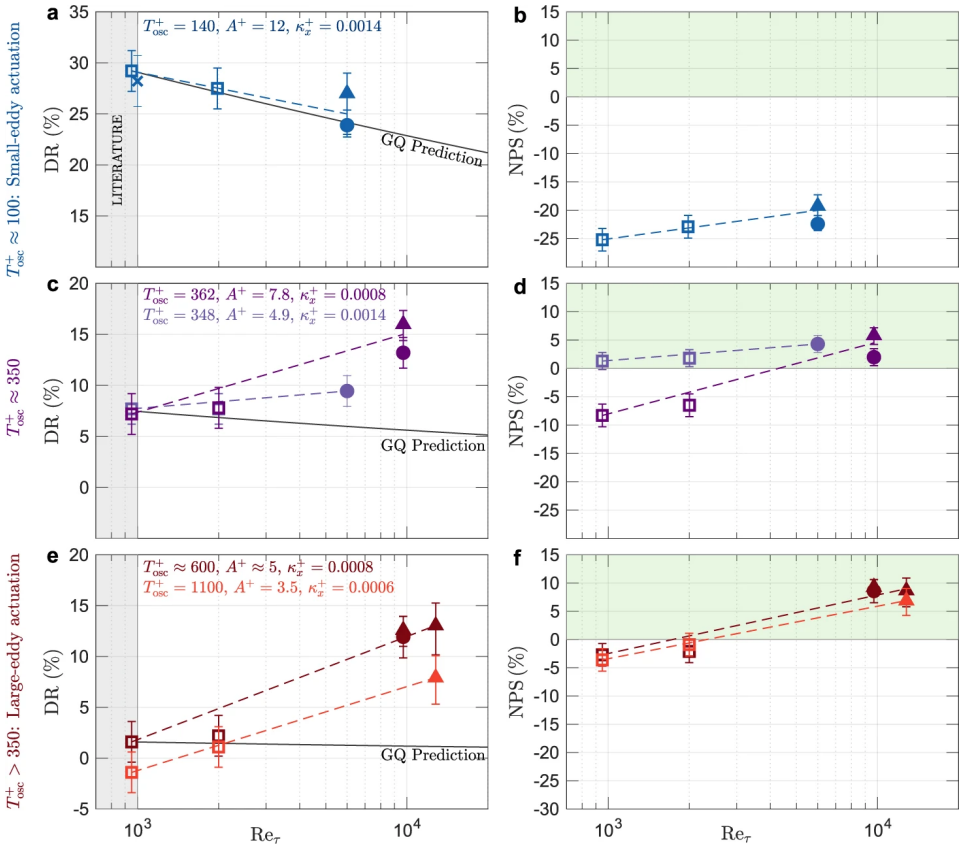

Figure 3.30: Drag reduction and net power saving obtained by streamwise travelling waves of Marusic et al. (2021) compared to the predictive model by Gatti and Quadrio (2016). ISA is indicated with small-eddy actuation, OSA is indicated by large-eddy actuation. Open squares, LES simulation; circles, HWA measurements; Triangles, drag balance measurements; cross, DNS by Gatti and Quadrio (2016).

The effect of ISA and OSA on the near-wall turbulence was also assessed using spectra of the wall shear stress presented in Figure 3.31. The premultiplied spectra are plotted against the non-dimensional period, furthermore, the actuation period is indicated by the arrow. Both actuation schemes show an attenuation of turbulence energy spanning a broadband range of both inner- and outer-scales. For ISA, strong attenuation of small-scale energy below the actuation period can be seen, as well as an attenuation of large-scale energy below $T^+ \lesssim 1{,}000$. The OSA strategy shows a significant suppression between $50 \lesssim T^+ \lesssim 2{,}000$. The effect on the small scales is however less strong, and they are virtually unaffected at $T^+ \lesssim 50$. Deshpande et al. (2022) explains that the broadband attenuation is a result of the inter-scale interaction between the inner- and the

outer-scales. They prove that both the ISA and the OSA pathway can effectively act on this inter-scale interaction resulting in a drag reduction for both strategies.

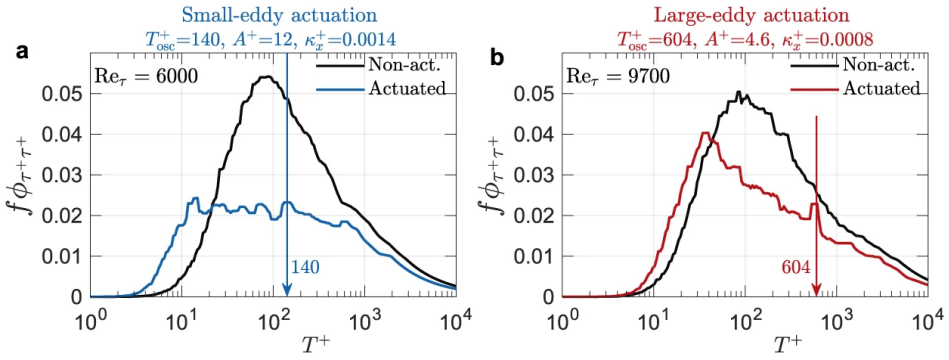

Figure 3.31: Spectra of wall shear stress with and without actuation for (a) ISA at $Re_\tau = 6,000$ and (b) OSA at $Re_\tau = 9,700$. ISA is indicated with small-eddy actuation, OSA is indicated by large-eddy actuation. (Marusic et al., 2021)

The literature on ISA cannot explain the working mechanism behind the DR of the OSA pathway. Although not supported by data or scientific evidence yet, the author of this review proposes some preliminary ideas and hypotheses about the working mechanism of the new pathway. One of the working mechanisms could be that the Stokes layer breaks up or attenuates the interaction between the VLSMs in the log-layer and the near-wall turbulence, so reducing the footprinting and modulation on the near-wall cycle. This idea is based on the broken interaction for conventional actuation between the QSVs and streaks of the near-wall cycle. At the larger oscillatory periods associated with this new pathway, the penetration depth of the Stokes layer increases. This could result in the spanwise displacement of the complete near-wall region with respect to the log layer, thereby breaking up the interaction of the VLSMs.

Another working mechanism could be the time dependent interaction of the forcing with the VLSMs, as put forward by Quadrio and Ricco (2004) for ISA. Following the two requirements for time dependant interaction of the spanwise forcing with the turbulence by Quadrio and Ricco (2011), in that (1) the wavespeed should be significantly different from the convection velocity and (2) the equivalent period observed by the turbulence is smaller than the lifetime scale of the turbulence. For the first requirement the convection velocity of the VLSMs can be assumed, which convect with approximately the mean velocity at the geometric mean location if the log-layer. Roughly speaking $\mathcal{U} \approx 20-30$ but this is of Reynolds number dependant as the log-layer grows. For the second requirement, this would mean the threshold value for the equivalent period is probably defined by the typical lifetime of the large-scale structures. As presented by Blackwelder (1972) the lifetime scales are significantly higher for VLSMs (in the order of 7 boundary layer convections), meaning actuation can be forced at higher periods.

In conclusion, the results of Marusic et al. (2021) are promising and show that OSA is indeed a possibility using spanwise forcing. The DR trends with Re_τ for ISA and OSA are in line with the expectations presented in Section 2.3. In addition, both actuation strategies attenuate a broadband range or turbulent scales. Even though practical implementation of spanwise forcing may not find its way into industry, this still presents an interesting research gap to be filled. A better understanding of the OSA flow mechanics can be leveraged for the development of passive techniques to create the desired spanwise disturbances.

3.7. Practical considerations

From Table 3.1 it can be seen that spanwise forcing has been widely implemented through the OW scheme. Experimental realisations of the other two forcing schemes are relatively scarce, to the knowledge of the author, only three realisations were made for TW forcing and SW forcing is still unexplored. This section sheds light on the advantages and disadvantages of practical implementation of spanwise forcing through wall motion, they are summarised in Table 3.3. In addition to this, a new idea is presented to realise SW forcing experimentally.

From a practical point, the implementation of the OW is the easiest. Only a simple mechanism like the cam-shaft system of Laadhari et al. (1994) is needed to oscillate the entire wall section. Travelling waves

require a waveform that is usually discretized using a number of spanwise oscillating elements (Auteri et al., 2010; Marusic et al., 2021) or by the deformation of a flexible skin like the experiments of Bird et al. (2018). This requires a more complex cam-shaft or other driving mechanisms, making the practical implementation more tedious. An inherent problem that oscillating wall elements have is that they usually have a fixed displacement amplitude. This means that with increasing the period, the spanwise velocity amplitude decreases. This is especially important when applying the OSA pathway, where the timescales are much slower. As an example, for the results of Marusic et al. (2021), the amplitude decreased from $A^+ = 12$ for ISA at $T^+ = 140$ to $A^+ = 3.5$ at $T^+ = 1,100$ for OSA. SW forcing does not have this problem since a fixed spanwise velocity can be imposed. However, the fact that SW forcing has not been realised experimentally may be due to the imposing of a steady wall velocity at a given spatial distribution, which is more difficult to implement than oscillatory wall elements.

Technique	Advantages	Disadvantages
Oscillating wall	Easy implementation	Lowest DR and NPS potential
Standing wave	High DR and NPS potential; Has the potential for passive recreation	No practical realisations
Travelling wave	Highest DR and NPS potential	Complex implementation; High DR region is sensitive to specific actuation conditions

Table 3.3: The advantages and disadvantages for practical application of the three forms of spanwise wall motion.

When it comes to application in industry, the DR and especially NPS potential of the flow control method is of high importance. It was found in Section 3.3 that OW forcing has the lowest potential compared to TW with the highest potential. One disadvantage is however the sensitivity to the exact actuation parameters required to be on the high DR ridge in the parameter space. SW forcing has relatively high DR and NPS potential while being less sensitive to the exact wavelength.

Another consideration, which especially applies to the ISA pathway is the viscous scaling of actuation parameters. Ricco et al. (2021) point out that if the viscous scaling applies, the spatial dimensions and temporal scales reduce as the Reynolds number grows. As a result, the spanwise displacement amplitude of TW and SW forcing decreases and the frequencies increase drastically in physical units. As an example, the OW of Quadrio and Ricco (2004) is considered, at optimal NPS conditions ($A^+ = 4.5$, $T^+ = 125$ and $D^+ = 179$). The comparison is made between low Re_τ experimental conditions and along the fuselage of an Airbus A350 at cruise conditions. The viscous scales are computed using the power law for C_f of a turbulent boundary layer, Equation 2.13. The scaling for both cases is presented in Table 3.4. For experimental conditions, the oscillation frequencies and displacements are reasonable to attain using mechanical actuation. However, at full-scale flight conditions, the frequency becomes especially high and is not considered feasible.

Parameter	Experiment	A350 cruise
x (m)	1	30
U_∞ (m/s)	5	900
δ (mm)	26.0	262
Re_τ	403	16,400
δ_ν (µm)	65.0	1.60
u_τ (m/s)	0.23	24.4
A (m/s)	1.05	110
T (s)	0.035	3.17×10^{-6}
f (Hz)	29.0	31,500
D (mm)	11.6	0.286

Table 3.4: Scaling of OW forcing ($A^+ = 4.5$, $T^+ = 125$ and $D^+ = 179$), for experimental conditions at 20 °C and along the fuselage of the Airbus A350 at cruise conditions (11,000 m).

Due to the outer scaling of the VLSMs, the OSA pathway has larger length scales and lower frequencies. The frequencies are however still too high to realise with oscillating elements. For OSA the oscillation needs

to target structures with a wavelength are in the order of δ, now using the convection velocity at $y/\delta = 0.06$ a timescale can be found. For the A350, this still results in a high frequency of $f \approx 2,500$. With OSA, the wavelength scales in the order of δ i.e. 262 mm, these scales are more reasonable, making SW forcing an interesting option.

This brings the author to present a novel idea for implementing spanwise forcing in view of industrial applications. Specifically, SW forcing, for its high DR potential and reduced sensitivity to the characteristic wave parameters. Furthermore, standing waves have the most potential at full-scale applications due to the high frequencies for the other two schemes that cannot be realised practically. This also presents a valuable addition to the academic body of literature, since SW forcing has not been realised experimentally.

The idea is to use spanwise running belts, placed in a sequential streamwise manner to form a standing square wave. The square wave is a reasonable approximation as was shown in Section 3.5. The idea is an extension with more belts of the experimental setup of Kiesow and Plesniak (2003), which used a single spanwise running belt to analyse the effects of crossflow on the boundary layer. The wavelength can be tailored by having a multitude of belts to make up a single waveform, allowing for both ISA and OSA to be tested. Furthermore, this allows full control over the spanwise velocity amplitude.

II

Outer-scaled actuation using passive spanwise forcing

4

Experimental methodology

This chapter presents the experimental methodology for Part II of the thesis. This part is a preliminary investigation into outer-scaled actuation (OSA) using passive spanwise forcing. A series of wind tunnel experiments was performed to investigate the drag characteristics using direct force measurements. The influence on the inner- and outer turbulent scales was further investigated using hot-wire anemometry (HWA). Details on the experimental facility are presented in Section 4.1. The passive techniques are realised through a number of test plates (TPs) that fit the direct force balance. The test plate development is presented in Section 4.2. The flow measurement techniques are elucidated in Section 4.3 and Section 4.4.

4.1. Experimental facility

To investigate flow control using the OSA pathway a substantial contribution and influence of the outer-scaled flow structures is required in the turbulent boundary layer. As mentioned in Chapter 2, their contribution increases with the frictional Reynolds number. Hence a sufficiently high Re_τ is required to investigate the hypotheses regarding OSA. Hutchins and Marusic (2007a) argued that the minimum requirement is $Re_\tau \geq 2{,}000$ but the outer-peak will be small in magnitude. Smits et al. (2011) concluded that at least a $Re_\tau \geq 4{,}000$ is required for sufficient scale separation. The latter was used as a criterion for wind tunnel selection for the current experiments. The frictional Reynolds number can be estimated using the power law expressions from Section 2.1. From this, the frictional Reynolds number shows a dependence on:

$$Re_\tau = f(U_\infty, x, \mu, \rho) \tag{4.1}$$

For the considered experimental facilities, ρ and μ are dictated by the atmospheric conditions and are therefore fixed. Consequently, a desired Re_τ can be tuned using the freestream velocity and development length. The response of the boundary layer properties on U_∞ and x is presented in Figure 4.1

From Figure 4.1c it can be seen that a drawback of increasing U_∞ is a decrease in δ_ν, making flow measurements more difficult. Specifically, the measurement resolution to capture the inner-layer with the available flow-measurement techniques decreases. The criteria $15\delta_\nu \geq 0.2$ mm is used for a sufficient resolution. This means the wind tunnel should be run at a moderate freestream velocity. To attain a sufficient Re_τ the development length of the wind tunnel can be increased. The infeasible regions under the conditions on the viscous length scale and Re_τ are indicated in Figure 4.1 by the hatched areas.

Measurements were performed in the M-tunnel and W-tunnel at the wind tunnel laboratories of DUT. An overview of the experimental conditions for both tunnels at U_∞ =10 and 30 m/s is presented in Table 4.1. The M-tunnel is an open loop tunnel with a test section of 0.4 m × 0.4 m. The maximum freestream velocity is $U_\infty \approx 35$ m/s with a turbulence intensity in the order of 0.7%. The test section has parallel walls giving rise to a slight favourable pressure gradient due to blockage of the growing boundary layer. To increase Re_τ, an extension to the original test section was used, increasing the development length from 1.5 m to 3.9 m. At $U_\infty = 30$ m/s, Re_τ is increased from 2,300 to 4,800 based on the theoretical calculations.

The W-tunnel has a similar layout and performance to the M-tunnel. The test section is 0.6 m × 0.6 m or 0.3 m × 0.6 m for a maximum freestream velocity of $U_\infty \approx 15$ m/s and 30 m/s. The test section has a length

of 3.6 m resulting in $Re_\tau = 4{,}500$ at $U_\infty = 30$ m/s. A zero pressure gradient was realised in the text section by adjusting the moving top wall.

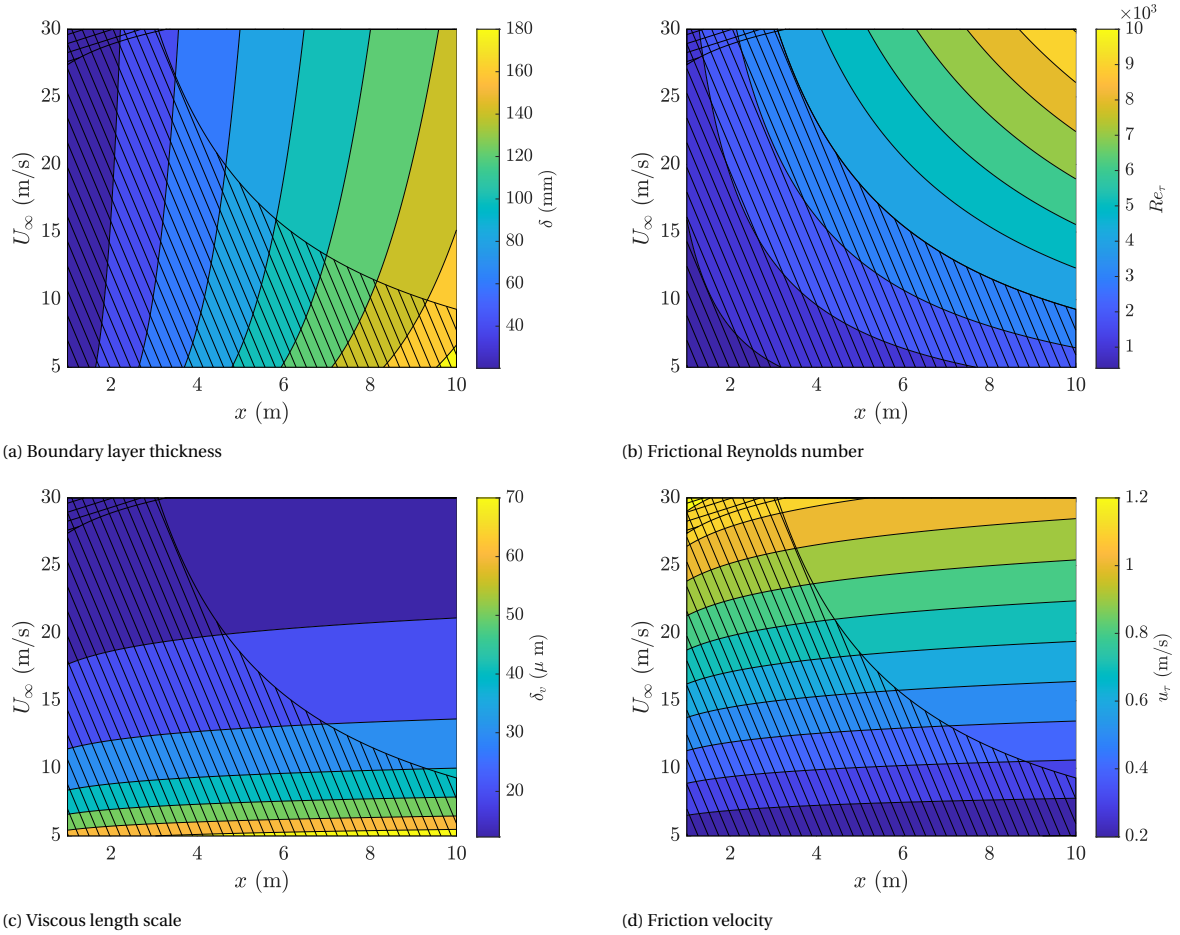

(a) Boundary layer thickness

(b) Frictional Reynolds number

(c) Viscous length scale

(d) Friction velocity

Figure 4.1: Response of the boundary layer properties for development length and freestream velocity in air at $T = 20$ °C: $\rho = 1.204$ kg/m^3 and $\mu = 1.825 \times 10^{-5}$ kg/ms, according to theoretical calculations of Section 2.1.

Parameter	M-tunnel		W-tunnel	
	$U_\infty = 10$ m/s	$U_\infty = 30$ m/s	$U_\infty = 10$ m/s	$U_\infty = 30$ m/s
δ (mm)	75.8	64.8	70.7	60.5
Re_τ	2,020	4,800	1,900	4,500
δ_ν (µm)	37.4	13.5	37.2	13.4
u_τ (m/s)	0.40	1.12	0.41	1.12

Table 4.1: Experimental conditions for M-tunnel and W-tunnel with development lengths $x_{dev} = 3.9$ m and 3.6 m, respectively. Calculations for air at $T = 20$ °C: $\rho = 1.204$ kg/m^3 and $\mu = 1.825 \times 10^{-5}$ kg/ms, according to theoretical relations of Section 2.1.

4.2. Model development for outer-scaled actuation

This section discusses the model development for the experiments to test passive techniques for OSA. The techniques were made on test plates (TPs) with specified dimensions to fit the direct force balance. Three techniques were selected from the literature survey preceding this thesis (Knoop, 2023), these techniques are: dimples, sinusoidal undulations, and oblique wavy walls. They all show potential in passively recreating a spanwise forcing by realising some sort of spatially oscillating spanwise velocity profile representative of a spatial Stokes layer. To allow for OSA, the spatial oscillation must be sized to target outer-scaled structures effectively. Subsection 4.2.1 discussed the sizing requirements for OSA. A large number of passive TPs is already available at the company Dimple Aerospace B.V.. Subsection 4.2.2 presents the selection of a number

of TPs that are correctly sized for OSA. In addition, two new TP designs are proposed to supplement the existing designs.

4.2.1. Sizing for outer-scaled actuation

This section discusses the sizing requirements for OSA on passive TPs. Sizing was based on the work of Marusic et al. (2021) and Chandran et al. (2022), because they present the first realisation of OSA using spanwise forcing, and the only one at the time of writing. Their work focuses on streamwise travelling waves. The low-frequency outer-scales can be effectively actuated upon by reducing the actuation frequency. Their characteristic actuation parameters can be transformed into an equivalent wavelength to get an idea of the actuation parameters required for spatial forcing. The transformation is made in two steps. First, an equivalent period ($\mathcal{T}$) is calculated using Equation 3.9, which relies on Taylor's hypothesis to transform the spatio-temporal wave seen by the turbulence into a purely temporal oscillation. The convection velocity of the near-wall turbulence is used, i.e. $\mathcal{U}_w^+ \approx 10$ (Kim and Hussain, 1992; Krogstad et al., 1998). Secondly, the temporal oscillation is transformed into a spatial wave according to Equation 3.10.

$$\mathcal{T} = \frac{\lambda_x}{\mathcal{U}_w - c} \tag{Equation 3.9}$$

$$\lambda_{x,eq} = \mathcal{T}\mathcal{U}_w \tag{Equation 3.10}$$

Three options are considered for sizing based on the work of Marusic et al. (2021) and Chandran et al. (2022). Firstly, by simply transforming the spatio-temporal wave according to the above-mentioned method. The second method transforms the actuation period into a wavelength using Equation 3.10, (note $\mathcal{T} = T$). This temporal transformation is an option since the wavelength in their work is fixed at $\lambda_x = 0.3m$, and the DR response is relatively insensitive to the exact wavelength (Quadrio et al., 2009). A third option is based on the idea that OSA targets the outer-scaled structures. Hence the wavelength should be tuned to match the outer length scales, i.e. $\lambda_x = \mathcal{O}(\delta)$.

In Table 4.2, a subset of the OSA parameters of Chandran et al. (2022) is presented. All cases have a positive NPS between 0 and 10%. The equivalent wavelengths for spatial forcing are presented in inner- and outer-scaling for the aforementioned spatio-temporal and temporal transformations. Based on this a range for effective OSA is considered of $\lambda_x^+ = \mathcal{O}(2,000 - 20,000)$ or $\lambda_x/\delta = \mathcal{O}(0.3 - 2)$. It can be observed that OSA is effective over a wide range of actuation length scales. Hence, OSA is likely less sensitive to the exact actuation conditions compared to ISA, which shows an optimum around $\lambda_x^+ = 1,000 - 1,250$ (Viotti et al., 2009). These sizing requirements will be used for model selection in Subsection 4.2.2 where a number of TPs designs are selected with correct wavelengths for OSA.

Conditions				ST transform		T transform	
Re_τ	$DR(\%)$	T^+	k_x^+	$\lambda_{x,eq}^+$	$\lambda_{x,eq}/\delta$	$\lambda_{x,eq}^+$	$\lambda_{x,eq}/\delta$
4,500	9	405	0.0018	1,900	0.42	4,000	0.89
6,000	6	700	0.0014	2,700	0.46	7,000	1.17
9700	5.2	1,812	0.008	5,500	0.56	18,000	1.86
9700	11.5	604	0.008	3,400	0.35	6,000	0.62
12,800	8.3	1,100	0.006	5,400	0.42	11,000	0.86
12,800	13.3	653	0.006	4,000	0.31	6,500	0.51
15,000	4.7	1,975	0.00046	17,000	1.15	20,000	1.33

Table 4.2: Transformation of actuation parameters from Chandran et al. (2022) into an equivalent wavelength in viscous and outer scaling for spatial forcing. All considered entries are effective at OSA, with an NPS between 0 and 10%. ST and T indicate the spatio-temporal and temporal transformation as outlined in the text.

4.2.2. Model selection

This section presents the model selection and development of TPs for passive OSA. The passive techniques were realised on TPs that have a size of 881.3 mm × 366.3 mm × 5 mm As mentioned in the introduction, three passive techniques show potential for OSA. These are: dimples, sinusoidal undulations, and oblique wavy walls. Many TPs are already available at Dimple Aerospace B.V., and six of the designs show potential with streamwise wavelengths in the correct order for OSA. Two new design derivatives are proposed as an

addition to the available TPs. The designs and their corresponding streamwise wavelengths are presented in Table 4.3. The viscous wavelengths are also indicated for freestream velocities of $U_\infty = 20, 30$ m/s for the M-tunnel at a development length of $x_{dev} = 3.9$ m. From this, all eight TPs have streamwise wavelengths in the correct order for OSA, especially at higher velocities where the viscous length scale is smaller. The following subsections present the characteristic geometrical parameter of each TP, and shortly discuss their workings for generating spanwise forcing. For a detailed account of the techniques, the reader is referred back to Chapter 5 of the literature survey preceding this thesis (Knoop, 2023).

Name	Test plate	λ_x (mm)	λ_x^+	
			$U_\infty = 20$ m/s	$U_\infty = 30$ m/s
Staggered dimples (van Nesselrooij et al., 2016)	TP0001	57.9	2,940	4,290
Staggered dimples (Tay et al., 2015)	TP0005	129.9	6,600	9,620
Staggered SUs based on TP0001	TP0004	57.9	2,940	4,290
Aligned SUs based on TP0001	TP0124 (new)	57.9	2,940	4,290
OWW (Ghebali et al., 2017)	TP0007	89.5	4,550	6,630
OWW high H (Denison et al., 2015)	TP0011	44.1	2,240	3,270
OWW low H (Denison et al., 2015)	TP0012	44.1	2,240	3,270
Superimposed OWW based on TP0007	TP0125 (new)	89.5	4,550	6,630

Table 4.3: Overview of new and selected TPs from Dimple Aerospace B.V.. Streamwise wavelength λ_x^+ is indicated for the M-tunnel at $x_{dev} = 3.9$ m for $U_\infty = 20, 30$ m/s, calculations are made for air at $T = 20°C$: $\rho = 1.204$ kg/m^3 and $\mu = 1.825 \times 10^{-5}$ kg/ms, according to theoretical calculations of Section 2.1.

Dimples

Dimples are shallow surface indentations seemingly similar to the geometry found on golf balls. Dimples were originally studied for their enhancement of heat transfer. A group at the Kurchatov Institute of Atomic Energy (Kiknadze et al., 1984) first suggested that the dimples may also reduce skin friction. Since the first reported results, various studies have been performed, with some reporting drag increases, while other studies found moderate drag reductions.

The dimple geometry is hypothesised to generate a spanwise forcing similar to a spatial Stokes layer. Van Nesselrooij et al. (2016) showed that this spanwise forcing results from a converging-diverging flow inside a dimple. When the dimples are placed in the staggered configuration, these spanwise velocities profiles are arranged to resemble a spatial forcing like the spatial Stokes layer. In this case, one spatial oscillation's wavelength equals the dimples' streamwise spacing of the dimples i.e $\lambda_x = L_x$. Van Campenhout et al. (2018) measured the spanwise meandering at $y/\delta = 0.2$, and made a comparison to the oscillating wall by Quadrio and Ricco (2004), finding $A^+ = 0.74$ and $T^+ = 135$. These results suggest that the spanwise velocity profile from the dimples penetrates deeper into the boundary layer, since the Stokes profile for the pure spanwise forcing would have decayed to zero at this height. This is confirmed in the MSc. thesis of Lin (2021), which showed the spanwise velocities above the dimple geometry with a penetration around $y/\delta = 0.2 - 0.4$.

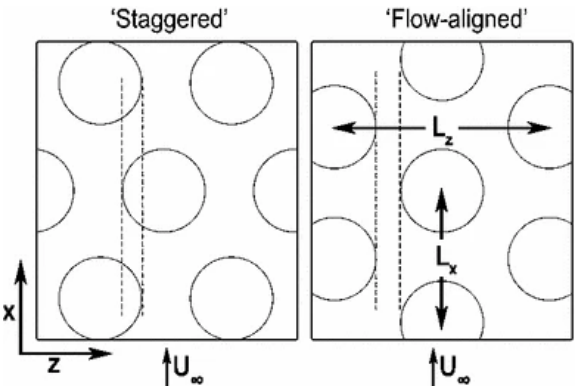

Figure 4.2: Staggered and flow-aligned dimple configurations (van Nesselrooij et al., 2016).

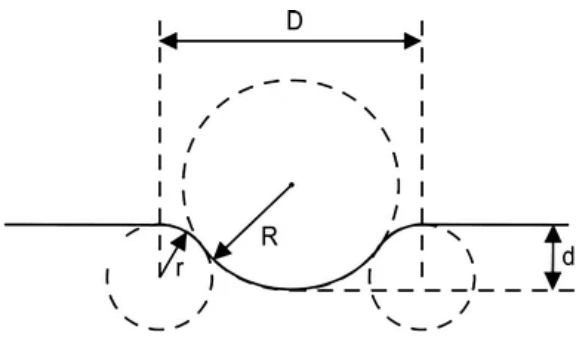

Figure 4.3: Cross-sectional geometry of the dimple geometry van Nesselrooij et al. (2016).

A number of parameters describe the dimple geometry. The main ones are the dimple diameter D, dimple

depth d, and their streamwise- and spanwise spacing L_x and L_z. The combination of the latter two dictate the configuration, as either staggered or flow aligned, as depicted in Figure 4.2. The dimple edges are rounded by a rounding radius r, in combination with D and d, the dimple cross-sectional geometry is fully described (Figure 4.3). A detailed overview of the dimpled geometries for the TPs is presented in Table 4.4, and a photograph of the two TPs is depicted in Figure 4.4.

Name	Test plate	D (mm)	d (mm)	d/D (%)	r (mm)	L_x (mm)	L_z (mm)
Staggered dimples (van Nesselrooij et al., 2016)	TP0001	20	0.5	2.5	10	57.9	33
Staggered dimples (Tay et al., 2015)	TP0005	50	2.5	5	42	129.9	75

Table 4.4: Overview of the geometric parameters of the considered dimpled test plates

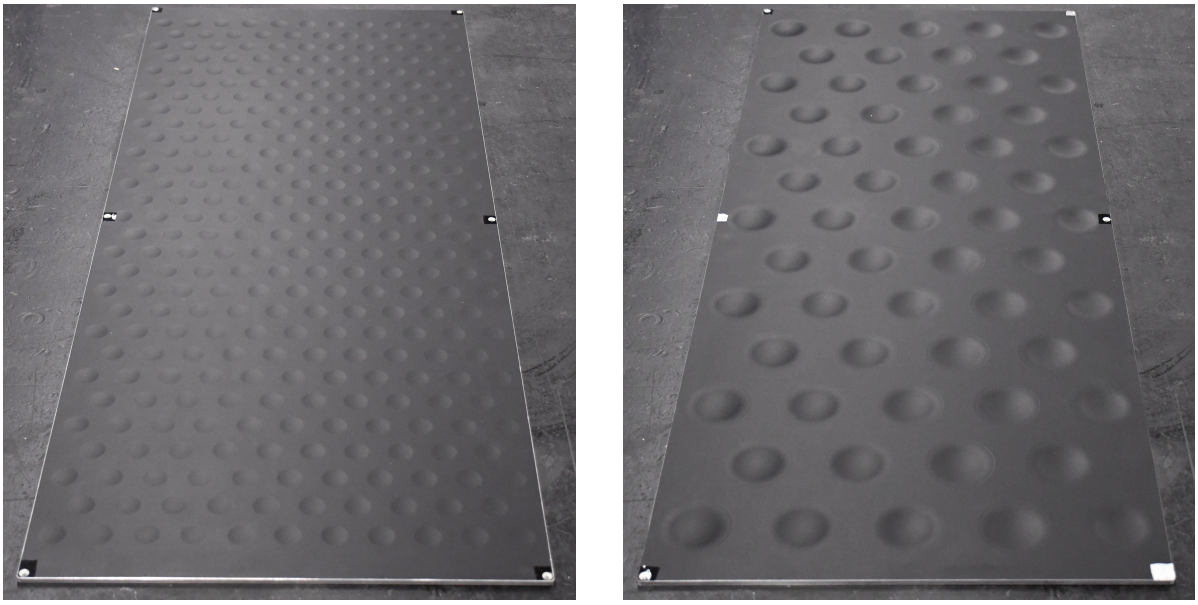

(a) TP0001-Staggered dimples of van Nesselrooij et al. (2016)

(b) TP0005-Staggered dimples of Tay et al. (2015)

Figure 4.4: Overview of the TPs with the dimpled geometry selected for the experiments

Sinusoidal undulations

A technique which had not been discussed in open literature is sinusoidal undulations (SUs). The idea originated from Dimple Aerospace B.V. and was patented (van Nesselrooij et al., 2020). SUs are a derivative of the dimple geometry. They consist of shallow sinusoidal surface indentations of a streamwise oriented wave with a spanwise displacement amplitude. This surface wave is believed to result in a spatially oscillating spanwise velocity profile. An example of different SUs is presented in Figure 4.5, where the leftmost image shows the closest analogy to sinusoidal riblets.

The SUs considered in this thesis are based on Fig.1 of the patent depicted in Figure 4.5. The streamwise waveform can is characterised by the Equation 4.2, which describes the spanwise path z as a function of x, with W as the spanwise displacement amplitude. The cross-section of the undulations is similar to the dimple geometry with a width D, a depth d, and a rounding radius r. L_z gives the spanwise spacing of the individual undulations. In addition to the existing staggered SUs (TP0004), an aligned variant was added. Which has the same geometrical parameters but the streamwise waves are in-phase. A detailed overview of the SU geometry is presented in Table 4.5, and the pictures of the two TPs can be found in Figure 4.6.

$$z(x) = W \sin(k_x x) \tag{4.2}$$

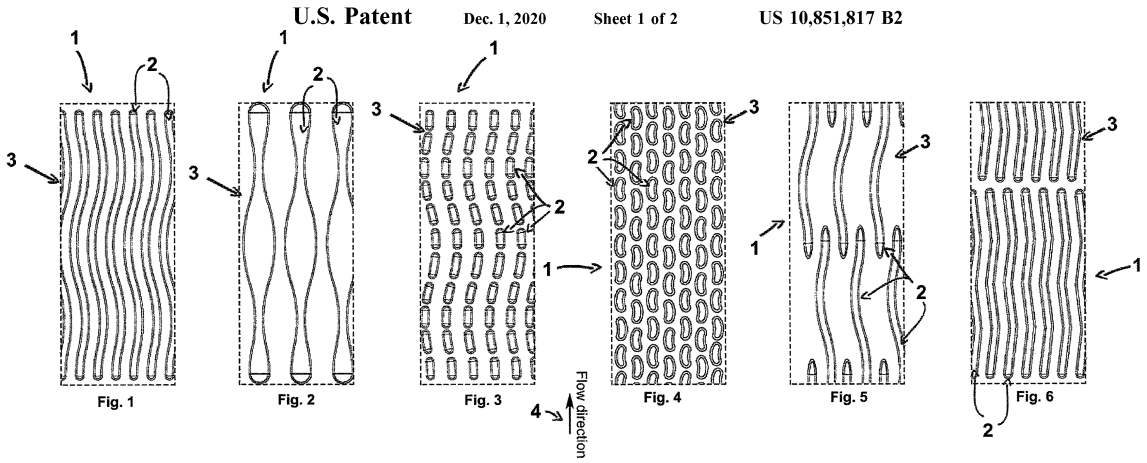

Figure 4.5: Different sinusoidal undulations from the patent by van Nesselrooij et al. (2020).

Name	Test plate	λ_x (mm)	W (mm)	D (mm)	d (mm)	d/D (%)	r (mm)	L_z (mm)
Staggered SUs	TP0004	57.9	6.5	10	0.5	5	10	16.5
Aligned SUs	TP0124	57.9	6.5	10	0.5	5	10	16.5

Table 4.5: Overview of the geometric parameters of the sinusoidal undulations test plates

(a) TP0124-Staggered sinusoidal undulations

(b) TP0124-Aligned sinusoidal undulations

Figure 4.6: Overview of the TPs with the sinusoidal undulations geometry selected for the experiments

Oblique wavy walls

Oblique wavy walls (OWWs) are stationary wavy walls, where waves of wall-normal displacement are oriented at an angle with respect to the freestream. A schematic of the OWW is presented in Figure 4.7. The idea of the oblique waves is that the flow over the waveform results in a variable spanwise pressure gradient driving the fluid in the spanwise direction. Only small geometrical changes are needed to attain relatively large spanwise velocities. This geometry creates a sinusoidal spanwise shear strain layer similar to the SSL (Chernyshenko, 2013; Ghebali et al., 2017). As a result of the geometry, an additional mean spanwise crossflow flow is also introduced.

The wall-normal height of the OWW surface is described by Equation 4.3, where H is the height amplitude, and λ_x and λ_z are the wavelengths in streamwise and spanwise directions. In literature, the geometry of

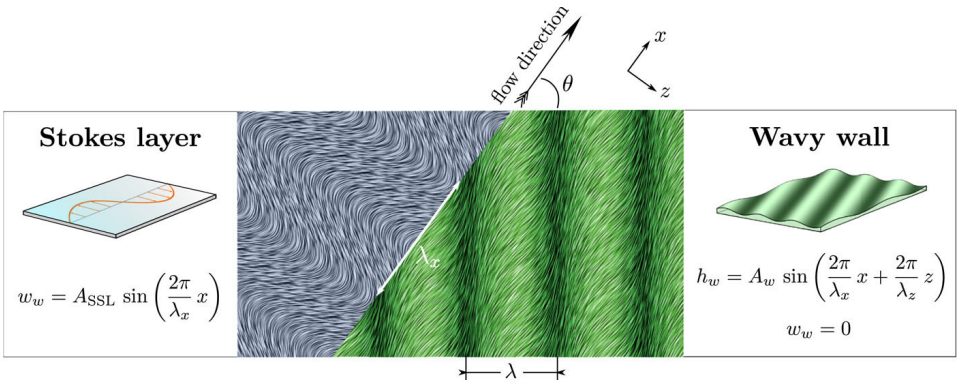

Figure 4.7: The concept of oblique wavy walls that mimics the SSL (Ghebali et al., 2017).

OWWs is often characterised by three parameters, namely the wavelength λ, the oblique angle of the crests with respect to the freestream α and the height amplitude H. The wavelengths in streamwise and spanwise directions are then defined as $\lambda_x = \lambda/\sin(\alpha)$ and $\lambda_z = \lambda/\cos(\alpha)$. The streamwise wavelength is equivalent to the wavelength of the generated spatial Stokes layer forcing. In Table 4.6 an overview of the considered OWW geometries is presented, $2H$ is the peak to crest height to make a valid comparison to the depth of the dimples d. For the dimples the depth-to-diameter ratio is also considered; this is a sort of steepness. For the OWWs an equivalent steepness is defined at $2H/\lambda_x$.

$$y_w(x,z) = H\sin(k_x x + k_z z) \tag{4.3}$$

Apart from the existing TPs at Dimple Aerospace B.V., which are TP0007, TP0011 and TP0012, a new design was added. This is the superimposed OWW, where two oblique waves are superimposed with an oblique angle in the positive and negative direction respectively. The new geometry is defined in Equation 4.4. The idea behind this geometry is to counteract the possible negative effects of the mean spanwise flow introduced by the OWW surface. An overview of the TP geometries is presented in Table 4.6, the photographs of the four TPs can be found in Figure 4.8

$$y_w(x,z) = H/2\sin(k_x x + k_z z) + H/2\sin(k_x x - k_z z) \tag{4.4}$$

Name	Test plate	λ_x (mm)	α (°)	$2H$ (mm)	$2H/\lambda_x$ (%)
OWW (Ghebali et al., 2017)	TP0007	89.5	20	1.2	1.3
OWW high H (Denison et al., 2015)	TP0011	44.1	37.4	1.045	2.4
OWW low H (Denison et al., 2015)	TP0012	44.1	37.4	0.232	0.5
Superimposed OWW (Ghebali et al., 2017)	TP0125	89.5	±20	1.2	1.3

Table 4.6: Overview of the geometric parameters of the considered OWW TPs

(a) TP0007-OWW of Ghebali et al. (2017)

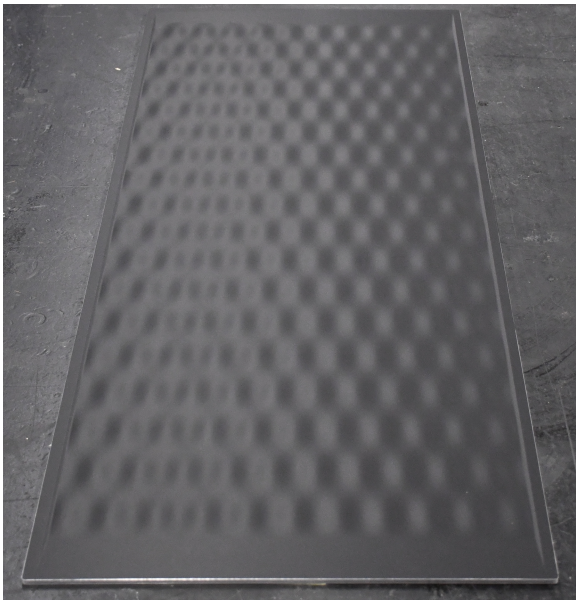

(b) TP0011-OWW with high H of Denison et al. (2015)

(c) TP0011-OWW with low H of Denison et al. (2015)

(d) TP0125-Superimposed OWW based on TP0007

Figure 4.8: overview of the TPs with the oblique wavy wall geometry selected for the experiments

4.3. Direct force measurements

Drag measurements on the passive techniques were performed using 'The Hill'. This is a wind tunnel agnostic experimental apparatus developed by Dimple Aerospace B.V. for direct force measurements of flat plates in subsonic flow conditions. Automated drag measurements are performed on the standardised TPs. Pressure effects, sensor drift and other sources of error are accounted for in the measurement process. The drag measurements are referenced to a known flat plate to find the drag reduction ΔC_d. The apparatus was validated with riblets, and the 95% confidence level of drag measurements is below 0.5% ΔC_d for drag forces below 1 N. (Van Nesselrooij et al., 2022).

An overview of the Hill can be seen in Figure 4.9. The Hill accepts TPs (a) of the specified size which can be placed in the connector (b). The connector is connected to the base (c) with four titanium flexures (e). The flexures allow the connector to move freely in the streamwise direction while constraining the motion in the spanwise and wall-normal directions. As such, a small gap of 0.3 mm between the connector and the base

allows for this streamwise movement. Which allows the force sensor (j) to measure the streamwise integral drag force. The Hill is equipped with a Pitot tube, temperature sensor and humidity sensor (m) to measure the freestream and atmospheric conditions. Additionally, it is equipped with a hot-wire traverse (l).

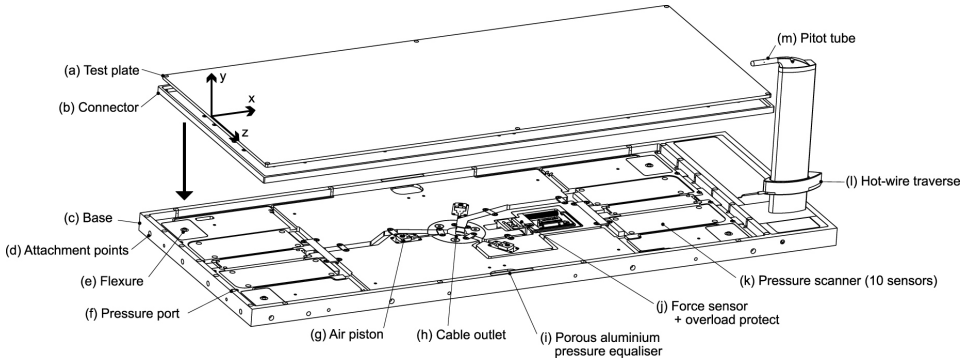

Figure 4.9: 'The Hill', experimental apparatus for direct force measurements (Van Nesselrooij et al., 2022).

When performing measurements with the Hill a standardised test sequence is employed, which is presented in Table 4.7. In case the wind tunnel has not seen use for several hours, a warm-up run is first recommended. One velocity sweep takes eight minutes. The tunnel and measurement room require a cooldown of five minutes after each velocity sweep. The sweep starts with a force reading at $U_\infty = 0$ m/s. Following this are measurements at ten linearly spaced freestream velocities ranging between $U_\infty \approx 7.5-35$ m/s. The measurement is ended with an additional measurement at $U_\infty = 0$ m/s, which is used for the null-force correction of the force sensor. Data is acquired at a sampling frequency of 10 kHz with a measurement interval of 15 s.

As aforementioned, the TPs are referenced to the flat plate reference plate, TP0000. Two reference measurements taken before and after the tested design are used and averaged to account for potential drift in the measurement equipment. Multiple designs can be measured between reference measurements, but more than four is not recommended. For example, for all four designs with index 2-x the mean of reference measurements 1 and 2 (with index 1 and 3) is used to reference the drag difference ΔC_D of the design.

Index		Measurement name	Measurement- & cooldown time (min)
0		Warm-up (TP0000)	8 + 5
1		Reference 1 (TP0000)	8 + 5
2	2-1	Design 1	8 + 5
	2-2	Design 2	8 + 5
	2-3	Design 3	8 + 5
	2-4	Design 4	8 + 5
3		Reference 2 (TP0000)	8 + 5
4	4-1	Design 1	8 + 5
	4-2	Design 2	8 + 5
	4-3	Design 3	8 + 5
	4-4	Design 4	8 + 5
5		Reference 3 (TP0000)	8 + 5
6	6-1	Design 1	8 + 5
	6-2	Design 2	8 + 5
	6-3	Design 3	8 + 5
	6-4	Design 4	8 + 5
7		Reference 4 (TP0000)	8 + 5
		Total time	221

Table 4.7: Measurement sequence for measuring four designs

In post-processing, two types of correction are applied to the raw force data: the null-force correction and pressure correction. The null-force correction is calculated based on the first and last measurements of the velocity sweep, which are at $U_\infty = 0$ m/s. If there is a discrepancy between these measurements, the drift in force is corrected by linear interpolation. Note that this correction is supposed to be small. Large

corrections likely indicate a measurement error, for example, if the connector is not freely swinging, resulting in erroneous force measurements. The small gap between the connector and the base results in a small pressure differential between the leading and trailing edges of the connectors. This pressure differential results in an additional force on the connector, which does not result from the skin friction or pressure drag of the to-be-tested design. The additional pressure force is calculated and subtracted from the measurement to correct this. The force is determined using two spanwise arrays of seven pressure ports located in the base at the leading- and trailing edges of the connector. An additional pressure port on the trailing edge is used to determine the vertical pressure distribution.

4.4. Hot wire anemometry

This section presents the details the HWA measurement technique, and discusses the important considerations for the experiments. Further details on the HWA post-processing procedure can be found in Appendix B. HWA is a technique that allows for high temporal resolution single-point measurements. HWA was used to obtain turbulence statistics profiles like the mean and turbulent fluctuation. Due to its high temporal resolution, HWA can be used for spectral analysis, which is a powerful tool for obtaining scale specific information of the turbulence. Spectral analysis will be used to test the hypothesis regarding the OSA pathway. Analysis like the boundary layer spectrogram and scale decomposition of TKE are useful applications of spectral analysis.

The book by Bruun (1996) is used as a reference to explain the working principle. HWA is based on the cooling effect of fluid flow over a heated body. A hot-wire probe consists of two prongs and a small metal wire that is heated using the Joule effect. The convective term governs the heat transfer of the wire. Therefore, conduction and radiation are neglected. There are two operating modes, constant temperature anemometry (CTA) and constant current anemometry (CCA). CTA is most common since it is less susceptible to burnout and has a better frequency response than CCA. For the experimental campaigns, CTA was used.

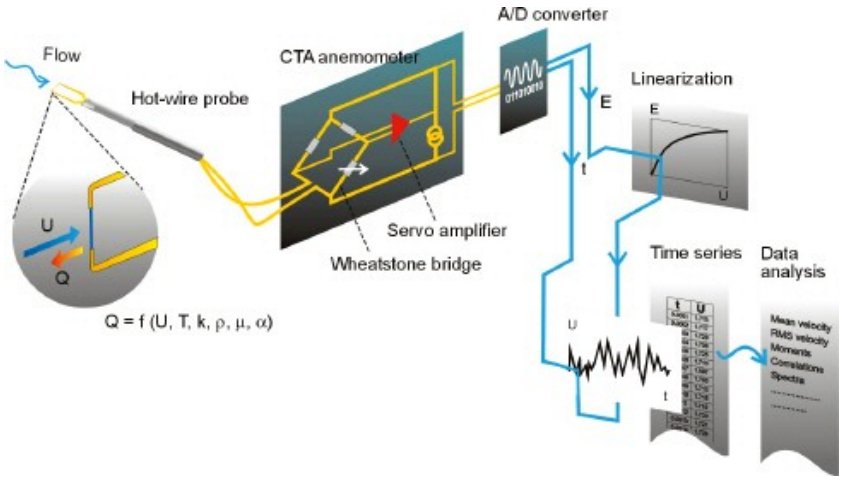

Figure 4.10: Schematic of the CTA measurement principle (Dantec, 2022).

In CTA, the wire is supplied with a variable voltage signal through a Wheatstone bridge to keep the wire at a constant temperature. The relation between the voltage input to the wire and the flow velocity was derived by King (1914), commonly known as King's law. King's law can be approximated by a fourth-order polynomial. The HWA system can then be calibrated by measuring the voltage of a number of known freestream velocities and fitting the fourth-order polynomial to obtain a calibration curve. The raw HWA data is a high-frequency voltage signal which is converted into a velocity signal using the calibration curve.

For good quality spectral analysis, a number of things are important. To prevent the aliasing of high-frequency components, an analogue low-pass filter should be applied to the signal at or below the Nyquist frequency. Furthermore, a sufficiently high sampling frequency (f_s) is required to capture the high-frequency turbulence associated with the near-wall cycle. Hutchins et al. (2009) explained that a minimum timescale of $\Delta T^+ \leq 3$ is required to resolve all energetic turbulent scales. Which translates to a requirement on the cut-off

frequency (f_c) of the low-pass filter:

$$f_c \geq \frac{u_\tau^2}{3\nu} \tag{4.5}$$

At $U_\infty = 30$ m/s and a development length of $x = 4$ m, this translates to a cut-off frequency of roughly $f_c = 28$ kHz.

There are also requirements on the hot-wire dimensions. Ligrani and Bradshaw (1987) showed that a sufficient length over wire diameter ratio of $l/d \leq 200$ is required to prevent heat conduction effects from the prongs. Furthermore, the wire length is an important consideration. Ligrani and Bradshaw (1987) noted that wire lengths above $l^+ \geq 20-25$ tend to attenuate small-scale energy, by averaging out small-scale fluctuations, thereby decreasing the measured peak of the TKE peak at $y^+ = 15$ (Ligrani and Bradshaw, 1987; Hutchins et al., 2009). When attaining high Re_τ flows by increasing the freestream velocity, the last constraint may be hard to satisfy due to a decreasing viscous length scale. This attenuation effect should be kept in mind when assessing the data.

For statistically converged data, the sampling time should be sufficient. Which is especially important at Re_τ where the VLSM can exceed lengths of 20δ. Hutchins et al. (2009) explains that the convection of several hundred structures is required. This leads to the requirement of 15,000-20,000 boundary layer turnovers, where T is the sampling time:

$$\frac{TU_\infty}{\delta} \geq 15{,}000 \tag{4.6}$$

Two HWA systems were used in the experiments for the thesis. The Hill has a built-in HWA and traversing system, which was used in conjunction with the drag measurements to characterise the boundary layer. Like the drag measurements, the measurement procedure is largely automated; only wall referencing has to be done by hand. Sampling is performed at 10kHz at 100 points over the boundary height, and no analogue filter is applied, so aliasing is present. With a measurement distribution of 50 points evenly spaced over the lowest 25% of the boundary layer, 25 points in the next 25%, and 25 locations in the upper 50% (Van Nesselrooij et al., 2022).

The acquisition system of the Delft University of Technology (DUT) was employed to perform spectral analysis. The DUT system consists of the TSI IFA-300 controller in combination with a Zaber traverse stage of 150mm. The TSI IFA-300 allows sampling at 51.2kHz, a low-pass filter at 20kHz was applied to prevent aliasing. The traverse has a linear encoder to position the hot-wire with an accuracy of 1 µm. The Zaber traverse was used to sample the boundary layer profiles at 40 logarithmically spaced wall-normal points, from 0.1 mm to δ. The wall-positioning was determined using a microscope which can measure the wall-normal distance between the probe and its reflection into the wall. For both acquisition systems, a Dantec55P15 miniature boundary layer probe was be used as the hot-wire sensor. The probe has a 5 µm 1.25 mm sensor diameter and length respectively, resulting in a sufficient length over diameter ratio of $l/d = 250$[1]. An overview of the characteristic parameters describing the two systems is presented in Table 4.8.

Parameter	The Hill		TSI IFA-300	
	$U_\infty = 10$ m/s	$U_\infty = 30$ m/s	$U_\infty = 10$ m/s	$U_\infty = 30$ m/s
f_s (Hz)	10,000	10,000	51,200	51,200
f_c (Hz)	-	-	20,000	20,000
l (mm)	1.25	1.25	1.25	1.25
d (µm)	5	5	5	5
l/d	250	250	250	250
l^+	32.9	92.6	32.9	92.6
ΔT^+	1.08	8.32	0.54	4.16

Table 4.8: Characteristic parameters for the two considered acquisition systems at $x_{dev} = 3.9$ for two freestream velocities. Calculations for air at $T = 20$ °C: $\rho = 1.204$ kg/m^3 and $\mu = 1.825 \times 10^{-5}$ kg/ms, according to theoretical relations of Section 2.1.

[1] https://www.dantecdynamics.com/product-category/hot-wire-probes/single-sensor-miniature-wire-probes/

5

Results

This chapter presents the experimental outcome for Part II of the thesis. The aim of these experiments is to answer research questions (1c) and (2). The experiments first focused on wind tunnel characterization using hot-wire anemometry to see if sufficient scale-separation could be attained, answering question (1c). To address question (2), first, direct force measurements were conducted to assess the drag characteristics of the passive test plates that employ OSA. Secondly, hot-wire measurements were conducted to assess the scale-specific influence on streamwise turbulence kinetic energy of three selected test plates. An overview of the experiments is presented in Section 5.1. The wind tunnel characterization of the M- and W-tunnel is elaborated on in Section 5.2. Finally, the results of the OSA passive test plates are presented in Section 5.3.

5.1. Overview of the experiments

This section presents an overview of the experiments, which can be found in Table 5.1. To characterise both the M- and W-tunnel HWA measurements were made to assess the velocity profiles and turbulence statistics. The flat plate reference (TP0000) was used in all measurements. The M-tunnel was characterised at two considered development lengths, with the HWA system built into the Hill. The W-tunnel was characterised using the Delft University of Technology (DUT) in-house HWA system.

Balance measurements were performed in the M-tunnel with the eight selected TPs, with an approximate velocity range of $U_\infty = 7.5-35$ m/s. TP0000 was used to reference all the drag results to obtain drag differences with respect to the reference (ΔC_D). All test plates were tested with the extended development length of $x_{dev} = 3.9$ m resulting in a larger frictional Reynolds number compared to the original development length. To test the effect of Re_τ on drag, three designs were selected for testing at the original development length of $x_{dev} = 1.5$ m. Three additional HWA measurements were taken for the same TPs to assess the influence on the different energetic scales of the streamwise turbulence kinetic energy.

Name	Test plate	Balance (M-tunnel)		Hot-wire	
		$x_{dev} = 1.5$ m	$x_{dev} = 3.9$ m	M-tunnel	W-tunnel
Flat reference	TP0000	$U_\infty \approx 7.5-35$	$U_\infty \approx 7.5-35$	$U_\infty \approx 10,20,30$, $x_{dev} = 1.5,3.9$	$U_\infty \approx 10,20,30$
Staggered dimples	TP0001		$U_\infty \approx 7.5-35$		
Staggered dimples	TP0005		$U_\infty \approx 7.5-35$		
Staggered sinusoidal	TP0004	$U_\infty \approx 7.5-35$	$U_\infty \approx 7.5-35$		$U_\infty \approx 30$
Aligned sinusoidal	TP0124		$U_\infty \approx 7.5-35$		
OWW	TP0007	$U_\infty \approx 7.5-35$	$U_\infty \approx 7.5-35$		$U_\infty \approx 30$
OWW	TP0011		$U_\infty \approx 7.5-35$		
OWW	TP0012	$U_\infty \approx 7.5-35$	$U_\infty \approx 7.5-35$		$U_\infty \approx 30$
Superimposed OWW	TP0125		$U_\infty \approx 7.5-35$		

Table 5.1: An overview of the experiments conducted in Part II of the thesis, units for development length and velocity are m and m/s respectively.

5.2. Wind tunnel characterization

This section presents the wind tunnel characterisation for the two experimental facilities, the M- and W-tunnel. This characterisation aims to assess the influence of large-scale turbulence structures by evaluating the significance of the outer energetic peak in the boundary layer spectrograms. With this assessment, research question (1c) can be answered. For each tunnel, the boundary layer properties are first presented, which were obtained by fitting a composite profile (Chauhan et al., 2009) to the mean velocity profiles. The mean velocity and streamwise stress profiles are presented. Lastly, the scale-specific turbulence kinetic energy for the W-tunnel is assessed using the boundary layer spectrogram.

5.2.1. M-tunnel

This section presents the wind tunnel characteristics of the M-tunnel. In this facility, drag measurements were performed at two development lengths to test the Re_τ scaling for OSA. Table 5.2 shows the boundary layer properties for three freestream velocities of $U_\infty \approx 10$, 20, and 30 m/s at the development lengths of x =1.5 and 3.9 m. The boundary layer is characterised by sampling the boundary layer profiles with 100 points at the downstream end of the reference TP (TP0000). The sampling times are non-dimensionalised with the free stream velocity and boundary layer thickness (TU_∞/δ), which is a measure of the amount of boundary layer turnovers in the sampling interval.

As the freestream velocity increases, the boundary layer thickness decreases in combination with the viscous length scale. The frictional Reynolds number, which is the ratio of the two, increases. Furthermore, a higher Re_τ is found when the development length increases as expected from the theoretical calculations. At $U_\infty \approx 30$ m/s the Reynolds number increases from $Re_\tau = 1{,}930$ to $Re_\tau = 3{,}970$ with the added development length of 2.4 m

Boundary layer properties						Hot-wire acquisition		
x (m)	U_∞ (m/s)	δ (mm)	u_τ (m/s)	δ_ν (µm)	Re_τ	l^+	ΔT^+	TU_∞/δ
1.5	9.92	33.7	0.409	37.8	890	33.1	1.08	8,550
1.5	20.00	26.9	0.794	19.2	1,400	65.2	4.14	27,400
1.5	29.20	28.9	1.040	14.9	1,930	83.7	6.98	10,100
3.9	9.88	67.6	0.385	40.1	1,690	31.2	0.96	4,530
3.9	20.00	62.1	0.721	21.4	2,900	58.3	3.37	9,990
3.9	29.70	59.8	1.030	15.1	3,970	82.9	6.80	9,950

Table 5.2: Boundary layer characterisation and hot-wire acquisition properties for the M-tunnel, using the Hill acquisition system

In Figure 5.1, the mean streamwise velocity and stress profiles are presented. From the streamwise velocity profile. it can be observed that the boundary layer fit is not perfect, especially in the viscous sublayer and buffer layer. This is because the Hill HWA system does not use perfect logarithmic spacing resulting in sparse sampling points close to the wall. Which translates into larger uncertainty of the fitting parameters, especially the wall offset Δy. Because the x-axis spacing is logarithmic, the effect of a spurious wall offset can only be observed close to the wall. The requirement of at least one sampling point in the region $y^+ \leq 10$ (Rodríguez-López et al., 2015), is met for most of the measurements, however, more points in the region would likely improve the accuracy of the fitter. The fit is better in the logarithmic region, but there is still a significant variance between the profiles.

Assessing the streamwise stress profiles, for $U_\infty \approx 10$ m/s, the near-wall fluctuations peak around $y^+ = 15$ can be seen although its magnitude is higher than expected, especially for the longer development length. As the freestream velocity increases, the peak diminishes in magnitude. The decrease in intensity is attributed to the attenuation of small-scale energy due to the increasing non-dimensional wire length (l^+), and lack of temporal resolution, which exceeds $\Delta T^+ > 3$ for the two higher freestream velocities (Hutchins et al., 2009). As freestream velocity increases, the turbulence kinetic energy in the outer-layer increases, indicative of the emergence of the outer-site in the spectrogram. This growth is further highlighted in Figure 5.1c where outer scaling is applied. The geometric mean of the log layer, at $y/\delta = 0.06$ (Hutchins and Marusic, 2007a), is indicated by the dotted line. With increasing Re_τ, the outer layer stress grows in magnitude, especially at $U\infty = 30$ m/s. This is further evidence of increased energetic content of the outer-scaled structures.

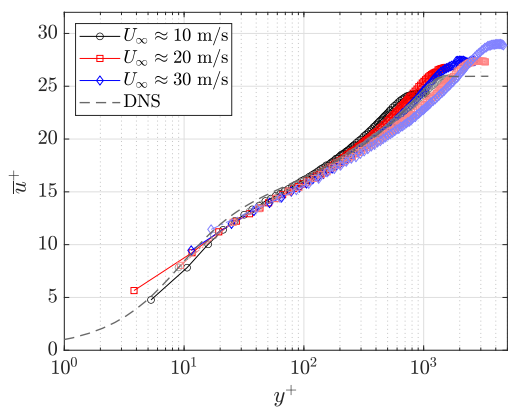

(a) Mean streamwise velocity

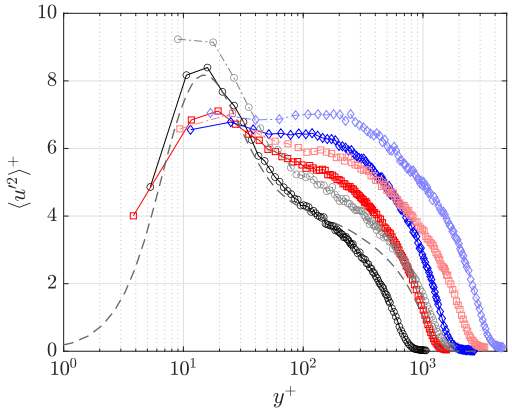

(b) Streamwise stress

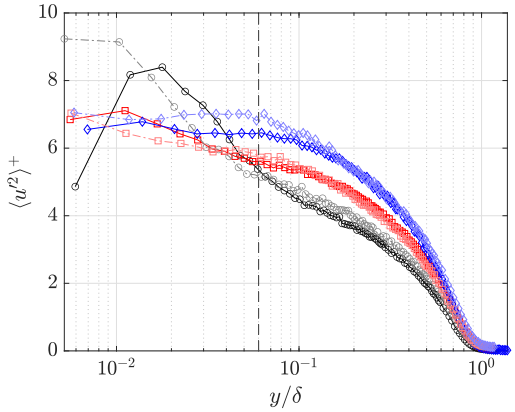

(c) Outer-scaled streamwise stress

Figure 5.1: Turbulence statistics profiles for the M-tunnel at three freestream velocities and two development lengths. Solid lines, indicate x_{dev} = 1.5 m, dash-dotted lighter coloured lines indicate x_{dev} = 3.9 m. DNS data by Schlatter and Örlü (2010) at Re_τ = 1,273

5.2.2. W-tunnel

This section presents the characterisation of the W-tunnel. All measurements in the W-tunnel were made using the DUT hot-wire acquisition system. This system has a higher sampling frequency of f_s = 51.2 kHz and a spectral low-pass filter at f_c = 20 kHz, which allows for spectral analysis and better resolving of the small-scale (i.e. high frequency) energetic scales. Again, the characterisation was performed on the downstream part of reference TP0000. In Table 5.3 shows the boundary layer characteristics for three freestream velocities of $U_\infty \approx$ 10, 20, and 30 m/s at the length of x_{dev} = 3.6 m.

Similar to the M-tunnel, the boundary layer properties behave as expected, with a decreasing boundary layer thickness and viscous length scale as the freestream velocity increase. At $U_\infty \approx$ 30 m/s a frictional Reynolds number of Re_τ = 4,160 is found. Interestingly the Re_τ is slightly higher than the M-tunnel, for similar freestream conditions but at a lower development length. This difference could be attributed to the zero pressure gradient in the W-tunnel. The non-dimensional sampling resolution ΔT^+, is calculated with the low-pass filter frequency. Which now satisfies the minimum requirements of $\Delta T^+ \leq 3$ specified by Hutchins et al. (2009) for a sufficient temporal resolution to resolve the small-scale energy.

Boundary layer properties						Hot-wire acquisition		
x (m)	U_∞ (m/s)	δ (mm)	u_τ (m/s)	δ_ν (µm)	Re_τ	l^+	ΔT^+	TU_∞/δ
3.6	9.87	72.7	0.364	42.9	1,690	29.1	0.42	19,200
3.6	20.10	70.7	0.685	22.7	3,110	55.0	1.51	17,900
3.6	28.90	69.3	0.949	16.6	4,160	75.1	2.85	16,700

Table 5.3: Boundary layer characterisation and hot-wire acquisition properties for the W-tunnel, using the DUT acquisition system

In Figure 5.2 the mean streamwise velocity and stress profiles are displayed. It can be observed that the boundary layer fit of Chauhan et al. (2009) is a lot better for this data. All the profiles collapse in the logarithmic region. The fit in the viscous sublayer is good for $U_\infty \approx 10$ and 20 m/s. As the velocity increases to $U_\infty \approx 30$ m/s the near-wall velocity is higher than the expected linear behaviour. This behaviour likely results from conduction effects close to the wall (Hutchins and Choi, 2002). When assessing the streamwise stresses, the profiles behave as expected for the lower two velocities, where the reduced peak intensity results from spatial attenuation due to a finite sensor length. For the case $U_\infty \approx 30$ m/s, additional energy in the region $y^+ \leq 20$ can be observed in the streamwise stress. This increased energy likely results from vibrations of the hot-wire probe and sting in the near-wall region, at higher freestream velocities. This results in spurious stresses close to the wall. These vibrations are further elucidated when discussing the spectrogram at the end of this subsection.

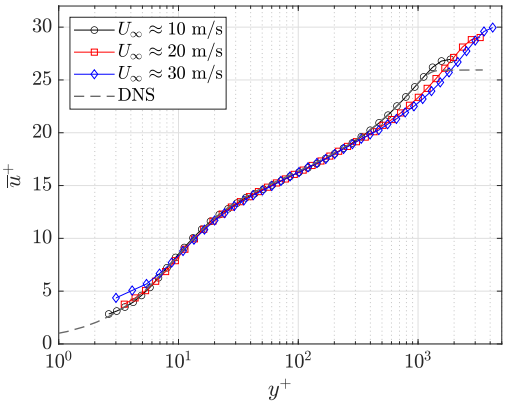

(a) Mean streamwise velocity

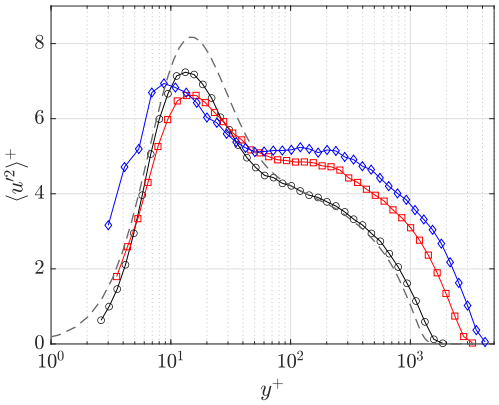

(b) Streamwise stress

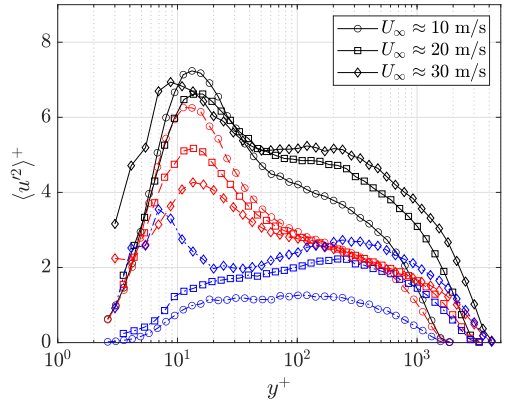

(c) Scale-decomposition for the streamwise stress profiles. Red dashed lines indicated the small-scale component, blue dash-dotted lines indicate the large-scale component. Spectral filter located at $\lambda_x^+ = 7{,}000$.

Figure 5.2: Turbulence statistics profiles for the W-tunnel at three freestream velocities. DNS data by Schlatter and Örlü (2010) at $Re_\tau = 1{,}273$.

Again, from the streamwise stress profiles a growing influence of the outer-scaled with structures Re_τ can again be observed. As aforementioned, the HWA acquisition system's better specifications now allow for spectral measurements. Scale-decomposition of the streamwise stresses into their respective small- and large-scale components. The cut-off filter is placed at $\lambda_x^+ = 7{,}000$, a commonly adopted value in literature (Hutchins and Marusic, 2007b; Mathis et al., 2011; Baars et al., 2017). The scale-decomposition is presented in Figure 5.2c. The red dashed lines indicate the small-scale component should be mostly invariant with Re_τ. In the logarithmic region, this is the case. However, the near-wall small-scale energy peak decreases due to spatial attenuation as a result of the increasing sensor length l^+. As expected, the outer-scaled component increases in magnitude as Re_τ increases, especially in the logarithmic region. The spurious measurements due to sensor vibrations at $U_\infty \approx 30$ are reflected in the outer-scaled component.

To further investigate the inner- and outer-scales, the boundary spectrograms for the W-tunnel are assessed, which are displayed in Figure 5.3. The horizontal dashed line indicates the cut-off wavelength used for scale decomposition. A few observations can be made. Firstly, the emergence of the outer-peak in the spectrogram as Re_τ increases. This shows the increased energetic content of the outer-scaled turbulent structures. These results agree with the findings of Hutchins and Marusic (2007a). Secondly, similar to the declining inner peak for the streamwise stresses, it can be seen that the energetic content of the inner peak declines, while this is expected to be invariant with Re_τ. This is again due to the aforementioned spatial attenuation. A third observation is the emergence of spurious energy peaks close to the wall. These are most likely energetic peaks from hot-wire vibrations close to the wall. At $U_\infty \approx 20$ m/s, the magnitude of the spurious fluctuations is sufficiently small that it does not reflect visibly in the streamwise stresses. However, as observed earlier for $U_\infty \approx 30$ m/s this added energy increases the streamwise stresses in the near-wall region.

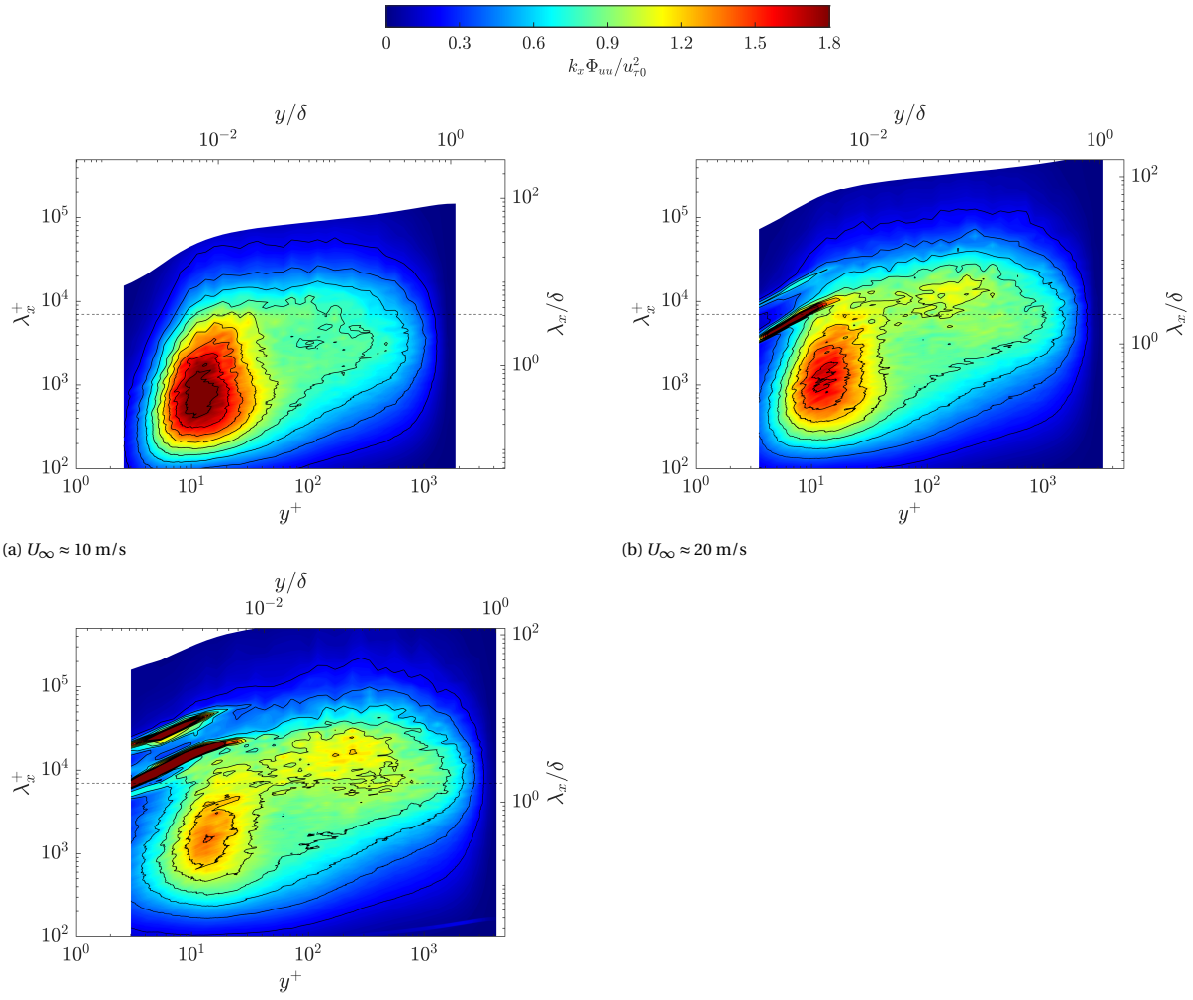

(a) $U_\infty \approx 10$ m/s

(b) $U_\infty \approx 20$ m/s

(c) $U_\infty \approx 30$ m/s

Figure 5.3: Boundary layer spectrograms of the pre-multiplied spectral energy of the streamwise stress for the W-tunnel, the horizontal dashed line shows the wavelength $\lambda_x^+ = 7,000$ used for scale-decomposition.

5.3. Outer-scaled actuation using passive spanwise forcing

This section presents the results of the OSA passive TPs that were considered. The aim of this is to answer research question (2). Subsection 5.3.1 presents the drag characteristics of the eight TPs under high Reynolds number conditions (i.e. long development length) thereby answering the first sub-question. Based on these findings three TPs that showed the best drag performance were subjected to measurements with the short test section. These results, presented in Subsection 5.3.2, allow us to assess the effect of Re_τ on the drag. Thereby addressing research question (2b). Finally, to assess the effects of the techniques on the different scales of turbulence kinetic energy, spectral analysis is made in Subsection 5.3.3, answering sub-question (2c).

5.3.1. Drag characteristics

This subsection discusses the drag characteristics of the eight selected TPs for OSA, at the development length of $x_{dev} = 3.9$ m. A 10-point velocity sweep was performed, ranging from $U_\infty \approx 7.5-35$ m/s. The velocity is expressed as a unit Reynolds number (Re_1) with a reference length of 1 m, resulting in an approximate range of $Re_1 \approx 0.5\times10^6 - 2.3\times10^6$. In Figure 5.4 the drag characteristics for the TPs are presented, at two unit Reynolds numbers of $Re_1 = 1\times10^6$ and 2×10^6. The drag is expressed as a percentage difference ($\Delta C_D(\%)$) with respect to the flat plate reference TP0000. Negative values of ΔC_D indicate a drag reduction, i.e. a decrease in drag with respect to TP0000. The uncertainty bars indicate the 95% confidence interval calculated using Student's t-distribution accounting for the small sample size of three measurements. The complete drag data and the accompanying corrections for the full velocity sweeps can be found in Appendix A.

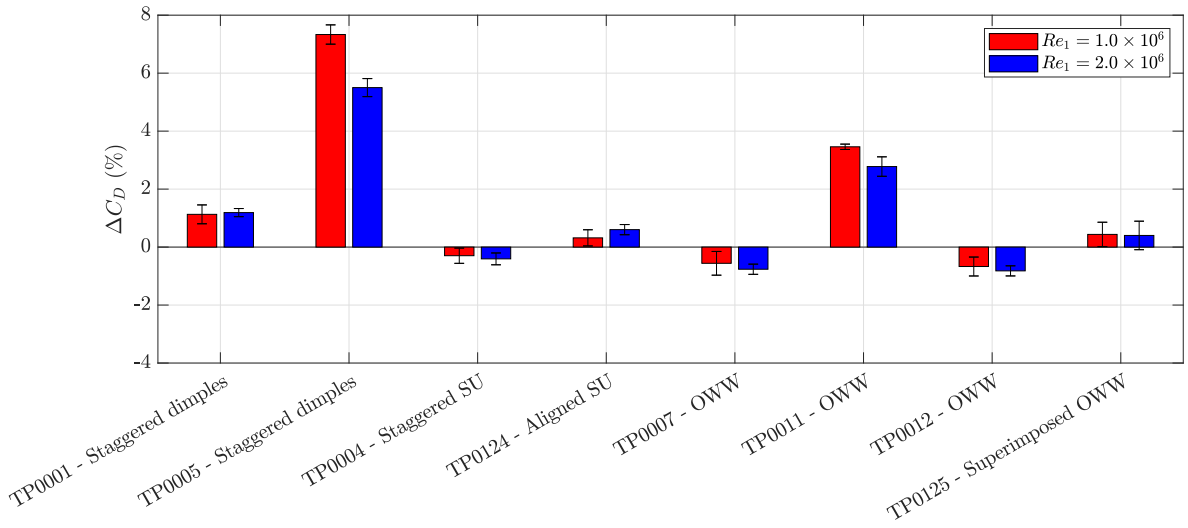

Figure 5.4: Drag characteristics for all passive TPs at $Re_1 = 1\times10^6$ and 2×10^6

Both dimpled plates, TP0001 and TP0005 show an increase in drag. TP0001 are the dimples of van Nesselrooij et al. (2016), which shows a slight drag increase around $\Delta C_D = 1\%$, in agreement with van Campenhout et al. (2022). No significant Reynolds number trends can be observed. The dimples of Tay et al. (2015) show a substantial increase in drag between $\Delta C_D = 5-7\%$ and a declining trend with Reynolds number. This drag increase likely results from the deeper and larger dimples compared to the geometry of van Nesselrooij et al. (2016), giving the design more pressure drag.

The sinusoidal undulations (SUs) are designed to mimic the spanwise forcing of the dimpled plate TP0001. Two variations are tested, TP0004 the staggered configuration, where the streamwise undulations are out of phase by half a streamwise wavelength and the phase-aligned configuration TP0124. The staggered SUs show a slight drag reduction within 1%. The aligned case shows a slight drag increase but is also confided to the 1% region. Interestingly both plates have the same geometry apart from the streamwise shift of the undulations, this hints at the idea that the staggered configuration is more effective at reducing skin friction.

Four configurations of oblique wavy walls (OWWs) are considered. TP0007 is a recreation of the geometry by Ghebali et al. (2017). TP0125 is a variant of TP0007 where two oblique waves of the TP0007 geometry at a positive and negative oblique angle are superimposed. TP0011 and TP0012 are the geometries of Denison et al. (2015), the waves have the same wavelength and oblique angle but with two wave height amplitudes.

TP0011 has a high amplitude and TP0012 has a more shallow geometry. Interestingly, two OWW geometries show a slight drag reduction, albeit less than 1%. The effect of superimposing the OWW of TP0007 results in an increased drag for TP00125 compared to the drag reduction found for the original. When considering the TPs of Denison et al. (2015), a small drag reduction for the shallow waves is found compared to an increased drag of $\Delta C_D = 3-5\%$. This drag increase is in line with their numerical results, where they found the high amplitude geometry to increase the pressure drag substantially.

From these results alone, no conclusions can be drawn about the effectiveness of actuation on the outer-scaled structures. Therefore it is interesting to test the hypothesis that drag reduction correlates positively with Re_τ. This trend is observed for OSA using active spanwise forcing(Marusic et al., 2021). To test this, three TPs that have a slight but positive drag reduction are selected to be further tested at a smaller Re_τ. These are the staggered SU TP0004, the two OWWs of Ghebali et al. (2017) TP0007 and the shallow OWW of Denison et al. (2015) TP0012. The Reynolds number behaviour of these plates is elaborated on in the following subsection.

5.3.2. Reynolds number dependant drag characteristics

This subsection discusses drag dependence on the frictional Reynolds number of the three selected TPs. An additional set of measurements was performed on these TPs with the original shorter test section at a development length of $x_{dev} = 1.5$ m resulting in conditions at a lower value of Re_τ at similar freestream velocities. The actuation parameters between the two tests should be fixed to make a valid assessment of the Reynolds number behaviour. The best way of doing this is to consider a fixed viscous scaling between the measurements, this means the streamwise wavelength of actuation λ_x^+ is fixed. The uncertainty in the estimate of u_τ from the M-tunnel characterisation is too large to make a fair comparison between the two development lengths. Therefore we refer back to the theoretical relations as outlined in Chapter 2. The viscous length scale was fixed using these theoretical calculations to compare the low- and high Re_τ case. This results in two Re_1 values which can be interpolated from the two data sets. The results of the low- and high Re_τ conditions are presented in Figure 5.5 for three fixed values of δ_v.

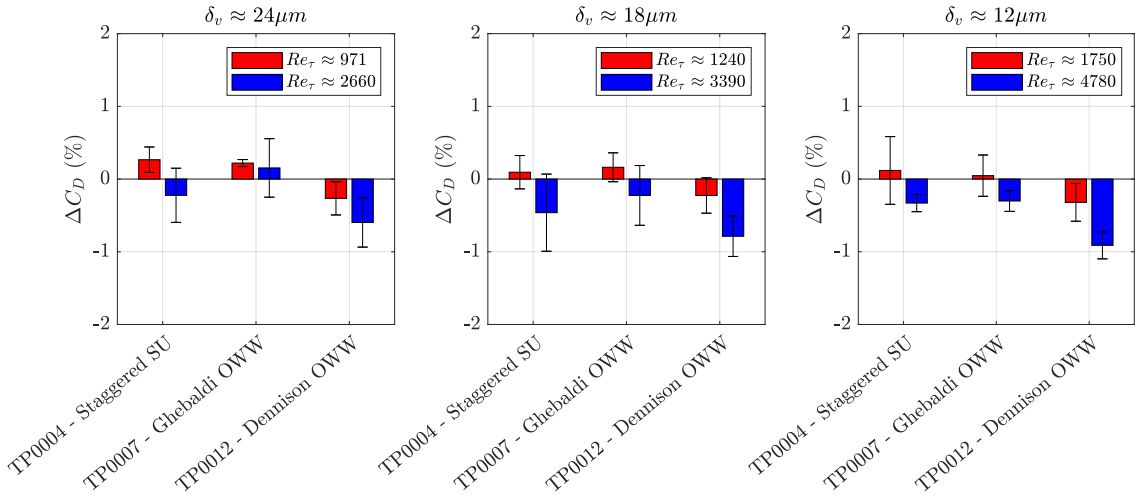

Figure 5.5: Drag response with Re_τ for selected OSA TPs.

From the results it can be seen that at fixed δ_v, the value of Re_τ differs by a factor of almost three between the two test sections. The value of Re_τ increases as the viscous length scale decreases. For all three considered TPs an interesting trend can be seen, the value of ΔC_D decreases when going from the low- to high Reynolds number conditions. This suggests a positive correlation between Re_τ and DR hinting at effective OSA, similar to the DR trends observed for OSA by Marusic et al. (2021), Chandran et al. (2022), and Deshpande et al. (2022). It should be noted that the ΔC_D values are low and that the confidence interval is relatively large for most of the results.

This first evidence of OSA is promising, but a note on the validity of the results should be made. The pressure correction that is applied to the results is presented in Figure 5.6. This graph shows striking similarity, to

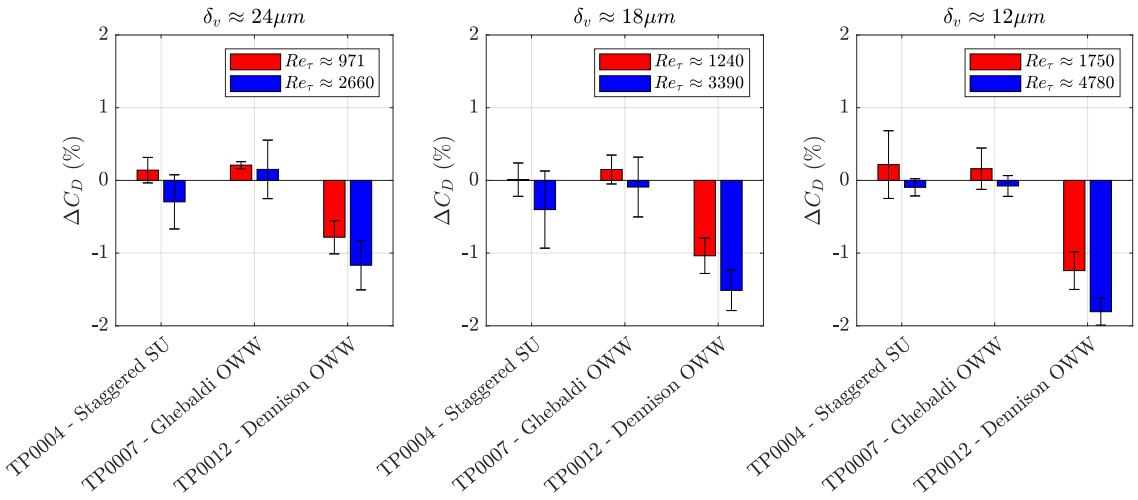

Figure 5.6: Pressure correction to the results of Figure 5.5.

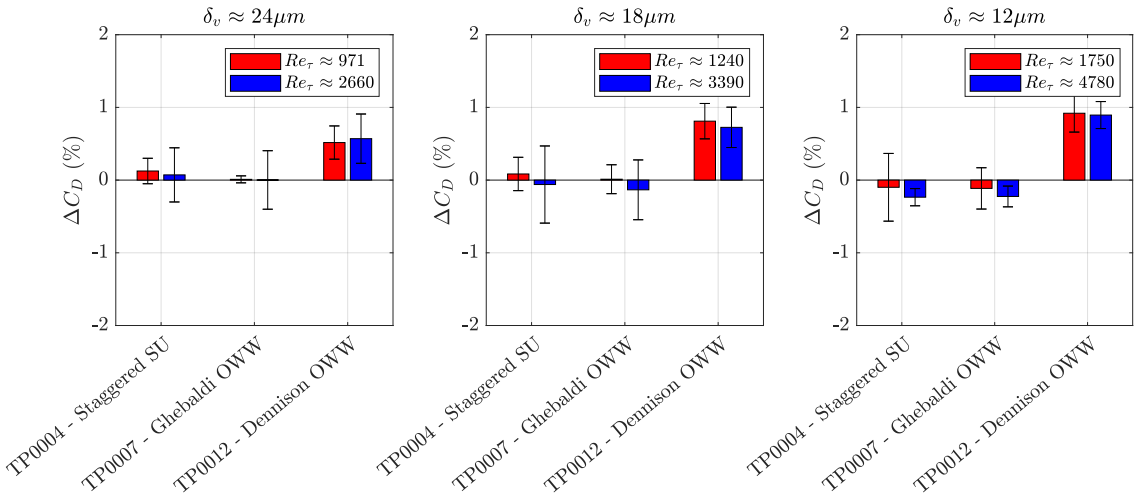

Figure 5.7: Uncorrected results of Figure 5.5.

Figure 5.5, in the ΔC_D change between the two Reynolds numbers. This means that the correlation between DR and Re_τ is solely due to the changes in pressure correction. To further highlight this Figure 5.7 that shows the results without the pressure correction applied. In this case, the result shows no significant differences or trends with Re_τ. The differences in pressure correction may be attributed to the different freestream conditions between the two test-section lengths. This means the results are inconclusive on the Reynolds number trends for OSA using the selected TPs. Another explanation for this result, or rather the lack of a significant Re_τ trend, could be attributed to the still small influence of the outer-scaled structures at the considered Reynolds numbers.

5.3.3. Spectral analysis

This last subsection further elucidates the effects that passive OSA has on the inner- and outer turbulent scales by performing spectral analysis. Spectral analysis is performed in the W-tunnel on the three selected TPs, at a freestream velocity of $U_\infty \approx 30$ m/s. The non-dimensional sampling times are similar to characterisation experiments discussed in Subsection 5.2.2, at $TU_\infty/\delta \approx 16{,}700$. The boundary spectrograms of the reference and three selected TPs are presented in Figure 5.8. Following this analysis, scale-decomposition is performed on these same measurements, as depicted in Figure 5.9. This scale decomposition allows for separately assessing the streamwise stress profiles of the inner- and outer-scales. Scaling is applied using the

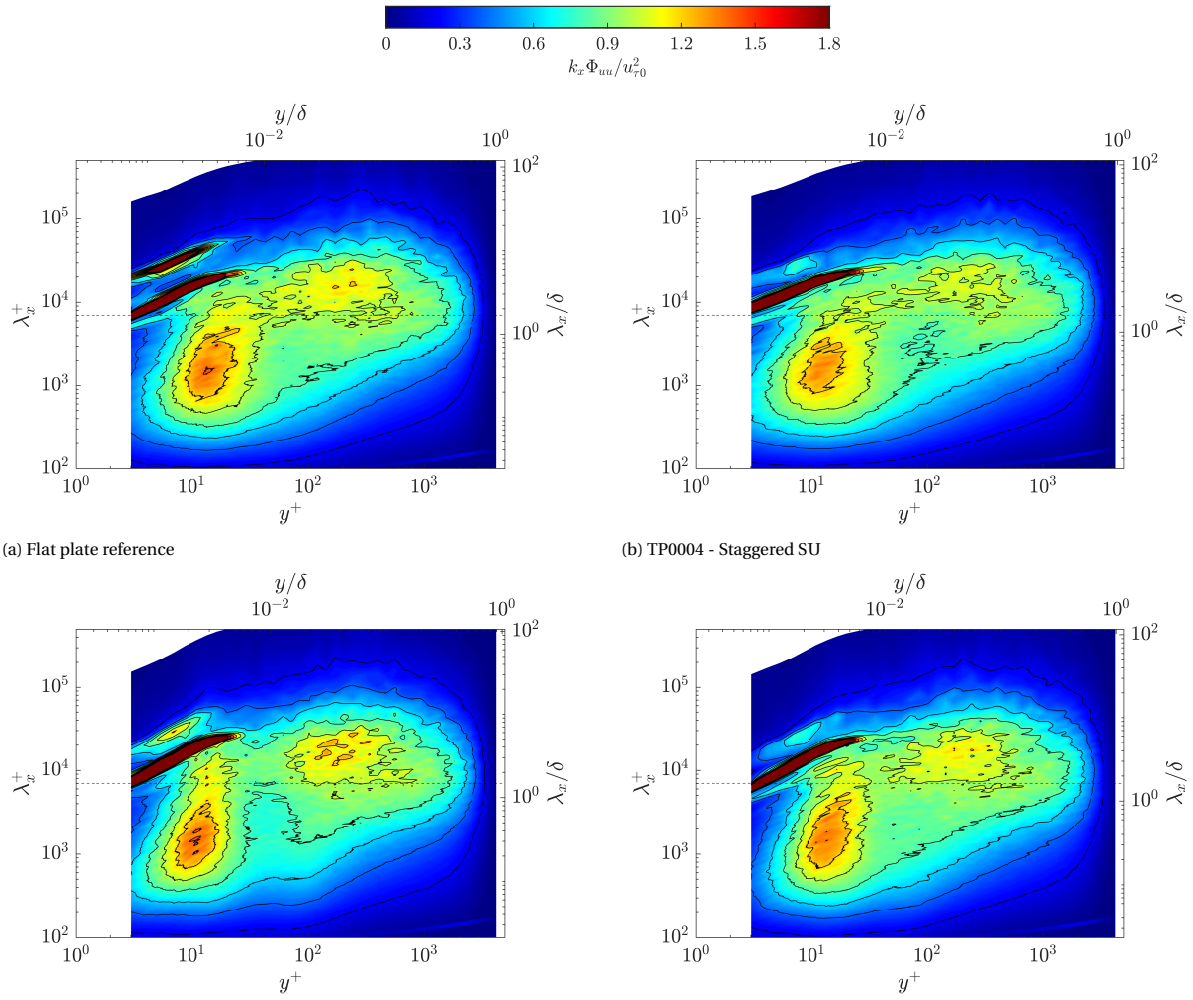

(a) Flat plate reference

(b) TP0004 - Staggered SU

(c) TP0007 - Ghebaldi OWW

(d) TP0012 - Dennison OWW

Figure 5.8: Boundary layer spectrograms of the pre-multiplied spectral energy of the streamwise stress for the OSA TPs, measurements at $U_\infty \approx 30$ m/s. The horizontal dashed line shows the wavelength $\lambda_x^+ = 7{,}000$ used for scale-decomposition.

reference $u_{\tau 0}$ of the flat-plate reference to highlight the absolute changes in energy with respect to the baseline.

From the spectrograms, it can be seen that the spurious energy peaks due to sensor vibrations are present in all cases. However, the inner- and outer-spectral peaks can still be observed and assessed qualitatively. For TP0004, the staggered SUs, a small reduction in spectral energy of both peaks can be observed. For the OWW of (Ghebali et al., 2017), TP0007, some interesting results can be observed. A slight increase in the outer-peak can be seen. Furthermore, spectral energy is significantly reduced over a wide range of scales, in the wall-normal region $10 \leq y^+ \leq 100$ between the inner- and the outer-peak. This result also makes the inner peak appear over a smaller wall-normal boundary layer region. Lastly, TP0012, shows no significant changes with respect to the flat plate reference.

The findings of the boundary layer spectrograms are reflected in the scale-decomposed streamwise stresses. Note that the spurious measurements make it impossible to draw conclusions on the large-scale component of the decomposed stress in the region $y^+ \leq 20$. For TP0004 a reduction of the outer peak of the total stress can be observed up to a height of $y^+ = 500$, which is found in both the small- and large-scale components. This result is promising and can be seen as evidence that OSA may be effective for this type of geometry. The small-scale stress component reflects the energy attenuation in the region $10 \leq y^+ \leq 100$ for TP0007. The increase of the outer-peak can also be seen in the large-scale component in the log-region. Lastly, in line with the spectrogram, no significant energy differences are observed for TP0012.

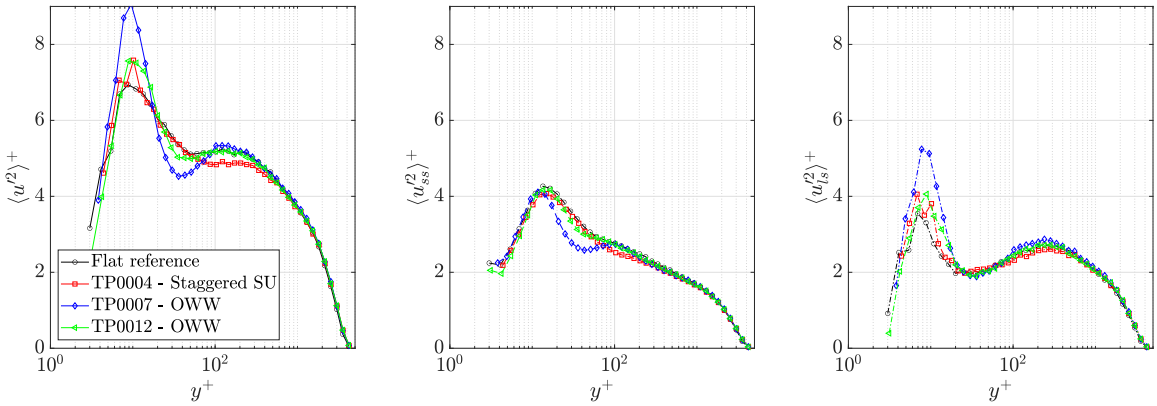

(a) Streamwise stress

(b) Small-scale streamwise stress component

(c) Small-scale streamwise stress component

Figure 5.9: Scale decomposition of the streamwise stress. Spectral filter located at $\lambda_x^+ = 7,000$.

These results conclude the assessment of OSA using passive spanwise forcing. The results from the spectral analysis are promising, even though the energy reductions are small in magnitude. The most promising finding is the result for TP0004, which shows a slight but noticeable energy reduction of the outer-peak. This hints at effective actuation upon the outer-scaled structures. Hence this is regarded as the first possible evidence for effective OSA using passive techniques. The results of TP0007 are interesting, with a reduction of small-scale TKE of the inner-peak and the region between the two peaks. The spurious energy resulting from probe vibrations makes it impossible to assess the near-wall large-scale energy and a possible reduction of its footprint. Therefore, a stiffer HWA sting and holder are recommended for future experiments.

6

Concluding remarks

This chapter presents the concluding remarks for Part II of the thesis. Firstly, the relevant research questions are addressed. Following this, the results are shortly discussed.

6.1. Research questions

This section addresses the relevant research questions corresponding to Part II of the work, which are, research questions (1a) and (1b), and question (2).

1. **To what extent can outer-scaled flow structure modulation effects through spatial periodic forcing be experimentally investigated within the available resources?**

   (a) *How can spatial periodic forcing be realised using passive flow control methods? Would such methods be suitable for investigation in the present experimental conditions?*
   Three passive flow control techniques were found to show potential for passive spanwise forcing: dimples, oblique wavy walls and sinusoidal undulations. OSA can be applied by increasing the streamwise wavelengths of the design to match the outer-scaled peak in the order of $\lambda_x = \mathcal{O}(\delta)$. Under the present experimental conditions, the physical wavelengths for OSA are realisable on TPs for the drag force measurements using the Hill system.

   (b) *Is it possible to attain flow conditions with a substantial influence of outer-scaled flow structures? Can their distinct contribution to the total turbulent kinetic energy be observed?*
   Using the extended development lengths of the current experimental facilities, a frictional Reynolds number of $Re_\tau = \mathcal{O}(4,000)$ can be attained. The emergency of an outer-scaled site in the spectrogram can be observed, but is still small in magnitude. To further investigate OSA, higher Reynolds numbers are required in the order of $Re_\tau = \mathcal{O}(1 \times 10^5)$.

2. **What is the drag reduction potential of outer-scaled actuation using passive spatial periodic forcing?**

   (a) *What are the drag characteristics of the selected techniques in terms of total integral drag?*
   Out of the tested eight TPs, three showed a moderate DR: the staggered sinusoidal undulations (TP0004), and the OWWs of Ghebali et al. (2017) (TP0007) and the low OWW variant of Denison et al. (2015) (TP0012). These three TPs were selected for further studies in the assessment of the following two sub-questions.

   (b) *How does the drag performance relate to the frictional Reynolds number? Can increased effectiveness of drag performance be observed as a function of the frictional Reynolds number, similar to trends by Marusic et al. (2021) ?*
   The drag measurements show a drag force reduction with increasing Re_τ, indicative of effective OSA. However, the results are inconclusive because they are within the 95% confidence interval, and the change in drag solely originates from the pressure correction.

   (c) *What is the effect of the selected techniques on the outer-scaled streamwise turbulence kinetic energy?*
   No significant changes in streamwise TKE are found TP0012. TP0004 shows a slight but visible

reduction in TKE in the outer-scaled peak. TP0007 shows attenuation in TKE for a broadband range of scales in the region between the inner- and outer peak ($10 \leq y^+ \leq 100$), the two energetic sites are not significantly affected.

6.2. Discussion of the findings

In Part II of the thesis, a number of passive techniques were tested for their applicability to the OSA pathway by performing direct force measurements. Of the eight TPs, three TPs showed a slight DR, these were selected for details studies into the OSA pathway. The measurements to test the Reynolds number scaling were promising, with an increased DR at higher values of Re_τ, indicative of effective OSA. However, the changes in C_D originated from the pressure correction term in the Hill. Some factors influencing the pressure correction could be that the M-tunnel does not have a zero pressure gradient, and the growing boundary layer on the side-walls may influence the pressure correction.

The hypothesis that OSA shows an increasing effectiveness with Re_τ still stands, but in hindsight, the frictional Reynolds numbers in the current experiments are too small to have a significant outer-scaled influence, as is depicted in Figure 2.14. As a reference, the results of Marusic et al. (2021) only show moderate DR at the Reynolds numbers this work considers, and this is for active forcing, which can realise a more substantial flow control effect. Hence experiments at higher Re_τ are needed to investigate this hypothesis further.

The scale-specific influence on the TKE of the three TPs is promising. Firstly, TP0007 the oblique wavy wall of Ghebali et al. (2017) showed a reduction in TKE in between the inner- and outer-peaks of the spectrogram. Moreover, TP0004 the staggered sinusoidal undulations show a reduction of energy in the outer-scaled energy peak. Even tough the effect is small, this finding be regarded as the first evidence that these passive techniques may work on the OSA pathway. To strengthen this evidence further measurements at higher frictional Reynolds numbers are deemed valuable.

Besides the results on passive OSA, several findings were made regarding the hot-wire measurements. Firstly, it was found that the lacking temporal frequency means the Hill acquisition system is only usable for amplitude domain analysis. Furthermore, the sparse number of sampling locations results in uncertainties in the boundary layer fitting parameters, specifically the wall offset Δy^+. A good quality metric for this is given by Rodríguez-López et al. (2015), who state that at least one measurement point below $y^+ \leq 10$ is required, but more points are preferable. With the current workflow, this was not achieved for all cases

As for the boundary layer fitter, it was found that the method of Chauhan et al. (2009) outperformed the method of Rodríguez-López et al. (2015). The main reason is that the optimisation was a lot more robust by fixing the parameters κ and B. A downside of the boundary layer fitting method is that this only works for canonical profiles, and cannot account for drag-reduced cases with an additive constant ΔB. To account for this, all the results are scaled with the reference friction velocity, i.e. the flat plate reference TP0000. This highlights the absolute differences in TKE with respect to TP0000 and removes the inherent uncertainty between fits.

The DUT HWA acquisition system performed well for spectral analysis, due to the sufficient temporal resolution and the application of an analogue cut-off filter. However, contrary to the Hill system, which uses a rigid mounting and traversing system, the sting used with the DUT system was prone to vibrations. This resulted in the spurious vibration peaks observed in the spectra, close to the wall, for the streamwise stresses. These should be prevented in future measurements.

III

Active spatial spanwise forcing

7

Paper: An experimental realisation of steady spanwise forcing using spanwise running belts for turbulent drag reduction

Part III of the thesis focuses on active spanwise forcing; in particular, steady spatial forcing is investigated. In doing so, research question three will be addressed. A research gap on this topic was identified in Chapter 3, in that there have been no experimental realisations of spatial forcing in external flows to date. Furthermore, spatial forcing is of interest for translating active forcing to a passive spatial counterpart. This part presents a proof of concept for the first experimental realisation of spatial forcing in external flows. The forcing is realised by employing a series of spanwise running belts to create a spatial square wave forcing. The first chapter of this part is written in a paper format. The concept for the experimental setup is presented, and the associated flow modulation effects are discussed. Succeeding the paper, Chapter 8 provides additional results to address the remaining sub-questions that were not addressed in the paper. In addition, detailed methodology and post-processing procedure for the HWA and PIV measurements are presented in Appendix B and Appendix C.

An experimental realisation of steady spanwise forcing using spanwise running belts for turbulent drag reduction

M.W. Knoop*
Aerodynamics Group, Faculty of Aerospace Engineering, Delft University of Technology
(*m.w.knoop@student.tudelft.nl)
(Dated: March 24, 2023)

This study presents a proof of concept for the first experimental realisation of steady spatial forcing in boundary layer flows. The spatial forcing is generated by a series of spanwise running belts, running in alternating spanwise direction, thereby generating steady spatial square wave forcing. Stereo particle image velocimetry is used to investigate the turbulence statistics, drag reduction and spanwise velocity profiles, for a waveform of $\lambda_x^+ = 400$. The results show a significant flow control effect can be realised with this type of forcing, with a maximum drag reduction of 23%, and a reduction in turbulence kinetic energy production of 38%. An extension of the classical spatial Stokes-Stokes (SSL) is proposed by using linear superposition of a number of Fourier modes to describe a non-sinusoidal boundary condition. Qualitatively, the experimental spanwise profiles agree with the extended model. Besides the substantial flow control effect, we also observed possible secondary aerodynamic effects at higher freestream velocities and viscous wavelengths. Vibrations of the belts were observed at increased values of physical belt speed and freestream velocity, possibly adding to the turbulent energy close to the wall. We present recommendations for improvements to the experimental setup, and future research topics using spatial forcing are discussed.

I. INTRODUCTION

Turbulent drag reduction is a crucial research area in fluid dynamics, as reducing drag can lead to significant energy savings and emission reductions in various industrial and transportation applications. Over several decades spanwise forcing through wall motion has been studied with the aim of turbulent drag reduction (DR), with reported DR values reaching over 40% [1]. The method introduces an oscillatory in-plane motion in the spanwise direction. The forcing results in an oscillating spanwise velocity profile, which facilitates a useful interaction with the near-wall turbulence, giving rise to a drag-reduced state [2]. As this is an active flow control method, the energy expenditure associated with the wall forcing is also important to consider. This is expressed by the net power saving (NPS), which is defined as the difference between the DR and the idealised power input to drive the resultant spanwise velocity profile.

The early studies on spanwise forcing focus on oscillating wall motion (OW), where a wall section is subjected to a temporal oscillation. The wall motion is imposed by describing the spanwise wall velocity W_w:

$$W_w(t) = A \sin\left(\frac{2\pi}{T} t\right) \tag{1}$$

Where A and T are the spanwise velocity amplitude and period of oscillation, respectively. The characteristic parameters are commonly scaled in viscous units, with the kinematic viscosity ν and the friction velocity $u_\tau \equiv \sqrt{\tau_w/\rho}$. τ_w and ρ are the wall-shear stress and fluid density. The viscous length scale is defined as $\delta_v \equiv \nu/u_\tau$. Scaling in the case of a drag reduced-flow can take two forms, either with a reference $u_{\tau 0}$ from the non-actuated case (indicated with subscript '0' throughout this paper) or the actual u_τ of the drag-reduced flow case. Scaling is indicated by the superscript '+' and '*' for scaling with $u_{\tau 0}$ and u_τ, respectively.

The first numerical work is the study of Jung *et al.* [3] on OW forcing. They found a DR of 40% at an optimum period $T^+ = 100$ and an amplitude of $A^+ = 12$. Experimentally similar findings were made by Laadhari *et al.* [4], with a 36% DR at the same optimum period. Under drag-reduced conditions when scaling with $u_{\tau 0}$, a reduction of the near-wall velocity or thickening of the viscous sublayer can be observed. The near-wall streamwise stress peak reduces in magnitude and is shifted to higher wall-normal positions. The velocity profile shows similarity in the viscous sublayer when scaled with u_τ and an upward movement of the logarithmic layer can be observed, characterised by an additive constant ΔB that is correlated to the DR [4–6]. The resultant spanwise velocity profile under OW forcing is described by the laminar solution of the second Stokes problem [7], or temporal Stokes layer (TSL).

A new form of spanwise wall motion was introduced by Quadrio *et al.* [8], with an additional spatial component added to the wall forcing. This results in a travelling wave (TW) boundary condition in the form of:

$$w_w(x,t) = A \sin\left(k_x x - \omega t\right) \tag{2}$$

k_x and ω are the wavenumber and oscillatory frequency, respectively. The combination of wavenumber and frequency forms the propagation velocity of the wave $c \equiv \omega/k_x$. Their numerical investigation found a high DR region in the $k_x - \omega$ space,

with values of up to 48% at $A^+ = 12$. The high DR region is flanked by an area of the drag increase when the wavespeed is in the order of the convection velocity of the near-wall turbulence, $\mathscr{U}_w^+ \approx 10$ [8, 9]. Inspired by the work of Quadrio *et al.* [8], several experimental realisations of TW forcing have also been made that showed similar drag characteristics. Auteri *et al.* [10] employed a series of oscillating elements in a pipe flow, and Bird *et al.* [11] used a deformable kagome lattice in a channel flow to realise the wall-actuation. More recently, Marusic *et al.* [12] performed boundary layer experiments up to $Re_\tau = 12,800$, performing actuation using a series of synchronised spanwise oscillatory elements. Besides effective DR using the convectional actuation parameters, they show an alternative pathway to drag reduction through inter-scale interaction [13] by actuating the outer-scales at lower temporal frequencies. Contrary to conventional actuation, the DR for outer-scaled actuation is correlated positively with Re_τ. Additionally, the required power input is reduced due to the lower frequency of actuation, resulting in positive NPS compared to negative values for the conventional actuation parameters [12, 14].

A third actuation scheme is purely spatial forcing. This scheme imposes a steady wall velocity in the form of a standing wave (SW):

$$w_w(x) = A \sin\left(\frac{2\pi}{\lambda_x} x\right) \tag{3}$$

Where λ_x is the streamwise wavelength of actuation. SW forcing was first introduced and numerically studied by Viotti *et al.* [15]. For these actuation parameters, an optimum DR is found around $\lambda_x^+ = 1,000 - 1,250$. Their results were compared to OW simulations of Quadrio and Ricco [16], under the transformation $\lambda_x = \mathscr{U}_w T$. The same trends could be observed; quantitatively, the DR potential is about 20-30% higher for the same (transformed) actuation parameters.

The Stokes layer is a key driver behind the working of spanwise forcing. Choi *et al.* [17] showed that the varying spanwise velocity profile realigns the streamwise vorticity vector, resulting in a net negative spanwise vorticity component. This spanwise vorticity reduces the slope of the velocity profile at the wall and increases the velocity in the region above $y^+ = 25$. Furthermore, Ricco [2] presents evidence that the Stokes profile breaks up the interaction of the near-wall streaks and the quasi-streamwise vortices by laterally displacing the two entities. This weakens the strength of the near-wall cycle resulting in a drag-reduced state. For TW and SW forcing, the TSL does not apply anymore and the alternative generalised Stokes layer (GSL) is used, which was introduced by Quadrio and Ricco [18]. Under SW forcing, the GSL reduces to the spatial Stokes layer (SSL).

Despite its high DR and NPS potential, SW forcing has seen relatively little attention. This actuation scheme has been the focus of a small number of numerical studies [15, 19, 20]. Furthermore, the work of Auteri *et al.* [10] realised TW forcing using their pipeflow setup. By having multiple azimuthally rotating pipe segments, a travelling wave was generated. SW forcing was not the focus of their studies; however, in steady conditions, i.e. $\omega = 0$, spatial forcing was obtained. Besides this study, no experimental realisations of SW forcing have been made.

This paper presents a proof of concept for the first experimental realisation of spatial spanwise forcing in external flows to address this research gap. The experimental setup consists of an array of streamwise-spaced, spanwise-running belts, generating a steady spatial square wave boundary condition. The simplification of using square waves is justified by the studies of Cimarelli *et al.* [21] and Mishra and Skote [22], who showed that substantial DR and NPS could be obtained using non-sinusoidal forcing for both OW and SW forcing. SW forcing was also identified as having potential in practical applications like aircraft cruise of long-distance pipeflows. The oscillatory frequencies required for OW and SW forcing are expected to be challenging to realise in practical applications, with frequencies in the order of $f = O(30\text{ kHz})$ for $T^+ = 100$ in cruise conditions. The wavelengths for SW forcing are deemed more realistic, especially when considering the outer-scaled actuation pathway introduced by Marusic *et al.* [12], where the wavelength is in the order of the outer scale $\lambda_x = O(0.25\text{ m})$.

The aim of this study is to present a proof of concept for the experimental realisation of steady spanwise forcing using spanwise running belts. A prototype setup was developed that uses four spanwise running belts to generate the SW forcing. The effectiveness of this setup for flow control and turbulent drag reduction are assessed through measurements of mean velocity profiles and turbulence statistics using stereo particle image velocimetry (PIV). A model is proposed for the SSL for an arbitrary waveform by using linear superposition of a number of Fourier modes that describe the waveform. The resultant modified SSL is examined and compared to the experimental spanwise profiles. Lastly, we discuss the potential secondary aerodynamic influence of the mechanical implementation using spanwise running belts. The findings of this study will provide recommendations for a full-scale setup and research directions for future work.

II. EXPERIMENTAL METHODOLOGY

Experiments were performed in the M-tunnel of the low-speed laboratory of the Delft University of Technology. The open loop tunnel reaches a maximum freestream velocity of $U_\infty \approx 35$ m/s with a turbulence intensity in the order of 0.7%. The tunnel has a square test section of 0.4 m×0.4 m; the parallel walls give rise to a slight favourable pressure gradient. A clean turbulent boundary layer was generated using a flat plate with an elliptical leading edge and tripped using carborundum roughness,

achieving a development length of 3 m. The prototype setup was placed in an open-jet configuration behind the wind tunnel, flush with the floor. This is regarded as a valid choice for the proof of concept of the experimental apparatus since the qualitative flow modulation effects are of more importance than the quantitative results. A temperature sensor and Pitot-static tube were placed in the downstream part of the test sections to obtain the atmospheric conditions and freestream velocity.

Prior to the stereo particle image velocimetry experiments, the boundary layer was characterized using hot-wire anemometry for freestream velocities of $U_\infty \approx 10$, 20, and 30 m/s. The hot-wire was placed 3 mm downstream of the actuation surface to measure the streamwise profile and higher-order statistics. The viscous scaling and boundary layer thickness were obtained using the fitting method outlined in Section II C. Further details about the boundary layer characterization can be found in Appendix A. From the characterization, the boundary layer thickness was estimated by a power law fit to δ and Re_1. In a similar fashion, the required freestream conditions and actuation parameters were determined from a linear fit between u_τ and Re_1. The experimental conditions and actuation parameters for the cases discussed in this paper are outlined in Table I.

Boundary layer properties				Actuation parameters			
U_∞ (m/s)	$u_{\tau 0}$ (m/s)	δ (mm)	Re_τ	A (m/s)	λ_x (mm)	A^+	λ_x^+
6.7	0.27	67.4	1,230	0.57	22	2.1	400
6.7	0.27	67.4	1,230	1.13	22	4.2	400
6.7	0.27	67.4	1,230	1.70	22	6.3	400
6.7	0.27	67.4	1,230	2.27	22	8.4	400
6.7	0.27	67.4	1,230	2.83	22	10.5	400
6.7	0.27	67.4	1,230	3.40	22	12.6	400
10.9	0.41	56.8	1,590	3.40	22	8.2	613
15.2	0.56	52.8	1,990	4.53	22	8.1	825

TABLE I. Overview of the experimental conditions and actuation parameters. Note that δ was obtained implicitly from the boundary layer characterization (Appendix A), and that δ and Re_τ for the non-actuated case are indicated.

A. Steady spanwise excitation setup

A novel idea is proposed for an experimental setup named the steady spanwise excitation setup (SSES). The setup is the first of its kind to realise SW forcing experimentally in external boundary layer flows. The SSES realises the forcing by employing a series of spanwise running belts that run in alternating directions to generate a spatial square waveform. For this study, a prototype setup was developed, which is used to test out the mechanical aspects of SSES, and to perform a proof of concept of the aerodynamic workings. A schematic representation of the prototype setup and its accompanying features are presented in FIG. 1.

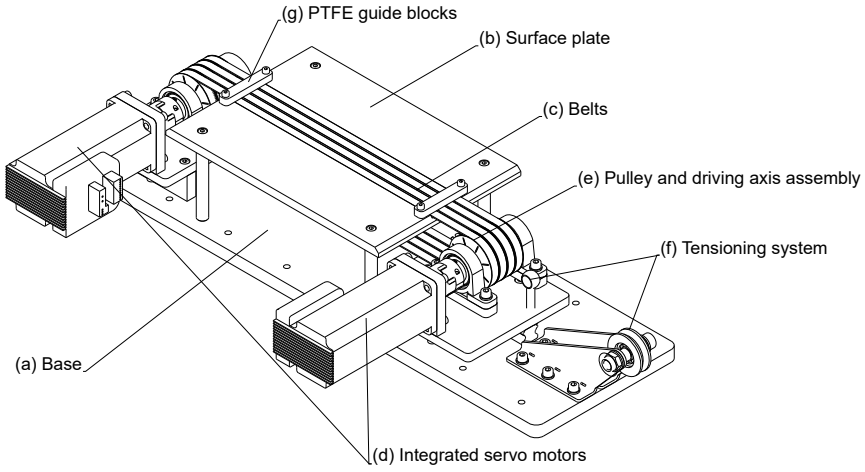

FIG. 1. Schematic representation of the SSES prototype

The prototype has four 9 mm wide neoprene belts, with a spanwise extent of 256 mm. The streamwise separation of 2 mm

between the belts is kept to a minimum within the mechanical feasibility of the design. This results in the smallest actuation wavelength of $\lambda_x = 22$ mm. The belts are embedded in an aluminium surface plate so as to run flush with the wall. In addition, the belts are guided by a PTFE strip to keep the belts constrained to the surface grooves. Tolerances on the grooves are specified to keep the gaps to a minimum, with a maximum gap size and step size of 50 μm, which translates to approximately $1.4\delta_v$ at typical freestream conditions of $U_\infty = 10$ m/s.

The belts are driven by a non-slip pulley system, which allows for individually controlling the rotation direction of the belts. This feature allows for the use of multiple belts for a single waveform; this way, the physical wavelength can be increased to 44 mm. The SSES prototype is powered by two 400 W iHSV60 integrated AC servo motors that drive the belts in alternating positive and negative spanwise directions. The motors have an adjustable feedback control loop for a fixed RPM output. The setup is designed to run from 0-2,000 RPM corresponding to a maximum spanwise velocity of 6 m/s. One advantage of a setup like this is the independent control over the A and λ_x, which are usually coupled in OW and TW forcing that employ oscillating elements with a fixed displacement amplitude.

One of the SSES prototype aims was to investigate the belt tension required to have the belts run flush with the surface, without lifting under aerodynamic loads. This was realised by placing one of the pulley systems on a linear guide to have it move freely. Belt tension can be applied by hanging a weight to the pulley system. A required belt tension of approximately 25 N per belt was found for operation in the range of $U_\infty = 0 - 30$ m/s.

B. Stereo particle image velocimetry

Stereo particle image velocimetry (PIV) was performed to measure the three velocity components in the streamwise $x-y$ plane. Stereo PIV was selected to simultaneously capture the streamwise and wall-normal turbulence statistics, as well as the out-of-plane Stokes profiles and the corresponding spanwise statistics. For each measurement, 1000 uncorrelated velocity fields were obtained at an acquisition frequency of 10 Hz. The time separation was set to have approximately 10 pixels displacement in the freestream between consecutive image pairs. A schematic representation of the experimental setup is depicted in FIG. 2.

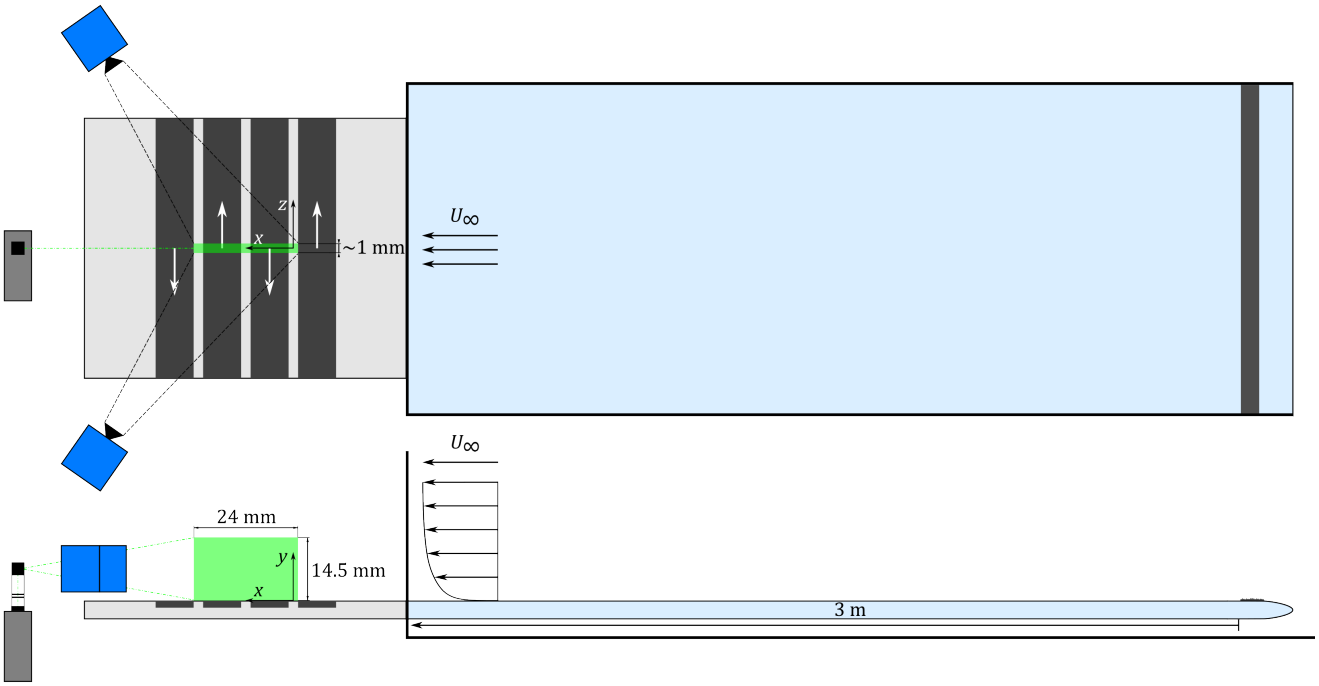

FIG. 2. Schematic representation of the experimental setup

Two digital LaVision sCMOS cameras (2,560×2,160 pixels, 6.5 μm pixel size, and 16 bit) were placed on either side of the laser sheet in back-scatter configuration. The field of view (FOV) was focused on the central two belts of the SSES prototype setup, spanning 24 mm×14.5mm in the streamwise and wall-normal directions, resulting in a resolution of 113 pixels/mm. Imaging was performed using Nikkor AF-S 200 mm lenses, with Kenko Teleplus PRO 300 2× teleconverters, at an f/11 aperture. The cameras were oriented at $\pm 30^\circ$ with respect to the laser sheet normal. Scheimpflug adapters were used to ensure uniform focus across the FOV.

Illumination was provided by a Quantel Evergreen 200 laser (double-pulsed ND:Yag, 532 nm), with a 100 mJ/pulse power setting. The laser was placed downstream of the setup, below the open jet. A set of spherical and cylindrical lenses were used to create a laser sheet with an approximate thickness of 1 mm. The laser sheet was directed towards the experimental setup using a 45° mirror. A knife edge was placed on the trailing edge of the surface plate to reduce reflections by clipping the bottom part of the laser sheet. Seeding was injected at the wind tunnel inlet by a SAFEX Fog 2010+ fog generator to create 1 μm tracer particles from a water-glycol mixture.

Calibration and vector processing were performed using the DaVis 10.2 software package. The LaVison type 7 calibration target was used for stereo calibration. Additionally, self-calibration was performed to reduce the calibration fit error to below 0.245 pixel or 2.16μm. For each camera, the individual two velocity component fields were obtained using cross-correlation. An initial pass of 96×96 pixels square interrogation windows with 75% overlap and two final passes with 16×16 pixels circular windows at 75% overlap were used. The resultant velocity fields of the two cameras were combined to obtain the 2D3C velocity field by a least squares fitting approach. The average stereo reconstruction error was below 0.1 pixel. The universal outlier detection method of Westerweel and Scarano [23] was applied with a 1× median filter region of 7×7 pixels, removing residuals larger than 2. Further post-processing and data analysis were performed in Matlab.

C. Boundary layer fitting and estimation of the drag reduction

The profiles for the mean-velocity and turbulence statistics are obtained by space averaging the vector fields in streamwise direction over the considered FOV. To find the boundary later properties and viscous scaling the parameters u_τ, wall-offset Δy, boundary layer thickness δ and wake parameter Π are fitted to the composite profile of Chauhan *et al.* [24] using a sequential quadratic programming iterative method. The log-layer constants $\kappa = 0.384$ and $B = 4.17$ are used [25]. Note that the considered FOV does not capture the outer part of the boundary layer, here the composite profile reduces to the Musker [26] profile. In this case, Π and δ are omitted from the fitting procedure.

Under actuation, the velocity profile deviates from its canonical state. In a drag-reduced state, when the viscous scaling is correct, the additive constant B increases, moving the logarithmic region upwards. This deviation from the canonical composite profile means that the fitting procedure becomes invalid. To obtain the viscous scaling under drag-reduced flow the viscous sublayer in the region of $3 \leq y^+ \leq 5.5$ is fitted to the profile $u^* = y^*$. Since the flow experiences a drag-reduced state the fitting region stays within the viscous sublayer as δ_v increases. After determining the actual friction velocity the DR is defined as the reduction in mean wall-shear stress, which can be expressed in terms of u_τ as:

$$\mathrm{DR} = 1 - \frac{\overline{\tau_w}}{\overline{\tau_{w0}}} = 1 - \frac{\rho u_\tau^2}{\rho_0 u_{\tau 0}^2} \tag{4}$$

III. LAMINAR SOLUTION OF THE SPATIAL STOKES LAYER FOR AN ARBITRARY WAVEFORM

Since we investigate the working of a square waveform compared to perfect sinusoidal forcing, an extension to the laminar model for the SSL is required that allows for the use of an arbitrary waveform. The Stokes solution is derived from the boundary layer equations [15, 18]. The solution is steady, and the x- and y-momentum equations are decoupled from the z-momentum equation as a results of the spanwise invariance of the system. Thus the governing equation for the spatial Stokes layer becomes the linear partial differential equation:

$$u\frac{\partial w}{\partial x} = \nu\left(\frac{\partial^2 w}{\partial x^2} + \frac{\partial^2 w}{\partial y^2}\right) \tag{5}$$

For sinusoidal SW forcing Eq. (5) is subjected to the boundary condition Eq. (3). The influence of the third term is neglected under the condition that λ_x is in the order of the outer length scale. From this the solution of the SSL was derived by Viotti *et al.* [15] to be :

$$w(x,y) = AC_x\Re\left[e^{ik_x x}Ai\left(-\frac{iy}{\delta_x}e^{-i4\pi/3}\right)\right] \tag{6}$$

$$\delta_x = \left(\frac{\nu}{k_x u_{y,0}}\right)^{1/3} \tag{7}$$

With $C_x = Ai(0)^{-1}$ as a normalization constant, i as the imaginary unit and δ_x the penetration depth, where $u_{y,0}$ is the slope of the streamwise velocity profile at the wall.

We now adapt the SSL solution to account for an arbitrary waveform. The approach taken by Cimarelli *et al.* [21] for the TSL is applied to the SSL. Since the governing Eq. (5) is linear, a superposition of various harmonics making up the waveform can be applied. In line with their method, the waveform describing the wall motion is expressed in terms of a Fourier series:

$$w_w(x) = A \sum_{n=-\infty}^{+\infty} B_n e^{ik_x nx} \tag{8}$$

For the nth term in this series the the wavenumber becomes, $k_x n$. The corresponding penetration depth is then defined as:

$$\delta_{x,n} = \left(\frac{\nu}{k_x n u_{y,0}} \right)^{1/3} = \delta_x n^{-1/3} \tag{9}$$

Substituting this and superimposing the elementary solutions, the SSL for an arbitrary waveform is then obtained as follows:

$$w(x,y) = AC_x \sum_{n=-\infty}^{+\infty} \Re \left[B_n e^{ik_x nx} Ai\left(-\frac{iy}{\delta_x n^{-1/3}} e^{-i4\pi/3} \right) \right] \tag{10}$$

IV. EXPERIMENTAL RESULTS AND DISCUSSION

The experimental setup was used in a configuration where the belts were moving alternating resulting in the sequence of two square waveforms of $\lambda_x = 22$ mm. Profiles were obtained by space-averaging the data in the streamwise direction over the two central belts; this method was selected to assess the integral phase-averaged influence of actuation on the flow. The flow modulation effects are assessed through the mean streamwise velocity profiles and the turbulence statistics. For this assessment, six cases are presented for $\lambda_x^+ = 400$ with the spanwise velocity amplitude increasing from $A^+ \approx 2$ to 12. The model of the modified SSL is examined and compared to the experimental results for the same wavelength at $A^+ \approx 6$. Lastly, we present a discussion on the secondary aerodynamic influence on the turbulence statistics at higher freestream velocities. For this three cases are considered: $\lambda_x^+ \approx 400$, 600, and 800 at $A^+ \approx 8$.

A. Mean velocity and drag characteristics

The mean streamwise velocity profiles are illustrated FIG. 3 (a-b), which show the scaling with the reference and actual friction velocity, respectively. Scaling with $u_{\tau 0}$ indicates a reduction of mean velocity below $y^+ \leq 15$, which suggests a 'thickening' of the viscous sublayer; indicative of a drag-reduced state. The behaviour is consistent with previous studies on spanwise forcing [4–6]. To further emphasise this, scaling with u_τ is applied. The profiles now show similarity in the viscous sublayer with an upward shift ΔB of the logarithmic region under actuation due to the reduction in skin friction velocity.

Based on the qualitative response of the mean profile, the DR increases monotonically at a decreasing rate with A^+. This trend is further highlighted in FIG. 3 (c), which plots the DR estimate for the considered cases. A maximum DR of 23% is found for the highest spanwise velocity amplitude. The DNS results of Viotti *et al.* [15], for a sinusoidal waveform with a similar wavelength of $\lambda_x^+ = 300$, are added for comparison. Although there is some variation in the data, the qualitative trend is in line with the observations of Viotti *et al.* [15]. It is important to note that the absolute drag reduction is lower compared to the DNS study, especially at higher values of A^+. Two possible causes are identified for this. Firstly, experimental realisation of the SW boundary condition, which may not perform to the same degree as the idealised conditions in the numerical studies. The surface has small spanwise cavities around the grooves that the belts run in, and the changes in surface roughness between the belts and the aluminium surface plate. These factors may negate some of the DR effects. Secondly, the measurement region considered is $0.13 \leq x/\delta \leq 0.49$ downstream of the start of actuation. As Ricco and Wu [5] have shown, there is a spatial transient of DR in the region $x/\delta \leq 3$, where the DR value is rising to its maximum steady value.

Another observation from the velocity profile, specifically FIG. 3 (a), is that there is an overshoot of the velocity profile in the region $20 \leq y^+ \leq 40$ compared to the non-actuated case. These results are consistent with the conceptual model of Choi [27], which suggests that this modification of the velocity profile is due to an induced negative spanwise vorticity. Modelling this negative spanwise vorticity as a point source around $y^+ = 15$ reduces the slope at the wall and increases the velocity above $y^+ = 15$ resulting in the observed overshoot.

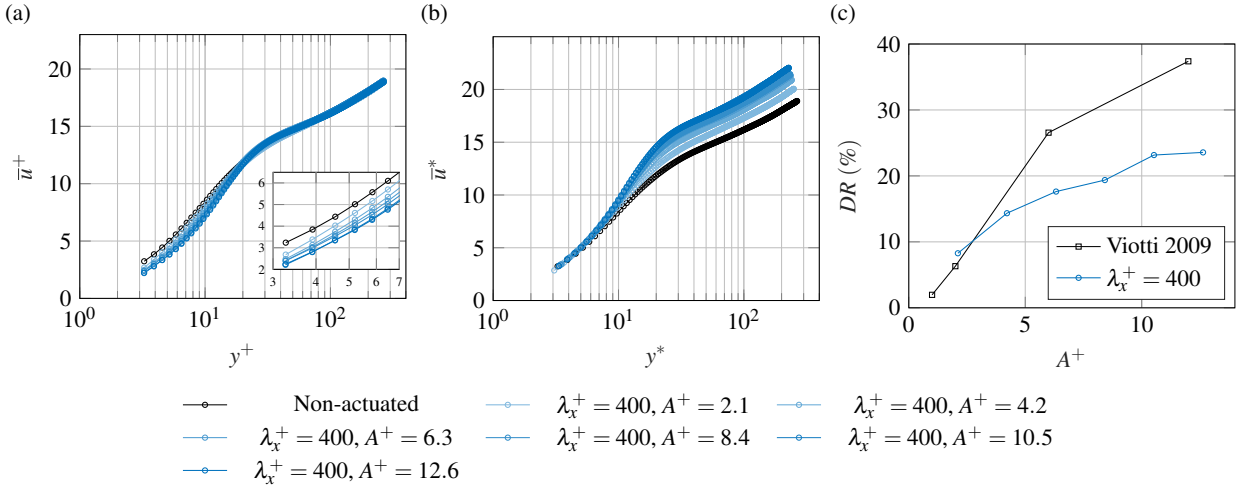

FIG. 3. (a-b) Streamwise velocity profiles for the non-actuated case and cases with $\lambda_x^+ = 400$. (a) scaling with $u_{\tau 0}$, (b) scaling with tu_τ. (c) DR vs A^+ with DNS results of Viotti *et al.* [15] for $\lambda_x^+ = 300$.

B. Turbulence statistics

The turbulence statistics in terms of the variance profiles for the three velocity components, the Reynolds shear stress, and turbulence kinetic energy (TKE) production are depicted in FIG. 4. Reference scaling with $u_{\tau 0}$ is applied to highlight the absolute chances with respect to the non-actuated case.

Assessing the streamwise stress $\langle u'^2\rangle^+$, we can observe that the energy is attenuated in the region up to $y^+ \approx 100$. The most significant reduction is in the near-wall stress peak centred around $y^+ = 15$ for the non-actuated case. A maximum energy reduction of almost 45% is found for $A^+ = 12$. In addition to the substantial energy reduction, the peaks are shifted to higher wall-normal locations. This behaviour is consistent with earlier experimental observations of drag-reduced flow under spanwise forcing [4, 5, 14]. It can be observed that the energy reduction is not linearly correlated with A^+ but decreases at a decreasing rate as A^+ increases, in line with the observed DR trend. The stresses $\langle v'^2\rangle^+$ and $-\langle u'v'\rangle^+$ show a similar response where the profiles shift to higher wall-normal locations and attenuation is most significant close to the wall.

The spanwise stress can be decomposed into its stochastic component and a phase-wise component as a result of the spanwise wall motion like: $\langle w'^2\rangle^+ = \langle w''^2\rangle^+ + \langle \tilde{w}^2\rangle^+$. In the case of spatial forcing, $\langle w'^2\rangle^+$ is obtained by adding the streamwise variance over the phase ($\langle \tilde{w}^2\rangle^+$) of the spanwise velocity profiles to the stochastic component obtained from the temporal variance ($\langle w''^2\rangle^+$). In the spanwise stress component $\langle w'^2\rangle^+$, a strong peak is observed in the near-wall region (note the log-log scale). This peak results from the phase-wise fluctuating component of the spanwise stress, corresponding to the variance of the spanwise velocity profile. Hence, the peak is correlated to the spanwise velocity amplitude. The peak decays in magnitude when moving in wall-normal direction. As a result of actuation, the stochastic fluctuations $\langle w''^2\rangle^+$ also increase in the near-wall region below $y^+ \leq 10$. Again the intensity is correlated with A^+. In agreement with the other stresses, we observe that under actuation, the $\langle w''^2\rangle^+$ profiles are shifted in the wall-normal direction and show a slight energy reduction up to a height of about $y+ = 100$. It should be noted that the strong increase in near-wall stochastic spanwise stress may be attributed to spurious measurements. This is further elucidated in Section IV D.

Lastly, the production of TKE is discussed. The production term is approximated by the product of Reynolds shear stress and mean shear: $P = -\langle u'v'\rangle dU/dy$ [28, 29]. The production is plotted in the premultiplied form (P^+y^+), where an equal area highlights an equal contribution to the TKE production. It can be observed that the actuation significantly reduces the peak in the buffer layer, and again, the profiles are shifted to higher wall-normal position. For $A^+ = 12$, a reduction of integral TKE production of 38% is found for the considered wall-normal region.

C. Comparison to the modified spatial Stokes layer

This section discusses the spanwise velocity profile resulting from the applied forcing. We compare the experimental results to the model of the modified SSL presented in Section III. The waveform comprises a 9 mm wide belt actuated at $\pm A^+$, with a streamwise separation of 2 mm. 10 single-sided Fourier coefficients approximate the wave. The transition is approximated by a linear increase from $-A^+$ to A^+ to prevent Gibbs phenomena. The waveform and its Fourier series approximation are depicted

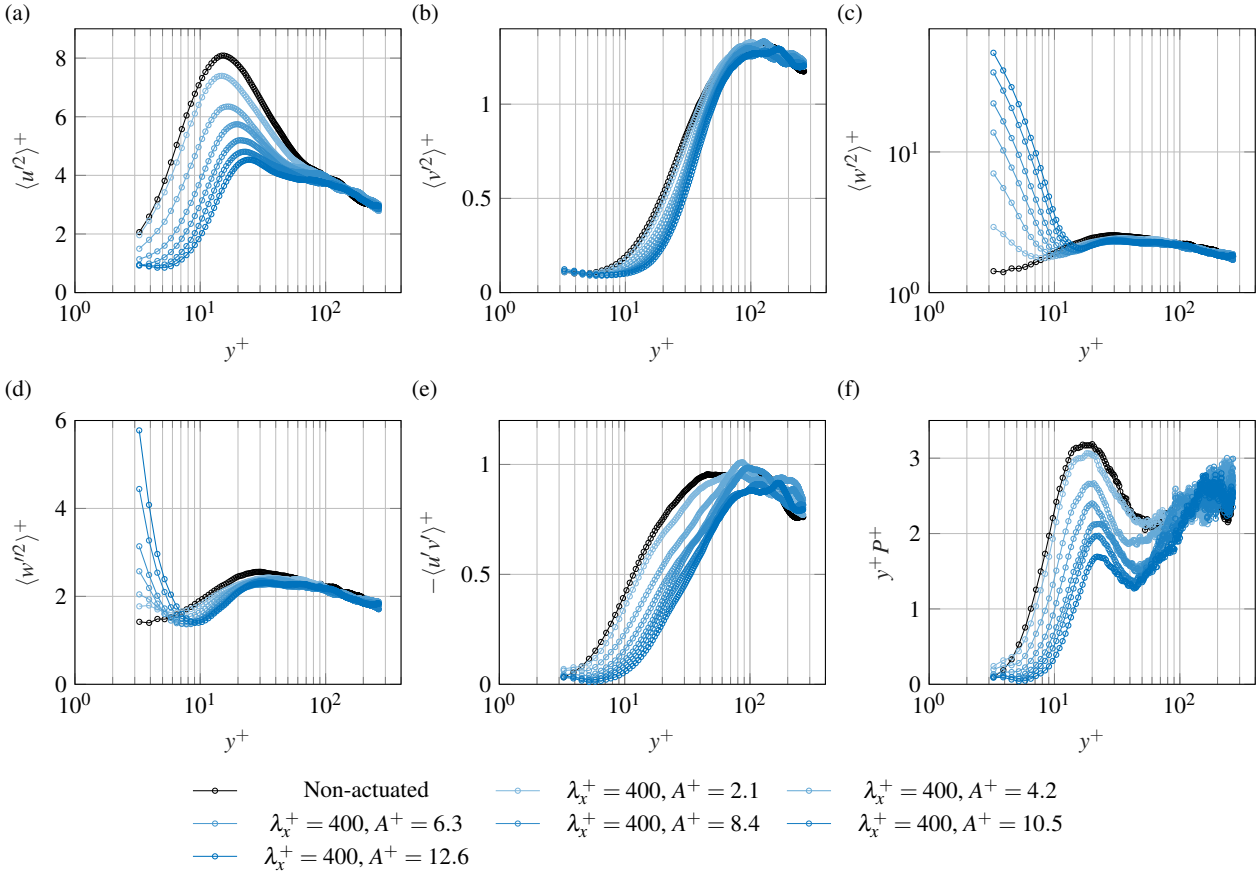

FIG. 4. (a-d) Normal Reynolds stresses and (e) Reynolds shear stress. Spanwise stress is decomposed in (c) total spanwise stress, plotted on a log-log scale and (d) the stochastic component. (f) Premultiplied production or turbulence kinetic energy.

in FIG. 5. We investigate the case from the previous discussion at $A^+ \approx 6$. This analysis examines the spanwise profiles at three locations for each half phase, located over the central two belts. In addition, the 2 mm region between the belts is studied with five linearly spaced points. The measurement locations are also depicted in FIG. 5. Note that the half-phase is used to normalize the streamwise location. Hence the same value after the decimal point indicates the same location on the half phase.

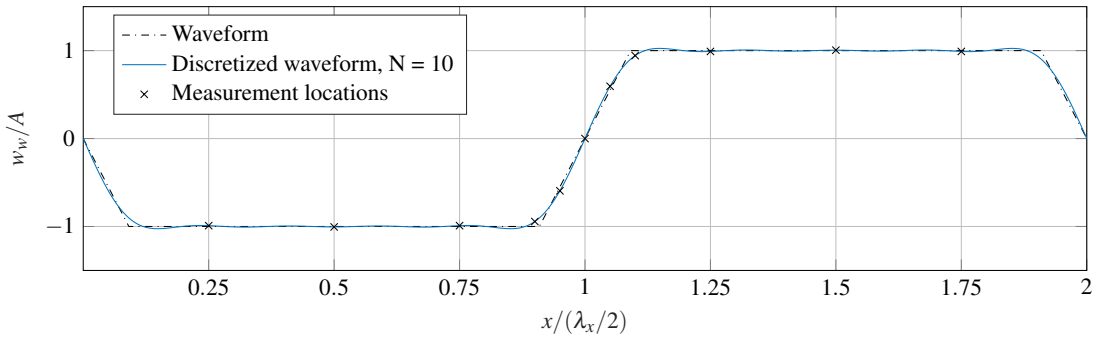

FIG. 5. The waveform, and Fourier series approximation using 10 single-sided coefficients, for the modified SSL model. Sample locations used in the analysis are indicated on the waveform.

Assessing the results in Fig. 6 (a), it can be observed that the spanwise velocity profile resembles a clear Stokes-like layer, which is confined to the near-wall region and decays to zero at $y^+ \approx 25$, in line with the SSL for perfect sinusoidal forcing at moderate wavelengths of λ_x^+ [15, 18]. Also similar to the SSL is the overshoot in the velocity profile, which moves to higher wall-normal locations when moving downstream over the belt. Some asymmetry between the two half phases can be observed.

This could be attributed to a spatial transient of the SSL due to the lack of a significant actuation region upstream of the FOV.

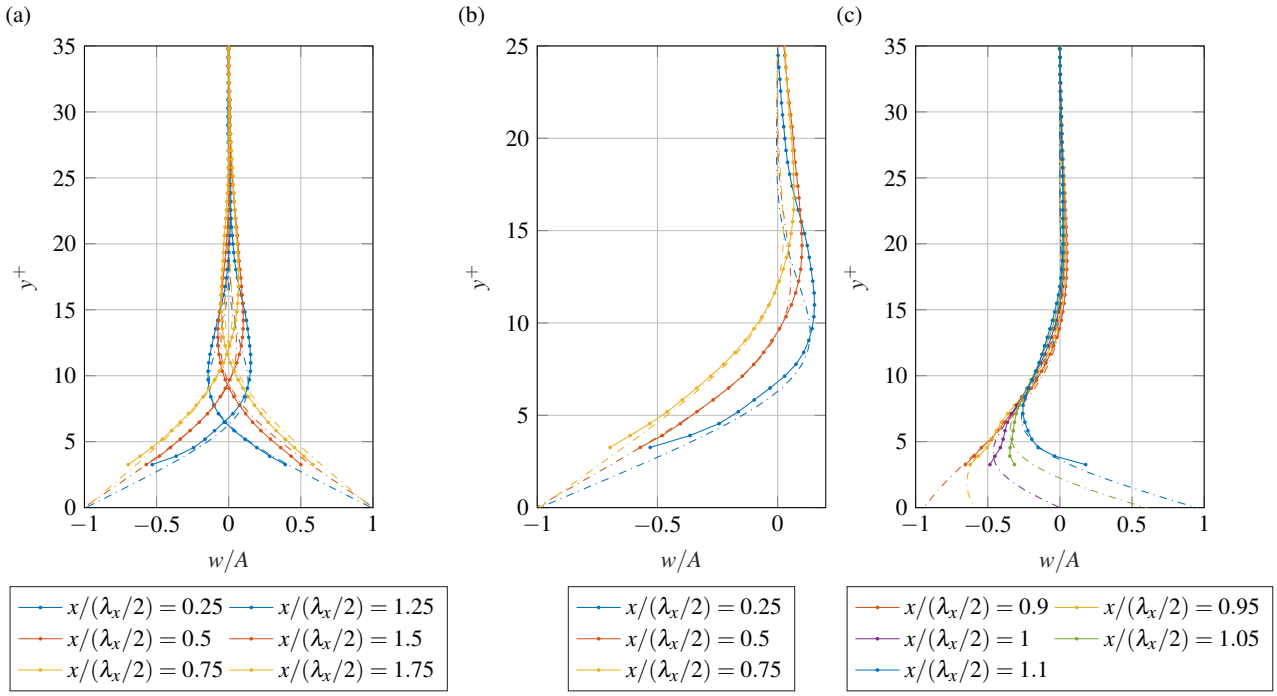

FIG. 6. Spanwise velocity profiles, experimental data piloted with solid lines, modified SSL displayed for the same colour indicated with a dashed-dotted line, profiles are given the same colour for the same location on the half phase. (a) Profiles over the belts at three locations per half phase, (b) a detailed view of the profiles over the first half phase, (c) profiles in the transition region between belts.

We now make a comparison to the theoretical model for the modified SSL. The first half phase is further highlighted in detail in Fig. 6 (b). Qualitatively the experimental profiles match the model well, with an almost exact match in the region $y^+ \leq 10$. The slope of the spanwise velocity profile is in line with the model; decreases when moving downstream over the belt. Hence, the model can be used meaningfully to estimate the power input to drive the spanwise profiles. Beyond $y^+ = 10$ it can be observed that the experimental data diverts slightly. The overshoot of the profile is larger in magnitude, present at higher wall-normal locations and penetrates deeper into the boundary layer. Recall that the SSL model is based on the laminar boundary layer equations. Hence, these differences could be attributed to the turbulent flow further away from the wall. The penetration depth is calculated as the wall-normal location where the phase-wise standard deviation reduces to $\langle \tilde{w} \rangle = Ae^{-1}$. The model and experiment values are $\delta^+_{s,mod} = 5.0$ and $\delta^+_{s,epx} = 4.8$, respectively. The two are in the same order, as expected from the good agreement in said region.

The model deviates from the practical realisation by linearly transitioning between half phases instead of the abrupt changes in the boundary condition. To assess the effect of this choice, the profiles in the transition region are studied, as depicted in Fig. 6(c). It can be observed that the match between the model and the experiment is almost perfect, with only slight deviations in the region $y^+ \leq 5$. This small deviation could be attributed to the uncertainty of the measurements close to the wall. Therefore we conclude that this way of modelling the change between half phases is valid and can be applied without significantly altering the response of the Stokes profiles.

D. Secondary aerodynamic influence from the mechanical implementation

This section discusses the secondary influence the mechanical implementation using spanwise running belts has on the aerodynamics of the flow, especially at higher freestream velocities. So far, we only considered the case where the streamwise wavelength of actuation was $\lambda_x^+ \approx 400$. There are two options to change the actuation wavelength. Firstly, one can change the physical wavelength by changing the rotation direction of the belts; as such multiple belts running in the same direction result in a larger square wave. The second option is to change the viscous actuation parameters by changing the freestream conditions. At a fixed physical wavelength, e.g. $\lambda_x = 22$ mm, the viscous wavelength can be increased by increasing the freestream velocity.

At higher freestream velocities, i.e. higher viscous wavelengths, an additional stress component is observed in the region

close to the wall. This is highlighted in Fig. 7, which shows the streamwise variance and stochastic component of the spanwise variance. In these two stress components, the effects are most pronounced. We consider the cases $\lambda_x^+ \approx 400$, 600, and 800 for $A^+ \approx 8$. Two possible reasons are identified for causing this additional stress. Firstly, they could be attributed to the mechanical implementation of the forcing. Secondly, strong diffractive reflections were observed on the edges of the spanwise surface grooves in the surface plate. It was not possible to filter out these reflections completely in post-processing. This is believed to cause additional spurious fluctuations.

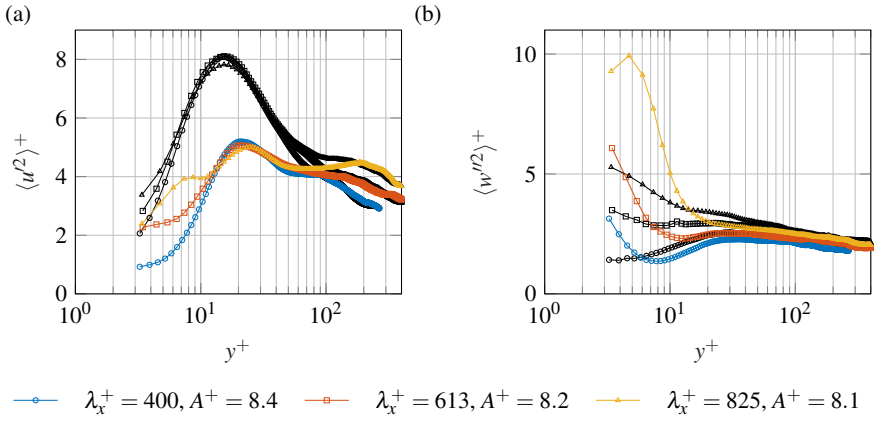

FIG. 7. (a) streamwise and (b) spanwise stochastic component of the normal Reynolds stresses for cases $\lambda_x^+ \approx 400$, 600 and 800 at $A^+ \approx 8$. Non-actuated cases share the same marker as for the corresponding actuated wavelengths, indicated by a black line.

Assessing $\langle u'^2\rangle^+$, the reduction in peak energy is in the same order for all three wavelengths. However, it can also be observed that the streamwise stress in the region $y^+ \leq 10$ shows an unexpected rise with increasing λ_x^+. A similar effect can also be observed for the non-actuated cases, albeit lower in magnitude. These are perhaps resultant from the complexity of the surface. Which shows discrete changes in roughness and the small spanwise oriented gaps between belts and the aluminium surface plate. While the gaps of approximately 50 μm are fixed in physical space, their viscous size grows as the wavelength increases. Adding to this complexity, is the increasing belt speed when keeping A^+ fixed between wavelengths. It was found that there are minute vibrations of the belts at higher belt speeds. Although the reflections mainly influenced the spanwise stress component, it is not possible to isolate the secondary aerodynamic influence and attribute the influence to the mechanical implementation.

Recall the stochastic spanwise stress component $\langle w''^2\rangle^+$ from Fig. 4. It can be observed that the spanwise fluctuations in the near-wall region do not tend to zero close to the wall for the non-actuated case, thereby deviation from the canonical behaviour [30]. In Fig. 7 (b), we observe that the magnitude of this effect is amplified for larger wavelengths, as well as penetrating to deeper y^+ values. Additionally, it also observed that the fluctuations for the actuated cases increase with increasing λ_x^+. Since the spanwise fluctuations are also significantly increased in the non-actuated case, this effect cannot be attributed to belt vibrations alone. We believe that the fluctuations are spurious as a result of strong reflections that could not be filtered out completely from the PIV images in post-processing. From the assessment of the raw-images and the scalar-fields, diffractive reflections were present on the edges of the spanwise grooves in the surface plate. They were observed up to a wall-normal height of approximately 0.6 mm, explaining the deeper penetration at higher λ_x^+. It is believed that the spanwise stress component is affected in particular. Since the reflections are fixed at the surface grooves in their $y-x$ coordinates, hence small spanwise variations of reflections between image pairs are correlated in vector processing, likely resulting in spurious spanwise vibrations. In the actuated cases, the belt vibrations resulted in more unsteadiness of the reflections, adding to the spurious variance. Furthermore, the increasing magnitude with λ_x^+ is explained by a decrease in time separation between consecutive image pairs.

Concluding, it is impossible to isolate and attribute the secondary aerodynamic effects to either of the two causes. This requires further investigation. It is valuable to perform hot-wire measurements to isolate the possible secondary aerodynamic influence of the mechanical implementation, thereby excluding the influence of reflections. These secondary effects are relatively minor, especially for $\langle u'^2\rangle^+$, confined to the near-wall region $y^+ \leq 10$ leaving the near-wall peak unaffected. Thus, the conclusions and findings in this study can still be regarded as valid since the qualitative response is of more importance for the proof of concept. A good alternative for future PIV measurements is imaging in the $y-z$ plane, away from the spanwise surface grooves.

V. CONCLUSIONS

This paper presented a proof of concept for the first experimental realisation of steady spatial forcing in boundary layer flows. The forcing was realised with four spanwise running belts, with alternating rotation directions, generating a steady spatial square wave boundary condition. We have shown that this type of forcing can induce a significant flow control effect.

The turbulence statistics and drag reduction were investigated for a wave with $\lambda_x^+ = 400$. The DR was shown to increase at a decreasing rate with A^+, for a maximum of 23%. Qualitatively the behaviour is in line with the expected trends from literature [5, 15], but lower in magnitude. We believe the reason for this is twofold. Firstly, the experimental realisation of the forcing using spanwise running belts, compared to the perfect imposition of the boundary conditions in numerical studies. Secondly, the measurement region is likely still within the rising spatial transient of the DR. The velocity profiles and turbulence statistics further confirm the significant flow modulation effect. In line with earlier observations [4, 5, 14], the stresses are reduced and shifted to higher wall-normal locations. The streamwise stress peak shows a reduction of almost 45% at $A^+ = 12$. Furthermore, for this case, the TKE production is reduced by 38%.

The Stokes layer is an important driver behind the working mechanism responsible for a drag-reduced state. An extension of the classical SSL was proposed to investigate the Stokes profile resulting from this non-sinusoidal waveform. Similar to the model of Cimarelli *et al.* [21] for the TSL, the boundary condition is derived by linearly superimposing a series of Fourier coefficients that makes up the non-sinusoidal waveform. Qualitatively the experimental profiles agree with the model, especially in the region $y^+ \leq 10$ where there is an almost exact match. Above this region, the overshoot of the profiles is larger in magnitude and penetrates deeper into the boundary layer. The penetration depth of the modified SSL is within the region where the two match, at $\delta^+_{s,mod} = 5.0$ and $\delta^+_{s,epx} = 4.8$, for the model and the experiment, respectively. With this general agreement, especially in the near-wall region, the model can be used for the theoretical power input to drive the Stokes profile in future work.

Besides a significant flow control effect, a secondary aerodynamic influence was observed at higher freestream velocities and belt speed. The additional energy in the streamwise stress is believed to result from a combination of two factors. Firstly, the complexity of the actuation surface and vibrations of the belts may result in a minor adverse interaction with the flow, at higher freestream and belt velocities. Secondly, affecting the spanwise stresses primarily, are spurious stresses resulting from strong diffractive reflections on the actuation surface. The influence of the two possible causes could not be separated in the current study. Hence further research is required to isolate and investigate a possible secondary aerodynamic effect resulting from the mechanical implementation. Hot-wire measurements should be performed to investigate this effect so as to mitigate spurious measurements due to reflections. If PIV measurements were to be performed, imaging should mainly be done in the $y-z$ plane, away from the spanwise grooves, to negate the influence of reflections.

VI. RECOMMENDATIONS FOR FUTURE RESEARCH

We have shown that a significant flow control effect can be attained with the proposed experimental realization of steady spanwise forcing. These results offer perspective for further research into the flow mechanisms and the response to the governing actuation parameters. The setup discussed in this paper is a prototype for a proof of concept of the workings. Therefore we propose future research with a next iteration 'full-scale' experimental setup. This section presents recommendations for a full-scale setup and outlines some interesting research directions.

We have seen that the DR is lower compared to the numerical work. A likely reason for this is that the field of view over the central two belts is located within the region of spatial transience of DR before it reaches a maximum steady-state value. Existing work shows that the steady state is reached after an actuation length of approximately $x_{act} \geq 3\delta$ [5]. To investigate the spatial transience of DR and determine the steady value, we recommended increasing the streamwise extent of the actuation surface to be in the order of 10δ. It was shown that at higher freestream velocities, the interaction of the belt with the flow may introduce some additional turbulence kinetic energy. To attain a streamwise wavelength in the order of the optimal wavelength $\lambda_x^+ \approx 1{,}000$ [15] it is recommended to implement wider belts. This way, we can investigate larger wavelengths while keeping moderate freestream velocities. In addition to the wider belts, further investigation is required to see if belt vibrations can be reduced via other measures. A recommendation to prevent string reflections is applying a light sandblasting to the surface, to give a more matt surface finish after anodization.

The introduction already touched upon the outer-scaled actuation pathway by Marusic *et al.* [12]. This new alternative to conventional inner-scaled actuation is promising for industrial applications, regarding its associated energy savings and the DR scaling with Re_τ. For outer-scaled actuation using SW forcing, we hypothesized that the wavelength of actuation should be increased to be in the order of outer-scales, $\lambda_x = O(\delta)$. These larger wavelengths can be obtained by having multiple belts run in the same rotational direction. This results in a single waveform with a larger wavelength using a multiple of 2 belts. The efficacy of this concept can be tested with the current prototype setup, but only up to a wavelength of $\lambda_x = 44$ mm. A significant influence of the outer-scales is a prerequisite to investigating outer-scaled actuation flow mechanics. Hence, experiments at

higher frictional Reynolds numbers are required [31, 32]. These conditions should primarily be attained by extending the boundary layer development length, to keep the freestream velocities moderate and the viscous length scale appropriate for flow measurement techniques.

Appendix A: Boundary layer characterization

This appendix presents the boundary layer characterization performed prior to the PIV experiment. HWA was used to obtain the streamwise velocity and stress profiles for three freestream velocities of $U_\infty \approx 10$, 20 and 30 m/s. The hot-wire probe was placed 3 mm downstream of the trailing edge of the last belt. Measurements were performed using a TSI IFA-300 constant temperature anemometer. Sampling was done at 51.2 kHz, with an analogue low-pass filter at 20kHz to prevent aliasing. The probe was the Dantec 55p15 miniature boundary layer probe, with a wire length and diameter of 1.25 mm and 5 μm, respectively. To obtain the profiles, a Zaber LRQ15HL traverse was used to sample 40 logarithmically spaced points in wall-normal direction, starting at $y = 0.125$ mm. The boundary properties and viscous scaling are found by fitting the composite profile of Chauhan *et al.* [24], further details can be found in Section II C.

The boundary layer profiles are presented in Fig. 8. Table II gives the corresponding boundary layer properties and HWA acquisition properties. It can be observed that the profiles match the DNS data well in the inner-layer. The outer-layer can be observed to grow with freestream velocity due to the higher value of Re_τ. In addition, the peak of the streamwise stress is reduced with Re_τ, as a result of attenuation of small-scale energy due to the increasing viscous wire length [33].

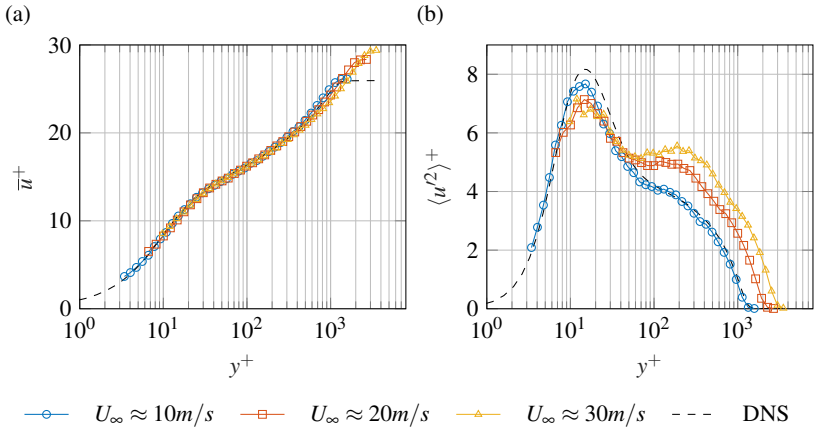

FIG. 8. Boundary layer profiles for three freestream velocities, (a) mean velocity profile, (b) streamwise Reynolds stress. DNS data by Schlatter and Örlü [30] for $Re_\tau = 1,272$

Boundary layer properties				Hot-wire acquisition		
U_∞ (m/s)	δ (mm)	u_τ (m/s)	Re_τ	l^+	ΔT^+	TU_∞/δ
9.8	59.2	0.38	1,440	30.4	0.46	1,660
20	51	0.70	2,280	55.9	1.55	3,920
30	49	1	3,130	79.9	3.2	6,120

TABLE II. Boundary layer characteristics and hot-wire acquisition properties for the non-actuated cases at a development length of $x_{dev} = 3.0m$. l^+ and ΔT^+ are the non-dimensional wire length and acquisition time step respectively. the sampling time (T) is non-dimensionalized with the number of boundary layer turn-overs.

[1] P. Ricco, M. Skote, and M. A. Leschziner, A review of turbulent skin-friction drag reduction by near-wall transverse forcing, Progress in Aerospace Sciences **123**, 100713 (2021).
[2] P. Ricco, Modification of near-wall turbulence due to spanwise wall oscillations, Journal of Turbulence **5**, 024 (2004).
[3] W. J. Jung, N. Mangiavacchi, and R. Akhavan, Suppression of turbulence in wall-bounded flows by high-frequency spanwise oscillations, Physics of Fluids A: Fluid Dynamics **4**, 1605 (1992).

[4] F. Laadhari, L. Skandaji, and R. Morel, Turbulence reduction in a boundary layer by a local spanwise oscillating surface, Physics of Fluids **6**, 3218 (1994).

[5] P. Ricco and S. Wu, On the effects of lateral wall oscillations on a turbulent boundary layer, Experimental Thermal and Fluid Science **29**, 41 (2004).

[6] D. Gatti and M. Quadrio, Reynolds-number dependence of turbulent skin-friction drag reduction induced by spanwise forcing, Journal of Fluid Mechanics **802**, 553 (2016).

[7] G. G. Stokes, On the effect of the internal friction of fluids on the motion of pendulums, Transactions of the Cambridge Philosophical Society **4** (1851).

[8] M. Quadrio, P. Ricco, and C. Viotti, Streamwise-travelling waves of spanwise wall velocity for turbulent drag reduction, Journal of Fluid Mechanics **627**, 161 (2009).

[9] J. Kim and F. Hussain, Propagation velocity and space-time correlation of perturbations in turbulent channel flow, NASA STI/Recon Technical Report N , 25082 (1992).

[10] F. Auteri, A. Baron, M. Belan, G. Campanardi, and M. Quadrio, Experimental assessment of drag reduction by traveling waves in a turbulent pipe flow, Physics of Fluids **22**, 115103 (2010).

[11] J. Bird, M. Santer, and J. F. Morrison, Experimental control of turbulent boundary layers with in-plane travelling waves, Flow, Turbulence and Combustion **100**, 1015 (2018).

[12] I. Marusic, D. Chandran, A. Rouhi, M. K. Fu, D. Wine, B. Holloway, D. Chung, and A. J. Smits, An energy-efficient pathway to turbulent drag reduction, Nature Communications **12**, 10.1038/s41467-021-26128-8 (2021).

[13] R. Deshpande, D. Chandran, A. J. Smits, and I. Marusic, The relationship between manipulated inter-scale phase and energy-efficient turbulent drag reduction, Manuscript in preparation, Journal of Fluid Mechanics (2022).

[14] D. Chandran, A. Zampiron, A. Rouhi, M. K. Fu, D. Wine, B. Holloway, A. J. Smits, and I. Marusic, Turbulent drag reduction by spanwise wall forcing. part 2: High-reynolds-number experiments, Manuscript in preparation, Journal of Fluid Mechanics (2022).

[15] C. Viotti, M. Quadrio, and P. Luchini, Streamwise oscillation of spanwise velocity at the wall of a channel for turbulent drag reduction, Physics of Fluids **21**, 10.1063/1.3266945 (2009).

[16] M. Quadrio and P. Ricco, Critical assessment of turbulent drag reduction through spanwise wall oscillations, Journal of Fluid Mechanics **521**, 251 (2004).

[17] J.-I. Choi, C.-X. Xu, and H. J. Sung, Drag reduction by spanwise wall oscillation in wall-bounded turbulent flows, AIAA Journal **40**, 842 (2002).

[18] M. Quadrio and P. Ricco, The laminar generalized stokes layer and turbulent drag reduction, Journal of Fluid Mechanics **667**, 135 (2011).

[19] A. Yakeno, Y. Hasegawa, and N. Kasagi, Spatio-temporally periodic control for turbulent friction drag reduction, in *Sixth International Symposium on Turbulence and Shear Flow Phenomena* (Begel House Inc., 2009).

[20] M. Skote, Comparison between spatial and temporal wall oscillations in turbulent boundary layer flows, Journal of Fluid Mechanics **730**, 273 (2013), edition: 2013/07/30.

[21] A. Cimarelli, B. Frohnapfel, Y. Hasegawa, E. De Angelis, and M. Quadrio, Prediction of turbulence control for arbitrary periodic spanwise wall movement, Physics of Fluids **25**, 075102 (2013).

[22] M. Mishra and M. Skote, Drag reduction in turbulent boundary layers with half wave wall oscillations, Mathematical Problems in Engineering **2015**, 10.1155/2015/253249 (2015).

[23] J. Westerweel and F. Scarano, Universal outlier detection for PIV data, Experiments in fluids **39**, 1096 (2005).

[24] K. A. Chauhan, P. A. Monkewitz, and H. M. Nagib, Criteria for assessing experiments in zero pressure gradient boundary layers, Fluid Dynamics Research **41**, 021404 (2009).

[25] H. M. Nagib and K. A. Chauhan, Variations of von kármán coefficient in canonical flows, Physics of Fluids **20**, 101518 (2008).

[26] A. J. Musker, Explicit expression for the smooth wall velocity distribution in a turbulent boundary layer, AIAA Journal **17**, 655 (1979).

[27] K.-S. Choi, Near-wall structure of turbulent boundary layer with spanwise-wall oscillation, Physics of Fluids **14**, 2530 (2002).

[28] I. Marusic, R. Mathis, and N. Hutchins, High reynolds number effects in wall turbulence, International Journal of Heat and Fluid Flow **31**, 418 (2010).

[29] R. L. Panton, Overview of the self-sustaining mechanisms of wall turbulence, Progress in Aerospace Sciences **37**, 341 (2001).

[30] P. Schlatter and R. Örlü, Assessment of direct numerical simulation data of turbulent boundary layers, Journal of Fluid Mechanics **659**, 116 (2010).

[31] A. J. Smits, B. J. McKeon, and I. Marusic, High–reynolds number wall turbulence, Annual Review of Fluid Mechanics **43** (2011).

[32] N. Hutchins and I. Marusic, Evidence of very long meandering features in the logarithmic region of turbulent boundary layers, Journal of Fluid Mechanics **579**, 1 (2007).

[33] N. Hutchins, T. B. Nickels, I. Marusic, and M. S. Chong, Hot-wire spatial resolution issues in wall-bounded turbulence, Journal of Fluid Mechanics **635**, 103 (2009), edition: 2009/09/10.

8

Supplementary results

This chapter presents supplementary results to the paper outlined in the previous chapter. The aim of this chapter is to address the remaining sub-questions of research question 3 that were not elucidated in the paper. An overview of the stereo particle image velocimetry (PIV) experiment is provided in Section 8.1. The drag reduction (DR) response to the characteristics actuation parameters is discussed in Section 8.2. This is followed by the investigation into the spatial transient of DR. Section 8.4 discusses spectral analysis to assess the scale-specific influence on the streamwise turbulence kinetic energy (TKE). Lastly, Section 8.5 elaborates on the validity of the PIV data with regard to the aforementioned reflections.

8.1. Overview of the measurements

This section presents an overview of the measurements performed on the spatial spanwise excitation setup (SSES) prototype. Chapter 7 discussed the results obtained using stereo PIV from the field of view (FOV) centred over the central two belts, hereafter named FOV2. For the supplementary results, we consider an additional four FOVs, which are depicted in Figure 8.1. FOV1, also referred to as the 'full-belts view', is centred over all four belts. To increase the resolution in the near-wall region, the 'zoomed-belts view' of FOV2, FOV3, and FOV4 are considered. As mentioned above, FOV2 captures the central two belts. FOV3 and FOV4 capture the first and fourth belts and a region down- and upstream of the actuation surface. FOV5 was used to capture and characterise the complete BL. Details on imaging properties of the five FOVs are presented in Table 8.1. A picture of the experimental setup used in the stereo PIV experiments is presented in Figure 8.2.

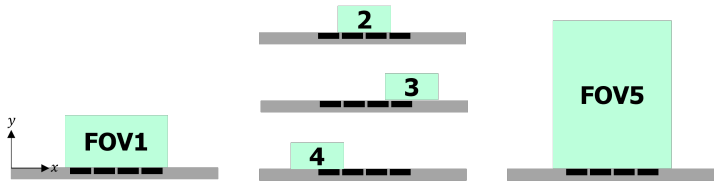

Figure 8.1: Schematic representation of the considered FOVs for the stereo PIV measurements

FOV#	size $x \times y$ (mm^2)	Resolution (px/mm)	Focal length (mm)	F-stop	Camera angle (°)
FOV1	47×17.5	60	200	11	30
FOV2	24×14.5	113	200 + 2× teleconverter	11	30
FOV3	24×14.5	113	200 + 2× teleconverter	11	30
FOV4	24×14.5	113	200 + 2× teleconverter	11	30
FOV5	98.5×69	26	105	11	35

Table 8.1: Overview of the five FOVs used in the PIV experiments.

In addition to the stereo PIV measurements discussed in the Chapter 7, hot-wire anemometry (HWA) measurements were also performed. These measurements were used to characterise the flow modulation

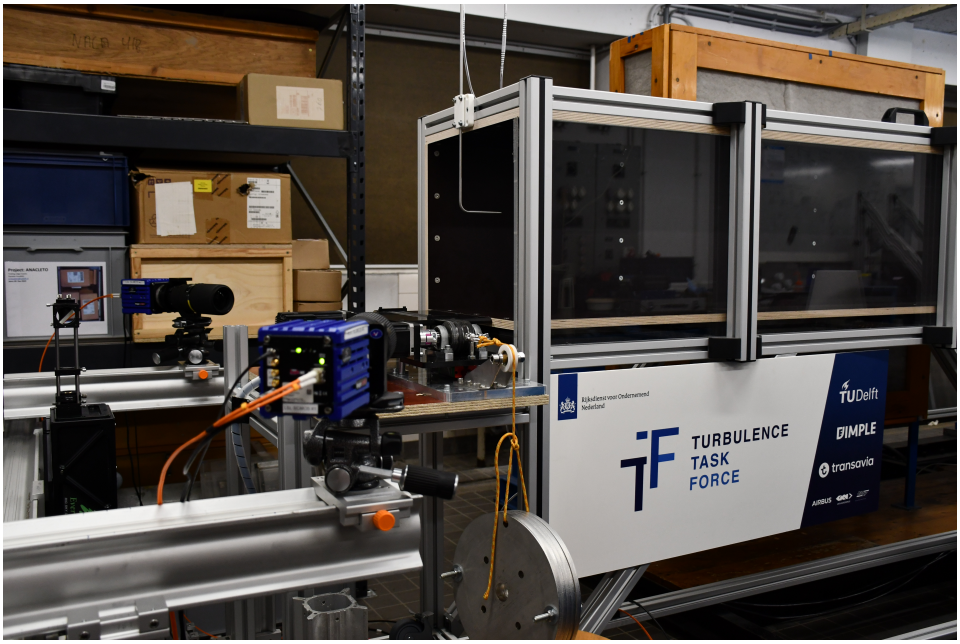

Figure 8.2: A picture of the experimental setup of the PIV experiments

effects and spectral analysis. The HWA acquisition system of DUT was used, with the same setup as used in Part II, further details on the methodology can be found in Section 4.4. All HWA measurements were made at 3 mm downstream of the last belt. For an overview of the PIV measurements, details on the acquisition, and additional results, the reader is referred to Appendix B to Appendix D.

8.2. Drag characteristics

This section presents additional drag characteristics of the (SSES) prototype. These additional results were omitted from Chapter 7 because at higher freestream velocities, i.e. higher λ_x^+, the DR estimate in FOV2 showed large deviations and uncertainties. Therefore this section focuses on FOV1, where the DR estimate was more reliable. The additional DR estimates from the other FOV2 can be found in Section D.4. DR estimation was performed in the same way as in Chapter 7, fitting the region $3 \leq y^+ \leq 5.5$ to the linear profile $u^* = y^*$.

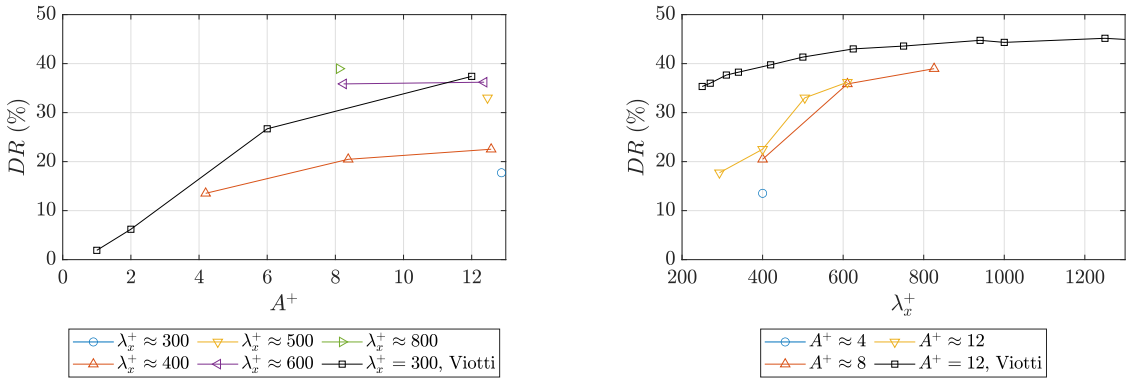

(a) DR response with A^+

(b) DR response with λ_x^+

Figure 8.3: DR characteristics for FOV1, DNS data for sinusoidal forcing by Viotti et al. (2009) is added as reference.

The results are depicted in Figure 8.3, with respect to A^+ and λ_x^+. The results of Viotti et al. (2009), which show the DNS data for a sinusoidal waveform, are added to the graphs for reference. Analysing Figure 8.3a, it

can be observed that the DR is increasing at a decreasing rate with A^+, in line with expectations from literature (Quadrio and Ricco, 2004; Viotti et al., 2009). The DR margin is lower compared to the results of Viotti et al. (2009), especially at higher values of A^+. Again, this is attributed to the experimental implementation of the forcing and the fact that the measurement region is likely still within the rising spatial transience of DR. In addition, it seems that the DR is less sensitive to A^+ at higher values; the rise in DR between $A^+ = 8$ and 12 is much less compared to the numerical results. Which may result from the flow responding differently to square-wave actuation compared to sinusoidal forcing.

A positive correlation between wavelength and DR can also be observed, which is further highlighted in Figure 8.3b. The behaviour for $\lambda_x^+ \leq 500$, shows a quick rise in DR, which deviates from the numerical trend. After this point, the qualitative trend of literature is matched, at a 10-15% lower DR margin compared to the numerical results.

8.3. Spatial transient of drag reduction

This section presents the spatial transient of DR over the belts. This section aims to compare qualitatively to the spatial DR investigation of Ricco and Wu (2004). They have shown for OW forcing that the DR rises to a steady state maximum in a spatial extent of $x/\delta \approx 3$ after the start of actuation. After the actuation stops, the DR rapidly declines to zero within 2δ. Further theoretical background on the spatial of transient can be found in Subsection 3.3.3. The case $\lambda_x^+ = 400$ is considered in this analysis. The origin is placed 1 mm upstream of the leading edge of the first belt. The spatial extent of the four belts spans around 0.6δ.

The first four FOVs are considered in this analysis. FOV1 only imaged the fields across the belts, without capturing the up- or downstream regions. FOV2, 3 and 4 are combined to show 0.2δ up- and downstream of the actuation surface. To estimate the DR, mean streamwise velocity profiles is averaged over a 0.5 mm streamwise sections. Following this, u_τ is estimated using the method from the paper: by fitting the region $3 \leq y^+ \leq 5.5$ the linear profile. The DR can now be calculated in two ways. Firstly, referencing the 'global' $u_{\tau 0}$, obtained from the composite boundary layer fit of the mean velocity profile, spanning the complete streamwise FOV. Secondly, using the 'local' $u_{\tau 0}$, which is estimated by fitting the local streamwise region of the non-actuated case to the linear sublayer profile. The results for the spatial transience are depicted in Figure 8.4. Figure 8.4a and Figure 8.4c shows scaling with the global $u_{\tau 0}$, for FOV1 and FOV2-4 respectively, Figure 8.4b and Figure 8.4d displays local-scaling. Note that for global-scaling, the non-actuated case is displayed to indicate the variance $u_{\tau 0}$ over the spatial extent.

From the results, it can be observed that there are significant differences in estimated DR for both scaling methods and FOVs. When global scaling is applied, the DR has significant streamwise variations, i.e. u_τ, for the non-actuated case. An explanation could be that the DR is estimated for a fixed wall-normal location obtained from the mean profiles. The wall location is estimated using a linear relation in the streamwise direction (details can be found in Appendix C). Hence slight local variations (e.g. a belt located slightly below or above the wall) in wall location are not accounted for. To overcome this effect, local-scaling can be applied. However, this method also does not highlight any trends, and there are large variations between the FOVs. Furthermore, for FOV1, there are outliers or large spikes in the local $u_{\tau 0}$ estimate, resulting in prominent spurious peaks in the DR. Based on these findings, the results of the spatial transience of DR are inconclusive, and a comparison to the work of Ricco and Wu (2004) can not be made. For future research, it is advised to investigate a different method for estimating the local DR effects. For example, by doing local HWA measurements.

However, a number of observations are still interesting to discuss. As expected, the DR is positively correlated with A^+. It can be observed that the DR values for A^+ are quite close over the first belt. This difference starts growing when moving downstream over the actuation surface. Secondly, the DR locally spike in regions around the leading and trailing edges of the belts. Based on the findings of Touber and Leschziner (2012) and Agostini and Leschziner (2014), this behaviour is expected, which showed that regions of high skin friction reduction are correlated with a high rate of change of the spanwise Stokes strain (i.e. where the belts change direction). A third finding, which is somewhat trivial, is that the DR decreases again after the actuation surface. The downstream extent is not large enough to see the recovery back to the non-drag-reduced state.

It is interesting to evaluate the scalar-fields of the streamwise Reynolds stress since a reduction in the near-wall peak indicates a drag-reduced state. From the space-averaged profiles in Chapter 7, a significant reduction in the near-wall peak could be observed while shifting to higher wall-normal locations under actuation. Figure 8.5 shows the scalar fields of the $\langle u'^2 \rangle^+$ for the non-actuated and the two actuated cases in FOV1.

The characteristic near-wall peak around $y^+ = 15$ can be observed in the non-actuated case. In line with the previous findings, under actuation, the energy peak is significantly reduced and shifted upwards within the region over the first belt. A steady-state energy state is reached after the first belt. Hence, it can be concluded that the TKE response does not follow the transient of DR expected to rise up to $\sim 3\delta$. This suggests that the DR lags behind and follows in response to the energy-reduced steady-state.

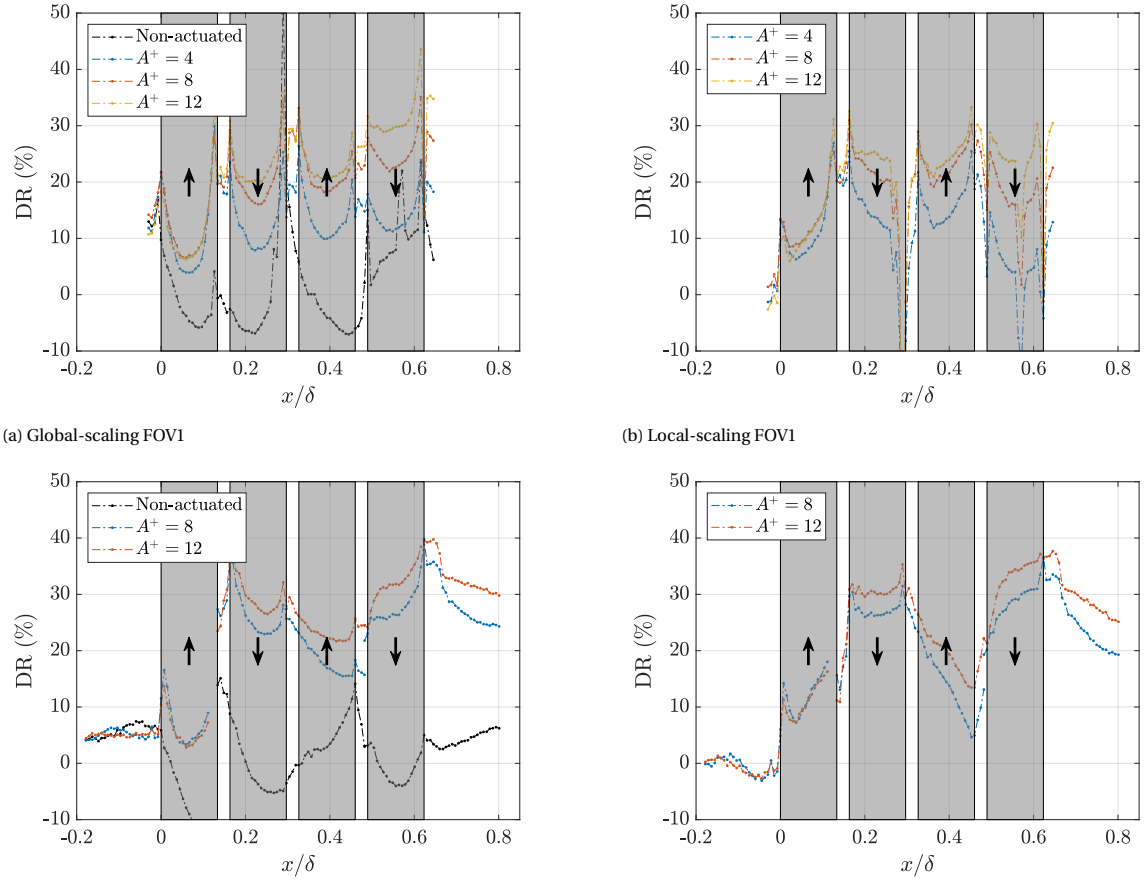

(a) Global-scaling FOV1

(b) Local-scaling FOV1

(c) Global-scaling FOV2-4

(d) Local-scaling FOV2-4

Figure 8.4: Spatial transience of DR for $\lambda_x^+ = 400$.

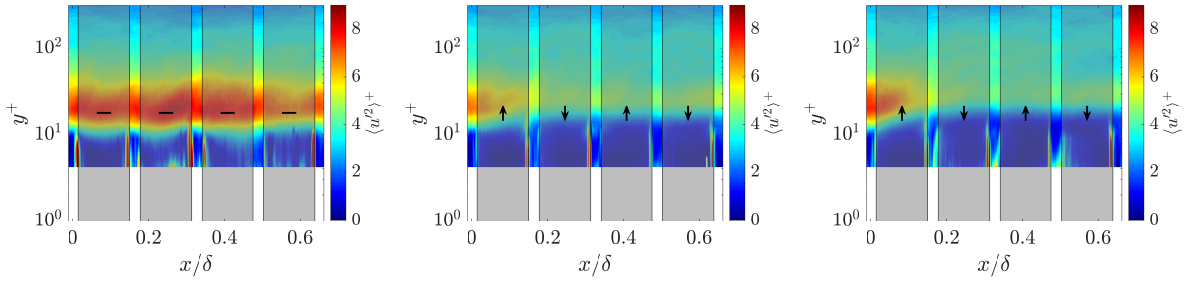

(a) Non-actuated

(b) $A^+ = 8.4$

(c) $A^+ = 12.6$

Figure 8.5: Scalar-fields of the streamwise normal stress for FOV1 at $\lambda_x^+ = 400$

8.4. Spectral analysis

This section presents the spectral analysis of the SSES prototype setup to assess the effects of actuation on the inner- and outer-scaled streamwise TKE components. Measurements were performed using HWA, prior

to the PIV experiments. The HWA probe was placed 3 mm downstream of the actuation surface. The non-dimensional sampling time was $TU_\infty/\delta \approx 20{,}000$. The freestream conditions and belt speeds were not tuned to a specific set of viscous actuation parameters. The case considered here was at a freestream velocity of $U_\infty \approx 10$ m/s resulting in a $Re_\tau = 1{,}440$. For actuation, the belt speed was 4.2 m/s for the actuated case, which translates to the viscous actuation parameters: $\lambda_x^+ = 533$ and $A^+ = 11$.

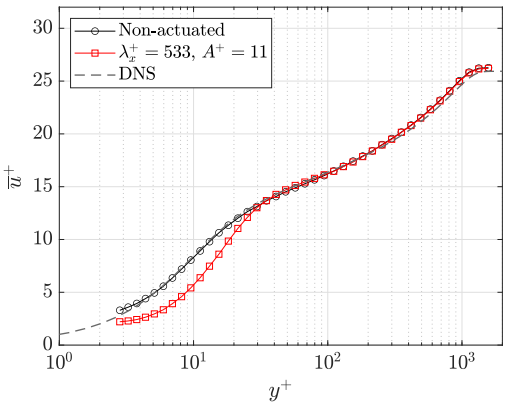

Figure 8.6: Streamwise velocity profiles for the SSES obtained with HWA. DNS data of Schlatter and Örlü (2010) at $Re_\tau = 1{,}272$

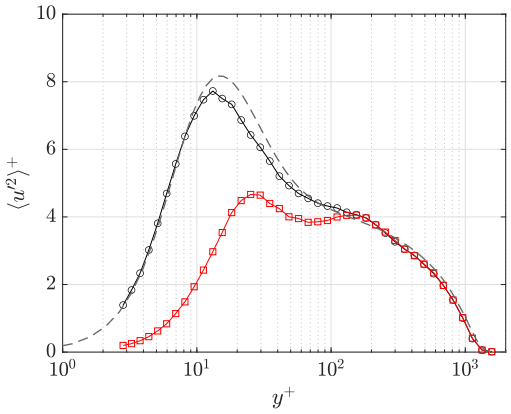

Figure 8.7: Streamwise Reynolds normal stress profile. Legend is depicted in Figure 8.6.

The mean streamwise velocity and streamwise stress profiles are presented in Figure 8.6 and Figure 8.7. In line with earlier observations, the near-wall velocity reduced under actuation, indicative of a drag-reduced state (Laadhari et al., 1994; Ricco and Wu, 2004). This is further confirmed in the streamwise stress profile, where the peak reduces significantly and is shifted to higher wall-normal locations. The boundary layer spectrograms for the two cases are depicted in Figure 8.8. In line with the observations in the streamwise stress profiles, actuation significantly reduces the energetic content of the near-wall peak by over 50%. Furthermore, the near-wall peak is shifted in the positive wall-normal direction. At this freestream velocity, the outer-scaled energy is relatively small. However, we see that the energetic content in this region is not significantly affected. Since the viscous wavelength is small, we have ISA. Hence the results are in line with the hypothesis that ISA does not affect the outer-scaled energy and only attenuated small-scale energy in the near-wall region.

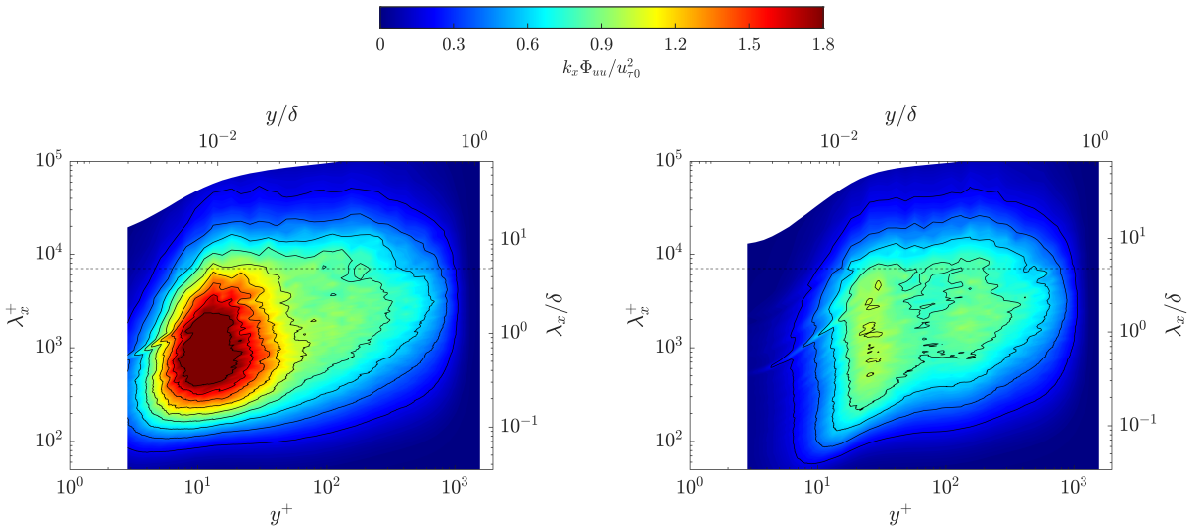

(a) Non-actuated case

(b) Actuation at $\lambda_x^+ = 504$ and $A^+ = 11.7$

Figure 8.8: Boundary layer spectrograms of the streamwise turbulence kinetic energy, scaling is done with the reference $u_{\tau 0}$ of the non-actuated case.

8.5. Validity of the PIV data

This section discusses the validity of the PIV measurements. As presented in the paper, the results indicated the presence of additional turbulence energy in the near-wall region, particularly in the streamwise and spanwise stresses. Two factors were identified as contributing to this phenomenon. Firstly, the complexity of the actuation surface with discrete changes in roughness and small spanwise cavities in combination with the observed belt vibrations. Secondly, despite efforts to filter them out, strong unsteady reflections were found in the PIV data, which affected the spanwise stress in particular. Examples of these reflections in the raw and pre-processed images can be found in Figure C.2. In this section, the influence of these reflections is further elucidated.

To examine the potential impact of reflections, scalar-fields of the spanwise stress are presented in Figure 8.9. The wall-normal region from 0-2 mm, where reflections are most significant, is displayed. The same cases discussed in the paper, with $\lambda_x^+ \approx$400, 600, and 800 at $A^+ \approx 8$, are considered. The figure shows noticeable peaks in the spanwise stress in the transition area between the belts and close to the wall. This effect is observed in all cases, whether actuated or non-actuated. In all instances, the peaks are visible up to a physical height of roughly 0.6 mm. However, the intensity of the peaks is so significant that they are likely spurious. As discussed in the paper, these spurious stresses are thought to arise from diffractive reflections on the edges of the spanwise surface grooves. The reflections are observed to a height of 0.5-1 mm in the wall-normal direction from the raw images, corresponding to the penetration depth of the spurious fluctuation peaks. Additionally, the stress peaks are concentrated around the transition locations where the strongest reflections occur. As discussed in the paper, these stresses mainly affect the spanwise stress because of slight spanwise variations in the reflections while the $x-y$ location remains fixed on the groove.

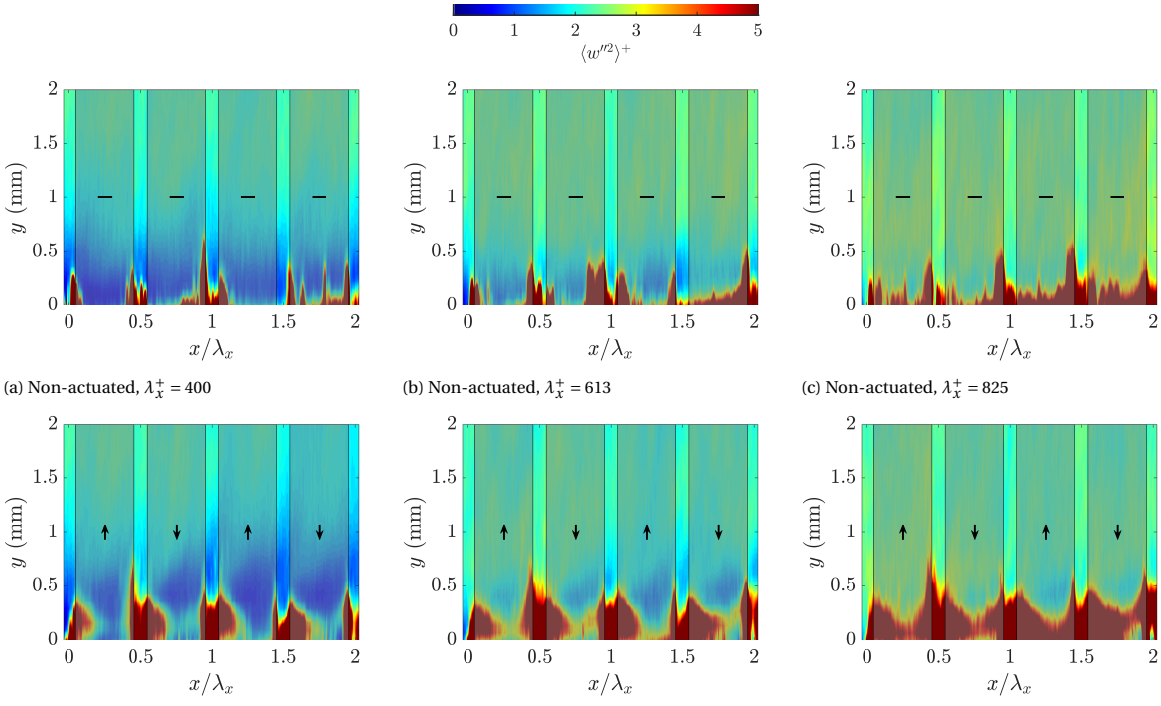

(a) Non-actuated, $\lambda_x^+ = 400$ (b) Non-actuated, $\lambda_x^+ = 613$ (c) Non-actuated, $\lambda_x^+ = 825$

(d) $\lambda_x^+ = 400$, $A^+ = 8.4$ (e) $\lambda_x^+ = 613$, $A^+ = 8.2$ (f) $\lambda_x^+ = 825$, $A^+ = 8.1$

Figure 8.9: Scalar-fields in FOV1 of the stochastic spanwise stress

To further illustrate this point, the streamwise stress scalar-fields for the same cases are shown in Figure 8.10. Local stress peaks can also be observed around the leading and trailing edges of the belts. However, the effect is more localised and much smaller in magnitude. It is worth noting that, especially for the streamwise stress, distinguishing between the influence of the mechanical implementation and spurious stresses resulting from reflections is not possible.

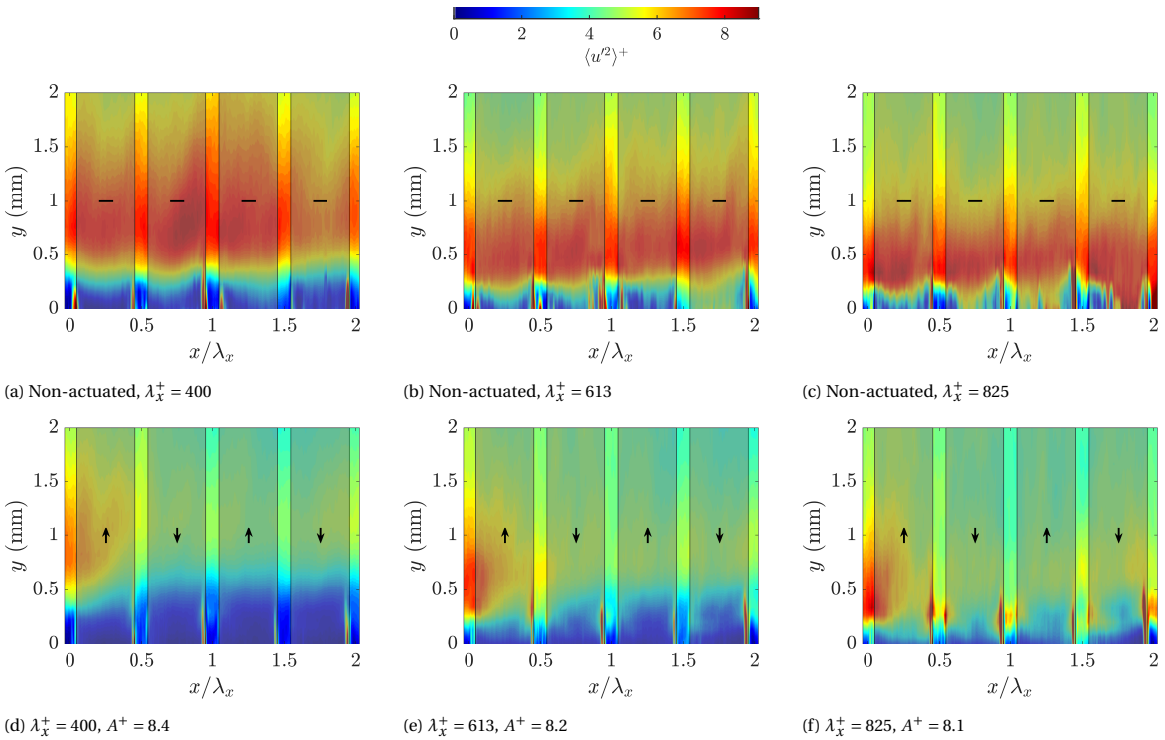

(a) Non-actuated, $\lambda_x^+ = 400$ (b) Non-actuated, $\lambda_x^+ = 613$ (c) Non-actuated, $\lambda_x^+ = 825$

(d) $\lambda_x^+ = 400$, $A^+ = 8.4$ (e) $\lambda_x^+ = 613$, $A^+ = 8.2$ (f) $\lambda_x^+ = 825$, $A^+ = 8.1$

Figure 8.10: Scalar-fields in FOV1 of the streamwise stress

Through this analysis, it has been demonstrated that reflections are likely the reason for the additional stresses noticed in the near-wall area. However, this discovery does not impact the key findings or conclusions of this research, as the affected region is confined to the near-wall region. As a result, the drag-reduced flow characteristics can still be observed, and the prototype remains a valid demonstration of the aerodynamic workings. While the mean profiles are unaffected, caution should be exercised while interpreting data in the $y \leq 0.6$ mm region, particularly in the DR estimate that relies on the region $3 \leq y^+ \leq 5.5$. Figure 8.11 illustrates the impact of excluding measurements from the $y \leq 0.6$ mm region on the data from FIG. 7 of Chapter 7. It is clear that a significant portion of the near-wall area is lost. Despite this, the drag-reduced flow characteristics are still observable, with both the streamwise and spanwise stresses exhibiting a considerable reduction in energy up to a $y^+ = 100$ region.

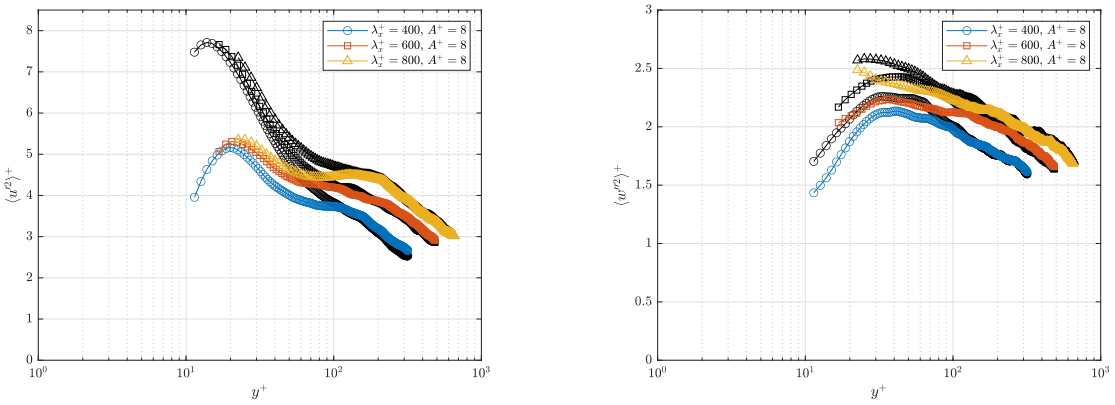

(a) Streamwise Reynolds stress (b) Stochastic component of the spanwise Reynolds stress

Figure 8.11: Recreation of FIG. 7. from the paper excluding measurements in the region $y \leq 0.6$ mm

9

Concluding remarks

This chapter presents the concluding remarks for Part III of this investigation. The relevant research questions are first discusses, followed by discussion of the findings.

9.1. Research questions

This section addresses the research questions that are related to Part III of the thesis, which are, question (1c) and (2).

1. **To what extent can outer-scaled flow structure modulation effects through spatial periodic forcing be experimentally investigated within the available resources?**

   (c) *How can spatial periodic forcing be realised using an experimental active flow control setup? To what extent are the wave parameters controllable? Can such a setup theoretically target the outer-scaled flow structures in the present experimental conditions?*
   Spatial periodic forcing can be realised experimentally with a series of spanwise running belts generating a square waveform forcing. A setup with spanwise running belts allows independent control over the characteristic actuation parameters: the streamwise wavelength and spanwise velocity amplitude. The spanwise velocity is simply controlled by the belt velocity. The wavelength can be changed by changing either the viscous scaling or the physical wavelength. Having multiple belts run in the same direction can change the physical wavelength. This way, the wavelength can be increased to perform OSA.

3. **What are the flow modulation effects associated with active spatial periodic forcing?**

   (a) *Are there undesired effects on the turbulence and skin friction of the experimental setup due to the physical implementation of spatial periodic forcing?*
   At higher values of freestream velocity and physical belt speed, vibrations of the belt on the actuation surface were identified. Furthermore, when the freestream velocity is increased, the gaps around the belts increase in viscous scales. These two effects combined may have a secondary influence on the aerodynamics in the near-wall region. The diffractive reflections on the spanwise grooves also negatively impacted the PIV data quality in the near-wall region. It was not possible to separate the potential secondary influence of the complexity of the surface due to the mechanical implementation from the reflections.

   (b) *What is the effect of the characteristic wave parameters A^+ and λ_x^+ on the mean streamwise velocity and stress profiles? Can a drag-reduced state be observed? How does the behaviour relate to the existing literature?*
   Under actuation, the mean streamwise velocity profile scaled with $u_{\tau 0}$, shows a decreased velocity in the region $y^+ \leq 15$. An upward shift of the logarithmic region is observed when scaling with u_τ, both findings are indicative of a drag-reduced state. The intensity of these effects is positively correlated with A^+. Further evidence of the drag-reduced state is found when assessing the Reynolds stresses. Specifically, the streamwise stress shows a significant energy reduction in the

region $y^+ \leq 100$, and the near-wall peak is shifted to higher wall-normal locations. Qualitatively, the DR characteristics showed similar trends to the work of Viotti et al. (2009), albeit at a lower DR margin. This is attributed to the experimental realisation of the forcing and the fact that the actuation surface is likely still within the rising transience of DR.

(c) *How are the small- and large-scale structures affected in terms of turbulence kinetic energy?*
Spectral analysis has shown a large reduction of the inner-scaled energetic peak. The outer-scales were not significantly affected, which is expected since ISA is performed in the measurements.

(d) *What are the downstream effects of the actuation? Over what spatial extent can a drag-reduced state be observed? How does this compare to the results of Ricco and Wu (2004)?*
The results on the spatial transience of DR showed substantial variation for different FOVs and scaling approaches. With a similar large variance in the non-actuated case, the results are inconclusive. Therefore, a comparison to the results of Ricco and Wu (2004) could not be made. This is attributed to the fact that the DR is estimated from a fixed in wall-normal region. This method does not account for local variations in the wall-height, likely resulting in spurious DR estimates. Evaluating the scalar-fields revealed that an energy-reduced state shows a shorter spatial transient to a steady state compared to the expected DR transient in the work of Ricco and Wu (2004).

(e) *Can a spatial Stokes layer be observed? How do the spanwise velocity profiles compare to the laminar solution? What is the penetration depth of the Stokes layer?*
A Stokes-like spanwise velocity profile could be observed. High rates of change of the spanwise Stokes strain were observed in the transition region where the belts change direction. A comparison of the modified laminar solution for square wave forcing shows qualitative similarity. With an almost exact match in the region $y^+ \leq 10$. This means the model can be used to estimate the power input to drive the spanwise profile. In the region $y^+ \geq 10$, the experiments show an overshoot that is slightly larger in magnitude and pertains to a deeper wall-normal location. The penetration depths compared well with $\delta^+_{s,exp} = 4.8$ and $\delta^+_{s,mod} = 5.0$.

9.2. Discussion of the findings

Part III of the thesis provided a proof of concept for the experimental realisation of steady spanwise forcing of the turbulent boundary layer using a series of spanwise running belts. The concept was found to be effective at realising a significant flow control effect for turbulent drag reduction. Showing a drag-reduced flow state, with a reduction of streamwise velocity close to the wall, and strong attenuation of the turbulent statistics. A maximum DR estimate of 39% was made. These results offer perspective for further research into the flow mechanisms and the response to the governing actuation parameters.

Despite demonstrating a significant flow control effect, the PIV measurements were subject to spurious stress measurements, most likely caused by strong reflections. Moreover, it was unclear whether these stresses resulted solely from the reflections or whether a secondary aerodynamic effect of the mechanical implementation was also involved. Several measures can be taken to avoid spurious measurements in future experiments and to isolate the possible effects from the mechanical implementation. Firstly, it is advised to perform HWA measurements, negating the influence of reflections altogether. Furthermore, this has the added advantage of enabling the identification of scale-specific turbulence statistics through spectral analysis. When PIV measurements are preferred, stereo PIV imaging can be conducted in the $y-z$ plane. Where the laser sheet will not exhibit diffractive reflections on the sharp edges of the spanwise surface grooves. However, imaging in this plane has the drawback of only providing the stochastic component of the spanwise stress, as the phase-wise component is obtained by taking the variance of the spanwise profiles over the streamwise extent. In addition, the surface finish of the aluminium surface plate, which is still reflective despite being anodised, can be improved to reduce reflections. This can be achieved by applying a light sandblasting before anodising to create a more matt finish. Another option is to perform HWA measurements,

In light of the current prototype's effectiveness, recommendations for a follow-up full-scale experimental setup are worth discussing. It is important to note that the streamwise extent of the actuation surface is small, which suggests that the DR may still be within its rising spatial transient. To better understand both this transient and the steady-state DR characteristics, it would be valuable to increase the streamwise extent of the actuation surface to be in the order of 10δ. Additionally, it would be advisable to widen the belt width, to bring the actuation wavelength closer to the ISA optimum found in literature, around $\lambda^+_x = 1,000 - 1,250$ (Viotti et al., 2009), while keeping the freestream velocities modest.

With a full-scale setup, it is also valuable to investigate the new OSA pathway. This can be achieved by increasing the actuation wavelengths in the order of $\lambda_x = \mathcal{O}(\delta)$. Larger physical wavelengths can be attained by having multiple belts run in the same spanwise direction, resulting in a larger square wave. The efficacy of 'adding' multiple belts for a larger wave should be investigated. With a high rate of change of the stokes strain being an important driver behind the DR (Touber and Leschziner, 2012; Agostini and Leschziner, 2014), the question remains how effective this may be. Since the square wave forcing only has significant phase-wise changes in the spanwise Stokes stain in the region at discrete locations where the wave changes from the positive to the negative half of the phase. There will be fewer of these abrupt phase-wise variations for larger wavelengths, in contrast to perfect sinusoidal forcing, which varies throughout the phase. However, due to the mechanical implementation with the small transition areas between belts, there are still smaller strain rate changes between belts.

IV

Conclusions, recommendations and future outlook

10

Conclusions

Recall that this thesis is part of a larger research project that envisions: *the development of passive flow control techniques for turbulent drag reduction that can reliably be applied in practical applications.* This research is motivated by the urgent need to address the rising global CO2 emissions, aiming to reduce fuel burn in aviation and other industries. By setting this goal, the research intends to contribute to a more sustainable planet for current and future generations. This thesis marks the first steps towards this project goal. The conclusions of this work reflect on the research philosophy as proposed in the introduction (Section 1.2). Subsequently, the key findings and general conclusions of the main body of the thesis are shortly discussed. In-depth concluding remarks, answers to the specific research questions and discussion on the findings can be found in: Chapter 6 and Chapter 9, for Part II and Part III, respectively.

A new development methodology was proposed in light of the overarching project goal. The central idea is to study active flow control, learning the key mechanisms and drivers behind the DR, and applying this knowledge to further develop passive techniques. This rationale is combined with the newly introduced outer-scaled actuation (OSA) pathway. In contrast to conventional flow control, OSA shows a positive correlation between drag reduction (DR) and Re_τ, making it an attractive alternative for industry applications operating at high Reynolds numbers, like aviation or long-distance pipe flows. In light of this methodology, spanwise forcing was found to be the active flow control technique of interest. Specifically spatial spanwise forcing since this is the closest analogy to a passive counterpart.

Three passive techniques for OSA spanwise forcing were considered in this thesis: dimples, sinusoidal undulations (SUs) and oblique wavy walls (OWWs). All techniques are hypothesised to create a spatially varying spanwise velocity profile through geometric surface deformations, which is how the analogy to active spatial forcing is made. Balance measurements were performed on eight designs, that were realised in a series of test plates (TPs). A modest DR was found for three designs, one plate with staggered SUs (TP0004) and two OWW designs (TP0007 & TP0012). It is hypothesised that effective OSA using these TPs would result in an increased DR margin when increasing Re_τ. The Reynolds number scaling of these three TPs was promising, showing an additional friction reduction when Re_τ is increased. However, the results are inconclusive due to the changes in drag with Re_τ almost solely resulting from the pressure correction and the drag changes being within the 95% confidence interval. Furthermore, only a modest outer-scaled flow modulation effect was expected since the outer-scales are still small in magnitude at the considered Reynolds numbers.

The scale-specific influence of the streamwise turbulence kinetic energy (TKE) was assessed by performing spectral analyses using hot-wire anemometry (HWA). The boundary layer spectrogram revealed that the staggered SUs reduce the energetic content of the outer-scaled peak. Even though the energy reduction is small, this can be regarded as possible evidence of effective OSA. In addition, TP0007 showed a reduction of TKE in the region between the two characteristic peaks.

An idea for an experimental setup named the steady spanwise excitation setup (SSES) was proposed in this work. The setup realises spatial spanwise forcing by applying a steady wall forcing using a series of streamwise spaced, spanwise running belts. The spanwise running belts run in alternating positive and negative spanwise to generate a spatial square wave forcing. The simplification of using square waves was

justified by the studies of Cimarelli et al. (2013) and Mishra and Skote (2015), who showed substantial DR and net-power saving values could be obtained using non-sinusoidal forcing. A prototype SSES was realised for this thesis work using four spanwise running belts. The aim of this setup was a proof of concept of the aerodynamic working and to test the flow modulation effects. Due to the limited spatial extent of the actuation surface, the prototype could only be applied to ISA. Besides being of interest to the research philosophy, this proof of concept also addresses a research gap where this is the first experimental realisation of spatial forcing in external flows.

The flow modulation effects and effectiveness of the prototype were investigated using stereo particle image velocimetry (PIV). Evidence of a drag-reduced flow state is presented, with the mean-velocity reducing in the viscous sublayer when scaling with $u_{\tau 0}$. The DR is positively correlated at a decreasing rate with the spanwise velocity amplitude of actuation (i.e. belt actuation velocity), in line with earlier observations from literature (Viotti et al., 2009). From the experiments, a maximum DR value of 39% was found. The influence of actuation on the turbulence statistics shows further evidence for DR, where the stresses are significantly attenuated to and shifted to a higher wall-normal location, in agreement with earlier findings of spanwise forcing (Laadhari et al., 1994; Ricco and Wu, 2004; Chandran et al., 2022). Even though the qualitative results on the spatial transient of DR were inconclusive, an interesting finding is made. Evaluating the scalar-field of the streamwise stress suggests that the DR transient lags behind the steady state energy reduction, which is already reached after the first belts. The experimental spanwise profiles are compared to a modified model for the Stokes layer that accounts for the square waveform forcing. The experiments indeed show Stokes-like spanwise velocity profiles. Qualitatively, the experiments agree with the model, with an almost exact match in the region $y^+ \leq 10$. Therefore, the proposed model is useful for estimating the idealised power input to drive the Stokes layer. The penetration depths of the Stokes layer of the model and experiments are also in agreement.

Reflecting on the work, this study has made significant steps in the right direction towards the overarching research objective. The newly proposed research philosophy presents a promising pathway towards developing effective and reliable passive flow control techniques in practical applications. Specifically, focusing on OSA is found to be a good choice. The positive correlation between Re_τ and DR is attractive for applications operating at high Reynolds numbers, like shipping, long-distance pipeflows and the aviation industry. The first evidence of an outer-scaled energy reduction using a passive technique sparks hope for the research philosophy. Furthermore, the proof of concept of the SSES shows that the proposed method shows good potential as an active flow control technique. However, it is essential to keep in mind that this is just the beginning, and there is still a long way to go. To further advance the development, the focus should be shifted to uncovering the essential working mechanics through investigating OSA with a full-scale realisation of the SSES. This is elucidated in Chapter 11, which discusses recommendations and a future outlook for follow-up research.

11

Recommendations and future outlook

This section presents the recommendations based on the findings of this research. Following these recommendations, the future outlook for the overarching research project is shortly discussed.

11.1. Recommendations

The outer-scale actuation (OSA) pathway is central to the proposed research philosophy. However, In the current experiments, the outer-scaled energy peak was still small in magnitude. Therefore, it is recommended to increase the frictional Reynolds numbers to the range $Re_\tau = \mathcal{O}(1 \times 10^5)$. The criterion on the viscous length scale for flow measurement techniques should be kept in mind. Hence, the Reynolds number should primarily be attained by extending the development length.

The first findings of OSA in Part II are promising. A set of recommendations is presented for future research on outer-scaled passive spanwise forcing. In this work, only the TPs that showed a modest drag reduction (DR) were subject to a detailed investigation. It is deemed valuable to also investigate the TPs that showed a small drag increase. In line with the hypothesised Re_τ scaling for OSA, these plates may result in a net DR at higher Reynolds numbers. The reduction in outer-scaled energy of the staggered sinusoidal undulations (SUs) may be regarded as possible evidence of effective OSA using this technique. However, the energy reduction is small in magnitude. To strengthen this evidence, it is recommended to perform further studies. By increasing the frictional Reynolds number, the hypotheses could be tested that there is a larger outer-scaled energy reduction as Re_τ is increased. Furthermore, the influence on inter-scale interaction between the outer-layer and the near-wall region can be investigated by performing synchronous two-probe hot-wire anemometry (HWA) in the two respective regions.

The proof of concept for the experimental setup in Part III showed a significant flow control effect. Therefore, creating a full-scale experimental setup that allows for OSA is considered a valuable next step. Recommendations are extending the streamwise actuation length in the order of 10δ, and increasing the belt width. Thereby, the spatial transient and steady-state DR can be investigated while keeping the actuation wavelength in the order of the ISA at moderate freestream velocities. Regarding OSA, it is recommended to investigate the efficacy of having a multiple of two belts that generate a waveform with an increased wavelength. From the particle image velocimetry (PIV) scalar-fields, it was found that spurious measurements from reflections could not be separated from a possible secondary aerodynamic influence. It is recommended to assess if there is any secondary aerodynamic influence by performing HWA, which removes the influence of reflections. Furthermore, the following measures are recommended to reduce the influence of reflections in future PIV experiments. Firstly, PIV can be performed in the $y-z$ plane away from the spanwise grooves. Secondly, the strength of the reflections can be reduced, by applying light sandblasting to the surface plate to create a more matt surface finish after anodisation.

A number of findings were made from the HWA experiments with the DUT and Hill acquisition systems. Recommendations are discussed to enhance the data quality for future experiments. Firstly, for the Hill system, increasing the number of sampling points in the near-wall region is recommended. Preferably a loga-

rithmically spaced sampling is employed. This way, the number of sampling points can be reduced (e.g. 40 instead of 100) while increasing the near-wall resolution. For the DUT system, it is recommended to improve the sensor mounting to prevent spurious energy peaks due to sting and probe vibrations. Regarding post-processing, the more robust boundary layer fitter of Chauhan et al. (2009) is recommended over the method of Rodríguez-López et al. (2015). The fitter only allows for correctly scaling canonical profiles; hence scaling with a non-actuated or reference u_τ is advised to highlight absolute differences. A valuable addition to the method of Chauhan et al. (2009) would be investigating the possibility of fitting non-canonical profiles (e.g. drag reduced state).

11.2. Future outlook

This section presents the future outlook for follow-up research. This thesis project's literature survey (Knoop, 2023) introduced a novel development methodology toward passive flow control. This strategy served as the backbone of the thesis project, which addressed the first steps in this development process. The method is outlined below:

1. Select an outer-scaled actuation predetermined active flow control technique that shows the potential to be translated into passive forcing.
2. Preliminary assessment of the potential to target outer-scaled flow structures for a number of passive techniques.
3. Develop the selected active flow control technique that employs outer-scaled actuation.
4. Study the working mechanism and flow modulation effects of the active technique, and note which specific forcing, modulation effects and working mechanisms are responsible for the drag reduction.
5. Use the findings from (4), to further develop a flow control technique that can recreate the desired forcing passively.

As part of the literature survey, step (1) was addressed, selecting spatial spanwise forcing as the flow control technique of interest. Subsequently, three potential passive techniques for OSA were scoped. Part II addressed step (2) with a preliminary assessment of the three selected passive techniques. Part III of the thesis work made the first developments regarding step (3) of the method. The current study showed promising results regarding steps (2) and (3). The focus should be placed on step (4), by uncovering the underlying inter-scale interaction working mechanisms using a full-scale experimental setup.

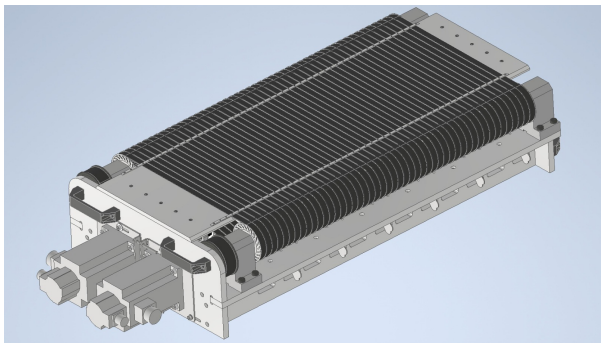

Figure 11.1: CAD schematic of the full-scale steady spanwise excitation setup.

The subsequent steps of this development methodology will be taken up in follow-up research. The next steps involve designing and producing a full-scale experimental setup, which is currently underway with the help of an external company, BerkelaarMRT. A CAD schematic of this setup is presented in Figure 11.1. The design features 48 consecutive belts with 15 mm wide belts, resulting in an actuation surface with a streamwise extent of over 75 cm. To achieve higher values of Re_τ, an experimental facility specifically for boundary layer experiments is being developed by the Delft University of Technology. This facility includes four independently moving test sections, which can attain Reynolds numbers in the order of $Re_\tau = \mathcal{O}(8,000)$. These developments represent significant progress in the field of OSA research, and with regard to the overarching project aim.

Bibliography

Abbas, A., Bugeda, G., Ferrer, E., Fu, S., Periaux, J., Pons-Prats, J., … Zheng, Y. (2017). Drag reduction via turbulent boundary layer flow control. *Science China Technological Sciences, 60*, 1281–1290. doi:10.1007/s11431-016-9013-6

Abbassi, M. R., Baars, W. J., Hutchins, N., & Marusic, I. (2017). Skin-friction drag reduction in a high-reynolds-number turbulent boundary layer via real-time control of large-scale structures. *International Journal of Heat and Fluid Flow, 67*, 30–41. doi:10.1016/j.ijheatfluidflow.2017.05.003

Abe, H., Kawamura, H., & Choi, H. (2004). Very large-scale structures and their effects on the wall shear-stress fluctuations in a turbulent channel flow up to re tau = 640. *Journal of Fluids Engineering, 126*(5), 835–843.

Agostini, L., & Leschziner, M. A. (2014). On the influence of outer large-scale structures on near-wall turbulence in channel flow. *Physics of Fluids, 26*(7), 075107. doi:10.1063/1.4890745

Agostini, L., Touber, E., & Leschziner, M. A. (2014). Spanwise oscillatory wall motion in channel flow: Drag-reduction mechanisms inferred from DNS-predicted phase-wise property variations at. *Journal of Fluid Mechanics, 743*, 606–635. doi:10.1017/jfm.2014.40

Agostini, L., Touber, E., & Leschziner, M. (2015). The turbulence vorticity as a window to the physics of friction-drag reduction by oscillatory wall motion. *International Journal of Heat and Fluid Flow, 51*, 3–15.

Akhavan, R., Jung, W., & Mangiavacchi, N. (1993). Control of wall turbulence by high frequency spanwise oscillations. In *3rd shear flow conference* (p. 3282).

Auteri, F., Baron, A., Belan, M., Campanardi, G., & Quadrio, M. (2010). Experimental assessment of drag reduction by traveling waves in a turbulent pipe flow. *Physics of Fluids, 22*(11), 115103. doi:10.1063/1.3491203

Baars, W., Hutchins, N., & Marusic, I. (2017). Reynolds number trend of hierarchies and scale interactions in turbulent boundary layers. *Philosophical Transactions of the Royal Society A: Mathematical, Physical and Engineering Sciences, 375*(2089), 20160077.

Balakumar, B., & Adrian, R. (2007). Large-and very-large-scale motions in channel and boundary-layer flows. *Philosophical Transactions of the Royal Society A: Mathematical, Physical and Engineering Sciences, 365*(1852), 665–681.

Baron, A., & Quadrio, M. (1996). Turbulent drag reduction by spanwise wall oscillations. *Applied Scientific Research, 55*(4), 311–326. doi:10.1007/bf00856638

Bird, J., Santer, M., & Morrison, J. F. (2018). Experimental control of turbulent boundary layers with in-plane travelling waves. *Flow, Turbulence and Combustion, 100*(4), 1015–1035. doi:10.1007/s10494-018-9926-2

Blackwelder, R. F. (1972). Time scales and correlations in a turbulent boundary layer. *Physics of Fluids, 15*(9), 1545. doi:10.1063/1.1694128

Blackwelder, R. F., & Kovasznay, L. S. (1972). Large-scale motion of a turbulent boundary layer during relaminarization. *Journal of Fluid Mechanics, 53*(1), 61–83.

Blesbois, O., Chernyshenko, S. I., Touber, E., & Leschziner, M. A. (2013). Pattern prediction by linear analysis of turbulent flow with drag reduction by wall oscillation. *Journal of Fluid Mechanics, 724*, 607–641. Edition: 2013/05/08. doi:10.1017/jfm.2013.165

Bradshaw, P., & Pontikos, N. (1985). Measurements in the turbulent boundary layer on an 'infinite'swept wing. *Journal of Fluid Mechanics, 159*, 105–130.

Bruun, H. H. (1996). Hot-wire anemometry: Principles and signal analysis. Publisher: IOP Publishing.

Cai, W.-H., Li, F.-C., Zhang, H.-N., Li, X.-B., Yu, B., Wei, J.-J., … Hishida, K. (2009). Study on the characteristics of turbulent drag-reducing channel flow by particle image velocimetry combining with proper orthogonal decomposition analysis. *Physics of Fluids, 21*(11), 115103.

Chandran, D., Zampiron, A., Rouhi, A., Fu, M. K., Wine, D., Holloway, B., … Marusic, I. (2022). Turbulent drag reduction by spanwise wall forcing. part 2: High-reynolds-number experiments. *Manuscript in preparation, Journal of Fluid Mechanics*.

Chauhan, K. A., Monkewitz, P. A., & Nagib, H. M. (2009). Criteria for assessing experiments in zero pressure gradient boundary layers. *Fluid Dynamics Research, 41*(2), 021404.

Chernyshenko, S. (2013). Drag reduction by a solid wall emulating spanwise oscillations. part 1. Place: Unpublished work. Retrieved from arXiv:1304.4638

Choi, H., Moin, P., & Kim, J. (1994). Active turbulence control for drag reduction in wall-bounded flows. *Journal of Fluid Mechanics*, *262*, 75–110.

Choi, J.-I., Xu, C.-X., & Sung, H. J. (2002). Drag reduction by spanwise wall oscillation in wall-bounded turbulent flows. *AIAA Journal*, *40*(5), 842–850. doi:10.2514/2.1750

Choi, K. S., & Graham, M. (1998). Drag reduction of turbulent pipe flows by circular-wall oscillation. *Physics of Fluids*, *10*(1), 7–9. doi:10.1063/1.869538

Choi, K.-S. (2000). European drag-reduction research—recent developments and current status. *Fluid Dynamics Research*, *26*(5), 325.

Choi, K.-S. (2002). Near-wall structure of turbulent boundary layer with spanwise-wall oscillation. *Physics of Fluids*, *14*(7), 2530. doi:10.1063/1.1477922

Choi, K.-S., & Clayton, B. R. (2001). The mechanism of turbulent drag reduction with wall oscillation. *International Journal of Heat and Fluid Flow*, *22*(1), 1–9.

Choi, K.-S., DeBisschop, J.-R., & Clayton, B. R. (1998). Turbulent boundary-layer control by means of spanwise-wall oscillation. *AIAA Journal*, *36*(7), 1157–1163. doi:10.2514/2.526

Cimarelli, A., Frohnapfel, B., Hasegawa, Y., De Angelis, E., & Quadrio, M. (2013). Prediction of turbulence control for arbitrary periodic spanwise wall movement. *Physics of Fluids*, *25*(7), 075102.

Clark, J. A., & Markland, E. (1971). Flow visualization in turbulent boundary layers. *Journal of the Hydraulics Division*, *97*(10), 1653–1664.

Coles, D., & Hirst, E. (1969). Proceedings computation of turbulent boundary layers-1968 AFOSR-IFP-stanford conference. In *Volume II. mech eng dept, stanford university*.

Coxe, D. J., Peet, Y. T., & Adrian, R. J. (2019). Vorticity statistics and distributions in drag reduced turbulent pipe flow with transverse wall oscillations. In *11th international symposium on turbulence and shear flow phenomena, TSFP 2019*.

Dantec. (2022). Measurement principles of CTA. Retrieved from https://www.dantecdynamics.com/solutions-applications/solutions/fluid-mechanics/constant-temperature-anemometry-cta/measurement-principles-of-cta/

De Graaff, D. B., & Eaton, J. K. (2000). Reynolds-number scaling of the flat-plate turbulent boundary layer. *Journal of Fluid Mechanics*, *422*, 319–346.

Del Álamo, J. C., & Jiménez, J. (2009). Estimation of turbulent convection velocities and corrections to taylor's approximation. *Journal of Fluid Mechanics*, *640*, 5–26. doi:10.1017/s0022112009991029

Del Alamo, J. C., Jiménez, J., Zandonade, P., & Moser, R. D. (2004). Scaling of the energy spectra of turbulent channels. *Journal of Fluid Mechanics*, *500*, 135–144.

Denison, M., Wilkinson, S. P., & Balakumar, P. (2015). On the effect of rigid swept surface waves on turbulent drag. In *45th AIAA fluid dynamics conference* (p. 3221).

Deshpande, R., Chandran, D., Smits, A. J., & Marusic, I. (2022). The relationship between manipulated inter-scale phase and energy-efficient turbulent drag reduction. *Manuscript in preparation, Journal of Fluid Mechanics*.

Duggleby, A., Ball, K. S., & Paul, M. R. (2007). The effect of spanwise wall oscillation on turbulent pipe flow structures resulting in drag reduction. *Physics of Fluids*, *19*(12), 125107.

Gad-el-Hak, M. (2000). *Flow control: Passive, active, and reactive flow management*. Cambridge: Cambridge University Press.

Gatti, D. (2015). *Turbulent skin-friction drag deduction via spanwise wall oscillations* (Doctoral dissertation, Technische Universität Darmstadt).

Gatti, D., Cimarelli, A., Hasegawa, Y., Frohnapfel, B., & Quadrio, M. (2018a). Global energy fluxes in turbulent channels with flow control. *Journal of Fluid Mechanics*, *857*, 345–373. Edition: 2018/10/22. doi:10.1017/jfm.2018.749

Gatti, D., Güttler, A., Frohnapfel, B., & Tropea, C. (2015). Experimental assessment of spanwise-oscillating dielectric electroactive surfaces for turbulent drag reduction in an air channel flow. *Experiments in Fluids*, *56*(5). doi:10.1007/s00348-015-1983-x

Gatti, D., & Quadrio, M. (2013). Performance losses of drag-reducing spanwise forcing at moderate values of the reynolds number. *Physics of Fluids*, *25*(12), 125109. doi:10.1063/1.4849537

Gatti, D., & Quadrio, M. (2016). Reynolds-number dependence of turbulent skin-friction drag reduction induced by spanwise forcing. *Journal of Fluid Mechanics*, *802*, 553–582. doi:10.1017/jfm.2016.485

Gatti, D., Stroh, A., Frohnapfel, B., & Hasegawa, Y. (2018b). Predicting turbulent spectra in drag-reduced flows. *Flow, Turbulence and Combustion*, *100*(4), 1081–1099. doi:10.1007/s10494-018-9920-8

Ge, M., & Jin, G. (2017). Response of turbulent enstrophy to sudden implementation of spanwise wall oscillation in channel flow. *Applied Mathematics and Mechanics*, *38*(8), 1159–1170. doi:10.1007/s10483-017-2226-9

Ghebali, S., Chernyshenko, S. I., & Leschziner, M. A. (2017). Can large-scale oblique undulations on a solid wall reduce the turbulent drag? *Physics of Fluids*, *29*(10), 105102.

Gouder, K., Potter, M., & Morrison, J. F. (2013). Turbulent friction drag reduction using electroactive polymer and electromagnetically driven surfaces. *Experiments in fluids*, *54*(1), 1–12.

Graver, B., Zhang, K., & Rutherford, D. (2019). Emissions from commercial aviation, 2018, ICCT.

Greidanus, A., Delfos, R., Tokgoz, S., & Westerweel, J. (2015). Turbulent taylor–couette flow over riblets: Drag reduction and the effect of bulk fluid rotation. *Experiments in Fluids*, *56*(5), 1–13.

Harun, Z., & Lotfy, E. R. (2018). Generation, evolution, and characterization of turbulence coherent structures. *Turbulence and Related Phenomena*.

Hasegawa, Y., Quadrio, M., & Frohnapfel, B. (2014). Numerical simulation of turbulent duct flows with constant power input. *Journal of Fluid Mechanics*, *750*, 191–209. doi:10.1017/jfm.2014.269

Hurst, E., Yang, Q., & Chung, Y. M. (2014). The effect of reynolds number on turbulent drag reduction by streamwise travelling waves. *Journal of fluid mechanics*, *759*, 28–55.

Hutchins, N., & Marusic, I. (2007a). Evidence of very long meandering features in the logarithmic region of turbulent boundary layers. *Journal of Fluid Mechanics*, *579*, 1–28. doi:10.1017/s0022112006003946

Hutchins, N., Nickels, T. B., Marusic, I., & Chong, M. S. (2009). Hot-wire spatial resolution issues in wall-bounded turbulence. *Journal of Fluid Mechanics*, *635*, 103–136. Edition: 2009/09/10.

Hutchins, N., Hambleton, W., & Marusic, I. (2005). Inclined cross-stream stereo particle image velocimetry measurements in turbulent boundary layers. *Journal of Fluid Mechanics*, *541*, 21–54.

Hutchins, N., & Marusic, I. (2007b). Large-scale influences in near-wall turbulence. *Philosophical transactions. Series A, Mathematical, physical, and engineering sciences*, *365*, 647–64. doi:10.1098/rsta.2006.1942

Hutchins, N., & Choi, K.-S. (2002). Accurate measurements of local skin friction coefficient using hot-wire anemometry. *Progress in Aerospace Sciences*, *38*(4), 421–446. doi:10.1016/S0376-0421(02)00027-1

IATA. (2019). Aircraft technology roadmap to 2050. *International Air Transport Association: Montreal, QC, Canada*.

Jiménez, J., & Pinelli, A. (1999). The autonomous cycle of near-wall turbulence. *Journal of Fluid Mechanics*, *389*, 335–359.

Jung, W. J., Mangiavacchi, N., & Akhavan, R. (1992). Suppression of turbulence in wall-bounded flows by high-frequency spanwise oscillations. *Physics of Fluids A: Fluid Dynamics*, *4*(8), 1605–1607. doi:10.1063/1.858381

Kempaiah, K. U., Scarano, F., Elsinga, G. E., Van Oudheusden, B. W., & Bermel, L. (2020). 3-dimensional particle image velocimetry based evaluation of turbulent skin-friction reduction by spanwise wall oscillation. *Physics of Fluids*, *32*(8), 085111. doi:10.1063/5.0015359

Kiesow, R. O., & Plesniak, M. W. (2003). Near-wall physics of a shear-driven three-dimensional turbulent boundary layer with varying crossflow. *Journal of Fluid Mechanics*, *484*, 1–39. Retrieved from https://dx.doi.org/10.1017/s0022112003004178

Kiknadze, G., Krasnov, Y. K., & Chushkin, Y. V. (1984). *Report: Investigation of the enhancement of heat transfer due to self-organization of ordered dynamic twisted heat-carrier structures on a heat-transfer surface*. Kurchatov Institute of Atomic Energy.

Kim, J., & Hussain, F. (1992). Propagation velocity and space-time correlation of perturbations in turbulent channel flow. *NASA STI/Recon Technical Report N*, 25082.

Kim, K. C., & Adrian, R. J. (1999). Very large-scale motion in the outer layer. *Physics of Fluids*, *11*(2), 417–422.

King, L. V. (1914). XII. on the convection of heat from small cylinders in a stream of fluid: Determination of the convection constants of small platinum wires with applications to hot-wire anemometry. *Philosophical transactions of the royal society of London. series A, containing papers of a mathematical or physical character*, *214*(509), 373–432.

Kline, S. J., Reynolds, W. C., Schraub, F., & Runstadler, P. (1967). The structure of turbulent boundary layers. *Journal of Fluid Mechanics*, *30*(4), 741–773.

Knoop, M. (2023). *Outer-scaled actuation using spanwise forcing for turbulent skin friction reduction - literature review \& research plan*. Delft University of Technology.

Krogstad, P. Å., Kaspersen, J. H., & Rimestad, S. (1998). Convection velocities in a turbulent boundary layer. *Physics of Fluids*, *10*(4), 949–957. doi:10.1063/1.869617

Laadhari, F., Skandaji, L., & Morel, R. (1994). Turbulence reduction in a boundary layer by a local spanwise oscillating surface. *Physics of Fluids*, *6*(10), 3218–3220. doi:10.1063/1.868052

Lardeau, S., & Leschziner, M. A. (2013). The streamwise drag-reduction response of a boundary layer subjected to a sudden imposition of transverse oscillatory wall motion. *Physics of Fluids*, *25*(7), 075109. doi:10.1063/1.4816290

Leschziner, M. A. (2020). Friction-drag reduction by transverse wall motion – a review. *Journal of Mechanics*, *36*(5), 649–663. doi:10.1017/jmech.2020.31

Ligrani, P., & Bradshaw, P. (1987). Spatial resolution and measurement of turbulence in the viscous sublayer using subminiature hot-wire probes. *Experiments in Fluids*, *5*(6), 407–417.

Lin, Y. Y. (2021). *Numerical investigation of the turbulent boundary layer over dimpled surfaces (MSc. thesis)*. Delft University of Technology.

Luchini, P. (1996). Reducing the turbulent skin friction. In *Computational methods in applied sciences '96* (pp. 466–470).

Luchini, P., & Quadrio, M. (2022). Wall turbulence and turbulent drag reduction. In *50+ years of AIMETA* (pp. 349–364). Springer.

Marusic, I., Mathis, R., & Hutchins, N. (2010a). Predictive model for wall-bounded turbulent flow. *Science*, *329*(5988), 193–196.

Marusic, I., Chandran, D., Rouhi, A., Fu, M. K., Wine, D., Holloway, B., … Smits, A. J. (2021). An energy-efficient pathway to turbulent drag reduction. *Nature Communications*, *12*(1). doi:10.1038/s41467-021-26128-8

Marusic, I., Mathis, R., & Hutchins, N. (2010b). High reynolds number effects in wall turbulence. *International Journal of Heat and Fluid Flow*, *31*(3), 418–428. doi:10.1016/j.ijheatfluidflow.2010.01.005

Mathis, R., Hutchins, N., & Marusic, I. (2009). Large-scale amplitude modulation of the small-scale structures in turbulent boundary layers. *Journal of Fluid Mechanics*, *628*, 311–337. Edition: 2009/06/01. doi:10.1017/S0022112009006946

Mathis, R., Hutchins, N., & Marusic, I. (2011). A predictive inner–outer model for streamwise turbulence statistics in wall-bounded flows. *Journal of Fluid Mechanics*, *681*, 537–566. doi:10.1017/jfm.2011.216

Mishra, M., & Skote, M. (2015). Drag reduction in turbulent boundary layers with half wave wall oscillations. *Mathematical Problems in Engineering*, *2015*. doi:10.1155/2015/253249

Miyake, Y., Tsujimoto, K., Kajishima, T., & Suzuki, Y. (1998). Management of streamwise vortices in near-wall turbulence. *Sadhana*, *23*(5), 541–556. doi:10.1007/BF02744578

Miyake, Y., Tsujimoto, K., & Takahashi, M. (1997). On the mechanism of drag reduction of near-wall turbulence by wall oscillation. *JSME International Journal Series B*, *40*(4), 558–566. doi:10.1299/jsmeb.40.558

Monkewitz, P. A., Chauhan, K. A., & Nagib, H. M. (2007). Self-consistent high-reynolds-number asymptotics for zero-pressure-gradient turbulent boundary layers. *Physics of Fluids*, *19*(11), 115101.

Musker, A. J. (1979). Explicit expression for the smooth wall velocity distribution in a turbulent boundary layer. *AIAA Journal*, *17*(6), 655–657. doi:10.2514/3.61193

Nagib, H. M., & Chauhan, K. A. (2008). Variations of von kármán coefficient in canonical flows. *Physics of Fluids*, *20*(10), 101518. doi:10.1063/1.3006423

Nelson, G. (2018). *Contribution of the global aviation sector to achieving paris agreement climate objectives*. Climate Action Network (CAN) and International Coalition for Sustainable Aviation (ICSA).

Nikitin, N. V. (2000). On the mechanism of turbulence suppression by spanwise surface oscillations. *Fluid Dynamics*, *35*(2), 185–190. doi:10.1007/BF02831425

Panton, R. L. (2001). Overview of the self-sustaining mechanisms of wall turbulence. *Progress in Aerospace Sciences*, *37*(4), 341–383. doi:10.1016/S0376-0421(01)00009-4

Quadrio, M., & Ricco, P. (2004). Critical assessment of turbulent drag reduction through spanwise wall oscillations. *Journal of Fluid Mechanics*, *521*, 251–271.

Quadrio, M. (2011). Drag reduction in turbulent boundary layers by in-plane wall motion. *Philosophical Transactions of the Royal Society A: Mathematical, Physical and Engineering Sciences*, *369*(1940), 1428–1442. doi:10.1098/rsta.2010.0366

Quadrio, M., & Luchini, P. (2003). Integral space–time scales in turbulent wall flows. *Physics of Fluids*, *15*(8), 2219–2227. doi:10.1063/1.1586273

Quadrio, M., & Ricco, P. (2003). Initial response of a turbulent channel flow to spanwise oscillation of the walls. *Journal of Turbulence*, *4*. doi:10.1088/1468-5248/4/1/007

Quadrio, M., & Ricco, P. (2011). The laminar generalized stokes layer and turbulent drag reduction. *Journal of Fluid Mechanics*, *667*, 135–157. doi:10.1017/s0022112010004398

Quadrio, M., Ricco, P., & Viotti, C. (2009). Streamwise-travelling waves of spanwise wall velocity for turbulent drag reduction. *Journal of Fluid Mechanics*, *627*, 161–178.

Quadrio, M., & Sibilla, S. (2000). Numerical simulation of turbulent flow in a pipe oscillating around its axis. *Journal of Fluid Mechanics*, *424*, 217–241. Edition: 2000/11/16. doi:10.1017/S0022112000001889

Raffel, M., Willert, C., Scarano, F., Kähler, C., Wereley, S., & Kompenhans, J. (2018). *Particle image velocimetry: A practical guide* (3rd ed.). Springer.

Ricco, P. (2004). Modification of near-wall turbulence due to spanwise wall oscillations. *Journal of Turbulence*, *5*(1), 024.

Ricco, P., Ottonelli, C., Hasegawa, Y., & Quadrio, M. (2012). Changes in turbulent dissipation in a channel flow with oscillating walls. *Journal of Fluid Mechanics*, *700*, 77–104.

Ricco, P., & Quadrio, M. (2008). Wall-oscillation conditions for drag reduction in turbulent channel flow. *International Journal of Heat and Fluid Flow*, *29*(4), 891–902. doi:10.1016/j.ijheatfluidflow.2007.12.005

Ricco, P., Skote, M., & Leschziner, M. A. (2021). A review of turbulent skin-friction drag reduction by near-wall transverse forcing. *Progress in Aerospace Sciences*, *123*, 100713.

Ricco, P., & Wu, S. (2004). On the effects of lateral wall oscillations on a turbulent boundary layer. *Experimental Thermal and Fluid Science*, *29*(1), 41–52. doi:10.1016/j.expthermflusci.2004.01.010

Rodríguez-López, E., Bruce, P. J. K., & Buxton, O. R. H. (2015). A robust post-processing method to determine skin friction in turbulent boundary layers from the velocity profile. *Experiments in Fluids*, *56*. doi:10.1007/s00348-015-1935-5

Sanderson, R. (1997). *Turbulent drag reduction due to an oscillating cross–flow*. APS Division of Fluid Dynamics.

Schlatter, P., & Örlü, R. (2010). Assessment of direct numerical simulation data of turbulent boundary layers. *Journal of Fluid Mechanics*, *659*, 116–126.

Sciacchitano, A., & Wieneke, B. (2016). PIV uncertainty propagation. *Measurement Science and Technology*, *27*(8), 084006.

Skote, M. (2011). Turbulent boundary layer flow subject to streamwise oscillation of spanwise wall-velocity. *Physics of Fluids*, *23*(8), 081703. doi:10.1063/1.3626028

Skote, M., Mishra, M., & Wu, Y. (2015a). Drag reduction of a turbulent boundary layer over an oscillating wall and its variation with reynolds number. *International Journal of Aerospace Engineering, 2015*. doi:10.1155/2015/891037

Skote, M. (2012). Temporal and spatial transients in turbulent boundary layer flow over an oscillating wall. *International Journal of Heat and Fluid Flow*, *38*, 1–12. doi:10.1016/j.ijheatfluidflow.2012.08.004

Skote, M. (2013). Comparison between spatial and temporal wall oscillations in turbulent boundary layer flows. *Journal of Fluid Mechanics, 730*, 273–294. Edition: 2013/07/30. doi:10.1017/jfm.2013.344

Skote, M. (2022). Drag reduction of turbulent boundary layers by travelling and non-travelling waves of spanwise wall oscillations. *Fluids*, *7*(2), 65. doi:10.3390/fluids7020065

Skote, M., Mishra, M., & Wu, Y. (2019). Wall oscillation induced drag reduction zone in a turbulent boundary layer. *Flow, Turbulence and Combustion*, *102*(3), 641–666. doi:10.1007/s10494-018-9979-2

Skote, M., Schlatter, P., & Wu, Y. (2015b). Numerical studies of active control of turbulent boundary layers using transverse travelling waves. In *9th int. symp. turbul. shear flow phenomena (TSFP9)* (pp. 1–6).

Smits, A. J., McKeon, B. J., & Marusic, I. (2011). High–reynolds number wall turbulence. *Annual Review of Fluid Mechanics*, *43*.

Spalart, P. R. (1988). Direct simulation of a turbulent boundary layer up to re theta= 1410. *Journal of fluid mechanics*, *187*, 61–98.

Stokes, G. G. (1851). On the effect of the internal friction of fluids on the motion of pendulums. *Transactions of the Cambridge Philosophical Society*, *4*.

Talluru, M. K. (2014). *Manipulating large-scale structures in a turbulent boundary layer using a wall-normal jet* (Doctoral dissertation, University of Melbourne).

Tay, C., Khoo, B., & Chew, Y. (2015). Mechanics of drag reduction by shallow dimples in channel flow. *Physics of Fluids (1994-present)*, *27*(3), 035109.

Taylor, G. I. (1938). The spectrum of turbulence. *Proceedings of the Royal Society of London. Series A-Mathematical and Physical Sciences*, *164*(919), 476–490.

Touber, E., & Leschziner, M. A. (2012). Near-wall streak modification by spanwise oscillatory wall motion and drag-reduction mechanisms. *Journal of Fluid Mechanics*, *693*, 150–200. doi:10.1017/jfm.2011.507

Trujillo, S. M. (1999). *An investigation of the effects of spanwise wall oscillation on the structure of a turbulent boundary layer* (Doctoral dissertation, The University of Texas at Austin).

Trujillo, S., Bogard, D., & Ball, K. (1997). Turbulent boundary layer drag reduction using an oscillating wall. In *4th shear flow control conference* (p. 1870).

Tsubokura, M. (2005). LES study on the large-scale motions of wall turbulence and their structural difference between plane channel and pipe flows. In *Fourth international symposium on turbulence and shear flow phenomena*, Begel House Inc.

Van Nesselrooij, M., Van Campenhout, O. W. G., Van Oudheusden, B. W., Schrijer, F. F. J., & Veldhuis, L. L. M. (2022). Development of an experimental apparatus for flat plate drag measurements and considerations for such measurements. *Measurement Science and Technology*, *33*(5). doi:10.1088/1361-6501/ac527f

van Campenhout, O., van Nesselrooij, M., Lin, Y., Casacuberta, J., van Oudheusden, B., & Hickel, S. (2022). Experimental and numerical investigation into the drag performance of dimpled surfaces in a turbulent boundary layer. *International Journal of Heat and Fluid Flow*.

van Campenhout, O. W., Van Nesselrooij, M., Veldhuis, L. L., van Oudheusden, B., & Schrijer, F. (2018). An experimental investigation into the flow mechanics of dimpled surfaces in turbulent boundary layers. In *2018 AIAA aerospace sciences meeting* (p. 2062).

van Nesselrooij, M., van Campenhout, O., & Veldhuis, L. L. M. (2020). *Body provided with a superficial area adapted to reduce drag*. Patents, G. US patent: 10,851,817.

van Nesselrooij, M., Veldhuis, L., Van Oudheusden, B., & Schrijer, F. (2016). Drag reduction by means of dimpled surfaces in turbulent boundary layers. *Experiments in Fluids*, *57*(9), 1–14.

Viotti, C., Quadrio, M., & Luchini, P. (2009). Streamwise oscillation of spanwise velocity at the wall of a channel for turbulent drag reduction. *Physics of Fluids*, *21*. doi:10.1063/1.3266945

Wallace, J. M., Eckelmann, H., & Brodkey, R. S. (1972). The wall region in turbulent shear flow. *Journal of Fluid Mechanics*, *54*(1), 39–48.

Walsh, M. J. (1983). Riblets as a viscous drag reduction technique. *AIAA journal*, *21*(4), 485–486.

Westerweel, J., & Scarano, F. (2005). Universal outlier detection for PIV data. *Experiments in fluids*, *39*(6), 1096–1100.

White, F. M., & Corfield, I. (2006). *Viscous fluid flow*. McGraw-Hill New York.

Wu, S. (2000). *An investigation of the reynolds number effect on the drag reduction by spanwise wall oscillation* (Doctoral dissertation, University of Texas at Austin).

Xu, C.-X., & Huang, W.-X. (2005). Transient response of reynolds stress transport to spanwise wall oscillation in a turbulent channel flow. *Physics of Fluids*, *17*(1), 018101–018101–4. doi:10.1063/1.1827274

Yakeno, A., Hasegawa, Y., & Kasagi, N. (2009). Spatio-temporally periodic control for turbulent friction drag reduction. In *Sixth international symposium on turbulence and shear flow phenomena*, Begel House Inc.

Yakeno, A., Hasegawa, Y., & Kasagi, N. (2014). Modification of quasi-streamwise vortical structure in a drag-reduced turbulent channel flow with spanwise wall oscillation. *Physics of Fluids*, *26*(8), 085109. doi:10.1063/1.4893903

Yang, Q., & Hwang, Y. (2019). Modulation of attached exact coherent states under spanwise wall oscillation. In *Eleventh international symposium on turbulence and shear flow phenomena (TSFP11)*, Begel House Inc.

Yao, J., Chen, X., & Hussain, F. (2019). Reynolds number effect on drag control via spanwise wall oscillation in turbulent channel flows. *Physics of Fluids*, *31*(8), 085108. doi:10.1063/1.5111651

Yuan, W., Zhang, M., Cui, Y., & Khoo, B. C. (2019). Phase-space dynamics of near-wall streaks in wall-bounded turbulence with spanwise oscillation. *Physics of Fluids*, *31*(12). doi:10.1063/1.5130161

Yudhistira, I., & Skote, M. (2011). Direct numerical simulation of a turbulent boundary layer over an oscillating wall. *Journal of Turbulence*, (12), N9.

Zhou, D., & Ball, K. S. (2008). Turbulent drag reduction by spanwise wall oscillations.

Zhou, D., & Ball, K. (2006). The mechanism of turbulent drag reduction by spanwise wall oscillation. In *42nd AIAA/ASME/SAE/ASEE joint propulsion conference & exhibit* (p. 4579).

V

Appendices

A

All drag data and corrections

This section presents all the drag data and the corrections of the individual test plates (TPs) from Part II. An overview of the considered TPs is presented in Table A.1. All TPs were measured with a boundary layer development length of x_{dev} = 3.45 m at the halfway point of the TP. For three TPs, an additional shorter development length of x_{dev} = 1.05 m was considered for testing the DR trends with Re_τ. For each TP, the results are presented on an individual page. When a TP was tested at two development lengths, the results are presented on a single page, starting with the shorter development length.

The results are presented in a dashboard figure with five individual subplots, indicated as by: “95% confidence interval", “w/o Pressure correction", “Null force correction", “Pressure correction" and “Final result". The main subplot indicated by "final result", displays of the drag difference in percentage (ΔC_D) with respect to the flat reference TP. For each TP, three velocity sweeps are measured and presented as individual lines. The velocity is expressed as a unit Reynolds number (Re_1) with a reference length of 1 m, with an approximate range of $Re_1 \approx 0.5 \times 10^6 - 2.3 \times 10^6$.

The subfigure “95% confidence interval" is the interval in percentage C_D for the mean value of the three individual measurements. The confidence interval is calculated using Student’s t-distribution to account for the small sample size (in this case $n = 3$). As explained in Section 4.3, a null-force and pressure correction are applied to the raw measurements. Their corresponding correction terms are presented in the subfigures “Null force correction" and “Pressure correction". The final result without the pressure correction is also displayed under the subfigure “w/o Pressure correction".

Name	Test plate reference	Two development lengths?
Staggered dimples (van Nesselrooij et al., 2016)	TP0001	No
Staggered dimples (Tay et al., 2015)	TP0005	No
Staggered SU based on TP0001	TP0004	Yes
OWW (Ghebali et al., 2017)	TP0007	Yes
Riblets (Greidanus et al., 2015)	TP0009	No
OWW high H (Denison et al., 2015)	TP0011	No
OWW low H (Denison et al., 2015)	TP0012	Yes
Aligned SU based on TP0001	TP0124	No
Superimposed OWW (Ghebali et al., 2017)	TP0125	No

Table A.1: Overview of the considered TPs, indicated is if two development lengths are considered.

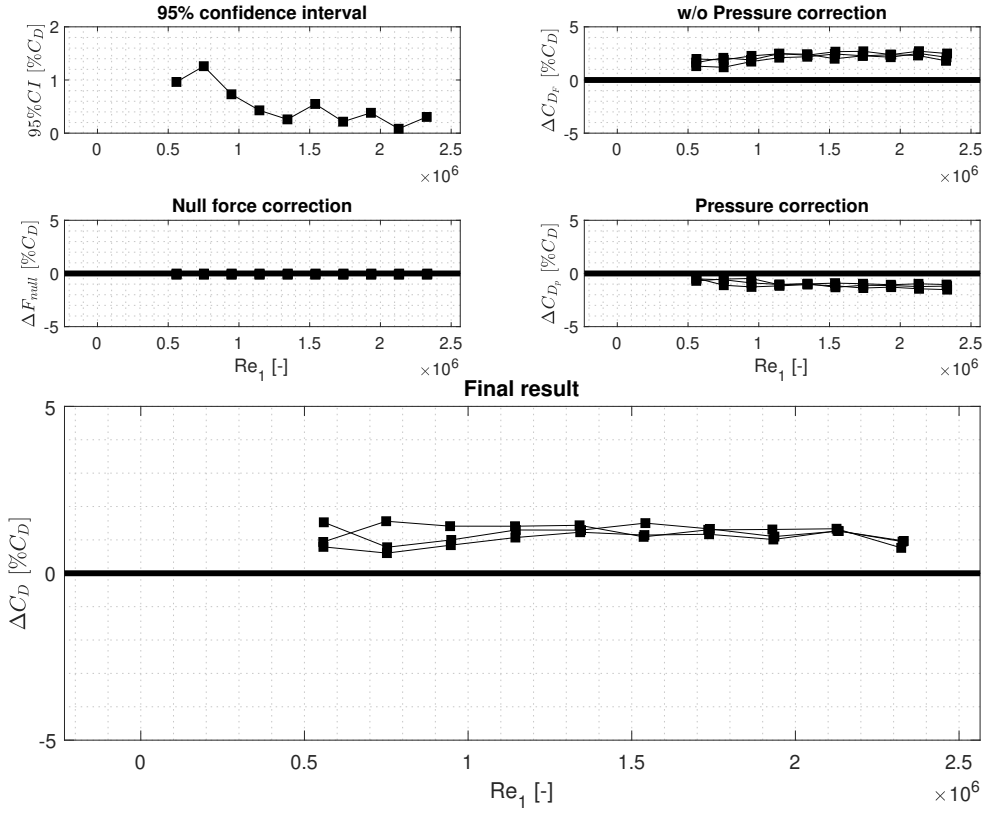

Figure A.1: Data for TP0001 with $x_{dev} = 3.45$ m.

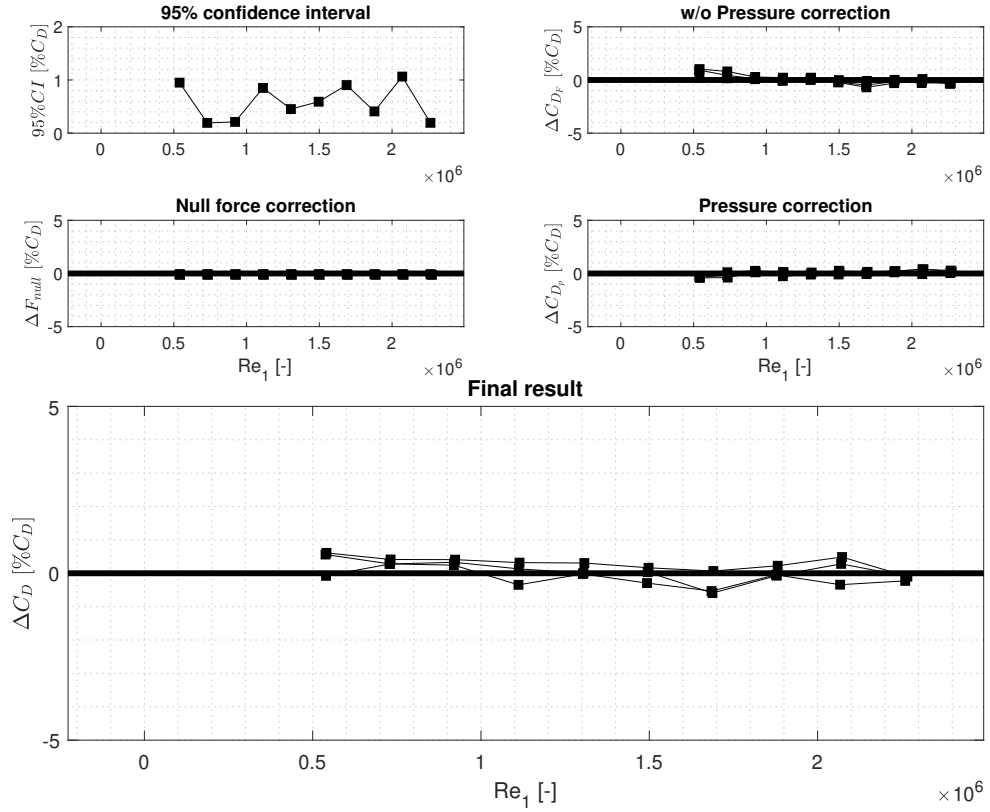

Figure A.2: Data for TP0004 with x_{dev} = 1.05 m.

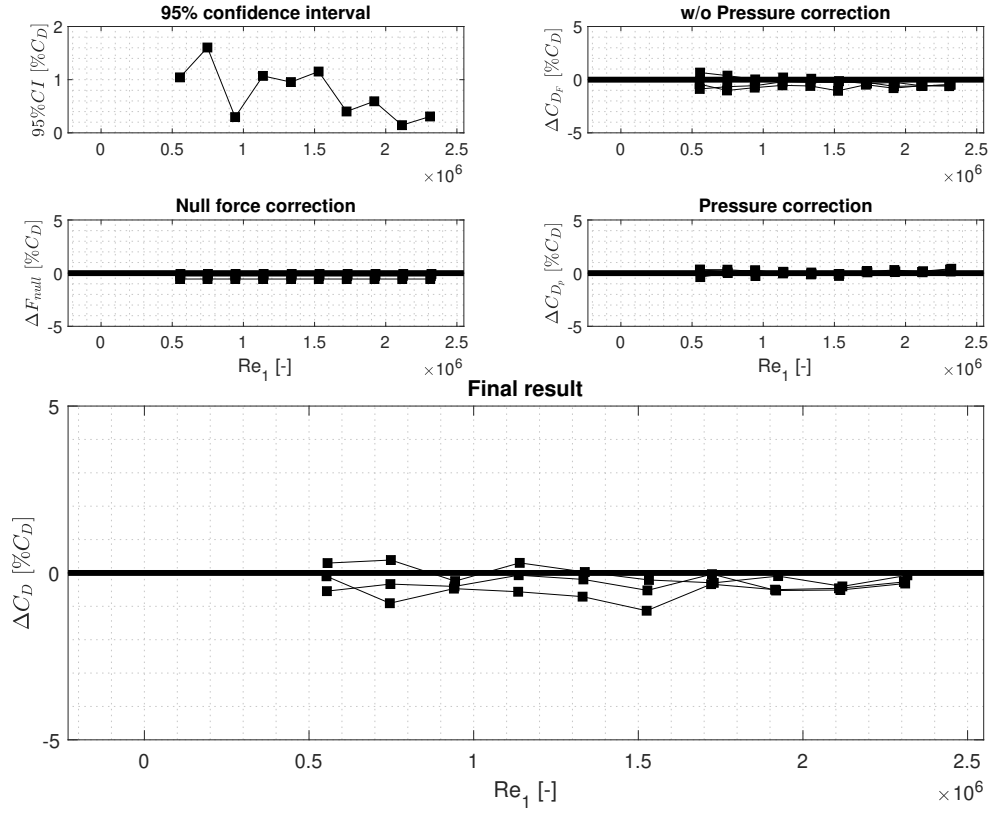

Figure A.3: Data for TP0004 with x_{dev} = 3.45 m.

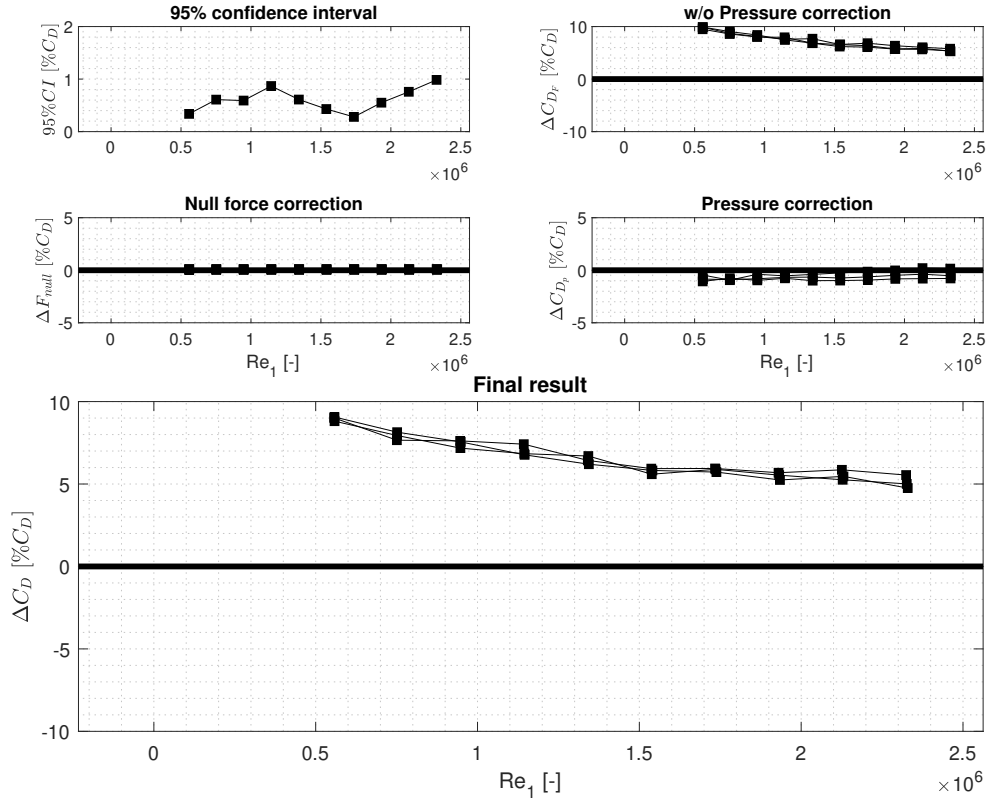

Figure A.4: Data for TP0005 with x_{dev} = 3.45 m. Note the change of y-axis scales from -10% to 10% for the subfigures “w/o Pressure correction" and “Final result".

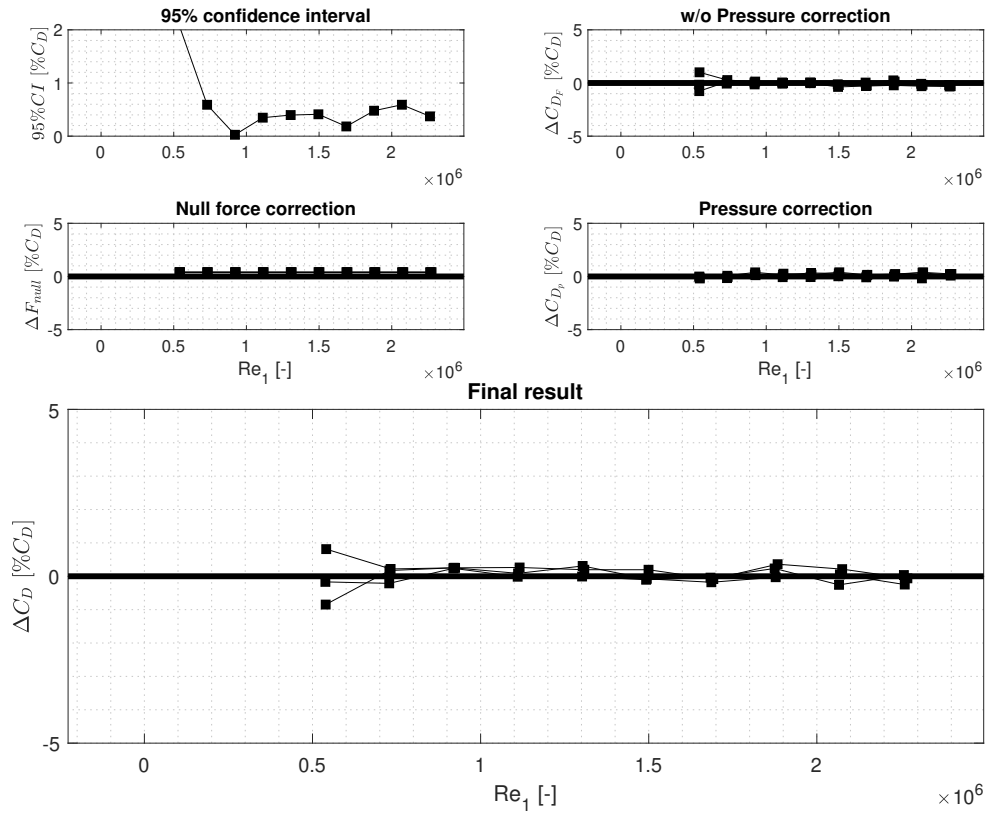

Figure A.5: Data for TP0007 with x_{dev} = 1.05 m.

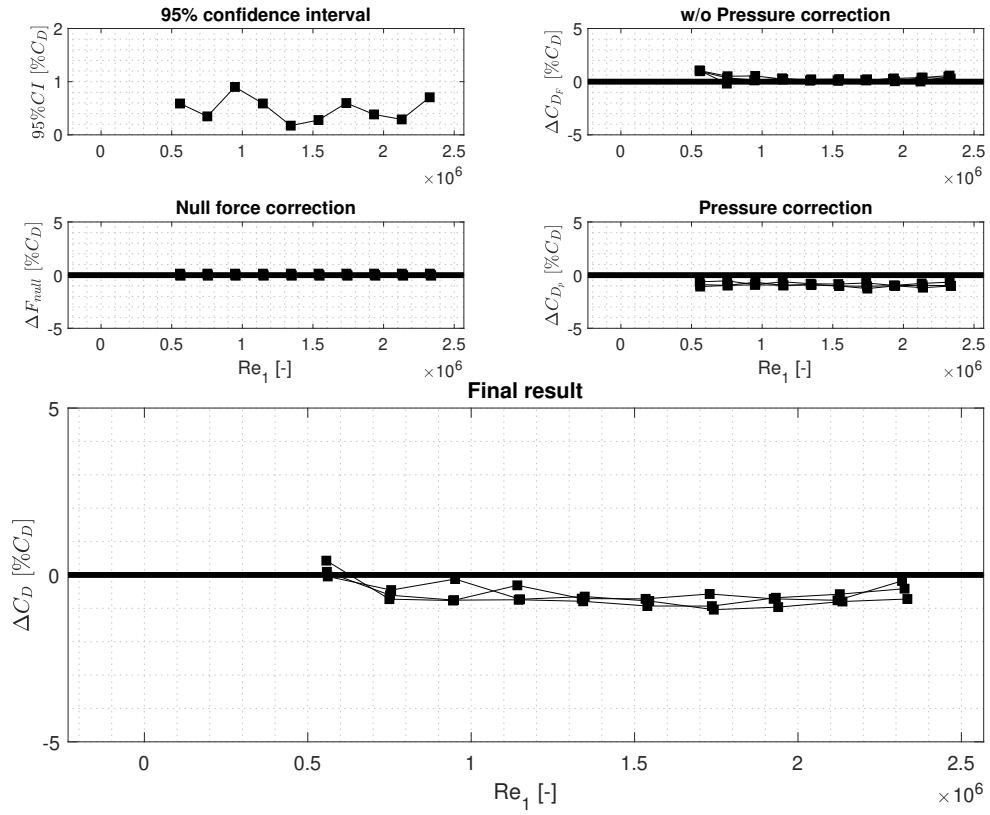

Figure A.6: Data for TP0007 with x_{dev} = 3.45 m.

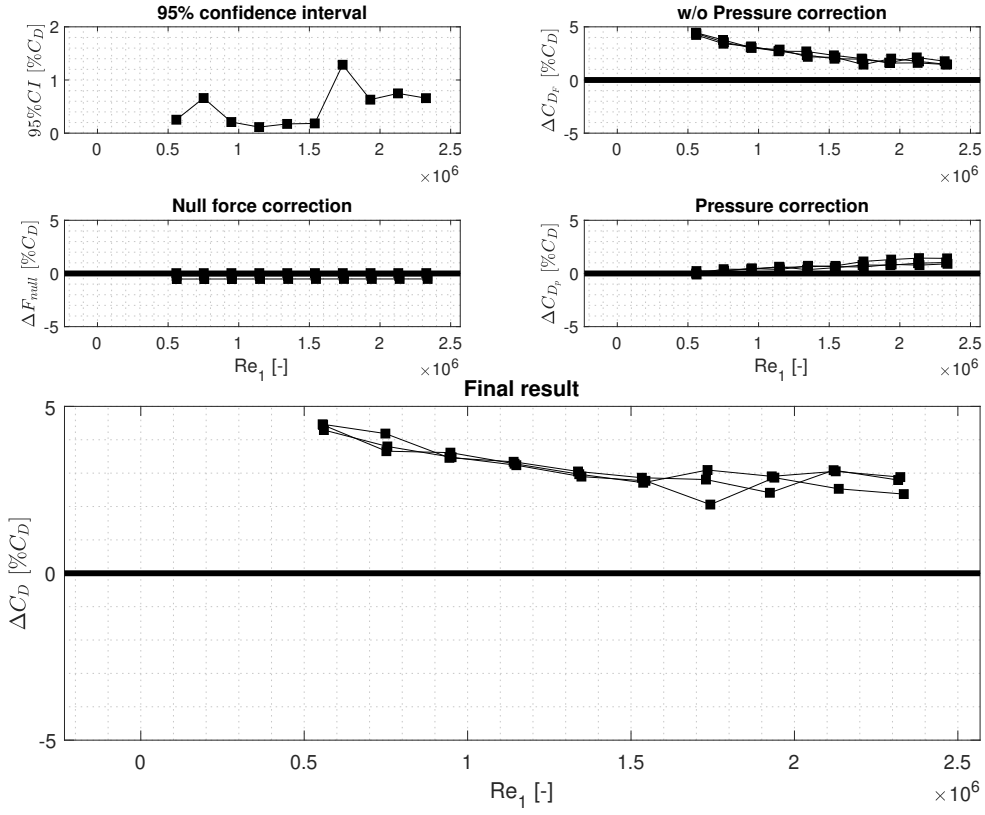

Figure A.7: Data for TP0011 with $x_{dev} = 3.45$ m.

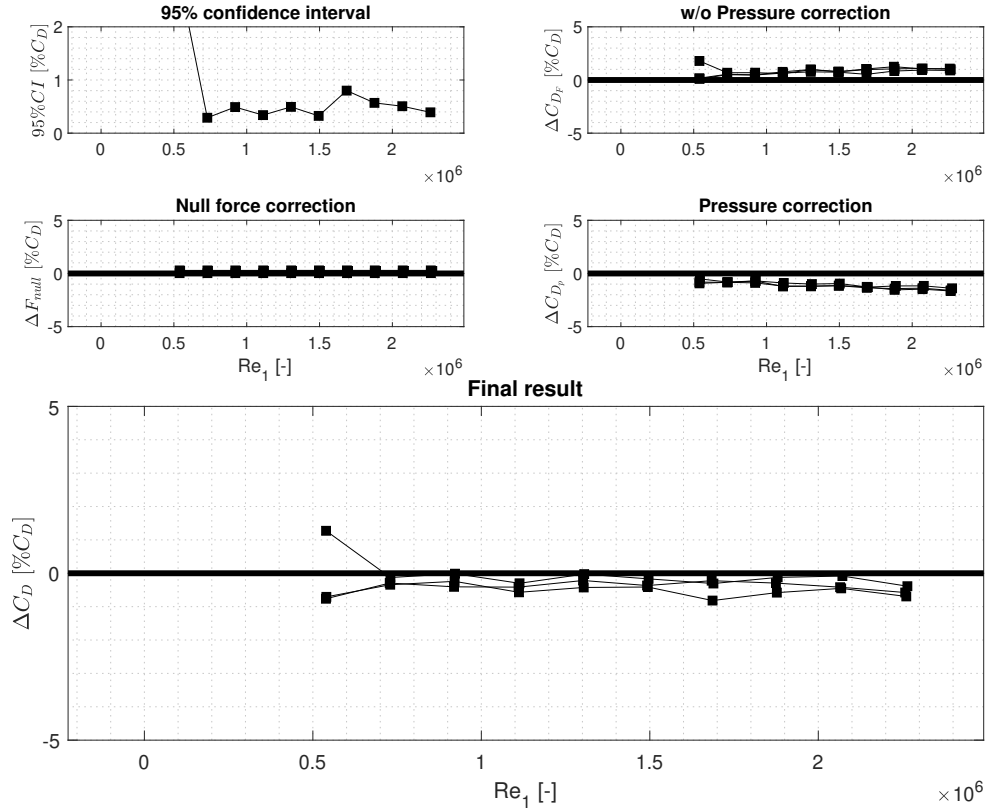

Figure A.8: Data for TP0012 with x_{dev} = 1.05 m.

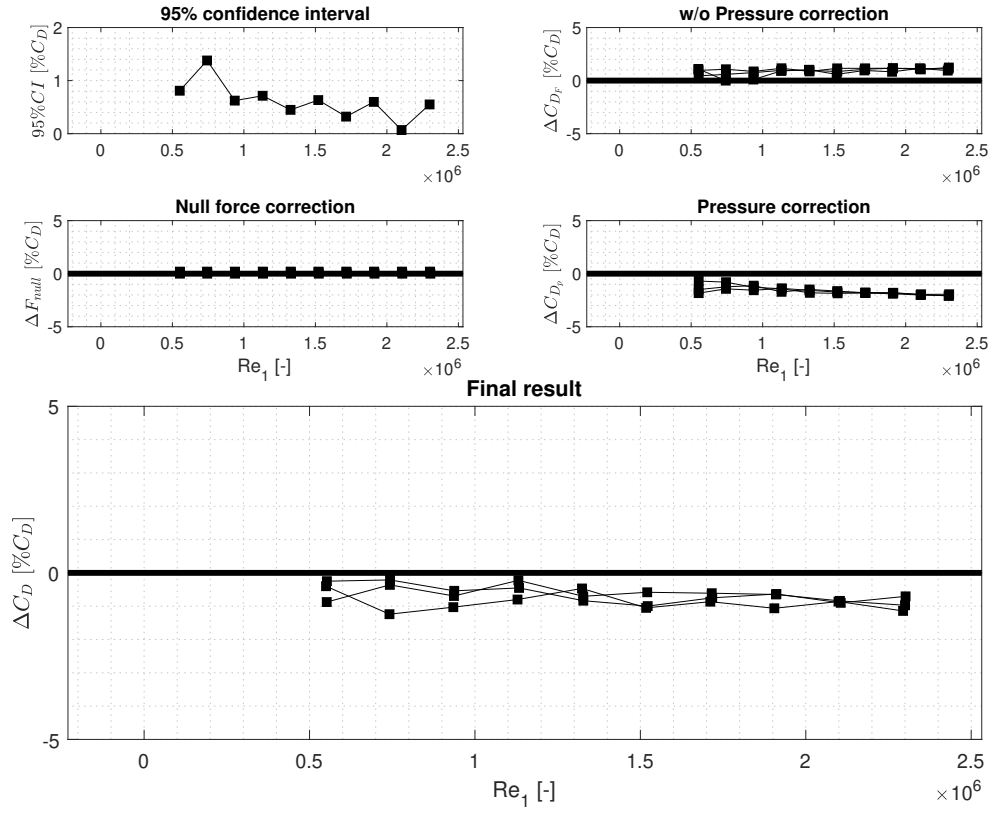

Figure A.9: Data for TP0012 with x_{dev} = 3.45 m.

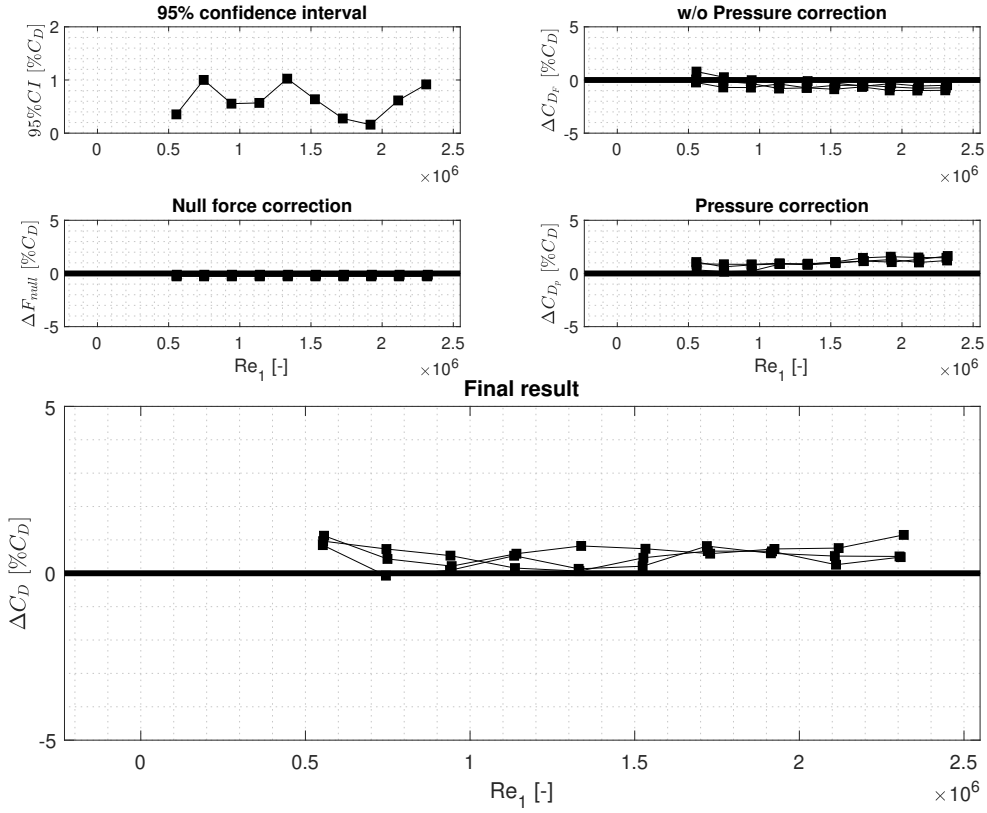

Figure A.10: Data for TP0124 with x_{dev} = 3.45 m.

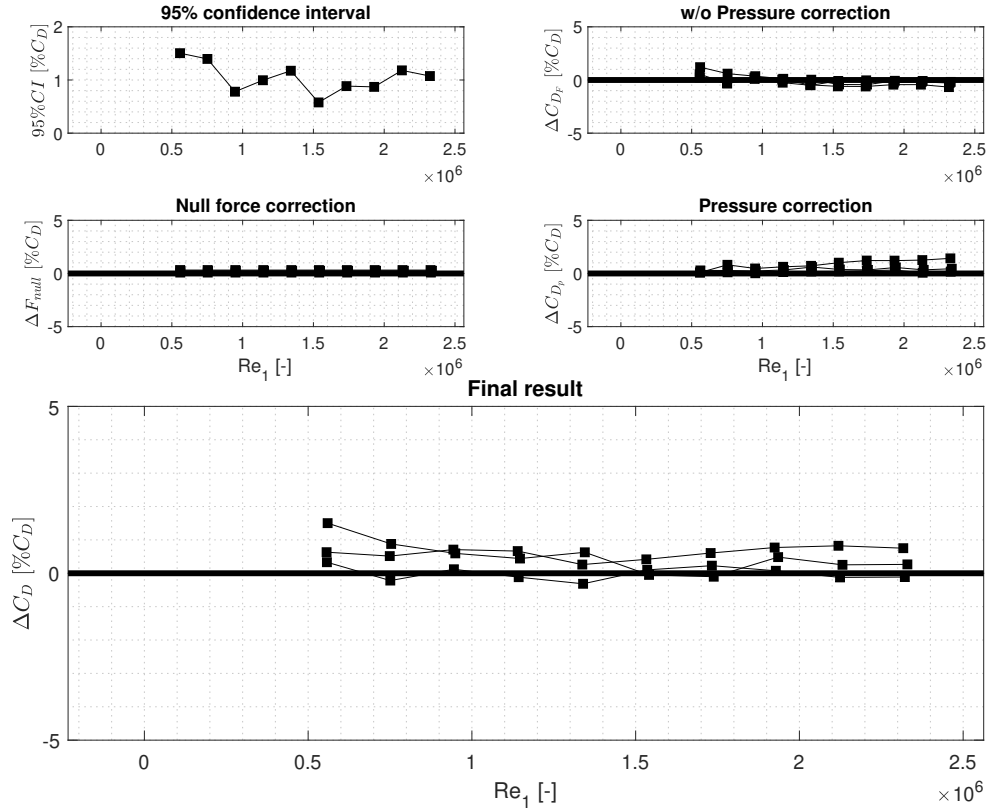

Figure A.11: Data for TP0125 with x_{dev} = 3.45 m.

B

Post-processing procedures HWA

This appendix presents the post-processing procedure and analysis methods used to process the HWA data. Firstly, the approach to calculating the mean and turbulence statistics profiles is outlined. Following this, the method to fit the boundary layer profiles is outlined. Lastly, the details of spectral analysis are presented.

B.1. Turbulence statistics

The HWA data can be used in amplitude domain analysis to obtain the mean velocity profile and higher-order turbulence statistics. Recall that a turbulent velocity signal can be decomposed into a mean and a fluctuating component around the mean as:

$$u = \overline{u} + u' \tag{B.1}$$

In this part of the thesis, we only quantify the mean flow and the velocity fluctuations. The mean of a time signal with N samples is calculated according to:

$$\overline{u} = \frac{1}{N}\sum_{i}^{N} = u_i \tag{B.2}$$

To quantify the intensity of the velocity fluctuations, the standard deviation of the velocity fluctuations u' is calculated according to Equation B.3. Note that the velocity fluctuations in this thesis are displayed using the variance of the signal, which is simply the square of the standard deviation as displayed in Equation B.4. Since the HWA data only contains a streamwise velocity signal, no covariance is considered.

$$\langle u' \rangle = \sqrt{\frac{1}{N-1}\sum_{i}^{N} = (u_i - \overline{u})^2} \tag{B.3}$$

$$\langle u'^2 \rangle = \frac{1}{N-1}\sum_{i}^{N} = (u_i - \overline{u})^2 \tag{B.4}$$

B.2. Boundary layer fitting

Profile fitting can be applied to obtain the boundary layer properties and the viscous scaling of the boundary layer. This is the task of fitting the experimental data to a model for the boundary later, which is a function of a number of fitting parameters. In this work, the method of Chauhan et al. (2009) is used, which uses a composite profile for the inner- and outer layers, respectively.

The inner layer is based on the profile of Musker (1979), also referred to as the Muskers profile. The profile asymptotes to the linear profile in the viscous sublayer and the logarithmic relation in the log layer. Chauhan et al. (2009) present an explicit definition for the inner profile:

$$u^+_{\text{inner}} = \frac{1}{\kappa}\ln\left(\frac{y^+ - a}{-a}\right) + \frac{R^2}{a(4\alpha - a)}\left[(4\alpha + a)\ln\left(-\frac{a}{R}\frac{\sqrt{(y^+ - \alpha)^2 + \beta^2}}{y^+ - a}\right)\right.$$
$$\left. + \frac{\alpha}{\beta}(4\alpha + 5a)\left(\arctan\left(\frac{y^+ - \alpha}{\beta}\right) + \arctan\left(\frac{\alpha}{\beta}\right)\right)\right] \tag{B.5}$$

With $\alpha = (-1/\kappa - a)/2$, $\beta = \sqrt{-2a\alpha - \alpha^2}$ and $R = \sqrt{\alpha^2 + \beta^2}$ In this profile the additive constant B is controlled with the parameter a. Nagib and Chauhan (2008) make the argument that the commonly used $\kappa = 0.41$ should be redefined to $\kappa = 0.384$ based on high Reynolds number experiments. Therefore this value is assumed in this thesis. This results in an additive constant $B = 4.17$ for a value of $a = -10.3061$. A feature not captured by the Muskers profile is a small '*bump*' in the velocity profile around $y^+ = 50$. This bump is highlighted in Figure B.1 by the indicator function $\Xi = u^+ - \left[1/\kappa \ln(y^+) + B\right]$. To correct this, the bump profile, defined in Equation B.6, can be added to the Muskers profile (Monkewitz et al., 2007).

$$u^+_{\text{bump}} = u^+_{\text{inner}} + \frac{\exp\left[-\log^2\left(y^+/30\right)\right]}{2.85} \tag{B.6}$$

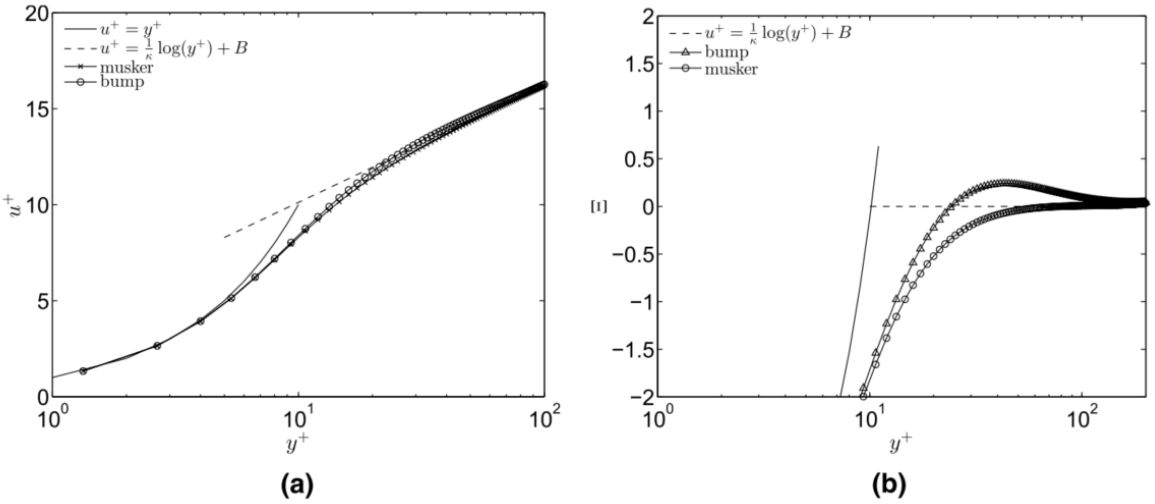

Figure B.1: The '*bump*' in the buffer layer for the Muskers and bump profiles (a) mean velocity profile (b) indicator function $\Xi = u^+ - \left[1/\kappa \ln(y^+) + B\right]$ (Rodríguez-López et al., 2015)

For the outer-layer, the law of the wake by Coles and Hirst (1969) is used, which takes the form of:

$$u^+_{\text{outer}} = \frac{1}{\kappa}\ln\left(y^+\right) + B + \frac{2\Pi}{\kappa}\mathcal{W}(\eta), \quad \eta \equiv y/\delta \leqslant 1 \tag{B.7}$$

It can be seen that the outer-layer is a function of the wake parameter Π, the outer-scaled height η and the wake function $\mathcal{W}$, which is defined as follows:

$$\mathcal{W}_{\text{exp}}(\eta) = \frac{1 - \exp\left[-(1/4)\left(5a_2 + 6a_3 + 7a_4\right)\eta^4 + a_2\eta^5 + a_3\eta^6 + a_4\eta^7\right]}{1 - \exp\left[-\left(a_2 + 2a_3 + 3a_4\right)/4\right]}$$
$$\times\left(1 - \frac{1}{2\Pi}\ln(\eta)\right) \tag{B.8}$$

With $a_2 = 132.8410$, $a_3 = -166.2041$, and $a_4 = 71.9114$.

Combining the inner- and outer-profiles results in the composite formulation of the velocity profile:

$$u^+_{\text{composite}} \equiv u^+ + u^+_{\text{bump}} + \frac{2\Pi}{\kappa}\mathcal{W}\left(\frac{y^+}{\delta^+}\right), \quad 0 \leqslant y^+ \leqslant \delta^+ \tag{B.9}$$

When the constants κ and B are fixed, the composite profile is a function of Π, u_τ and δ. Additionally, since the wall estimation of the HWA probe comes with some uncertainty, a Δ_y offset can be added as a

fitting parameter. With this, the composite profile is a functional of these four parameters. The parameters are fitted to the experimental data (u_{exp} using a least-squares approach which minimises the error function:

$$E\left(u_\tau, \Delta y, \Pi, \delta\right) = \left\langle \sqrt{\left(u^+_{\text{composite}}\left(u_\tau, \Delta y, \Pi, \delta\right) - u^+_{\text{exp}}\left(u_\tau\right)\right)^2} \right\rangle \tag{B.10}$$

In Figure B.2 an example of the composite fit for some experimental can be seen. The fit is generally good across the boundary layer. There is a slight deviation of the profile around $y^+ \leq 3$ due to the HWA cooling effects to the wall. It should be noted that a requirement for a proper fit of the viscous sublayer is a number of correct measurement points below $y^+ \leq 10$ (Chauhan et al., 2009; Rodríguez-López et al., 2015).

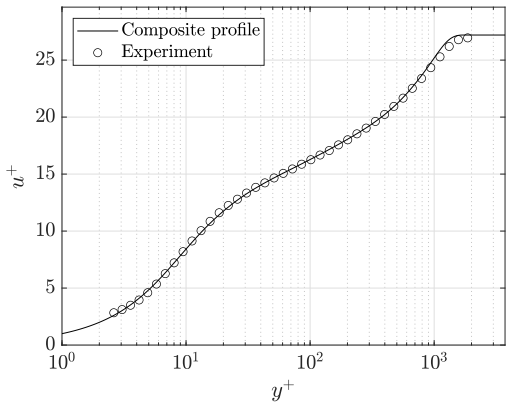

Figure B.2: An example of the composite fit method for HWA data at $U_\infty \approx 10 m/s$

B.3. Spectral analysis

Turbulence is a phenomenon which has a wide range of scales which can be found and assessed in the frequency domain. The high-frequency temporal signal of the HWA measurements can be transformed into frequency domain using the Fourier transform. This allows for identifying different modes of turbulence and characterising their relative importance in the overall flow. Two types of spectral analysis are performed in this thesis. Firstly, the creation of the boundary layer spectrogram, similar to Figure 2.9. The spectrogram shows the premultiplied spectral energy of the streamwise velocity fluctuation over the boundary layer height. Secondly, scale-decomposition is performed, similar to Figure 2.10; here the streamwise stress is decomposed into a small-scale component and a large-scale component.

Spectral analysis is performed by ensemble averaging using a sample size of $N = 2^{15}$, with a 50% overlap using Hanning windowing. A 5% moving bandwidth filter is applied to smooth out the frequency response. The spatial scales (i.e. wavenumber/wavelength) are calculated from the frequency using Taylor's hypothesis. To perform scale-decomposition, the frequency signal is low- and high-pass filtered at a wavelength of $\lambda_x^+ = 7{,}000$, and subsequently inverse Fourier transformed to obtain the small- and large-turbulent signal. An example of such a decomposition is presented in Figure B.3, which shows the raw fluctuations signal and the respective small- and large-scale components. Following the scale-decomposition, the corresponding stresses are found by taking the variance of the two respective signals.

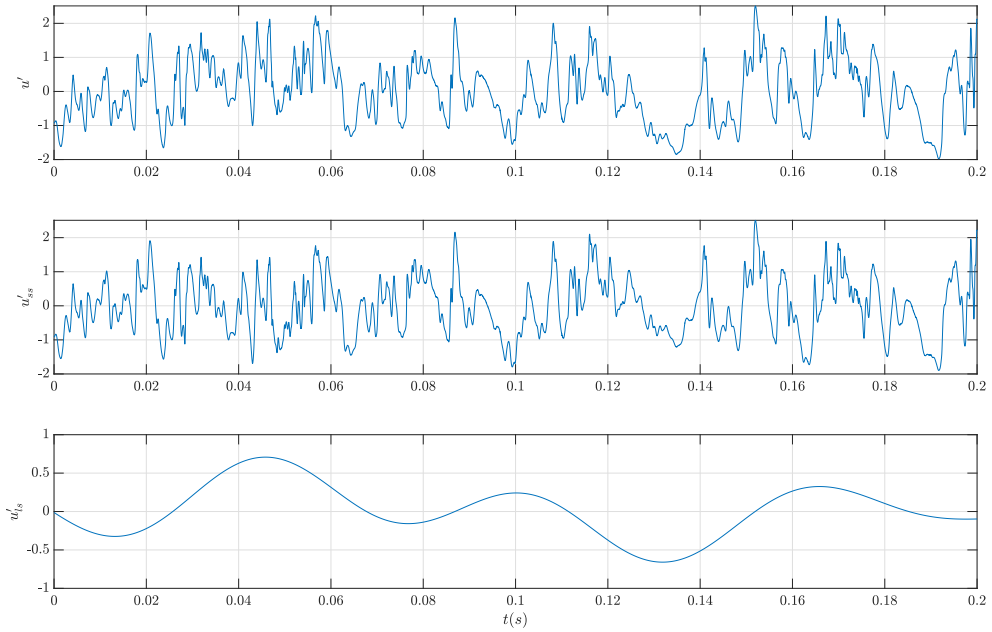

Figure B.3: An example of a time signal of the turbulent fluctuations u' and the scale-decomposed small- and large-scale signals, u'_{ss} and u'_{ls} respectively.

C

Post-processing procedures PIV

This appendix presents the post-processing procedure that is followed for the PIV data. Initial data processing is performed in DaVis10.2 to obtain the scalar-field. Post-processing of the raw scalar-fields is performed in Matlab.

C.1. DaVis vector calculations

This section presents the vector calculations performed to obtain velocity fields from the raw PIV images. Firstly, the calibration procedure is shortly discussed, and the details of the calibration errors are presented. Subsequently, image processing and vector calculations are discussed.

C.1.1. Stereo-calibration and self-calibration

Stereo calibration is performed using the LaVison calibration targets. FOV1-4 uses the type 7 calibration plate, and FOV5 the type 10. Calibration is made using the pinhole method. A self-calibration step is performed to further increase the accuracy of the calibration. Raffel et al. (2018) explains that in the self-calibration step, images at the same time instant from the two stereo cameras are cross-correlated. With this cross-correlation the disparity between the two cameras can be calculated, which is the mismatch or displacement of the same window between the cameras. This disparity is then reduced by applying an additional transformation to the original stereo-calibration. Using an iterative process, the disparity is decreased to improve the calibration. An example of the disparity maps at the start and end of the iterative procedure is presented in Figure C.1. It can be observed that there is a uniform disparity after the first cross-correlation. Following several iterations, the disparity is reduced significantly to a mean value below 1 px. An overview of the calibration fit-errors after self-calibration and the average remaining disparities for the five FOVs is presented in Table C.1.

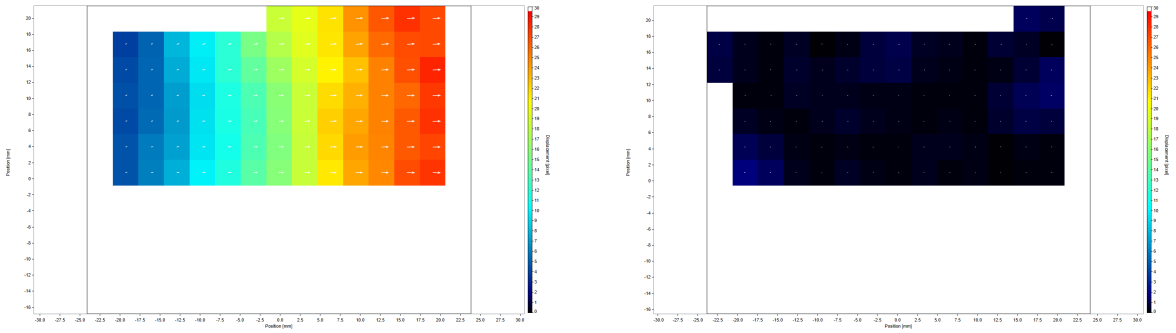

(a) First disparity map at the start of self-calibration

(b) Remaining disparity map after five iterations of self-calibration

Figure C.1: Disparity maps for FOV1 at the start and end of the self-calibration procedure. Colour scale ranges from 0-30 pixels displacement.

FOV	calibration fit error		average remaining disparity	
	(px)	(µm)	(px)	(µm)
1	0.029	0.477	0.386	6.44
2	0.245	2.16	1.601	14.1
3	0.190	1.67	1.437	12.6
4	0.152	1.42	2.76	25.8
5	0.090	3.44	2.428	93.8

Table C.1: Overview of the calibration fit errors and average remaining disparity, values presented in pixels and mm

C.1.2. Image processing and vector calculations

Image processing is performed in a number of steps. Firstly, the images are pre-processed to filter out the laser sheet's reflections on the surface. An example of such reflections can be observed in Figure C.2a and Figure C.2b for two snapshots of raw images from FOV1. From these images, it can be observed that the reflections change position along the streamwise direction. Due to the unsteadiness of the reflections, it was impossible to completely filter them out. The standard DaVis *image preprocessing* filter is used, which was found to give the best results. The first setting of the filter is *subtract minimum over time* with a filter length of 5 images. Following is a local *subtract sliding minimum* filter with a size of 3 px. This was found to result in the best pre-processed images. However, one can still observe the presence of the unsteady reflections in Figure C.2c and Figure C.2d.

Vector calculations are performed using standard cross-correlation. *Multi-pass vector calculations* are performed with an initial pass using square 96 px × 96 px interrogation windows and 75% overlap and two final-passes with circular 16 px × 16 px windows at 75% overlap. The *universal outlier-detection*, based on the method of Westerweel and Scarano (2005). 1× median filtering is applied, in a 7 px × 7 px filter region, vectors are removed for a residual below 2, and a minimum number of 5 vectors is required in the filter region.

Following the vector-calculations, the scalar-fields are calculated in DaVis. Scalar-fields are obtained for the three mean velocity components, their corresponding standard deviations and the respective uncertainties. The six components of the Reynolds stress are also calculated. These fields are exported to .dat files for further processing in Matlab.

C.2. Wall-estimation

In the post-processing of the data, the first step is to determine the location of the wall. One commonly used method for this is to use the reflection of the particles in the wall, which provides an accurate reflection of the mean velocity profile in the near-wall region. This technique has been employed by Kempaiah et al. (2020), who fit a polynomial to the inflection at the wall. The minimum of this curve corresponds to the estimated wall location. This process is performed over the streamwise field of view. Subsequently, a curve (e.g. a third order polynomial) can be fitted over the spatial extent the estimates to determine the wall location. However, due to the actuation surface's complexity, the measurements' reflections were distorted, making this method unsuitable for estimating the wall location.

Wall-estimation of the raw fields takes place in three steps. First, the streamwise space-averaged profile is used to obtain an approximate global wall location. There was a clear reflection in these space-averaged profiles, so the method explained above could be used.

The second step is to obtain the local estimate of the wall. The fact that the velocity profile is linear in the viscous sublayer is used. Based on this linearity, a fixed velocity in the viscous sublayer corresponds to a fixed wall-normal location. For the experiments the iso-velocity contour of $0.1U_\infty$ was used. This is within the viscous sublayer for all measurements since the maximum freestream velocity in viscous units is $U_\infty^+ \approx 27$. This gives the wall-normal height of said velocity contour. To obtain the wall location, the mean of the local wall-normal height is subtracted, resulting in a zero-centred wall offset location. Subsequently, the wall-offset is added to the global wall location resulting in the raw-wall estimate. Outlier filtering and smoothing is applied using a 5% sliding median to obtain a smooth distribution for the wall location. Following, the wall location is estimated using a linear polynomial. An example of the wall-estimation can be seen in Figure C.3. It can be observed that the wall-estimate is not completely uniform and shows variation; this is mainly attributed to irregularities and small steps due to the belts on the actuation surface.

The obtained wall location is used to correct the scalar fields, which is further elaborated in Section C.4, resulting in the corrected scalar-fields with a horizontal wall. A third additional step is to find the wall-offset,

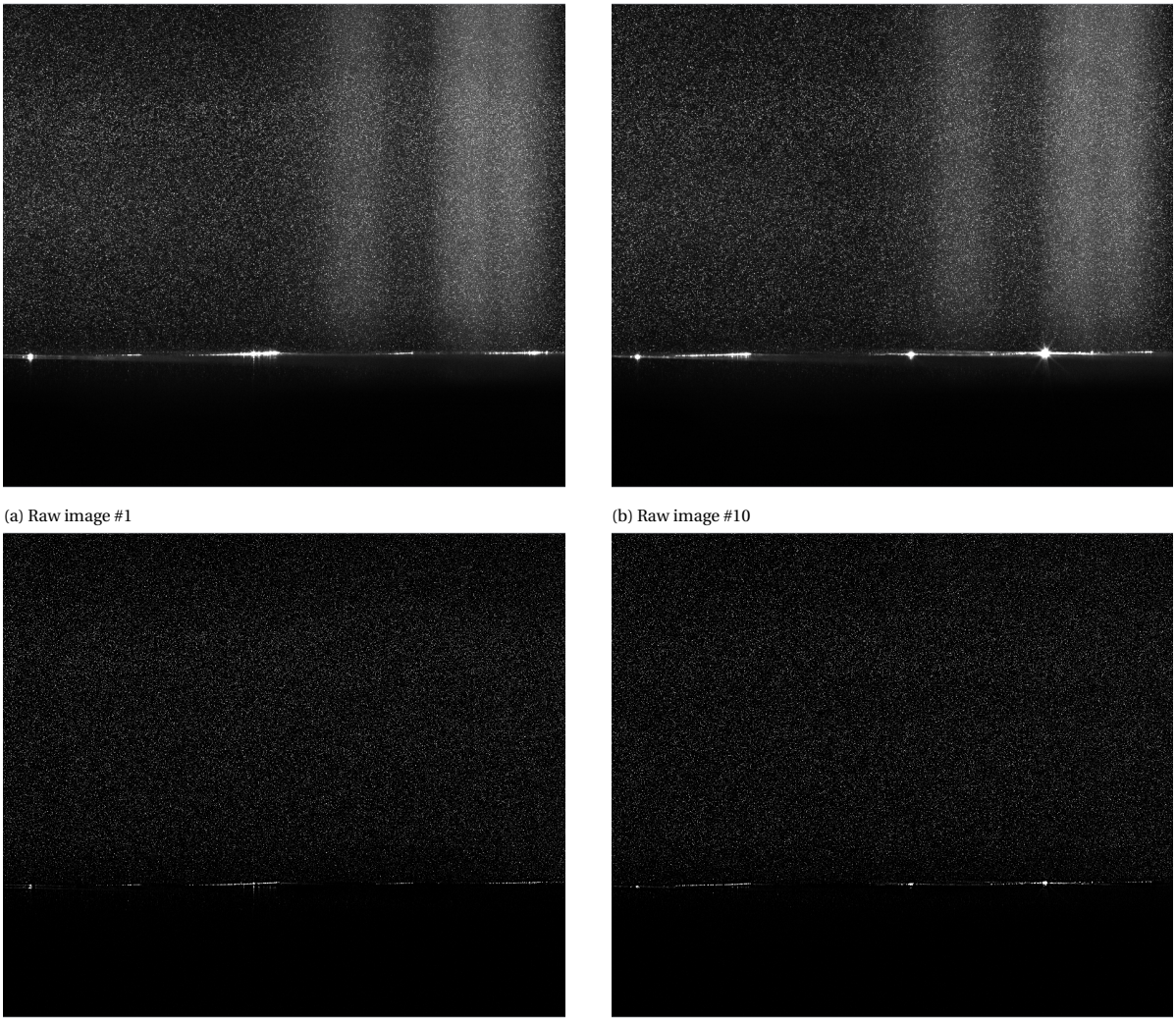

(a) Raw image #1

(b) Raw image #10

(c) Pre-processed image #1

(d) Pre-processed image #10

Figure C.2: Raw images and pre-processed images for two time instants in FOV1 at $\lambda_x^+ \approx 300$ and $A^+ \approx 12$.

if there is any, in the streamwise averaged profiles. The wall-offset Δy, is obtained from the boundary layer fit of the mean velocity profiles. The same fitting method is used for HWA measurements; further details can be found in Section B.2. The additional Δy is then added to the profiles. The wall-estimation is made for the non-actuated reference case and applied to the actuated cases.

C.3. Position-estimation

It is important to find the streamwise position of the belts to perform the analysis regarding the spatial transient of DR and the SSL. The position estimation process involves inserting a 50 µm shim between the belts and the surface plate and acquiring images at low laser light intensity. This generates a vertical reflection on the shim, which locates the edges of the belts. This process is repeated for all edges (eight in the case of FOV1), and the resulting images are dewarped using the calibration. The reflections are combined, and their intensity is normalised to create a final image. The resulting image can be seen in Figure C.4a. The horizontal lines are an artefact from the camera which only showed up when acquiring single images instead of image pairs. The intensity profile is obtained by averaging in wall-normal direction spanning ±200 px around the wall location, excluding the horizontal line artefacts. This intensity profile shows intensity peaks where the belt edges are located. Following this, the intensity profile is cross-correlated with the known theoretical positions to obtain a Δx offset with respect to the coordinates from DaVis. The cross-correlated intensity profile with the theoretical peaks can be seen in Figure C.4b. Regarding the accuracy of the position estimation, the

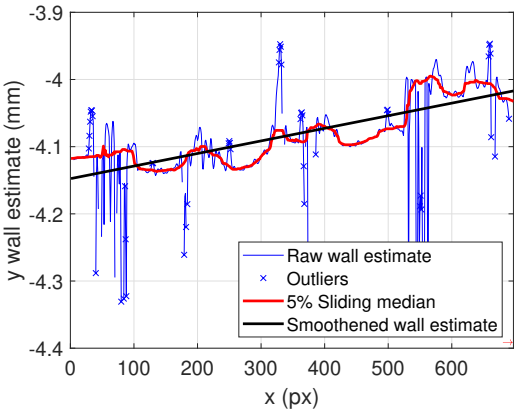

Figure C.3: Wall-estimation for FOV1 at $\lambda_x^+ \approx 300$

zero-crossings of the maximum cross-correlation peak are approximately 0.4-0.5 mm apart, depending on the FOV.

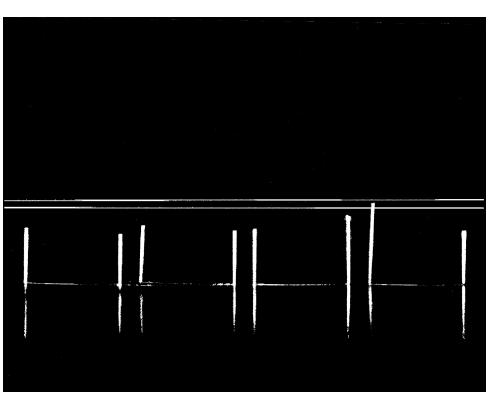

(a) Combined reflection images used for position estimation

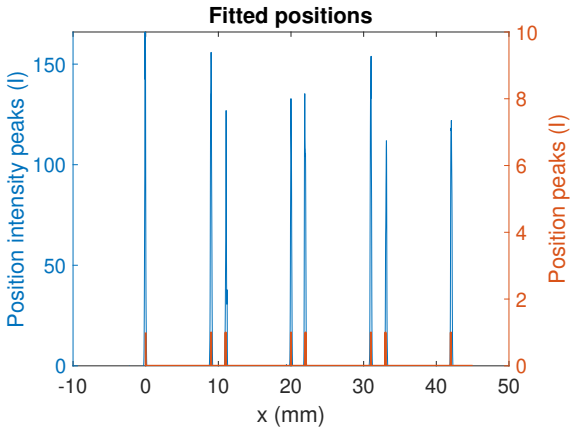

(b) Cross-correlated image intensity peaks with the theoretical positions

Figure C.4: Position estimation for FOV1

C.4. Scalar-field calculations and profiles

After performing the wall- and position-estimations, the scalar-fields are corrected using the wall-estimation. To achieve this, for each streamwise location, the raw scalar-fields are interpolated starting at $y = 0$, using the same vector pitch as the original image. A minimum number of 100 vectors is required for a valid vector in the scalar-fields. Figure C.5 shows an example of the raw- and corrected scalar-fields for the mean streamwise velocity. A selection of relevant scalar-fields that provide an overview of the measurements can be found in Section D.2.

The next step involves obtaining velocity and turbulence statistics profiles by space-averaging the data over the streamwise extent of the FOV. This approach is chosen to demonstrate the integral effect of actuation over the belts in a phase-averaged sense. To account for the phase-wise fluctuations in the spanwise stress component, the streamwise variance of the spanwise velocity field is added to the stochastic component (i.e. the temporal variance in the PIV images). The viscous scaling is obtained from boundary layer fitting using the same procedure as for the HWA data, as described in Section B.2. An example of the obtained velocity profiles is shown in Figure C.6. All profiles for FOV1 and FOV2 can be found in Section D.3.

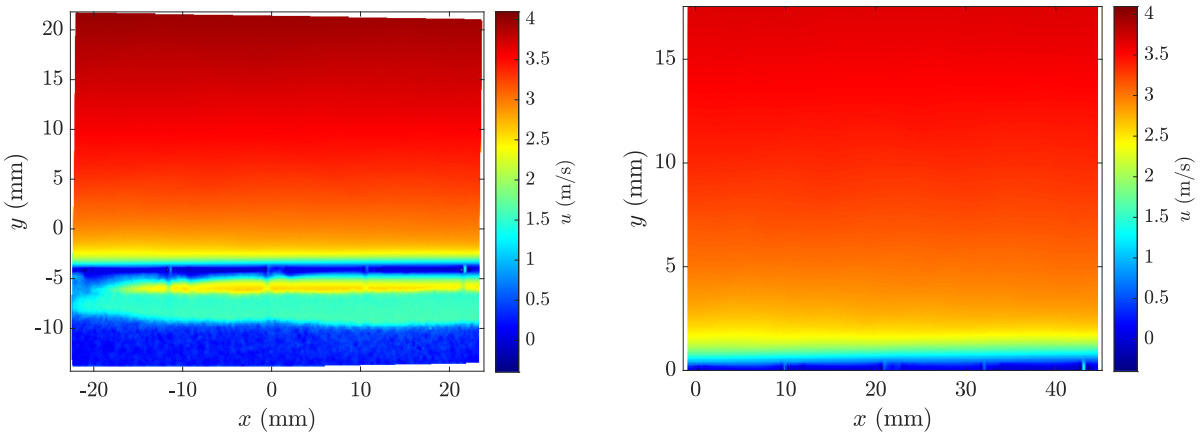

(a) Raw

(b) Corrected

Figure C.5: An example of the raw and corrected scalar-fields of the mean streamwise velocity for FOV1 at $\lambda_x^+ \approx 300$ and $A^+ \approx 12$.

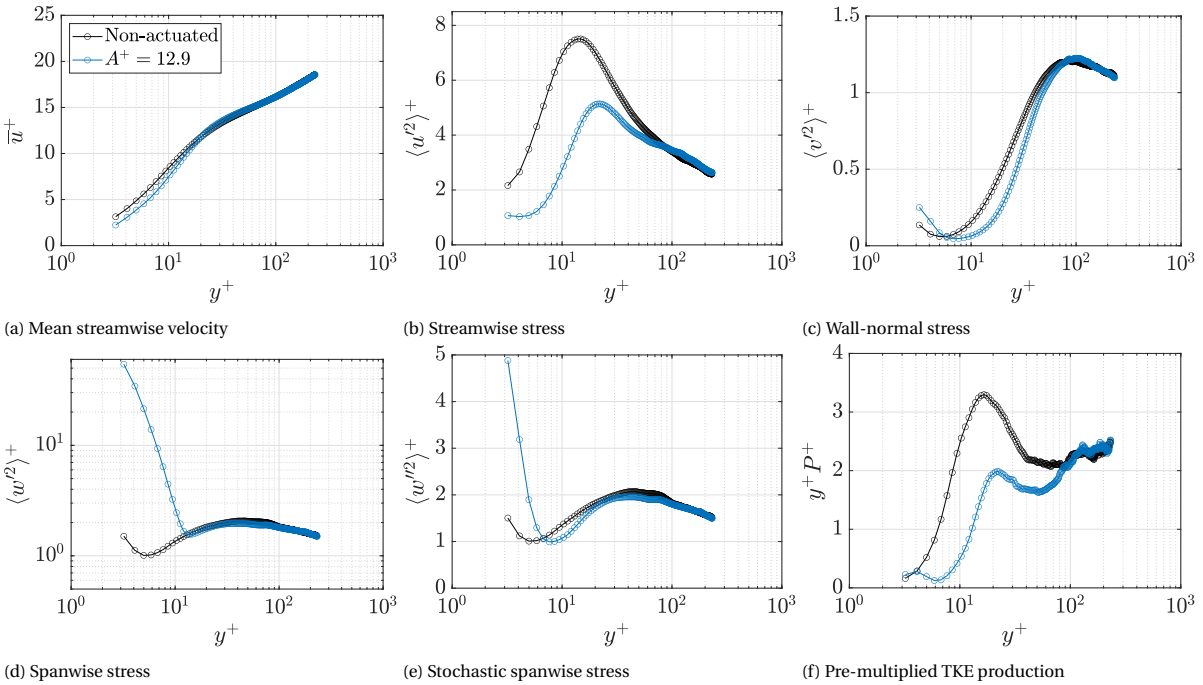

(a) Mean streamwise velocity

(b) Streamwise stress

(c) Wall-normal stress

(d) Spanwise stress

(e) Stochastic spanwise stress

(f) Pre-multiplied TKE production

Figure C.6: Profiles for FOV1 at $\lambda_x^+ \approx 300$

D

Additional PIV results

This appendix presents additional PIV results to the work from Part III. An overview of all the performed measurements is given in Section D.1. A selection of relevant scalar-fields is presented in Section D.2, in both dimensional and non-dimensional form. The turbulence statistics profiles of FOV1 and FOV2 for each considered wavelength can be found in Section D.3. The DR estimation from FOV2 is presented in Section D.4. Lastly, uncertainty quantification is performed on all measurements in Section D.5.

D.1. Overview of the measurements

This section presents an overview of the PIV measurements in Table D.1. Firstly, the FOV and time separation dt are indicated. Following the tunnel conditions and boundary layer properties are indicated. The friction velocity, boundary layer thickness and frictional Reynolds number for the non-actuated case are displayed. Since FOV1-4 only capture the inner-layer, δ is estimated implicitly from a power law fit between Re_1 and δ using the three non-actuated measurements in FOV5. The power law curve and the corresponding relation are presented in Figure D.1 and Equation D.1. Lastly, the actuation parameters are indicated. Config indicates the belt rotational configuration, starting from the first belt and moving downstream, the letters L and R correspond to a left (positive spanwise direction) or right (negative spanwise direction) rotational direction, 0 indicates that the belt is not running. The spanwise velocity amplitude and wavelength are shown in dimensional and non-dimensional forms.

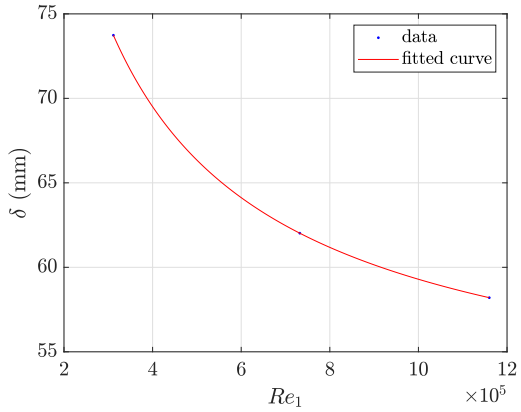

Figure D.1: Power law relation between Re_1 and δ from FOV5

$$\delta = 185.9 Re_1^{-0.7022} + 0.04791 \tag{D.1}$$

ID	FOV	dt (µs)	U_∞ (m/s)	$u_{\tau 0}$ (m/s)	δ (mm)	Re_τ	Config	A (m/s)	A^+	λ_x (mm)	λ_x^+
01	1	34	4.7	0.2	73.7	980	-	-	-	-	-
02	1	34	4.7	0.2	73.7	981	LRLR	2.6	12.9	22	293
03	1	23	6.7	0.27	67.7	1,230	-	-	-	-	-
04	1	23	6.7	0.27	67.7	1,230	LRLR	1.1	4.2	22	400
05	1	23	6.7	0.27	67.8	1,230	LRLR	2.3	8.4	22	400
06	1	23	6.7	0.27	67.8	1,230	LRLR	3.4	12.6	22	400
07	1	23	6.7	0.27	67.7	1,230	RLRL	3.4	12.6	22	400
08	1	23	6.7	0.27	67.7	1,230	LLLL	3.4	12.6	22	400
09	1	23	6.7	0.27	67.7	1,230	L0L0	3.4	12.6	22	400
10	1	18	8.8	0.34	64.3	1,480	-	-	-	-	-
11	1	18	8.8	0.34	64.3	1,480	LRLR	4.3	12.5	22	505
12	1	14	10.9	0.41	62	1,720	-	-	-	-	-
13	1	14	10.9	0.41	62	1,720	LRLR	3.4	8.2	22	611
14	1	14	10.9	0.41	62	1,720	LRLR	5.1	12.4	22	610
15	1	10	15.2	0.56	59.1	2,220	-	-	-	-	-
16	1	10	15.2	0.56	59.1	2,220	LRLR	4.5	8.1	22	826
17	1	34	4.6	0.19	73.7	963	-	-	-	-	-
18	1	34	4.7	0.19	73.7	962	LLRR	1.7	8.7	44	574
19	1	34	4.6	0.19	73.7	962	LLRR	2.6	13.1	44	574
20	1	23	6.7	0.27	67.8	1,220	-	-	-	-	-
21	1	23	6.7	0.27	67.7	1,220	LLRR	1.1	4.2	44	792
22	1	23	6.7	0.27	67.8	1,220	LLRR	2.3	8.4	44	792
23	1	23	6.7	0.27	67.7	1,220	LLRR	3.4	12.7	44	792
24	2	34	4.6	0.2	73.7	977	-	-	-	-	-
25	2	34	4.6	0.2	73.7	977	LRLR	1.7	8.7	22	292
26	2	34	4.6	0.2	73.7	977	LRLR	2.6	13	22	292
27	2	23	6.7	0.27	67.8	1,230	-	-	-	-	-
28	2	23	6.7	0.27	67.8	1,230	LRLR	0.6	2.1	22	401
29	2	23	6.7	0.27	67.8	1,230	LRLR	1.1	4.2	22	400
30	2	23	6.7	0.27	67.7	1,230	LRLR	1.7	6.3	22	400
31	2	23	6.7	0.27	67.7	1,230	LRLR	2.3	8.4	22	400
32	2	23	6.7	0.27	67.8	1,230	LRLR	2.8	10.5	22	400
33	2	23	6.7	0.27	67.8	1,230	LRLR	3.4	12.6	22	400
34	2	18	8.8	0.34	64.3	1,480	-	-	-	-	-
35	2	18	8.8	0.34	64.3	1,480	LRLR	2.8	8.3	22	505
36	2	18	8.8	0.34	64.3	1,480	LRLR	4.3	12.5	22	505
37	2	14	10.9	0.42	62	1,740	-	-	-	-	-
38	2	14	10.9	0.42	62	1,740	LRLR	1.7	4.1	22	616
39	2	14	10.9	0.42	62	1,740	LRLR	3.4	8.2	22	616
40	2	14	10.9	0.42	62	1,740	LRLR	5.1	12.3	22	616
41	2	12	13	0.49	60.4	1,980	-	-	-	-	-
42	2	12	13	0.49	60.4	1,980	LRLR	4.0	8.1	22	721
43	2	10	15.2	0.56	59.1	2,220	-	-	-	-	-
44	2	10	15.2	0.56	59.1	2,220	LRLR	2.3	4.1	22	827
45	2	10	15.2	0.56	59.1	2,220	LRLR	4.5	8.1	22	826
46	2	9	17.3	0.63	58.2	2,460	-	-	-	-	-
47	2	9	17.3	0.63	58.2	2,460	LRLR	5.1	8.1	22	930
48	3	23	6.7	0.27	67.7	1,230	-	-	-	-	-
49	3	23	6.7	0.27	67.7	1,230	LRLR	2.3	8.4	22	398
50	3	23	6.7	0.27	67.7	1,230	LRLR	3.4	12.7	22	398
51	3	14	10.9	0.41	62	1,710	-	-	0	-	0
52	3	14	10.9	0.41	62	1,710	LRLR	3.4	8.3	22	605
53	3	14	10.9	0.41	62	1,710	LRLR	5.1	12.5	22	605
54	4	23	6.6	0.27	67.7	1,230	-	-	-	-	-

ID	FOV	dt (µs)	U_∞ (m/s)	$u_{\tau 0}$ (m/s)	δ (mm)	Re_τ	Config	A (m/s)	A^+	λ_x (mm)	λ_x^+
55	4	23	6.6	0.27	67.7	1,230	LRLR	2.3	8.5	22	401
56	4	23	6.6	0.27	67.7	1,230	LRLR	3.4	12.7	22	401
57	4	14	10.7	0.41	62	1,730	-	-	-	-	-
58	4	14	10.7	0.41	62	1,730	LRLR	3.4	8.3	22	612
59	4	14	10.7	0.41	62	1,720	LRLR	5.1	12.5	22	612
60	5	81	4.6	0.19	73.7	960	-	-	-	-	-
61	5	81	4.6	0.19	73.7	960	LRLR	1.3	6.6	22	286
62	5	35	10.8	0.41	62	1,720	-	-	-	-	-
63	5	35	10.8	0.41	62	1,720	LRLR	2.6	6.2	22	610
64	5	22	17.1	0.63	58.2	2,470	-	-	-	-	-
65	5	22	17.1	0.63	58.2	2,470	LRLR	3.8	6.1	22	934

Table D.1: Overview of the performed PIV measurements

D.2. Overview of the scalar-fields

This section presents an overview of the scalar-fields of the measurements. To give an impression of the data quality, dimensional scalar-fields are provided. Three fields are considered; the absolute mean velocity, their standard deviation and a randomly selected instantaneous snapshot. The non-dimensional fields show three of the most relevant turbulence statistics; the mean spanwise velocity, the streamwise stress, and the spanwise stress. The y^+ axis is scaled logarithmically. For brevity, not all measurements are presented. For FOV1-4, all measurements for $\lambda_x^+ \approx 400$ are provided. Furthermore, to give an idea of the quality at higher freestream velocities, the fields of FOV1-2 at $\lambda_x^+ \approx 800$, showing both the non-actuated case and $A^+ = 8$. For FOV5, The non-actuated cases at $\lambda_x^+ \approx 300$, 600, and 900 are presented.

D.2.1. Dimensional fields

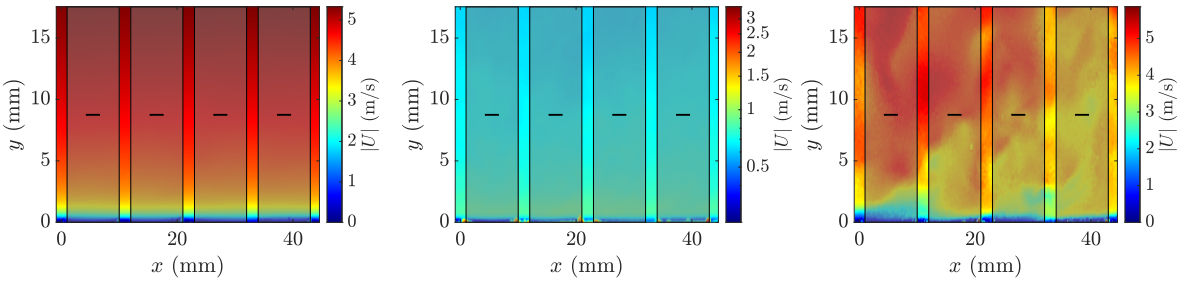

(a) Mean velocity (b) Standard deviation (c) Instantaneous velocity

Figure D.2: ID 03, FOV1, non-actuated, $\lambda_x^+ = 400$

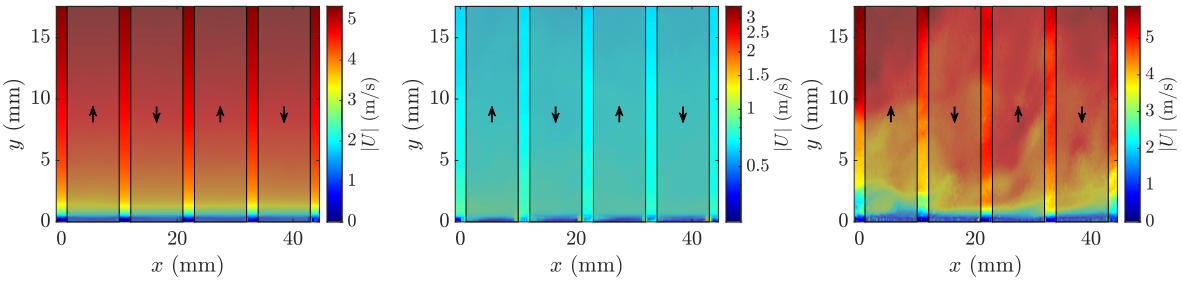

(a) Mean velocity (b) Standard deviation (c) Instantaneous velocity

Figure D.3: ID 04, FOV1, $A^+ = 4.2$, $\lambda_x^+ = 400$

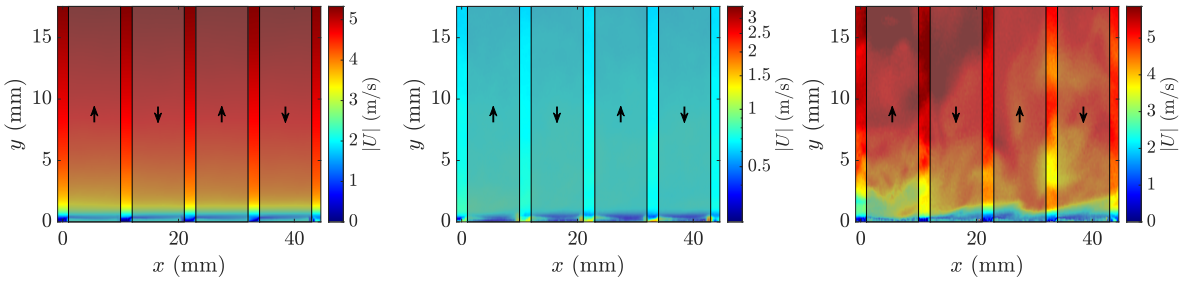

(a) Mean velocity (b) Standard deviation (c) Instantaneous velocity

Figure D.4: ID 05, FOV1, $A^+ = 8.4$, $\lambda_x^+ = 400$

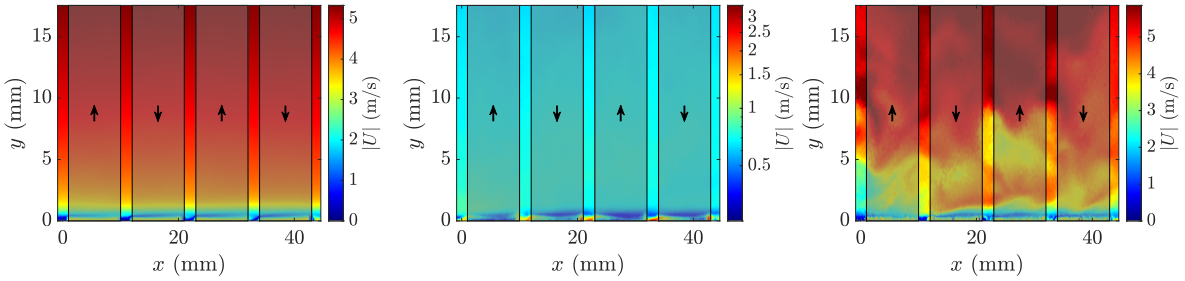

(a) Mean velocity (b) Standard deviation (c) Instantaneous velocity

Figure D.5: ID 06, FOV1, $A^+ = 12.6$, $\lambda_x^+ = 400$

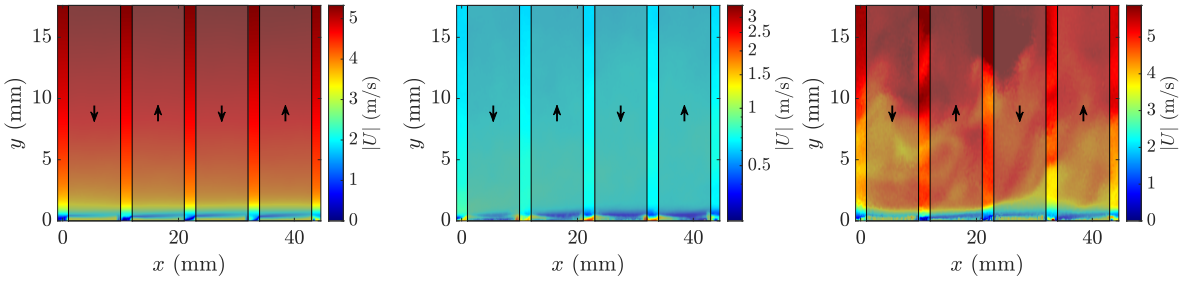

(a) Mean velocity (b) Standard deviation (c) Instantaneous velocity

Figure D.6: ID 07, FOV1, config RLRL, $A^+ = 12.6$, $\lambda_x^+ = 400$

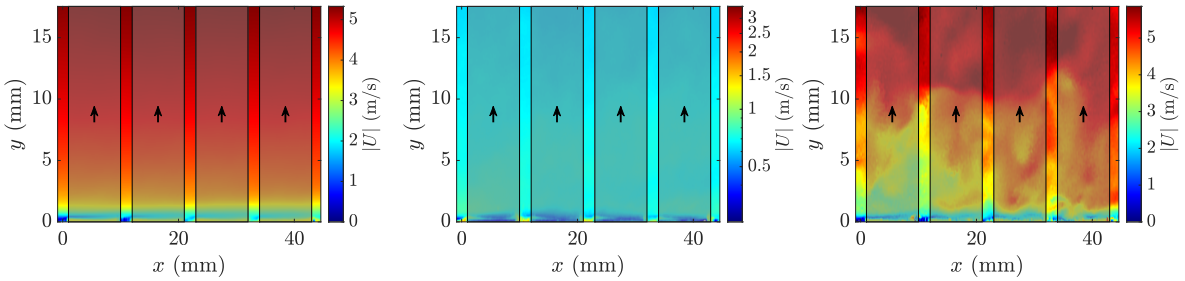

(a) Mean velocity (b) Standard deviation (c) Instantaneous velocity

Figure D.7: ID 08, FOV1, config LLLL, $A^+ = 12.6$, $\lambda_x^+ = 400$

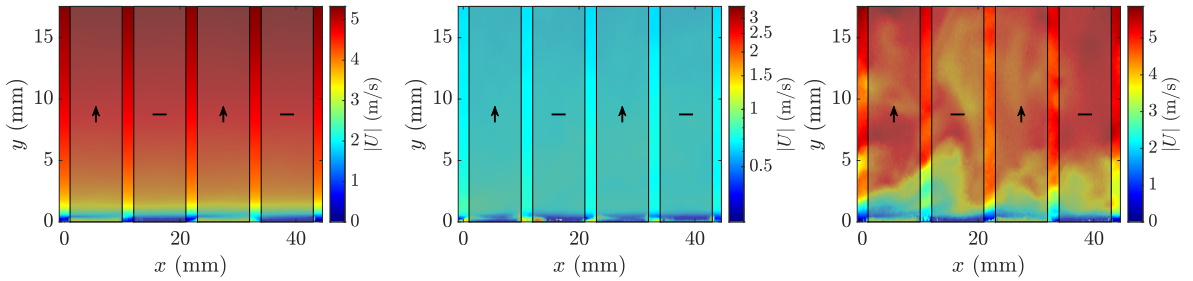

(a) Mean velocity (b) Standard deviation (c) Instantaneous velocity

Figure D.8: ID 09, FOV1, config L0L0, $A^+ = 12.6$, $\lambda_x^+ = 400$

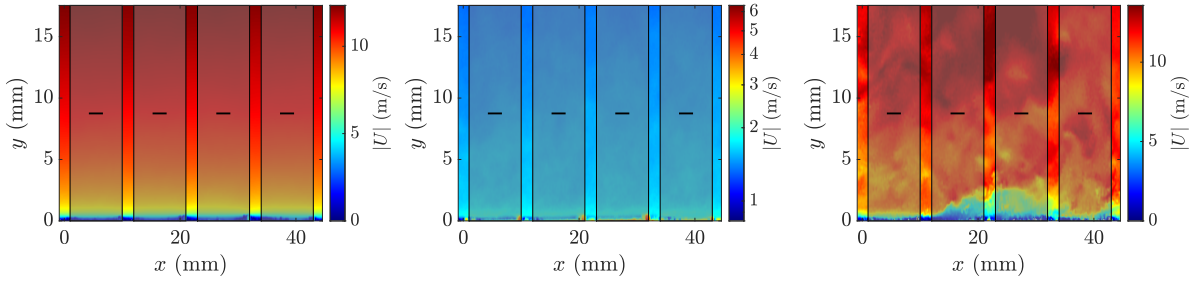

(a) Mean velocity (b) Standard deviation (c) Instantaneous velocity

Figure D.9: ID 15, FOV1, non-actuated, $\lambda_x^+ = 826$

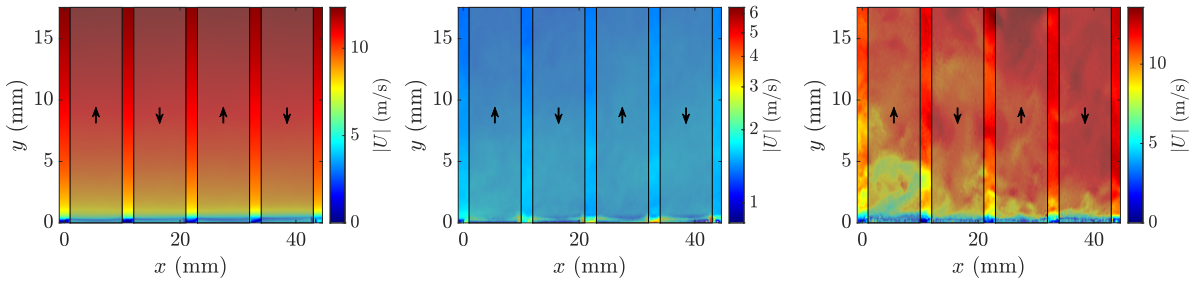

(a) Mean velocity (b) Standard deviation (c) Instantaneous velocity

Figure D.10: ID 16, FOV1, $A^+ = 8.1$, $\lambda_x^+ = 826$

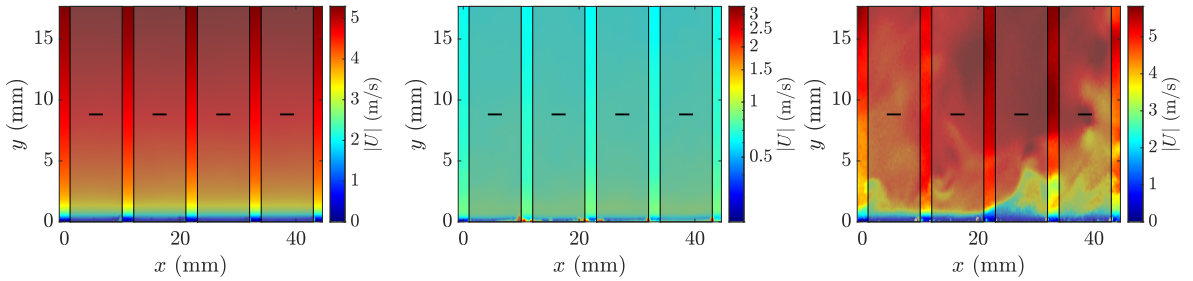

(a) Mean velocity (b) Standard deviation (c) Instantaneous velocity

Figure D.11: ID 20, FOV1, config LLRR with $\lambda_x = 44$ mm, non-actuated, $\lambda_x^+ = 826$

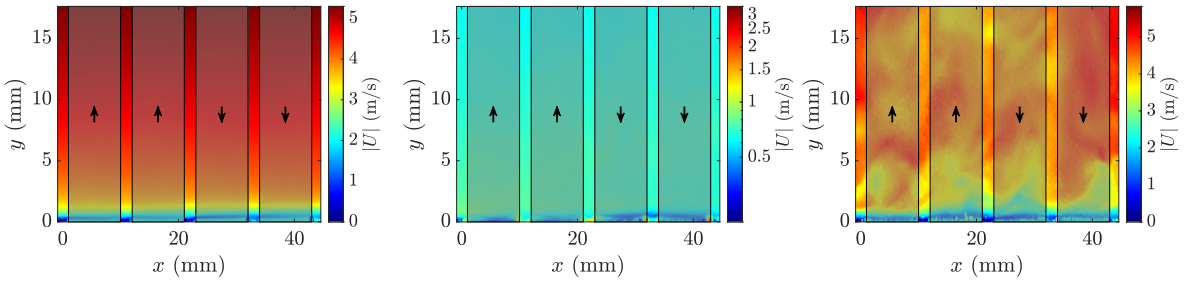

(a) Mean velocity (b) Standard deviation (c) Instantaneous velocity

Figure D.12: ID 22, FOV1, config LLRR with $\lambda_x = 44$ mm, $A^+ = 8.4$ $\lambda_x^+ = 826$

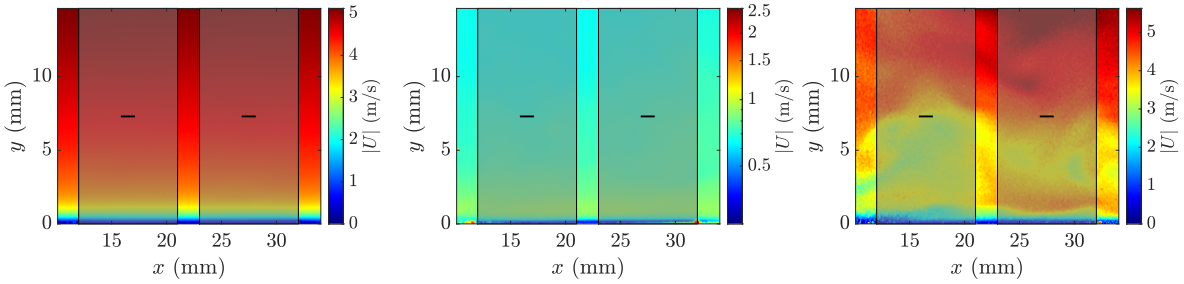

(a) Mean velocity (b) Standard deviation (c) Instantaneous velocity

Figure D.13: ID 27, FOV2, non-actuated, $\lambda_x^+ = 400$

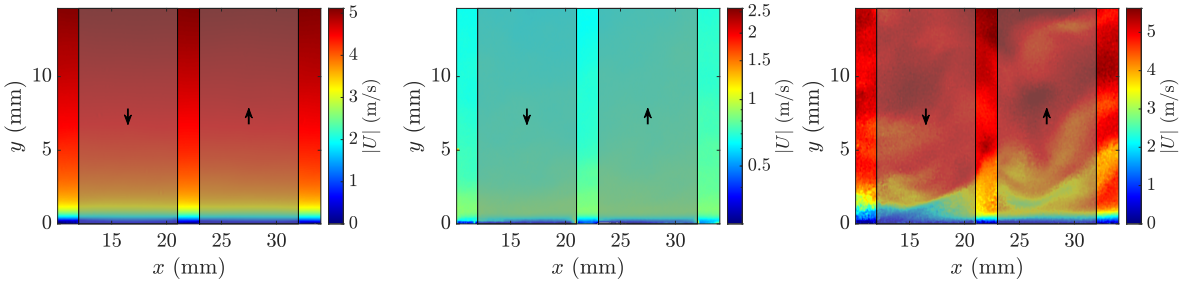

(a) Mean velocity (b) Standard deviation (c) Instantaneous velocity

Figure D.14: ID 28, FOV2, $A^+ = 2.1$, $\lambda_x^+ = 400$

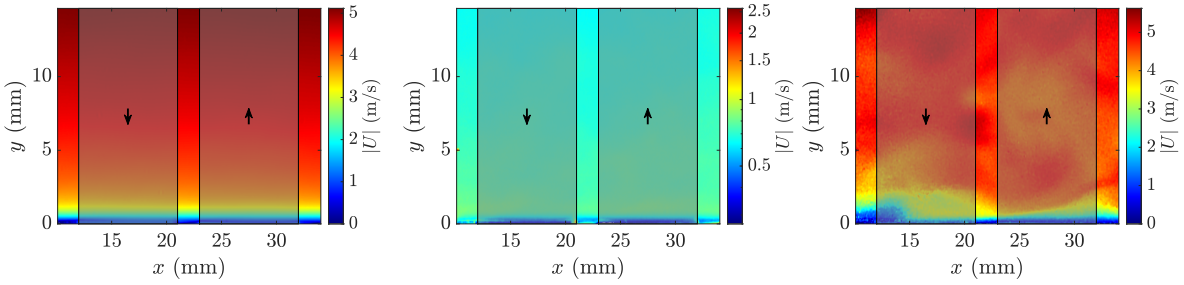

(a) Mean velocity (b) Standard deviation (c) Instantaneous velocity

Figure D.15: ID 29, FOV2, $A^+ = 4.2$, $\lambda_x^+ = 400$

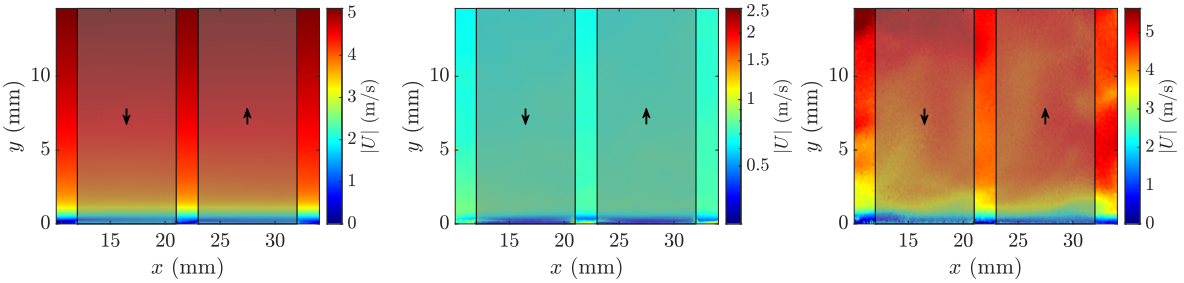

(a) Mean velocity (b) Standard deviation (c) Instantaneous velocity

Figure D.16: ID 30, FOV2, $A^+ = 6.3$, $\lambda_x^+ = 400$

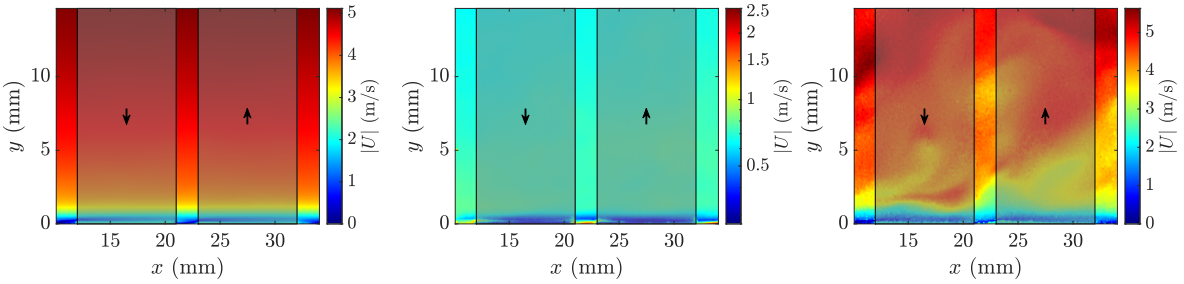

(a) Mean velocity (b) Standard deviation (c) Instantaneous velocity

Figure D.17: ID 31, FOV2, $A^+ = 8.4$, $\lambda_x^+ = 400$

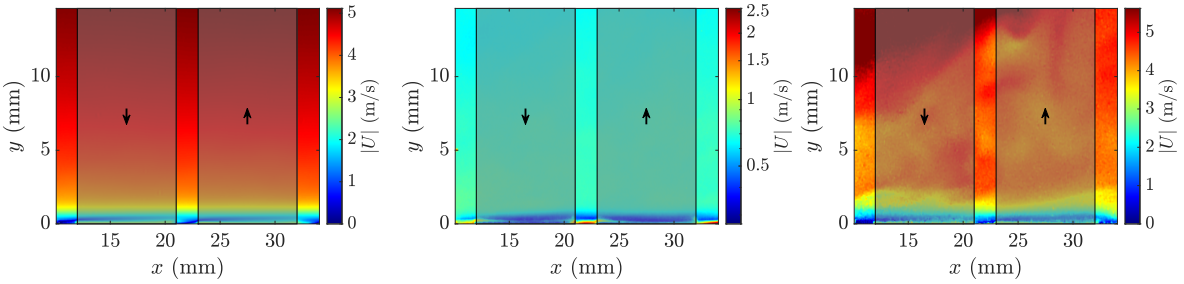

(a) Mean velocity (b) Standard deviation (c) Instantaneous velocity

Figure D.18: ID 32, FOV2, $A^+ = 10.5$, $\lambda_x^+ = 400$

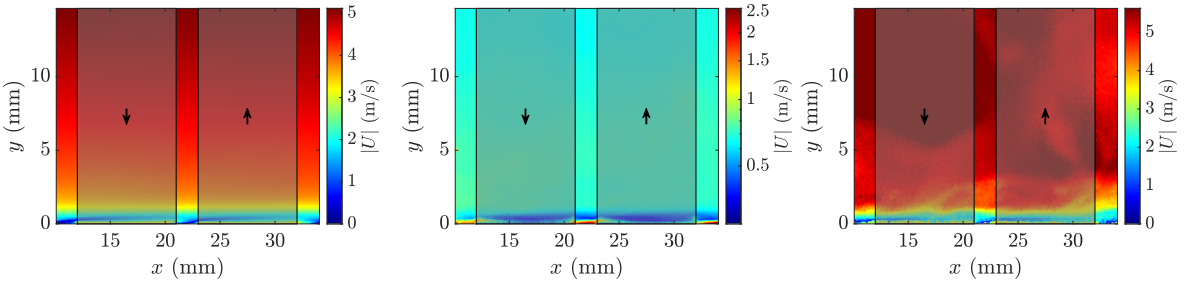

(a) Mean velocity (b) Standard deviation (c) Instantaneous velocity

Figure D.19: ID 33, FOV2, $A^+ = 12.6$, $\lambda_x^+ = 400$

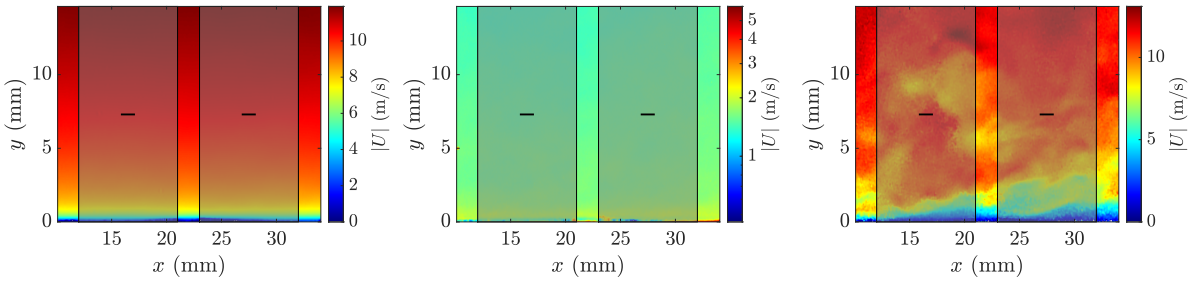

(a) Mean velocity (b) Standard deviation (c) Instantaneous velocity

Figure D.20: ID 43, FOV2, non-actuated, $\lambda_x^+ = 826$

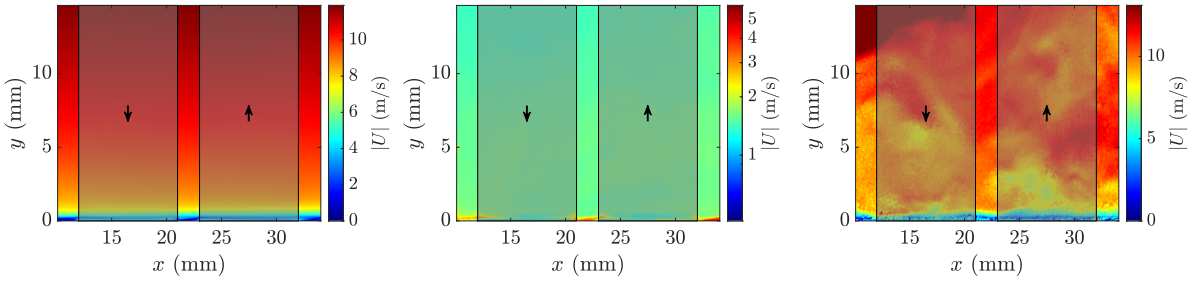

(a) Mean velocity (b) Standard deviation (c) Instantaneous velocity

Figure D.21: ID 45, FOV2, $A^+ = 8.1$, $\lambda_x^+ = 826$

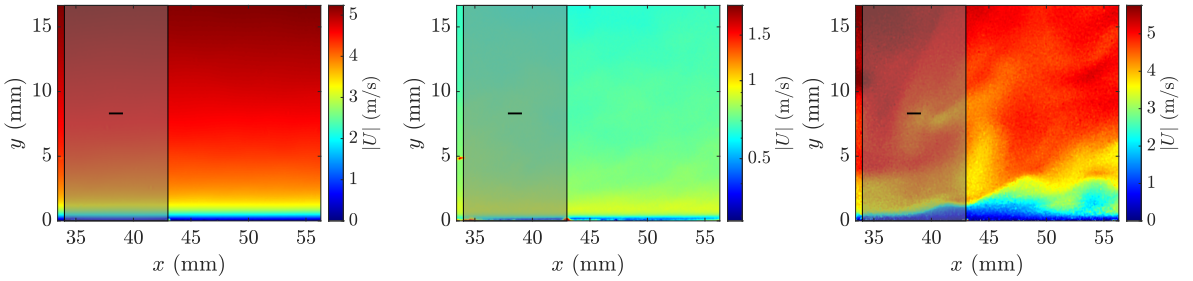

(a) Mean velocity (b) Standard deviation (c) Instantaneous velocity

Figure D.22: ID 48, FOV3, non-actuated, $\lambda_x^+ = 398$

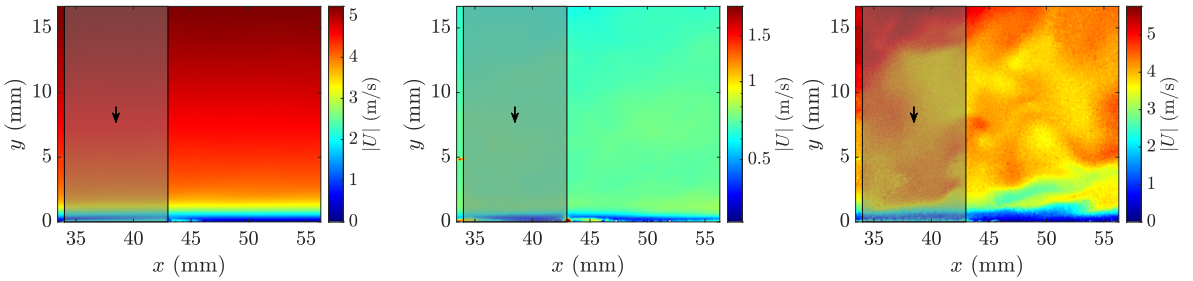

(a) Mean velocity (b) Standard deviation (c) Instantaneous velocity

Figure D.23: ID 49, FOV3, $A^+ = 8.4$, $\lambda_x^+ = 398$

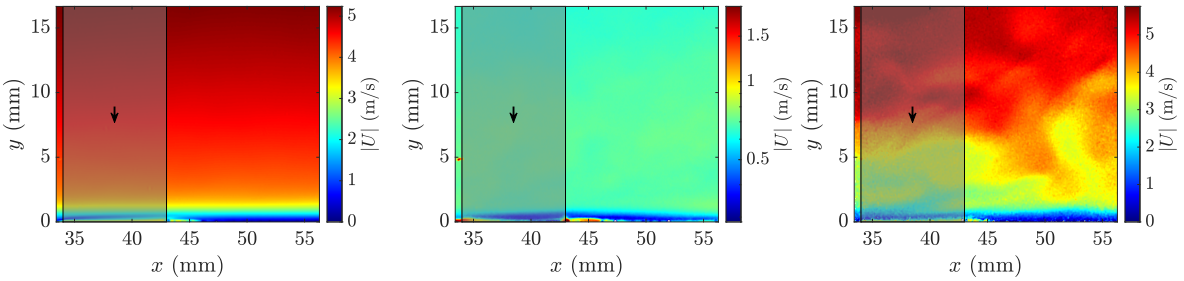

(a) Mean velocity (b) Standard deviation (c) Instantaneous velocity

Figure D.24: ID 50, FOV3, $A^+ = 12.5$, $\lambda_x^+ = 398$

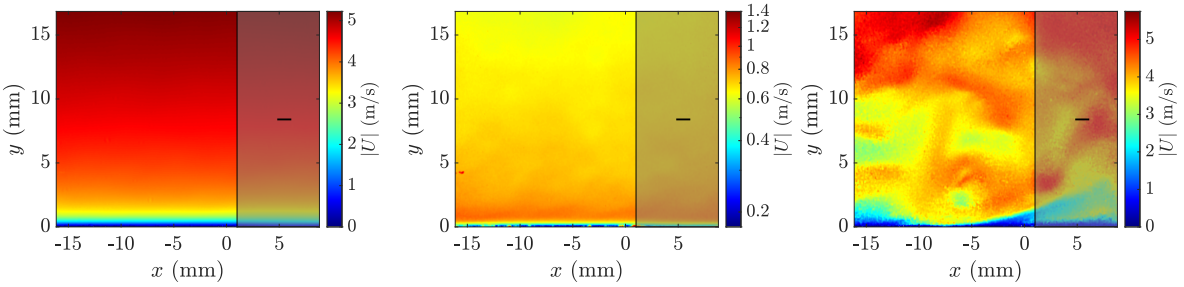

(a) Mean velocity (b) Standard deviation (c) Instantaneous velocity

Figure D.25: ID 54, FOV4, non-actuated, $\lambda_x^+ = 398$

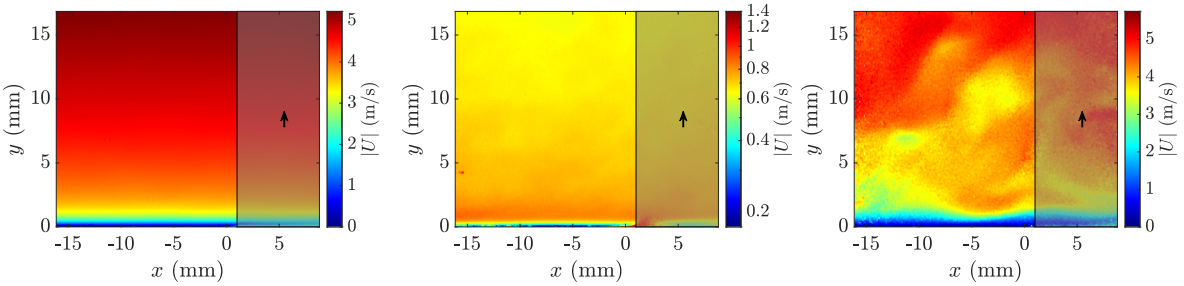

(a) Mean velocity (b) Standard deviation (c) Instantaneous velocity

Figure D.26: ID 55, FOV4, $A^+ = 8.5$, $\lambda_x^+ = 401$

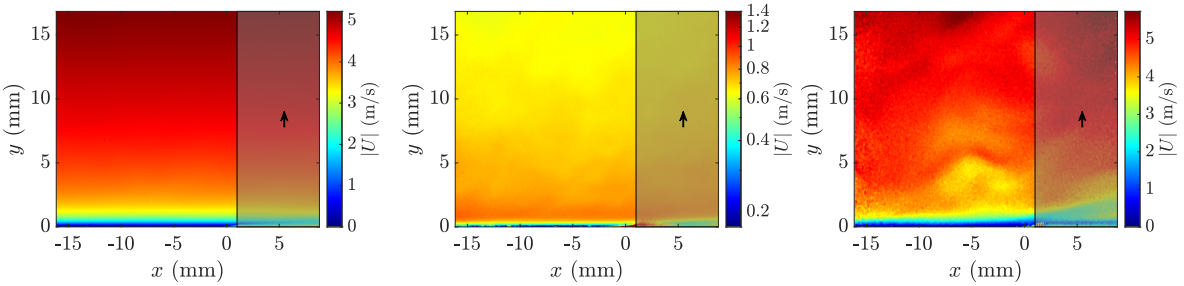

(a) Mean velocity (b) Standard deviation (c) Instantaneous velocity

Figure D.27: ID 56, FOV4, $A^+ = 12.7$, $\lambda_x^+ = 401$

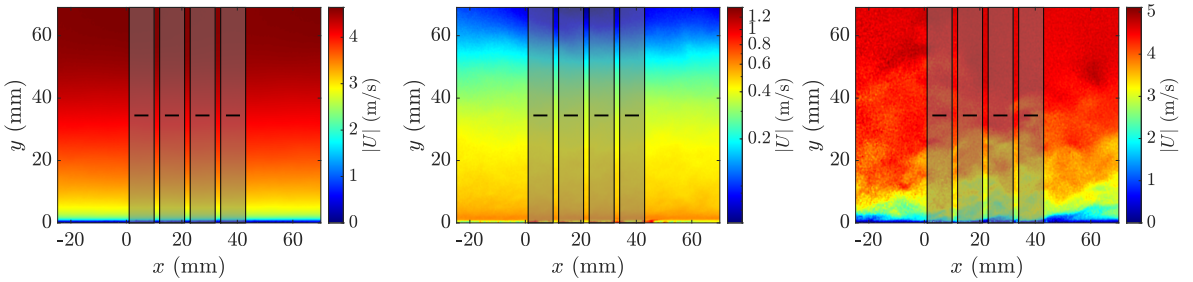

(a) Mean velocity (b) Standard deviation (c) Instantaneous velocity

Figure D.28: ID 60, FOV5, non-actuated, $\lambda_x^+ = 286$

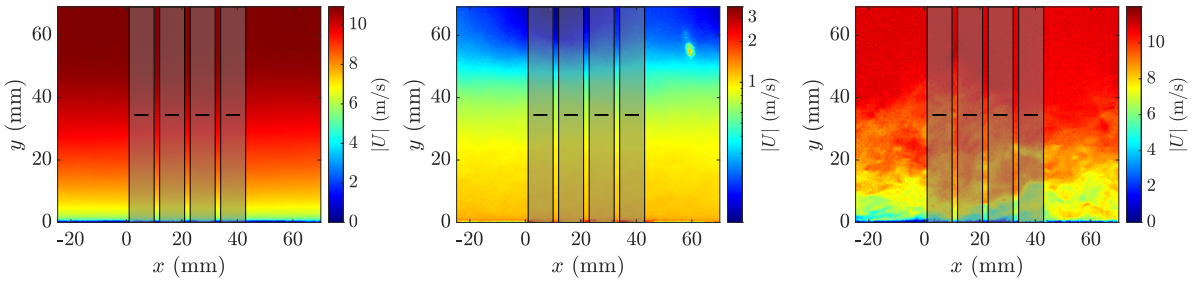

(a) Mean velocity (b) Standard deviation (c) Instantaneous velocity

Figure D.29: ID 62, FOV5, non-actuated, $\lambda_x^+ = 610$

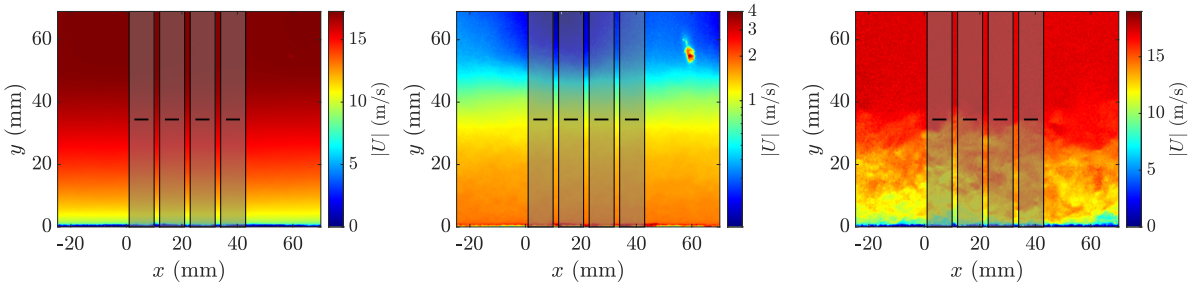

(a) Mean velocity (b) Standard deviation (c) Instantaneous velocity

Figure D.30: ID 64, FOV5, non-actuated, $\lambda_x^+ = 934$

D.2.2. Non-dimensional fields

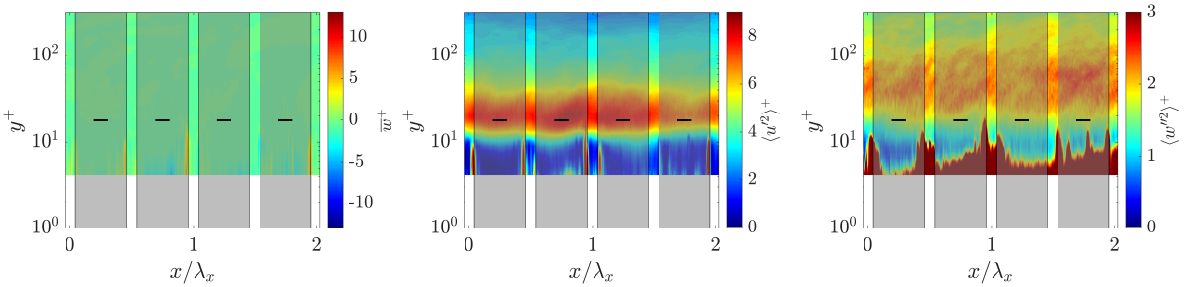

(a) Mean spanwise velocity (b) Streamwise stress (c) Spanwise stress

Figure D.31: ID 03, FOV1, non-actuated, $\lambda_x^+ = 400$

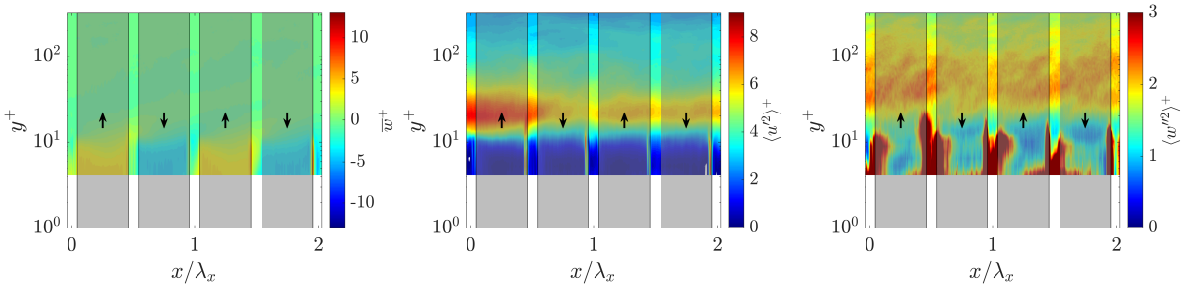

(a) Mean spanwise velocity (b) Streamwise stress (c) Spanwise stress

Figure D.32: ID 04, FOV1, $A^+ = 4.2$, $\lambda_x^+ = 400$

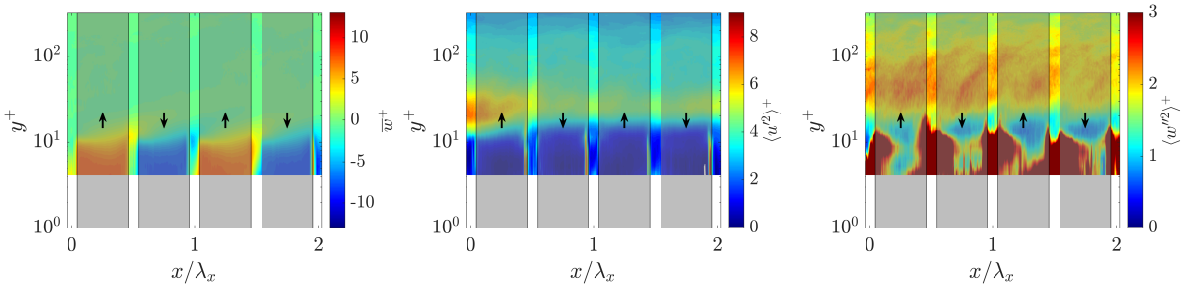

(a) Mean spanwise velocity (b) Streamwise stress (c) Spanwise stress

Figure D.33: ID 05, FOV1, $A^+ = 8.4$, $\lambda_x^+ = 400$

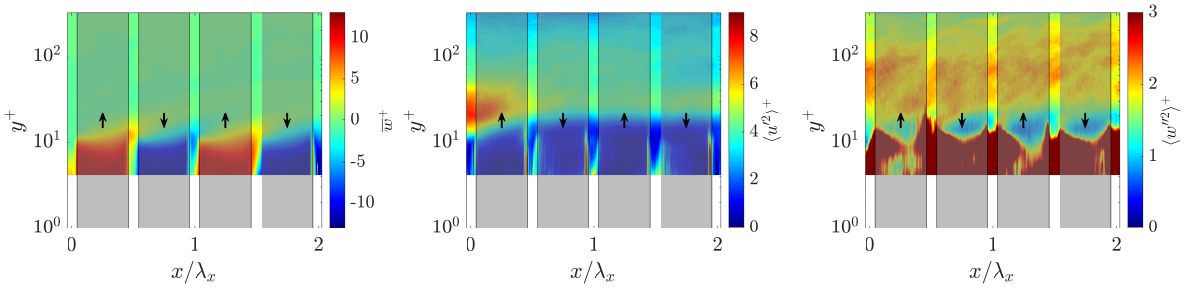

(a) Mean spanwise velocity (b) Streamwise stress (c) Spanwise stress

Figure D.34: ID 06, FOV1, $A^+ = 12.6$, $\lambda_x^+ = 400$

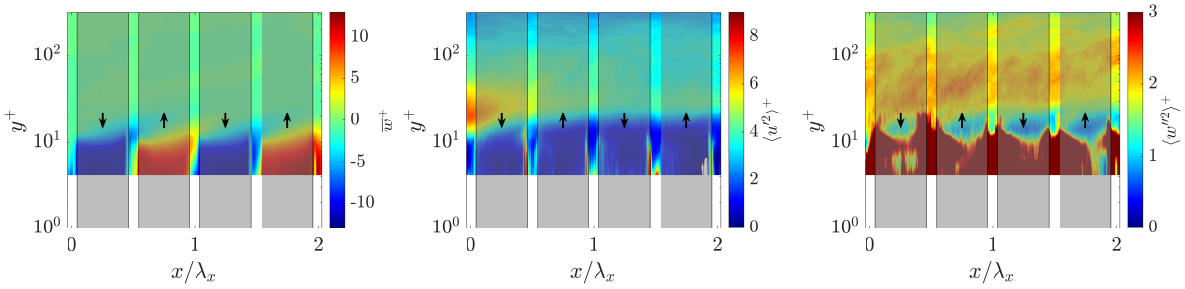

(a) Mean spanwise velocity (b) Streamwise stress (c) Spanwise stress

Figure D.35: ID 07, FOV1, config RLRL, $A^+ = 12.6$, $\lambda_x^+ = 400$

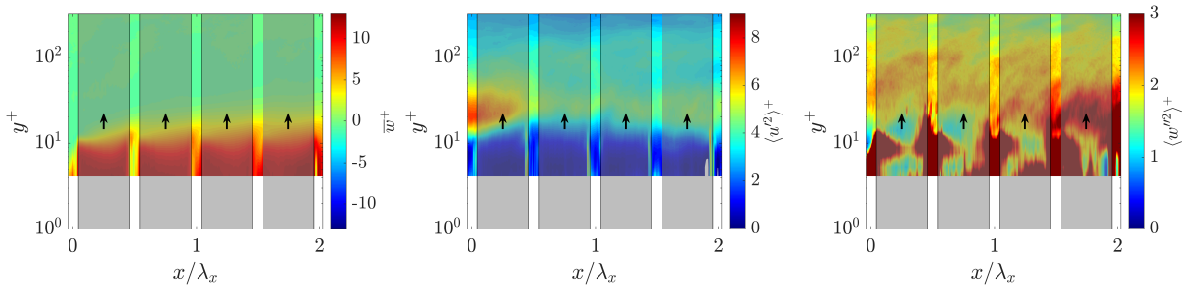

(a) Mean spanwise velocity (b) Streamwise stress (c) Spanwise stress

Figure D.36: ID 08, FOV1, config LLLL, $A^+ = 12.6$, $\lambda_x^+ = 400$

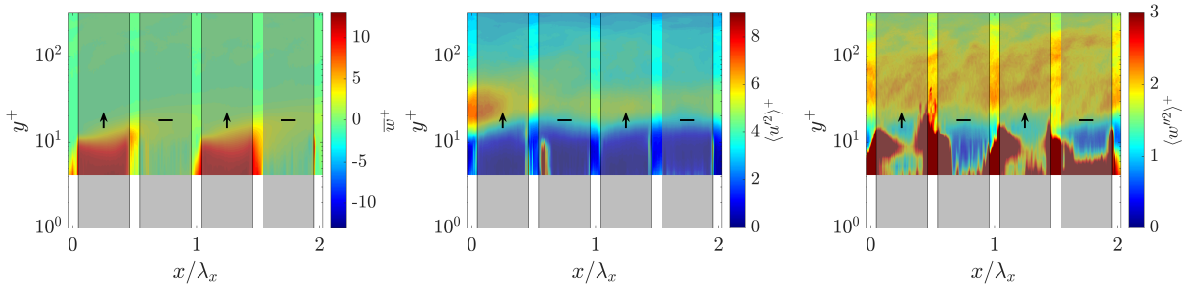

(a) Mean spanwise velocity (b) Streamwise stress (c) Spanwise stress

Figure D.37: ID 09, FOV1, config L0L0, $A^+ = 12.6$, $\lambda_x^+ = 400$

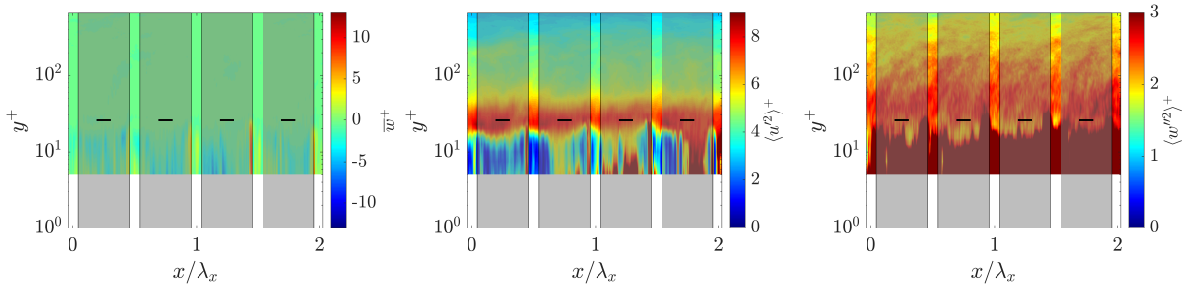

(a) Mean spanwise velocity (b) Streamwise stress (c) Spanwise stress

Figure D.38: ID 15, FOV1, non-actuated, $\lambda_x^+ = 826$

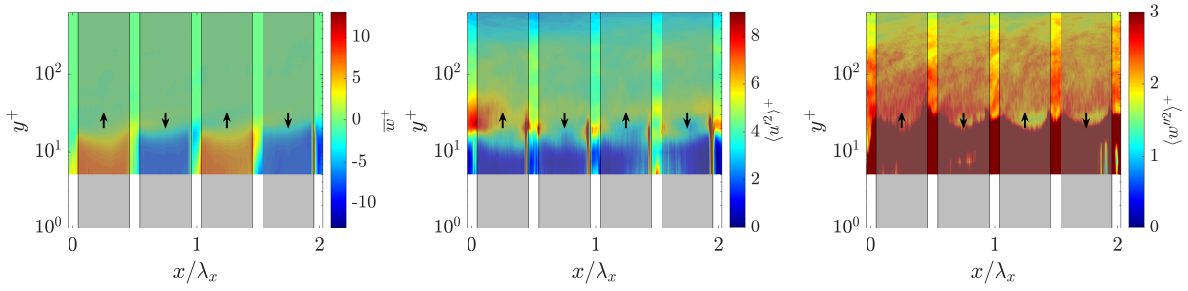

(a) Mean spanwise velocity (b) Streamwise stress (c) Spanwise stress

Figure D.39: ID 16, FOV1, $A^+ = 8.1$, $\lambda_x^+ = 826$

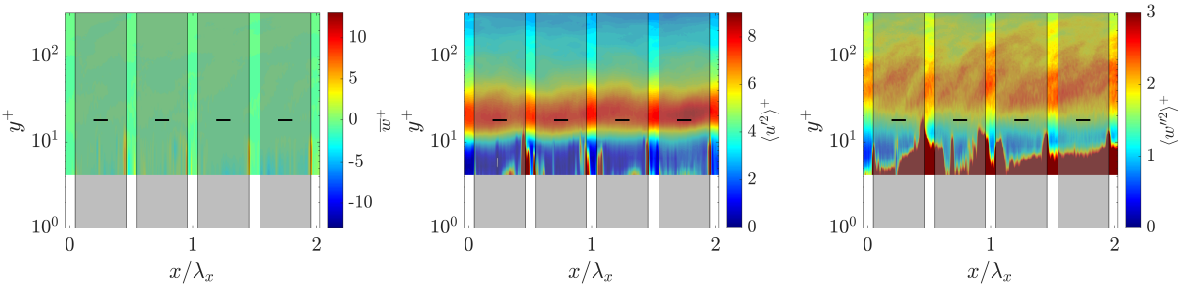

(a) Mean spanwise velocity (b) Streamwise stress (c) Spanwise stress

Figure D.40: ID 20, FOV1, config LLRR with $\lambda_x = 44$ mm, non-actuated, $\lambda_x^+ = 826$

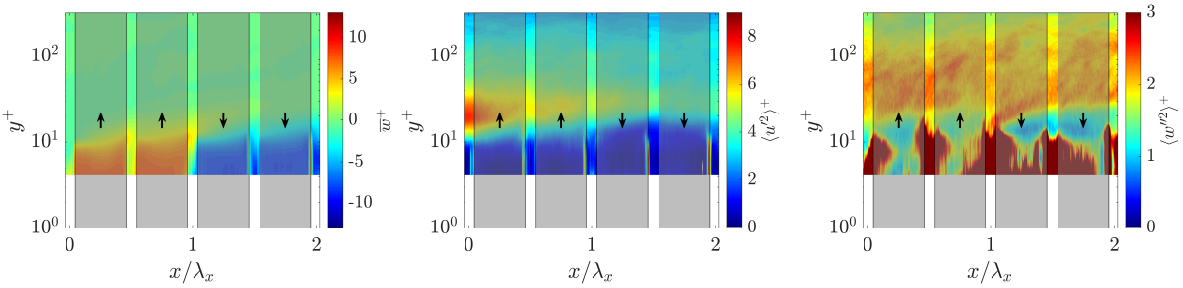

(a) Mean spanwise velocity (b) Streamwise stress (c) Spanwise stress

Figure D.41: ID 22, FOV1, config LLRR with $\lambda_x = 44$ mm, $A^+ = 8.4$ $\lambda_x^+ = 826$

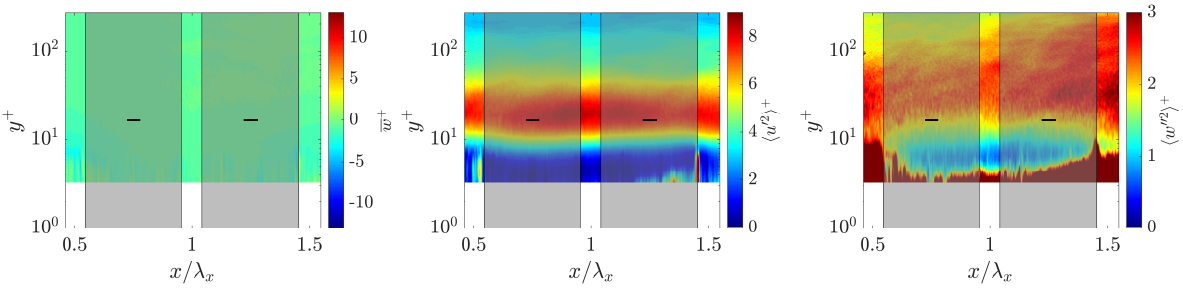

(a) Mean spanwise velocity (b) Streamwise stress (c) Spanwise stress

Figure D.42: ID 27, FOV2, non-actuated, $\lambda_x^+ = 400$

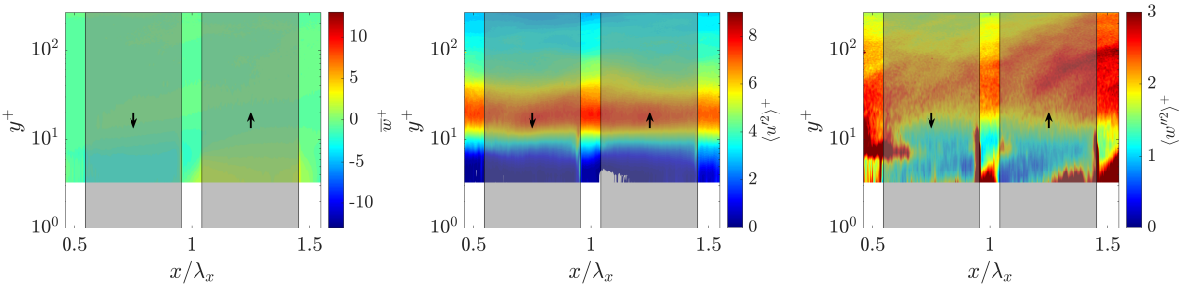

(a) Mean spanwise velocity (b) Streamwise stress (c) Spanwise stress

Figure D.43: ID 28, FOV2, $A^+ = 2.1$, $\lambda_x^+ = 400$

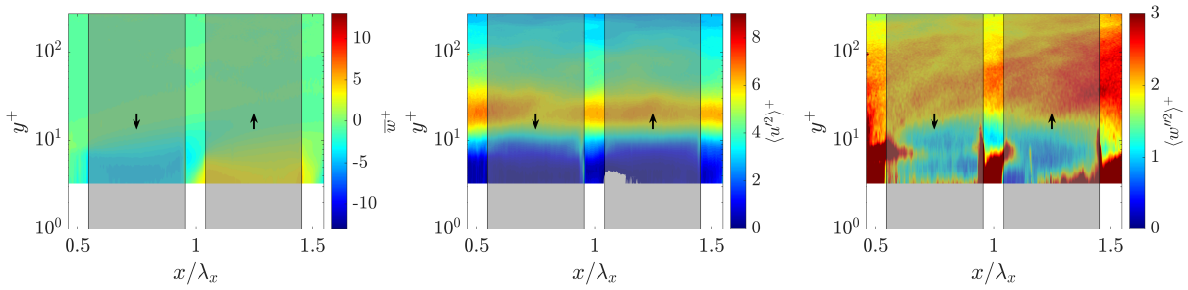

(a) Mean spanwise velocity (b) Streamwise stress (c) Spanwise stress

Figure D.44: ID 29, FOV2, $A^+ = 4.2$, $\lambda_x^+ = 400$

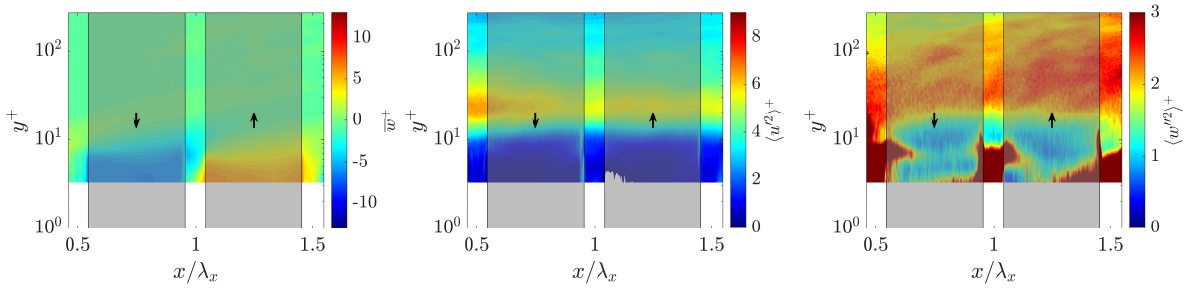

(a) Mean spanwise velocity (b) Streamwise stress (c) Spanwise stress

Figure D.45: ID 30, FOV2, $A^+ = 6.3$, $\lambda_x^+ = 400$

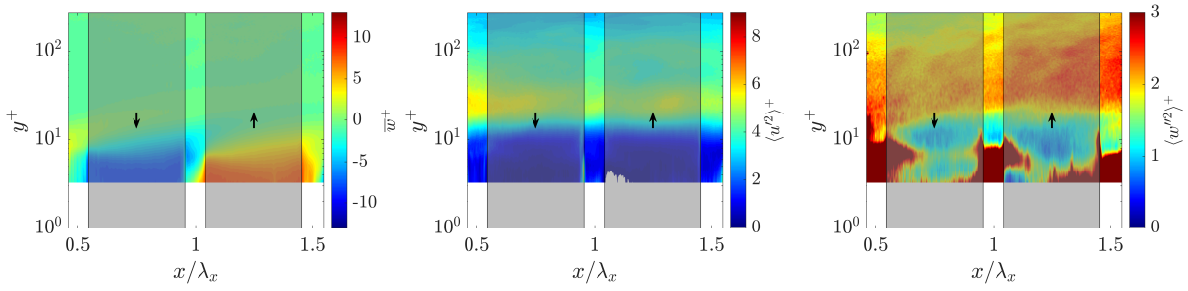

(a) Mean spanwise velocity (b) Streamwise stress (c) Spanwise stress

Figure D.46: ID 31, FOV2, $A^+ = 8.4$, $\lambda_x^+ = 400$

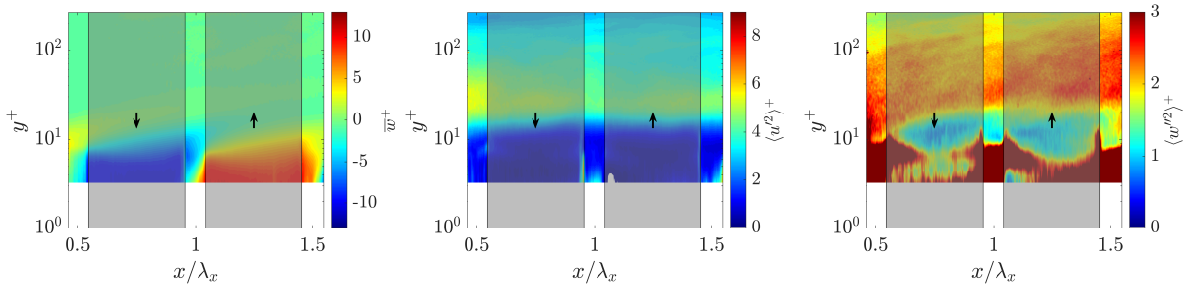

(a) Mean spanwise velocity (b) Streamwise stress (c) Spanwise stress

Figure D.47: ID 32, FOV2, $A^+ = 10.5$, $\lambda_x^+ = 400$

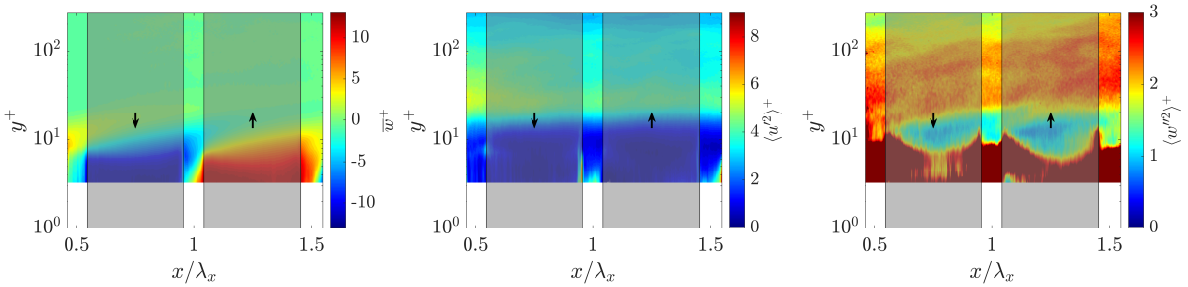

(a) Mean spanwise velocity (b) Streamwise stress (c) Spanwise stress

Figure D.48: ID 33, FOV2, $A^+ = 12.6$, $\lambda_x^+ = 400$

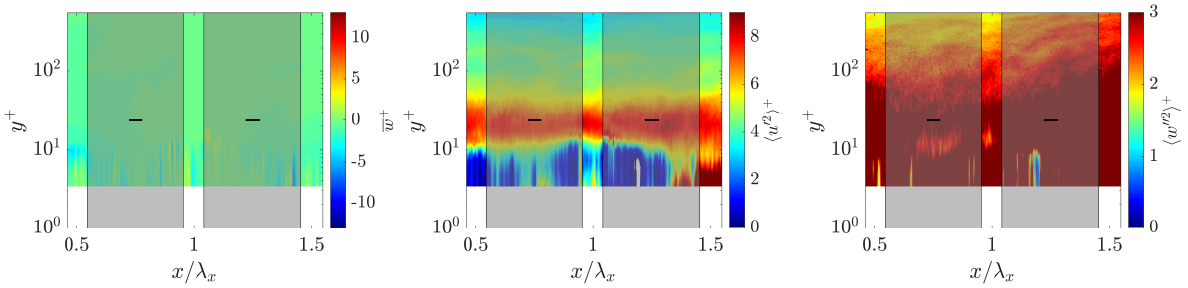

(a) Mean spanwise velocity (b) Streamwise stress (c) Spanwise stress

Figure D.49: ID 43, FOV2, non-actuated, $\lambda_x^+ = 826$

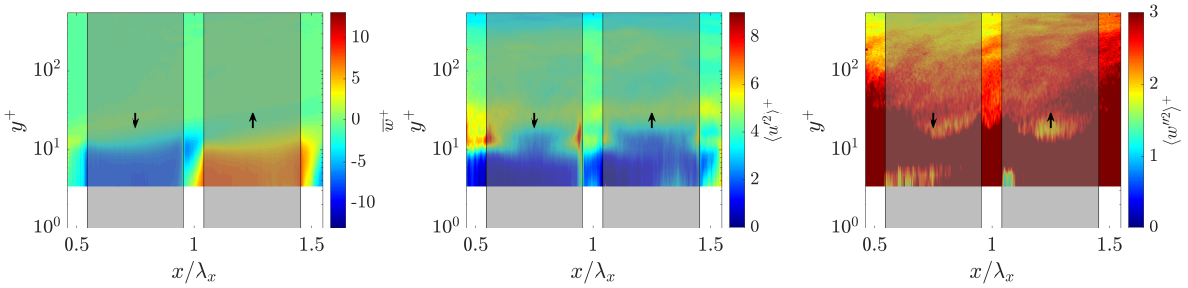

(a) Mean spanwise velocity (b) Streamwise stress (c) Spanwise stress

Figure D.50: ID 45, FOV2, $A^+ = 8.1$, $\lambda_x^+ = 826$

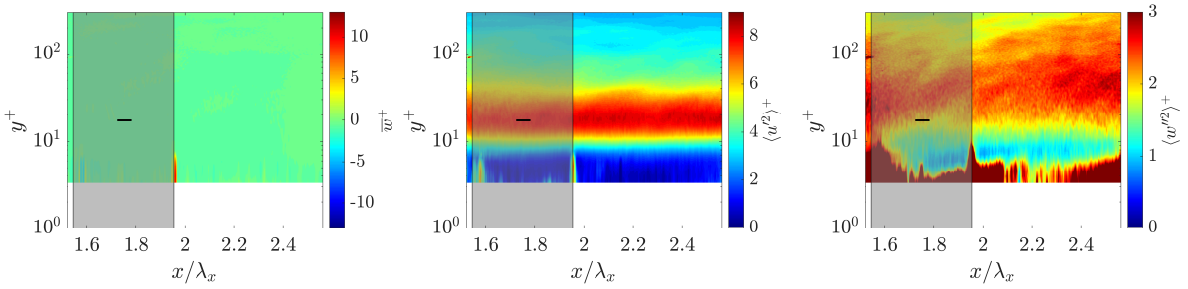

(a) Mean spanwise velocity (b) Streamwise stress (c) Spanwise stress

Figure D.51: ID 48, FOV3, non-actuated, $\lambda_x^+ = 398$

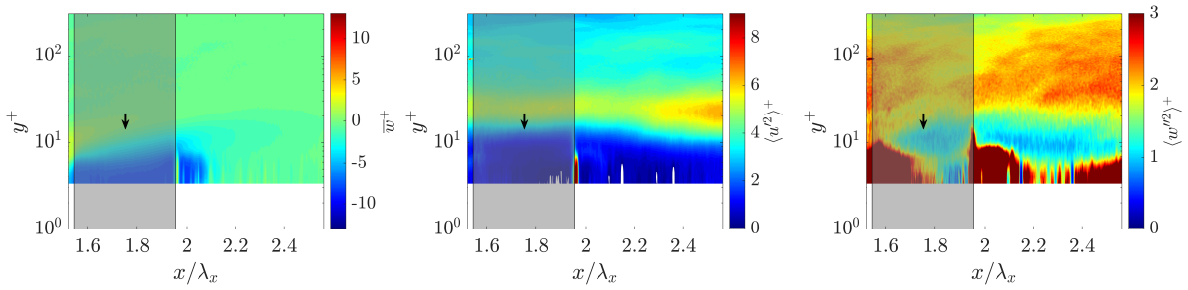

(a) Mean spanwise velocity (b) Streamwise stress (c) Spanwise stress

Figure D.52: ID 49, FOV3, $A^+ = 8.4$, $\lambda_x^+ = 398$

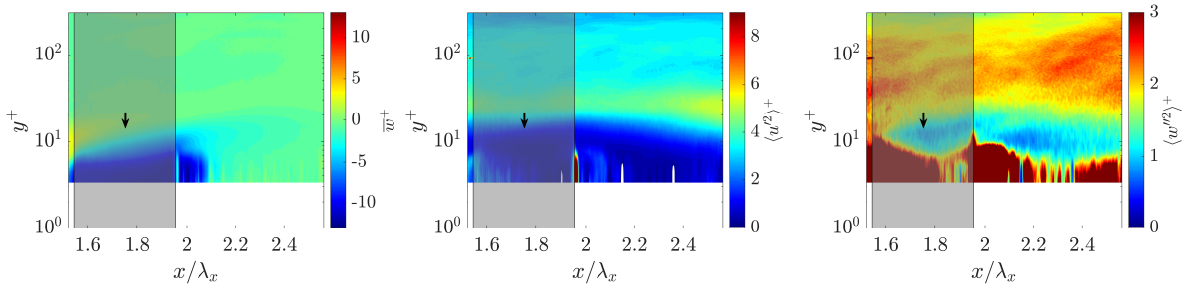

(a) Mean spanwise velocity (b) Streamwise stress (c) Spanwise stress

Figure D.53: ID 50, FOV3, $A^+ = 12.5$, $\lambda_x^+ = 398$

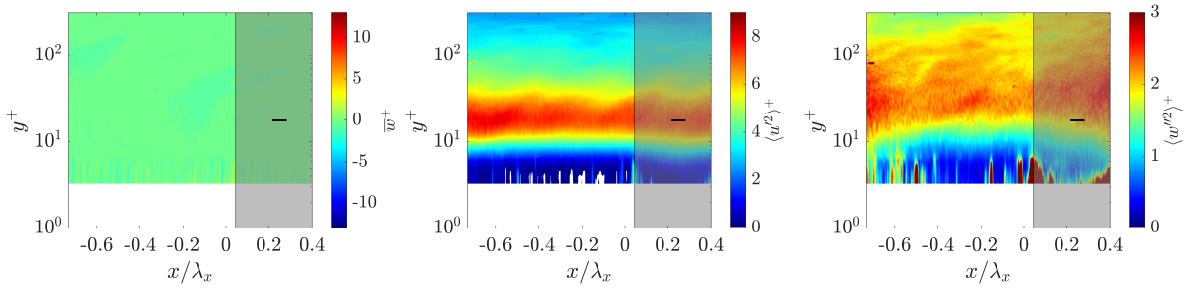

(a) Mean spanwise velocity (b) Streamwise stress (c) Spanwise stress

Figure D.54: ID 54, FOV4, non-actuated, $\lambda_x^+ = 398$

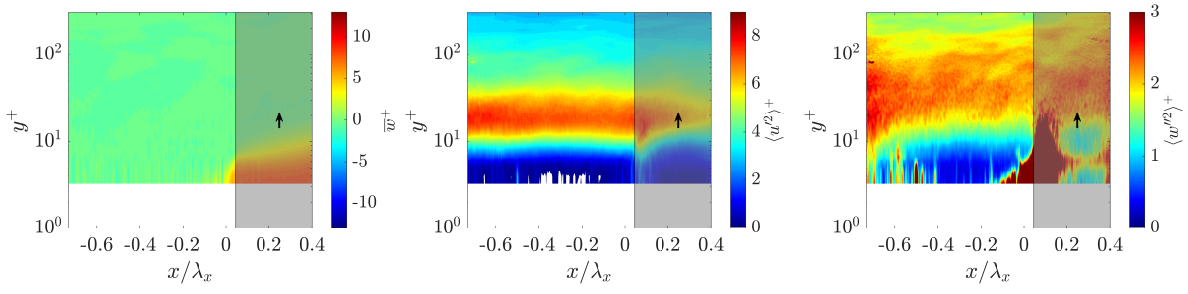

(a) Mean spanwise velocity (b) Streamwise stress (c) Spanwise stress

Figure D.55: ID 55, FOV4, $A^+ = 8.5$, $\lambda_x^+ = 401$

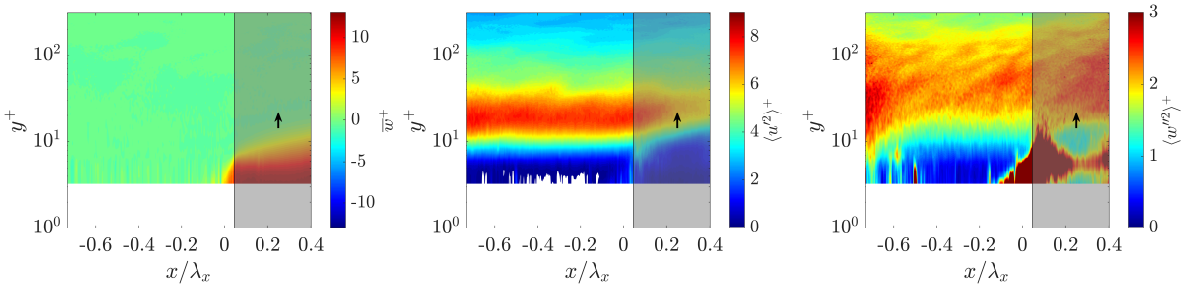

(a) Mean spanwise velocity (b) Streamwise stress (c) Spanwise stress

Figure D.56: ID 56, FOV4, $A^+ = 12.7$, $\lambda_x^+ = 401$

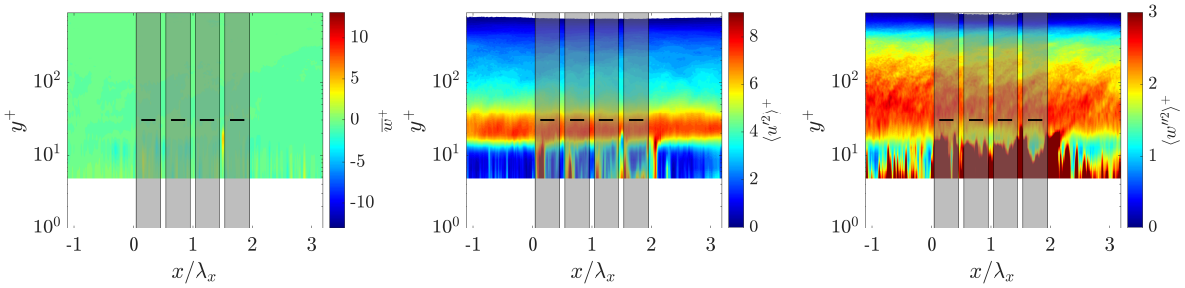

(a) Mean spanwise velocity (b) Streamwise stress (c) Spanwise stress

Figure D.57: ID 60, FOV5, non-actuated, $\lambda_x^+ = 286$

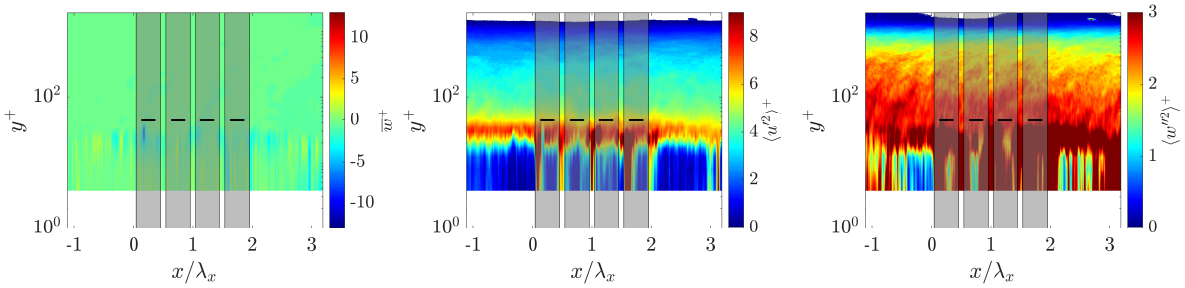

(a) Mean spanwise velocity (b) Streamwise stress (c) Spanwise stress

Figure D.58: ID 62, FOV5, non-actuated, $\lambda_x^+ = 610$

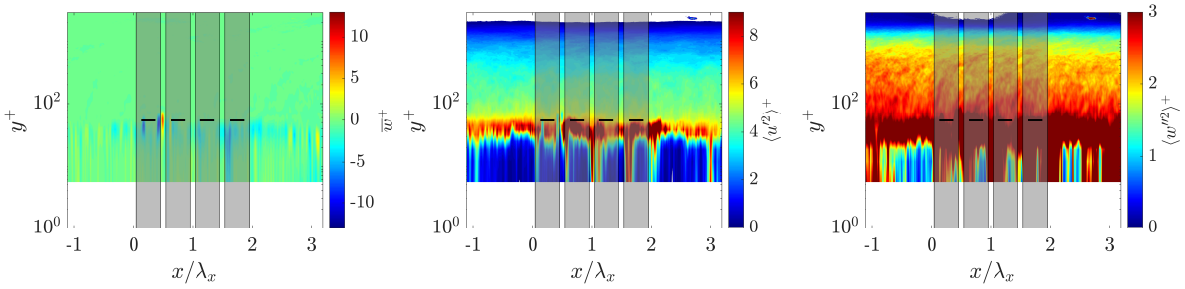

(a) Mean spanwise velocity (b) Streamwise stress (c) Spanwise stress

Figure D.59: ID 64, FOV5, non-actuated, $\lambda_x^+ = 934$

D.3. Turbulence statistics profiles

This section presents the turbulence statistics profiles of the measurements. The following statistics are presented: mean streamwise velocity, streamwise stress, wall-normal stress, the total and stochastic part of the spanwise stress and the pre-multiplied TKE production. The profiles are grouped per actuation wavelength, and the colour gradients represent the increase in spanwise velocity amplitude. Profiles are obtained by space averaging in the streamwise direction over the FOV to display the integral effect of actuation. Only FOV1 and 2 are considered since the actuation surface spans the complete FOV.

D.3.1. Profiles for FOV1

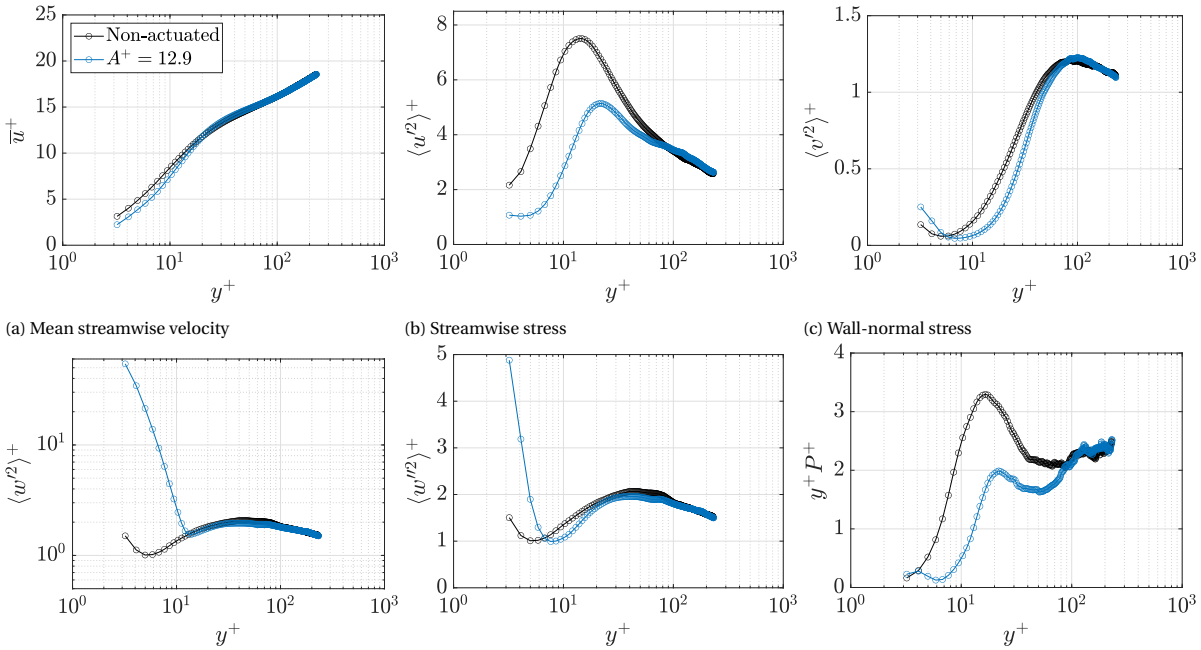

(a) Mean streamwise velocity

(b) Streamwise stress

(c) Wall-normal stress

(d) Spanwise stress

(e) Stochastic spanwise stress

(f) Pre-multiplied TKE production

Figure D.60: FOV1, $\lambda_x^+ = 293$

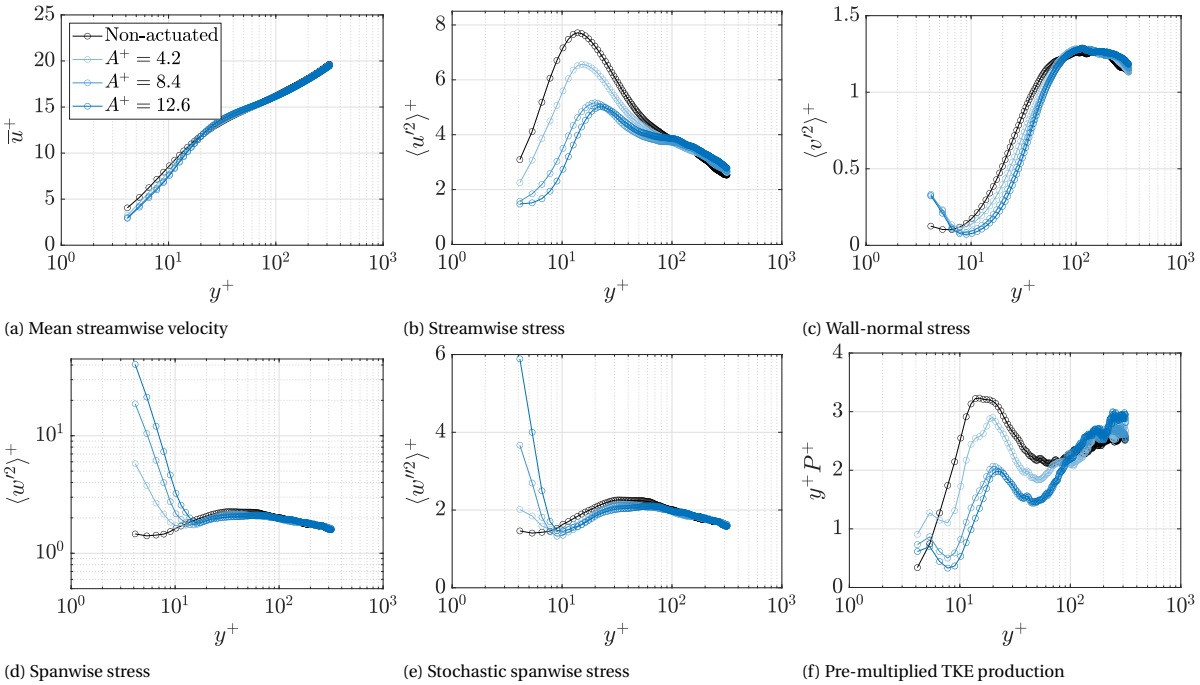

(a) Mean streamwise velocity (b) Streamwise stress (c) Wall-normal stress

(d) Spanwise stress (e) Stochastic spanwise stress (f) Pre-multiplied TKE production

Figure D.61: FOV1, $\lambda_x^+ = 400$

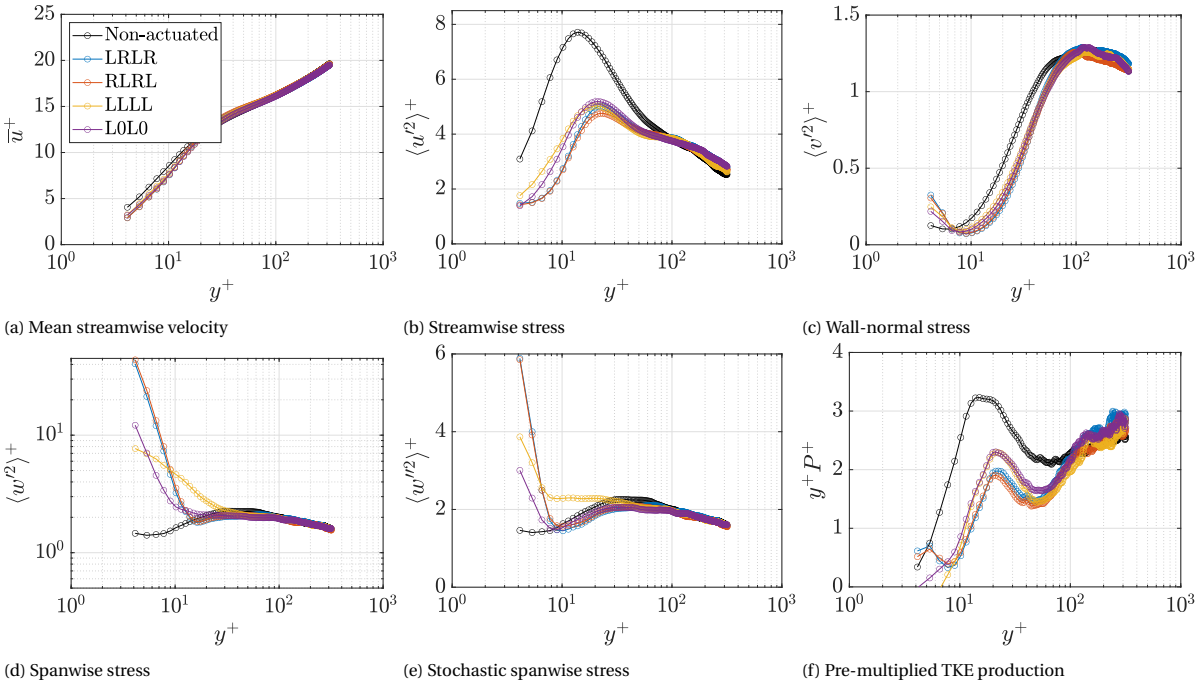

(a) Mean streamwise velocity (b) Streamwise stress (c) Wall-normal stress

(d) Spanwise stress (e) Stochastic spanwise stress (f) Pre-multiplied TKE production

Figure D.62: FOV1, $\lambda_x^+ = 400$. Note that here the different belt configurations are displayed

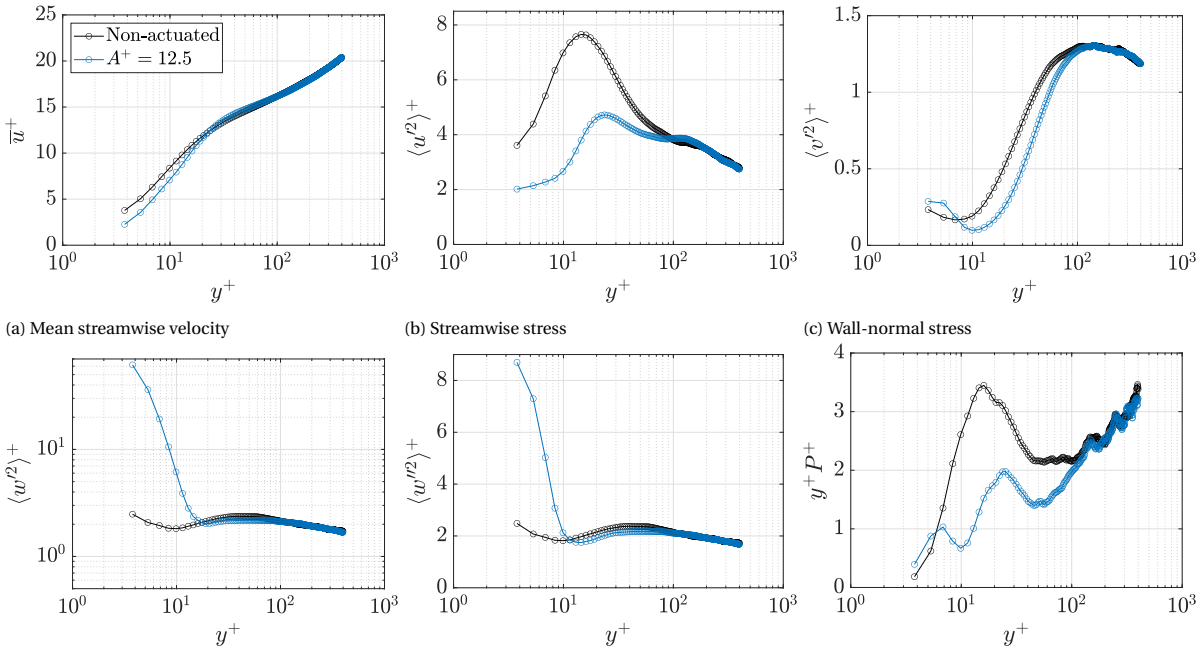

(a) Mean streamwise velocity (b) Streamwise stress (c) Wall-normal stress

(d) Spanwise stress (e) Stochastic spanwise stress (f) Pre-multiplied TKE production

Figure D.63: FOV1, $\lambda_x^+ = 505$

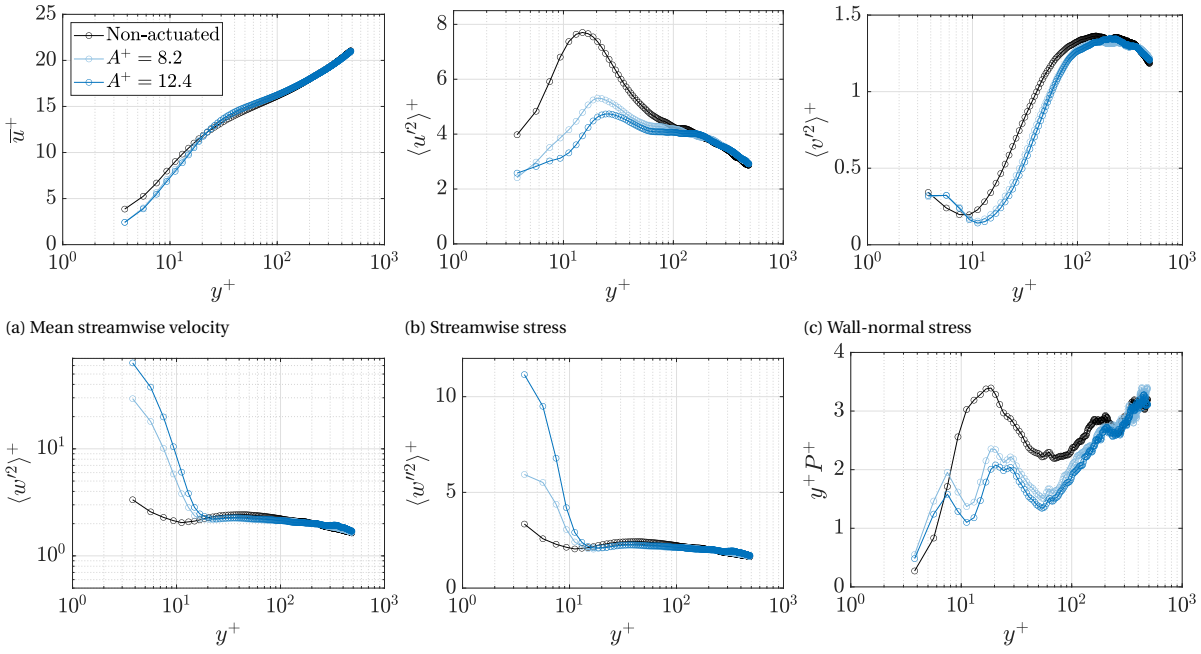

(a) Mean streamwise velocity (b) Streamwise stress (c) Wall-normal stress

(d) Spanwise stress (e) Stochastic spanwise stress (f) Pre-multiplied TKE production

Figure D.64: FOV1, $\lambda_x^+ = 611$

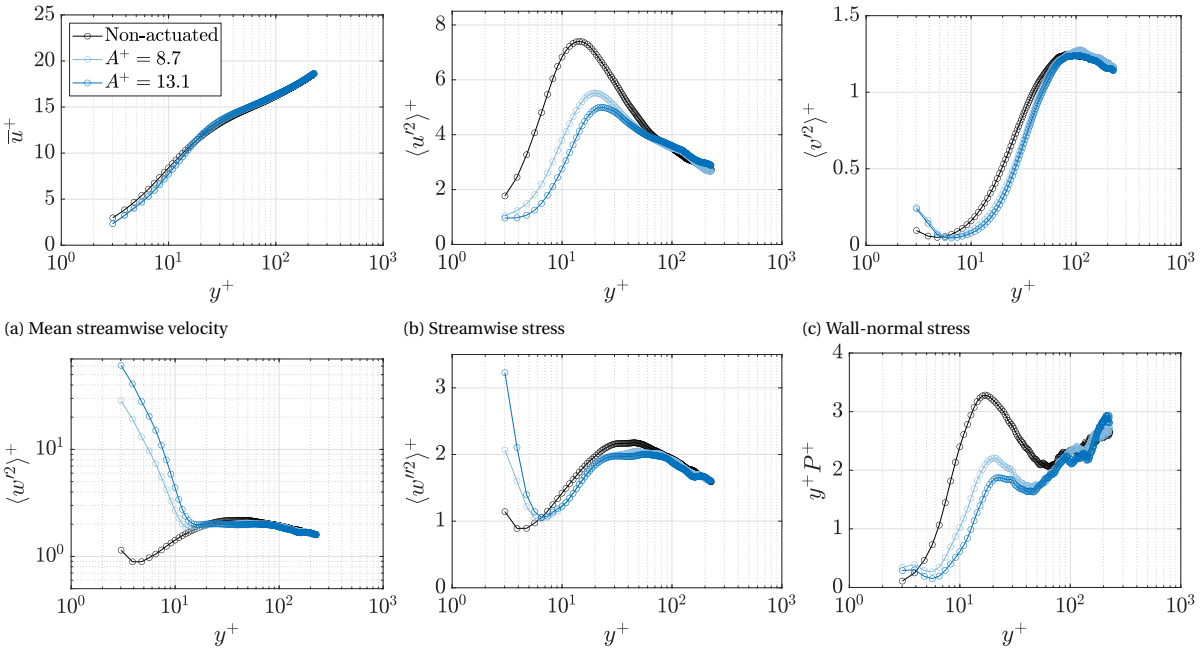

(a) Mean streamwise velocity (b) Streamwise stress (c) Wall-normal stress

(d) Spanwise stress (e) Stochastic spanwise stress (f) Pre-multiplied TKE production

Figure D.65: FOV1, $\lambda_x^+ = 616$. Note these are the cases with belt config LLRR for an actuation wavelength of $\lambda_x = 44$ mm.

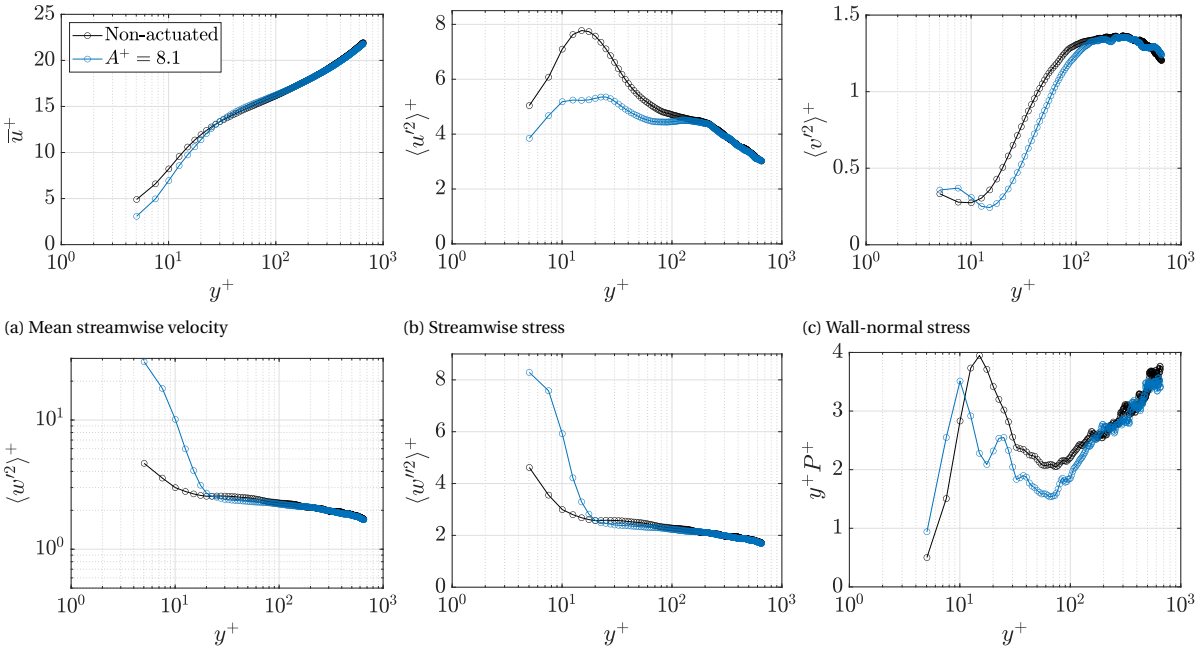

(a) Mean streamwise velocity (b) Streamwise stress (c) Wall-normal stress

(d) Spanwise stress (e) Stochastic spanwise stress (f) Pre-multiplied TKE production

Figure D.66: FOV1, $\lambda_x^+ = 827$

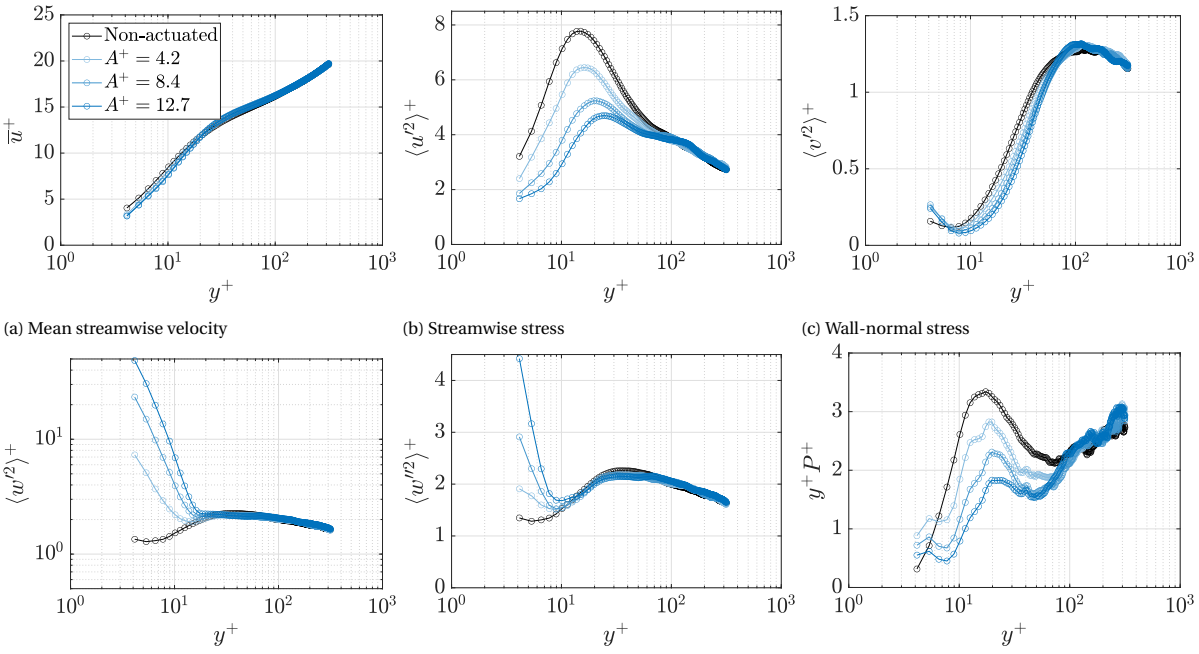

(a) Mean streamwise velocity (b) Streamwise stress (c) Wall-normal stress

(d) Spanwise stress (e) Stochastic spanwise stress (f) Pre-multiplied TKE production

Figure D.67: FOV1, $\lambda_x^+ = 792$. Note these are the cases with belt config LLRR for an actuation wavelength of $\lambda_x = 44$ mm.

D.3.2. Profiles for FOV2

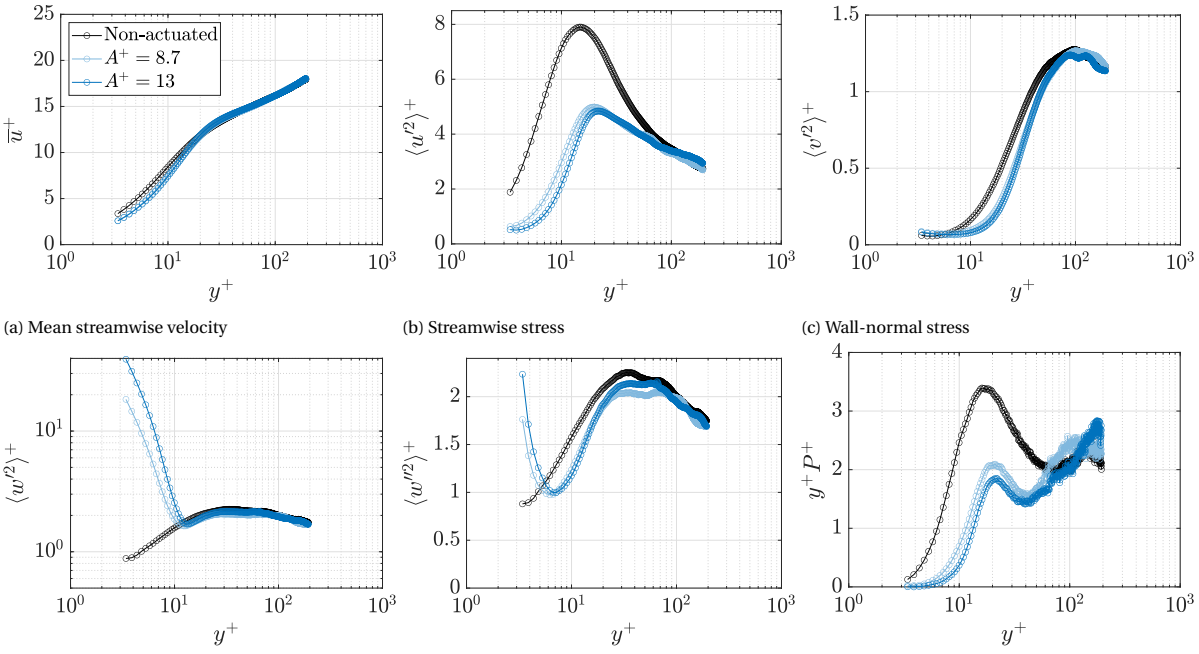

(a) Mean streamwise velocity (b) Streamwise stress (c) Wall-normal stress

(d) Spanwise stress (e) Stochastic spanwise stress (f) Pre-multiplied TKE production

Figure D.68: FOV2, $\lambda_x^+ = 292$

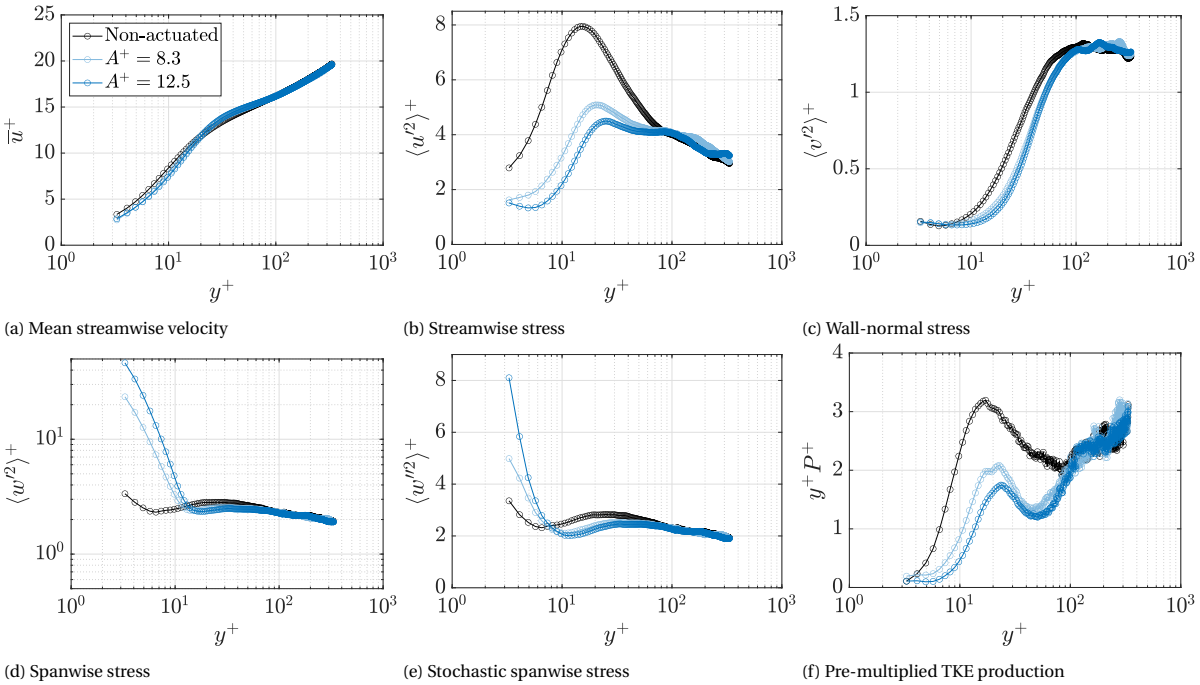

(a) Mean streamwise velocity
(b) Streamwise stress
(c) Wall-normal stress
(d) Spanwise stress
(e) Stochastic spanwise stress
(f) Pre-multiplied TKE production

Figure D.69: FOV2, $\lambda_x^+ = 505$

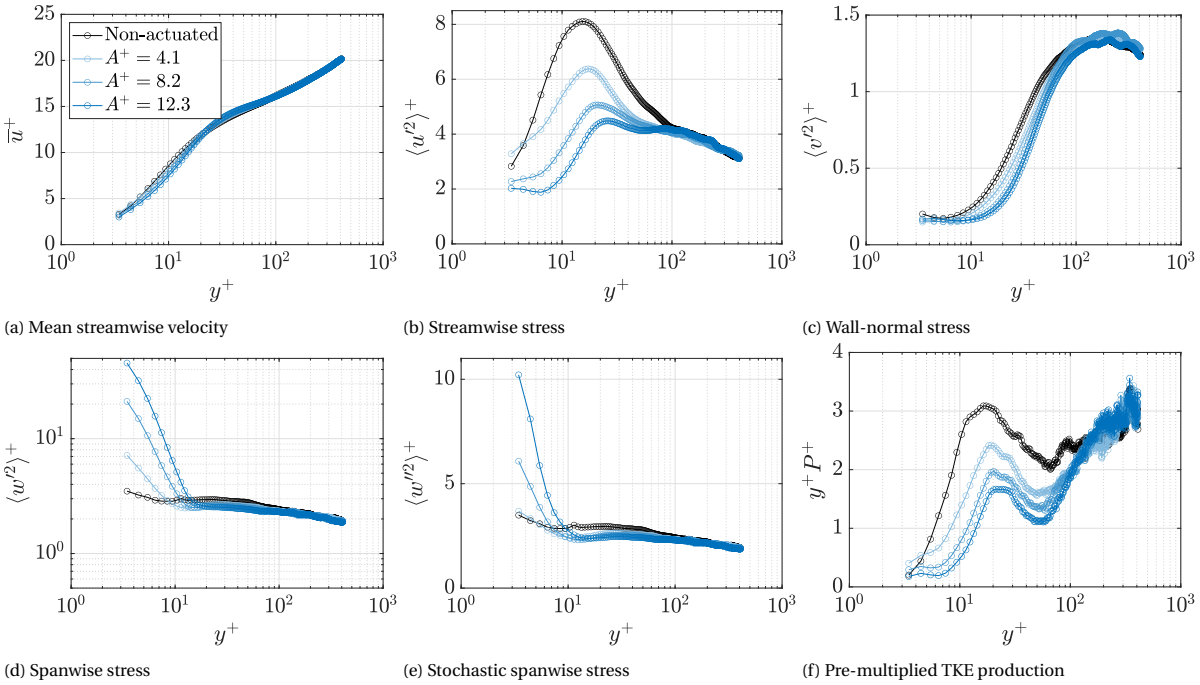

(a) Mean streamwise velocity
(b) Streamwise stress
(c) Wall-normal stress
(d) Spanwise stress
(e) Stochastic spanwise stress
(f) Pre-multiplied TKE production

Figure D.70: FOV2, $\lambda_x^+ = 616$

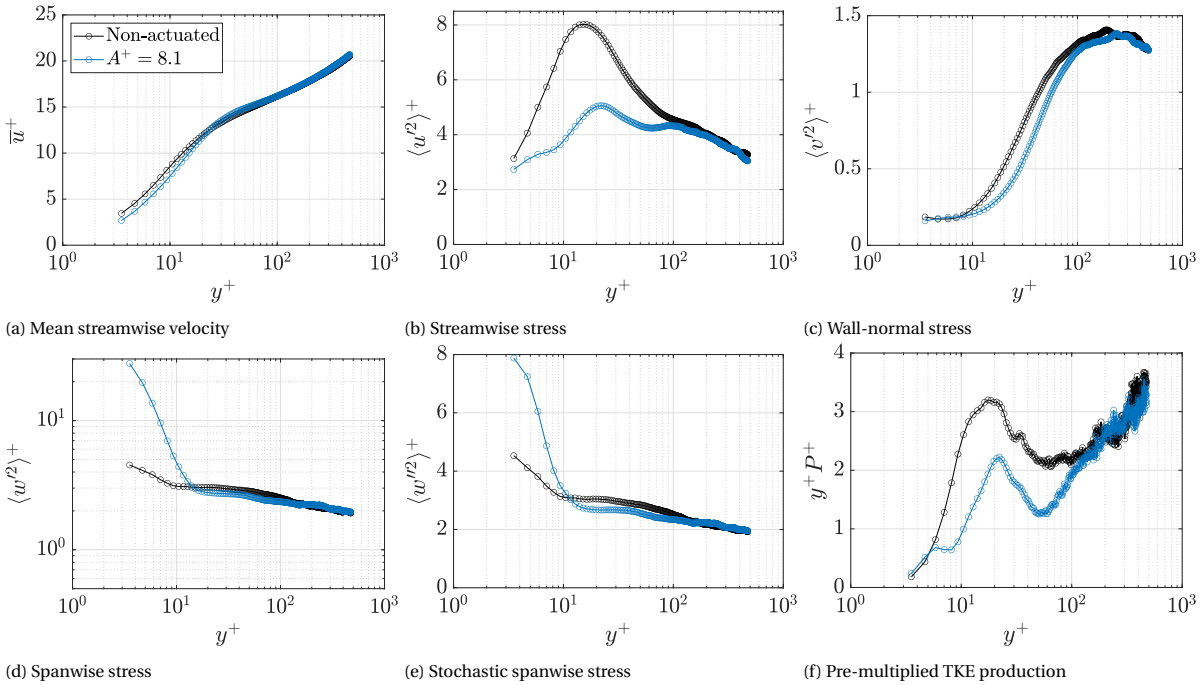

(a) Mean streamwise velocity (b) Streamwise stress (c) Wall-normal stress

(d) Spanwise stress (e) Stochastic spanwise stress (f) Pre-multiplied TKE production

Figure D.71: FOV2, $\lambda_x^+ = 721$

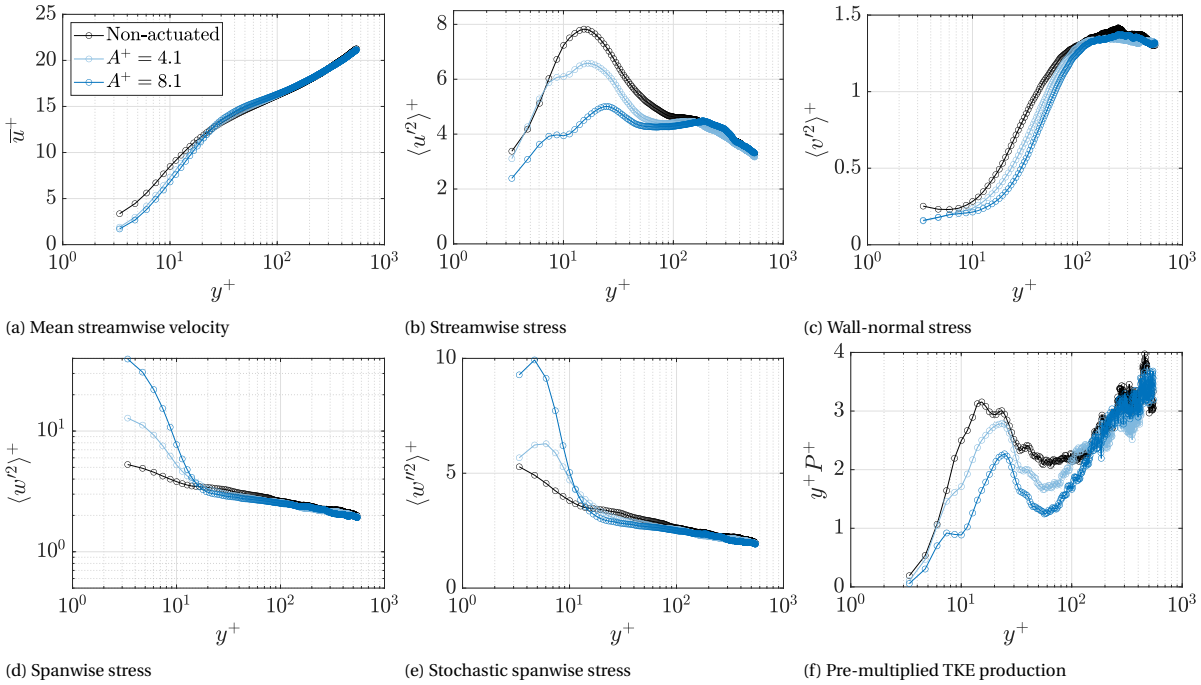

(a) Mean streamwise velocity (b) Streamwise stress (c) Wall-normal stress

(d) Spanwise stress (e) Stochastic spanwise stress (f) Pre-multiplied TKE production

Figure D.72: FOV2, $\lambda_x^+ = 827$

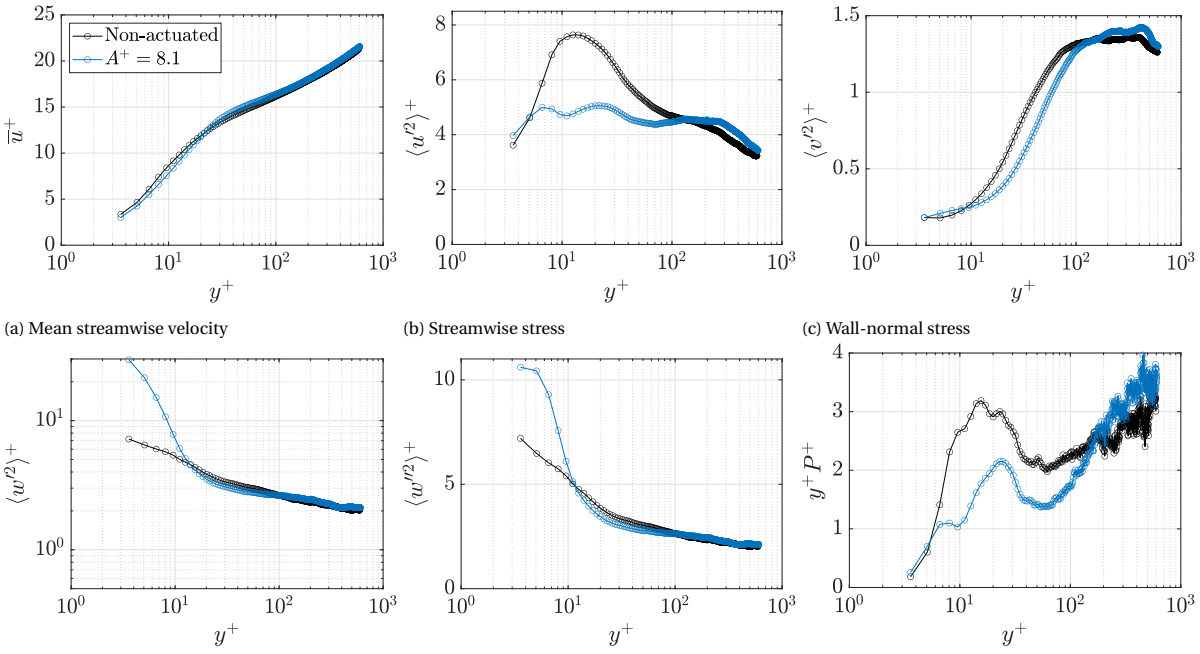

(a) Mean streamwise velocity

(b) Streamwise stress

(c) Wall-normal stress

(d) Spanwise stress

(e) Stochastic spanwise stress

(f) Pre-multiplied TKE production

Figure D.73: FOV2, $\lambda_x^+ = 930$

D.4. Drag characteristics from FOV2

This section presents the drag characteristics obtained from FOV2, in addition to the results discussed in Section 8.2.

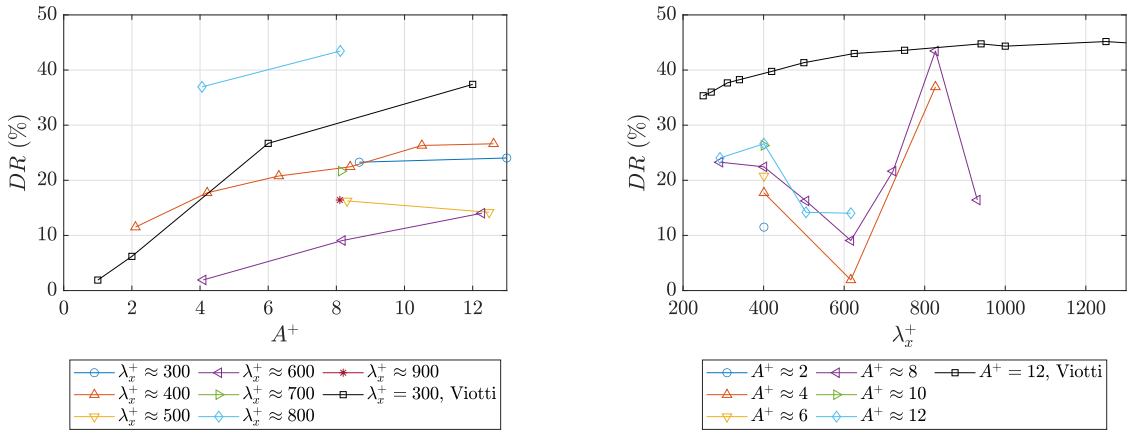

(a) DR response with A^+

(b) DR response with λ_x^+

Figure D.74: DR characteristics for FOV2, DNS data for sinusoidal forcing by Viotti et al. (2009) is added as reference.

D.5. Uncertainty quantification

Uncertainty quantification is performed for all the measurements, per the method of Sciacchitano and Wieneke (2016). The uncertainty of the instantaneous fields is omitted since the analysis in the thesis only regards statistical quantities. The uncertainty (ϵ) for the mean and variance of a velocity component calculated using N samples is defined as:

$$\epsilon_{\overline{u_i}} = \frac{\langle u_i' \rangle}{\sqrt{N}} \tag{D.2}$$

$$\epsilon_{\langle u_i'^2 \rangle} = \langle u_i'^2 \rangle \sqrt{\frac{2}{N-2}} \tag{D.3}$$

For these measurements, $N = 1{,}000$ corresponding to the 1,000 uncorrelated PIV images, in the case less vectors are available for a pixel location, the local number of vectors is used. The turbulence statistics profiles are obtained by space averaging in the streamwise direction, decreasing uncertainty with the inverse square root on the number of uncorrelated samples (N_{uncorr}). The interrogation windows have a 75% overlap. Hence every fourth streamwise point is considered an uncorrelated sample. For a given turbulence statistic (T) the uncertainty is:

$$\epsilon_T = \frac{\frac{1}{N_{uncorr}} \sum_{\xi=1}^{N_{uncorr}} \epsilon_T(\xi)}{\sqrt{N_{uncorr}}} \tag{D.4}$$

.

The average uncertainty of the profiles is expressed as a percentage with respect to the local statistic as:

$$\epsilon_T\ (\%) = \frac{1}{I} \sum_{i=1}^{I} \frac{\epsilon_T(y_i)}{T(y_i)} \times 100 \tag{D.5}$$

The uncertainty quantification of all the measurements is presented in Table D.2. The uncertainties for the relevant turbulence statistics are indicated, for brevity, the uncertainties of the covariance are omitted.

ID	FOV	U_∞ (m/s)	Config	A^+	λ_x^+	$\epsilon_{\overline{u}}$ (%)	$\epsilon_{\overline{w}}$ (%)	$\epsilon_{\langle u'^2 \rangle}$ (%)	$\epsilon_{\langle v'^2 \rangle}$ (%)	$\epsilon_{\langle w'^2 \rangle}$ (%)
01	1	4.7	-	-	-	0.040	1.40	0.344	0.344	0.344

ID	FOV	U_∞ (m/s)	Config	A^+	λ_x^+	$\epsilon_{\overline{u}}$ (%)	$\epsilon_{\overline{w}}$ (%)	$\epsilon_{\langle u'^2\rangle}$ (%)	$\epsilon_{\langle w'^2\rangle}$ (%)	$\epsilon_{\langle w'^2\rangle}$ (%)
02	1	4.7	LRLR	12.9	293	0.042	1.59	0.343	0.343	0.343
03	1	6.7	-	-	-	0.037	1.24	0.343	0.344	0.344
04	1	6.7	LRLR	4.2	400	0.065	1.71	0.343	0.343	0.343
05	1	6.7	LRLR	8.4	400	0.045	2.20	0.343	0.343	0.343
06	1	6.7	LRLR	12.6	400	0.042	1.79	0.343	0.343	0.343
07	1	6.7	RLRL	12.6	400	0.038	2.35	0.343	0.343	0.343
08	1	6.7	LLLL	12.6	400	0.036	1.29	0.342	0.343	0.342
09	1	6.7	L0L0	12.6	400	0.038	1.35	0.343	0.343	0.343
10	1	8.8	-	-	-	0.034	1.76	0.343	0.345	0.344
11	1	8.8	LRLR	12.5	505	0.038	2.46	0.343	0.343	0.343
12	1	10.9	-	-	-	0.035	1.55	0.344	0.344	0.344
13	1	10.9	LRLR	8.2	611	0.041	3.22	0.343	0.343	0.343
14	1	10.9	LRLR	12.4	610	0.037	3.21	0.343	0.343	0.343
15	1	15.2	-	-	-	0.033	1.76	0.343	0.344	0.344
16	1	15.2	LRLR	8.1	826	0.039	3.98	0.355	0.355	0.355
17	1	4.6	-	-	-	0.040	2.70	0.343	0.344	0.344
18	1	4.7	LLRR	8.7	574	0.055	2.01	0.343	0.343	0.343
19	1	4.6	LLRR	13.1	574	0.046	1.44	0.343	0.343	0.343
20	1	6.7	-	-	-	0.037	1.39	0.344	0.345	0.344
21	1	6.7	LLRR	4.2	792	0.048	1.79	0.342	0.343	0.343
22	1	6.7	LLRR	8.4	792	0.044	1.83	0.342	0.343	0.343
23	1	6.7	LLRR	12.7	792	0.041	2.20	0.343	0.343	0.343
24	2	4.6	-	-	-	0.038	1.16	0.345	0.345	0.345
25	2	4.6	LRLR	8.7	292	0.038	1.64	0.344	0.344	0.344
26	2	4.6	LRLR	13	292	0.037	1.35	0.344	0.345	0.344
27	2	6.7	-	-	-	0.036	1.12	0.345	0.345	0.345
28	2	6.7	LRLR	2.1	401	0.039	1.22	0.344	0.344	0.344
29	2	6.7	LRLR	4.2	400	0.037	1.20	0.344	0.344	0.344
30	2	6.7	LRLR	6.3	400	0.036	1.18	0.344	0.344	0.344
31	2	6.7	LRLR	8.4	400	0.035	1.41	0.344	0.344	0.344
32	2	6.7	LRLR	10.5	400	0.035	1.31	0.344	0.344	0.344
33	2	6.7	LRLR	12.6	400	0.034	2.23	0.345	0.345	0.345
34	2	8.8	-	-	-	0.034	1.39	0.347	0.347	0.347
35	2	8.8	LRLR	8.3	505	0.034	3.63	0.346	0.346	0.346
36	2	8.8	LRLR	12.5	505	0.033	1.99	0.345	0.345	0.345
37	2	10.9	-	-	-	0.033	1.36	0.345	0.345	0.345
38	2	10.9	LRLR	4.1	616	0.033	1.55	0.344	0.344	0.344
39	2	10.9	LRLR	8.2	616	0.033	2.03	0.344	0.345	0.345
40	2	10.9	LRLR	12.3	616	0.033	2.25	0.345	0.345	0.345
41	2	13	-	-	-	0.035	1.59	0.352	0.353	0.353
42	2	13	LRLR	8.1	721	0.034	1.71	0.345	0.345	0.345
43	2	15.2	-	-	-	0.032	1.87	0.345	0.346	0.346
44	2	15.2	LRLR	4.1	827	0.035	1.96	0.345	0.345	0.345
45	2	15.2	LRLR	8.1	826	0.035	1.71	0.345	0.345	0.345
46	2	17.3	-	-	-	0.033	1.72	0.346	0.346	0.346
47	2	17.3	LRLR	8.1	930	0.034	2.19	0.345	0.345	0.345
48	3	6.7	-	-	-	0.034	1.34	0.352	0.353	0.353
49	3	6.7	LRLR	8.4	398	0.034	1.65	0.351	0.353	0.353
50	3	6.7	LRLR	12.7	398	0.033	1.38	0.352	0.353	0.353
51	3	10.9	-	0	0	0.032	1.64	0.352	0.354	0.354
52	3	10.9	LRLR	8.3	605	0.032	1.75	0.352	0.353	0.353
53	3	10.9	LRLR	12.5	605	0.031	1.74	0.352	0.353	0.353
54	4	6.6	-	-	-	0.033	1.64	0.347	0.347	0.347
55	4	6.6	LRLR	8.5	401	0.034	1.50	0.347	0.348	0.348
56	4	6.6	LRLR	12.7	401	0.033	1.70	0.347	0.348	0.347

ID	FOV	U_∞ (m/s)	Config	A^+	λ_x^+	$\epsilon_{\overline{u}}$ (%)	$\epsilon_{\overline{w}}$ (%)	$\epsilon_{\langle u'^2\rangle}$ (%)	$\epsilon_{\langle w'^2\rangle}$ (%)	$\epsilon_{\langle w'^2\rangle}$ (%)
57	4	10.7	-	-	-	0.031	2.15	0.347	0.348	0.348
58	4	10.7	LRLR	8.3	612	0.031	1.74	0.347	0.347	0.347
59	4	10.7	LRLR	12.5	612	0.031	2.58	0.347	0.347	0.347
60	5	4.6	-	-	-	0.020	1.26	0.361	0.361	0.361
61	5	4.6	LRLR	6.6	286	0.029	1.58	0.362	0.362	0.362
62	5	10.8	-	-	-	0.019	1.28	0.361	0.361	0.361
63	5	10.8	LRLR	6.2	610	0.020	1.86	0.361	0.361	0.361
64	5	17.1	-	-	-	0.017	1.20	0.361	0.361	0.361
65	5	17.1	LRLR	6.1	934	0.019	1.60	0.361	0.361	0.362

Table D.2: Uncertainty quantification for the PIV measurements